Imperial College London

Department of Materials

Hybrid biomaterials with tuneable mechanical property gradients

Gloria Young

September 2019

Submitted for the degree of Doctor of Philosophy

Abstract

Sol-gel hybrid materials are made up of covalently bonded and interpenetrating networks of organic and inorganic components and produce a synergy of the properties of those components above the nanoscale. By altering the ratio of inorganic to organic content, the mechanical properties can be tuned. Here, a silica-poly(tetrahydrofuran) hybrid system was developed with the aim to form a graded stiffness structure that could imitate the radial variation in stiffness of the intervertebral disc and address the unmet clinical need of intervertebral disc replacement.

Hybrids were formed with a range of silica contents between 4 and 45 wt.%, varying from an elastomeric to a glassy material, with compressive stiffness between 2 and 200 MPa. High compressive strains are recoverable and mechanical properties were maintained on soaking up to 1.5 years and to 10000 cycles in compression. The hybrid surface was shown to support cell attachment and extract solutions containing the hybrid were non-cytotoxic.

A novel synthesis method was developed to join hybrid sols during their gelation, forming a single specimen with a variation in silica content along its length, producing a corresponding variation in stiffness. Samples joined in this way were at least as strong as single phase samples in tension and compression. This exploits the gradual gelation process of the hybrid sol, which can also be used to create a successful ink for 3D extrusion printing: porous scaffolds were formed in this way with 27.7 wt.% SiO_2. Meniscus and intervertebral disc replacement prototypes were formed and tested under cyclic loading at rates for comparison with human disc data.

Declarations

Declaration of originality

I hereby certify that the work presented in this thesis is the result of my own investigations, which were carried out at Imperial College London from January 2016 to September 2019, except where otherwise stated. Other contributions have been truly and properly acknowledged.

The synthesis process for multiphase hybrid materials is included in the invention patented: Tallia F, Jones JR, Cipolla LF, Russo L, Young G, "Hybrid materials and process for production thereof," GB 1605446.2, 2019.

Copyright declaration

Gloria Young

September 2019

Acknowledgements

Firstly I thank EPSRC for funding for this project.

My sincere gratitude to my supervisors Prof Julian R Jones and Dr Finn Giuliani. I would also like to acknowledge and thank Prof Jonathan Jeffers for invaluable advice at various points especially the Late Stage Review.

Julian thank you so much for your never-ending support and mentoring over the past 3 and a half years, as well as the freedom and trust you have given me. I just love being a part of this research group.

Thank you to everyone I have worked with: Dr Francesca Tallia for your supervision, guidance, advice and support every step of the way; Enric Juan Alcocer, Mani Chellappan, Toby Simpson, Seyed Ataollah Naghavi - thank you all for everything you taught me, it was really a pleasure to work with you; Jeff Clark for collaborating on DIC and DVC work, I enjoy working with you so much, thank you for all of your patience and help, I'm so happy to be your friend as well; Prof Sara Rankin and Dr Silvia Ferreira for cell culture experiments (and all your explanations and enthusiasm!); Dr Maria Parkes for guidance with RAMAN and AFM; Christoph Salzelechner for gamma irradiation at King's College London; Dr Nic Newell, Jeff Clark and Saman Tavana for collaboration on mechanical testing against IVDs; Prof John Hanna and Dr Josh Clark for solid state NMR carried out at Warwick University; Jeff Clark and Brett Clark for Micro-CT imaging at Natural History Museum; Dr Oriol Gavaldà Diaz for TEM & l'amistat; Prof Cristian Covarrubias and everyone from Laboratorio de Nanobiomateriales, Universidad de Chile, you made me so welcome and I will remember it forever. Thank you to Mr Richard Sweeney, Dr Victoria Bemmer, Dr Mahmoud Ardakani, Dr Cati Ware. Special thank you to Mr Ben Chan and Mr Russell Stracey for all of your help and expertise.

Thank you to everyone who runs our department and works to make life in it better, especially Mrs Darakshan Khan and Dr Alba Matas Adams; thank you to everyone who cleans it, who fixes and maintains it.

The best thing about being here has really been so many amazing people I have met along the way. Thank you to all of the JRJ group past and present, for all the laughter and support and friendship, Lizzie, Zhen, Tian, Justin, Maria, Pablo, Taneisha, Haffsah, Agathe, Breno and Stella especially. Paul thanks for so much fun in the lab. Ale you are like my big sister, thank you for being there for me always. Marco, grazie mille. Thanks to all of GradSoc, it has been great!

To everyone in CASC, I cannot tell you how much it has meant to me being there over the past year, you all look after me so much and I feel so happy in the office (and up the mountain). Eduardo thank you for your encouragement. Clare thank you for always looking out for me and being a great friend.

Thank you to everyone who has ever taught me and believed in me, I promise to pay it forward always.

Thank you to Jane and Richard for always being there for me even when you don't know it. Thank you to my precious baby brother Daniel, you are the best.

Thank you to Louise and to Giulia, you don't know how much you mean to me, thank you for your endless support of me and all of the laughter. Thank you Chris for being the most amazing person and friend, I owe you so much. James and Khadim, I can't tell you how much our friendship means to me, thanks for always laughing at me.

Fra (un'altra volta), non so come scrivere quanto ti voglio ringraziare. Dal primo giorno sei stata un'ispirazione costante e più di tutto una grande amica. Grazie dal profondo del cuore, non sarei ne dove sono ne chi sono senza di te. Ti voglio tanto bene.

Finally thank you to Louise, without whom nothing would be possible.

Table of Contents

List of Figures & Tables

List of Abbreviations

3D	Three-dimensional
ABAM	Antibiotic Antimycotic
AFM	Atomic Force Microscopy
ATR	Attenuated Total Reflectance
BEI	Backscattered Electron Imaging
$BF_3{\cdot}O(C_2H_5)_2$	Boron trifluoride diethyl etherate
CAD	Computer Assisted Design
$CDCl_3$	Deuterated chloroform
CNC	Computer numerical control
CROP	Cationic ring-opening polymerisation
CPMAS	Cross-polarisation magic angle spinning
DC	Direct Correlation
DIC	Digital Image Correlation
DMA	Dynamic Mechanical Analysis
DMEM	Dulbecco's modified Eagle medium
DSC	Differential Scanning Calorimetry
DVC	Digital Volume Correlation
FBS	Foetal Bovine Serum
FFT	Fast Fourier Transform
FTIR	Fourier transform infrared spectroscopy
GPTMS	(3-Glycidyloxypropyl)trimethoxysilane
HCl	Hydrochloric acid
ICPTS	3-(Triethoxysilyl)propyl isocyanate
IVD	Intervertebral disc
MAS	Magic angle spinning
Micro-CT	Micro-computed tomography
MMA	Methylmethacrylate
MTT	3-(4,5-dimethylthiazol-2-yl)-2,5-diphenyltetrazolium bromide
NMR	Nuclear Magnetic Resonance
PAAm	Polyacrylamide
PAMPS	Poly(2-acrylamido-2-methylpropanesulfonic acid)
PBS	Phosphate buffered saline solution

PBT	Triton-X 100 in PBS
PCL	Polycaprolactone
PE	Polyethylene
PET	Polyethylene terephthalate
PFA	Perfluroalkoxy
PGA	Poly(γ-glutamic acid)
PMMA	Polymethylmethacrylate
PMP	Polymethylpentene
PTFE	Polytetrafluoroethylene
PTHF	Polytetrahydrofuran
PVA	Polyvinylalcohol
RT	Room temperature
SBF	Simulated Body Fluid
SEI	Secondary Electron Imaging
SEM	Scanning Electron Microscopy
SiO_2	Silica
TCP	Tissue culture plastic
TEM	Transmission Electron Microscopy
TEOS	Tetraethylorthosilicate
TGA	Thermogravimetric analysis
THF	Tetrahydrofuran
TMSPMA	3-(Trimethoxysilyl)propylmethacrylate
UHMWPE	Ultra-high molecular weight polyethylene
WLIF	White Light Interferometry
XRD	X-ray diffraction
ZDEC	zinc diethyldithiocarbamate

Introduction

A child born in the UK today can expect to live 81.2 years [1]; however, quality of life can be limited by musculoskeletal problems. Lower back pain is the leading cause of disability globally [2] which is linked to degenerative changes in the intervertebral discs (IVDs) [3]. Articulating joints in the body like the knee and the hip are commonly and successfully treated by replacement of whole or part of the joint with a synthetic implant, and the number of these operations continues to rise year on year [4] promoted by their success in reducing pain and increasing mobility. Following this model, implants have been trialled using a ball-in-socket joint to replace the IVD. However, these total disc replacements (TDRs) have thus far not provided a successful route to restore the spine mobility and prevent pain.

Another route is to attempt to repair the disc, and in fact non-surgical rehabilitative treatments for chronic back pain associated with IVD degeneration have not shown a clear difference in patient outcomes with respect to stabilisation surgery [5] or TDR [6]. However, cartilage tissue is slow to repair and other reparative methods designed to regenerate the disc are in development [7, 8] which are most applicable to less severe disc damage and younger patients. The standard surgical solution after disc removal is stabilisation by spinal fusion, consisting of fixing adjacent vertebrae together and surrounding with a metallic cage, which retains the separation height between vertebrae but alters the biomechanics of the spine, which can affect the rest of the body, for example contributing to failure of hip replacements [9]. There is an unmet clinical need for a total disc replacement than can replicate the IVD, requiring materials that can match the mechanical properties of the disc.

'Hybrid' nanoscale co-networks of organic and inorganic components form a single-phase material above the nanoscale [10]. The result is a material that can combine the bioactive properties of an inorganic component with toughening via the organic constituent. By altering the relative amounts of organic and inorganic precursor, hybrid biomaterials offer the possibility of tuneable mechanical properties. Due to the intimate mixing of the components and potential for covalent coupling between them, hybrid materials improve on some of the disadvantages related to conventional composite materials. It is for this reason that a hybrid system is considered in this thesis for development towards an IVD replacement device.

This work follows on from the novel silica-poly(ε-caprolactone)-poly(tetrahydrofuran) hybrid (SiO_2-PCL-PTHF) developed by Tallia *et al.* [11, 12]. Without the inclusion of biodegradable PCL, the SiO_2-PTHF hybrid system is a new non-degradable biomaterial with highly elastomeric and tuneable properties. Implants for cartilage replacement require sufficient and stable mechanical properties

over large cycle numbers. Additionally, it is necessary to achieve a gradation of properties through the implant, as is present in the IVD, and reproduce its non-linear behaviour [13]. There is currently no biomaterial that can fully meet these requirements. Hybrid materials have the potential to address them.

Aim of this thesis

The aim of this thesis is the characterisation of a novel silica-poly(tetrahydrofuran) hybrid system in order to firstly achieve tuneable mechanical properties and secondly develop a method for the formation of mechanical property gradients. Ultimately this contributes towards the development of a device for the mimicking and replacement of cartilage structures in the body, specifically the intervertebral disc.

Chapter 1

Literature Review

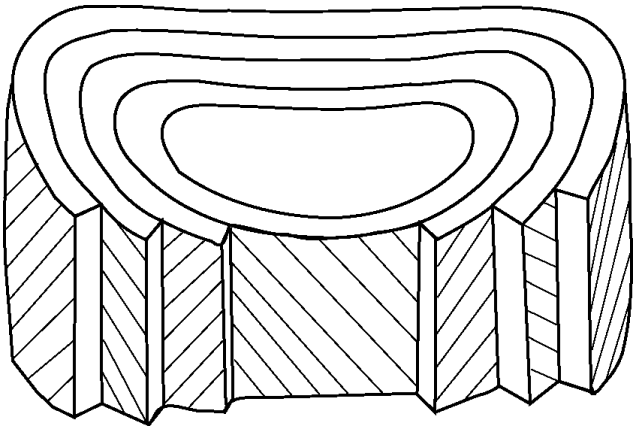

1.1 Introduction

This review will begin with a discussion of the cartilage structures, with the aim of developing a synthetic biomaterial that can replace cartilage. The design will be inspired by the mechanical behaviour of cartilage and current surgical options. This will be followed by a discussion of sol-gel hybrid materials and their potential to meet this need. The mechanical properties of hybrid biomaterials will be considered, including the fabrication of gradients of mechanical properties within structures or through a material.

1.2 Cartilage tissue replacement

Cartilage is made up mainly of collagen fibres, proteoglycans and up to 80% water. Its rigidity is achieved by water penetration in the hydrophilic matrix, which causes the fibres to stretch, increasing the modulus. The modulus can therefore vary as a function of position within the tissue, by varying the degree to which water is taken up; this itself is controlled by the variation in the fixed charge density of the material [14]. When compressed, water is expelled from the cartilage matrix, so high strains of over 50% are possible [15]. As the expulsion of water upon straining results in an increase in the relative concentration of the collagen fibrils, the effective modulus increases [16] and so subsequent straining requires greater applied stress.

There are three main types of cartilage found in the body: hyaline, elastic and fibrocartilage, classified by their relative quantities and arrangement of proteoglycans and collagen and elastin fibres in the extracellular matrix. The intervertebral disc (IVD) and meniscus structures (discussed below) that will be considered for the purpose of this thesis are made of fibrocartilage, with anisotropic properties due to the arrangement of collagen fibrils within their structures.

Cartilage shows a viscoelastic response under compression, tension and shear, controlled by the gradients of properties from the organisation of the chondrocytes, proteoglycans, elastin and collagen fibres and the interstitial fluid flow through the structure. Because of this time-dependent response, the measured mechanical properties of natural tissues are highly dependent on the strain rate used in testing [17]. For cartilage, replication of the fluid cycle that occurs *in vivo* would be necessary to mimic the physiological conditions experienced by the material. Thus it is important to consider how tests were carried out when using mechanical test data of tissues.

In order to effectively transfer load to surrounding tissue, the mechanical properties of the scaffold or implant should match as closely as possible those of the host tissue. An implant stiffer than the host tissue which it is in parallel with will take all the load as they are constrained to the same extension;

in the case of bone this stress-shielding leads to a reduction in bone density. For cartilage implants, mismatch in mechanical properties may lead to gaps being opened at the interface during unloading, due to shear between the native cartilage and the implant, which will lead to failure on subsequent loading [18]. Cartilage cells (chondrocytes) require mechanical stimulation to grow and develop well, and influence their shape and behaviour [19, 20], and this means that an implant or scaffold where ingrowth of tissue is desired must transfer load effectively to the cells. Dynamic compression of scaffolds, with cartilage cells cultured on them, improves the cell development [21].

The mechanical properties of implants will change over time whilst in use. Some are designed to be 'permanent' over an acceptable timescale for a patient (e.g. ten years), others are biodegradable over a variety of timescales. It should be noted that reliability is extremely important: even a very small proportion of failing implants could represent a large number of unnecessary extra surgeries and risk for patients, and wholesale rejection of a new technology. In the case of biodegradable scaffolds, the emphasis is on maintaining reliable strength for a relatively short period of time, while the surrounding tissue ingrowth increases in strength [22]. The surgical procedure and handling of the implant should also be taken into account, since there can be large stresses involved in getting an implant into place, and surgeons are unlikely to favour handling delicate scaffolds.

1.2.1 Intervertebral disc (IVD)

IVDs separate the vertebrae of the spine and they allow the range of motion of the spine without contact between vertebrae bones [23]. To support this motion without collapse or sustaining damage requires strength and deformability.

An IVD can be described in three regions: the nucleus pulposus, which supports applied load via osmotic pressure; the annulus fibrous, which experiences tensile stresses as the nucleus is compressed; and end-plate cartilage, which connects the IVD to the vertebrae to prevent slip or extrusion [23]. The annulus is made up of layers of cartilage containing collagen fibrils at approximately 65° [24], surrounding the highly elastic nucleus, Figure 1.1.

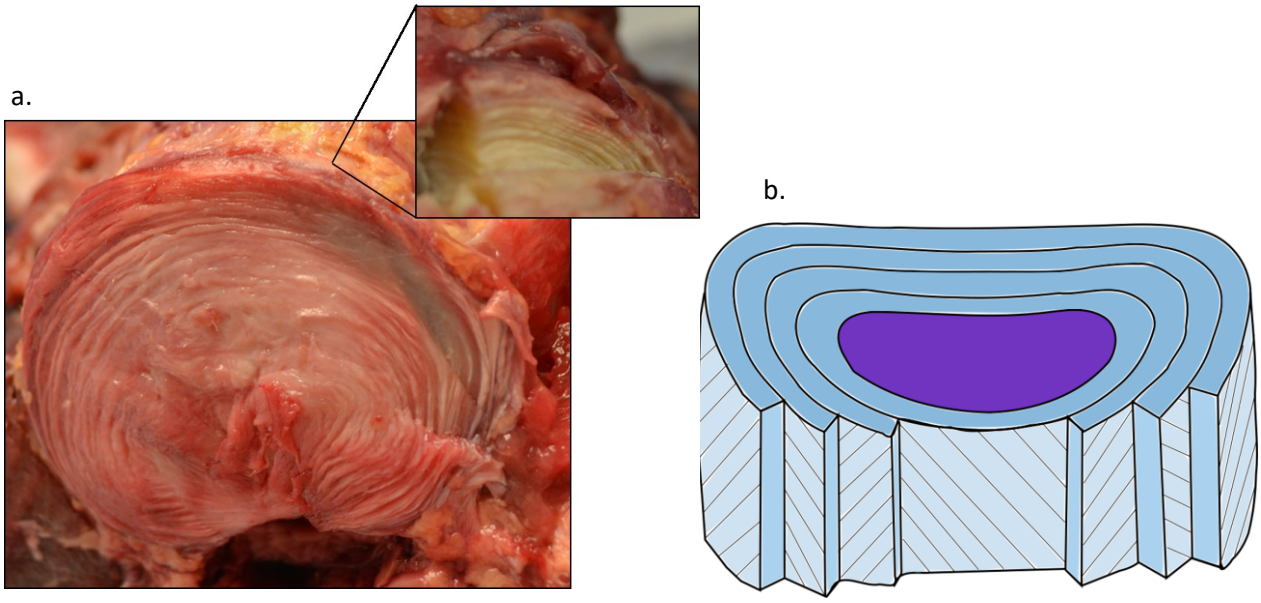

Figure 1.1: a. Human intervertebral disc sectioned perpendicular to spinal column, in which the lamellar structure can be seen, highlighted in the inset. From anonymous cadaver donated for medical research purposes with full consent. **b.** Schematic IVD, with the highly elastic nucleus shown in purple and the collage fibrils of the annulus fibrosis (blue) arranged in lamellae.

A variation in stiffness is achieved via the density and orientation of collagen fibres in the cartilage of the annulus (as well as the effect of water expulsion from cartilage). IVDs show time-dependent mechanical properties: stress relaxation occurs via polymeric relaxation (relative movement of fibres) and expulsion of water from the matrix. Over the course of a day, disc height reduces by about 10%, so the disc stiffness increases and pressure within the disc decreases [25]. The properties of the disc are recovered due to the flow of fluid back into the disc [26]. Between individuals and regions of the back the height of the disc can vary from 5-16 mm (with most in the range of 11-14 mm), as calculated from CT images [27]. The same study finds the footprint area at the fourth lumbar vertebrae to be 1492 mm^2.

For natural tissue and cartilage in particular, it is difficult to replicate physiological conditions in a laboratory and challenging to measure in the body and consequently difficult to give definitive values for mechanical properties. A study by Wilkes *et al.* using a pressure meter implanted directly into the nucleus pulposus (on a single test subject) found a pressure of 0.5 MPa in a relaxed standing position and 2.3 MPa lifting a 20 kg weight (greater than when running or climbing stairs) [28]. The modulus in compression for the annulus fibrosis is 0.5 MPa when confined [29], however this measurement involves achieving equilibrium in a way that is not physiological (in reality it would not be subject to a fixed load and would not allow time for significant flow of fluid out of the material) [30]. Newell *et al.* found an increase in stiffness of the human IVD with strain rate (0.001-1 s^{-1}) and with strain (4-12 %) and highlighted the large variation between individual IVD samples [31].

Current treatments

Current treatments for disc degeneration consist of partial removal of the IVD, which may need to be repeated as problems of nerve compression reoccur, until the whole disc is removed. To maintain the height between the vertebrae, spinal fusion is used, wherein a bone graft is used to fuse vertebra, with a metallic or polymeric cage to prevent relative motion of the adjacent vertebrae. This is illustrated schematically in Figure 1.2. However, outcomes of this surgery have not improved over time [32] and fixation of the spine in this way may adversely affect biomechanical motion, implicated for example in hip replacement failure [9].

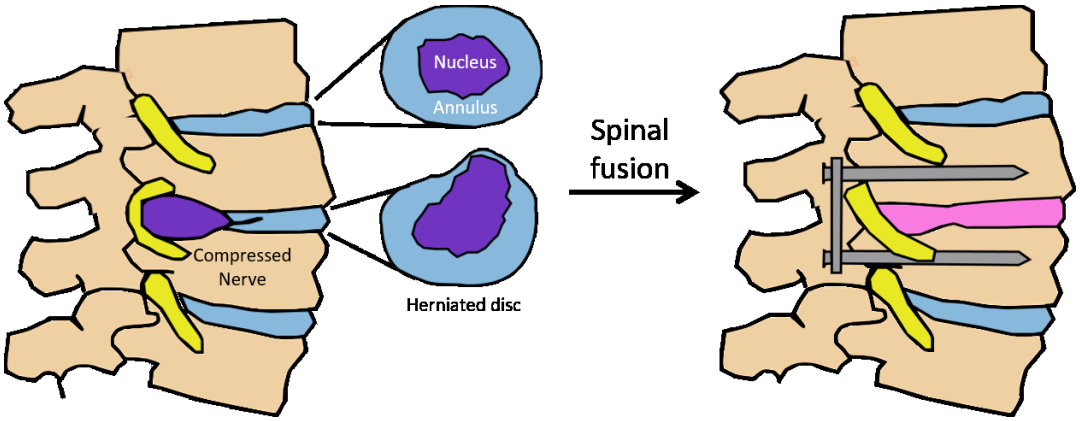

Figure 1.2: Schematic of a spine with herniated disc, which can cause pain by nerve compression and restrict mobility, and treatment by spinal fusion.

Total Disc Replacement (TDR) alternatives to spinal fusion exist, primarily using a ball-in-socket joint comprised of two metal plates with an ultra-high molecular weight polyethylene (UHMWPE) ball in between. This forms an articulating joint, unlike the one it has replaced. Among these are the Charité disk (Johnson & Johnson, USA) which had shown success over spinal fusion for specific types of spinal problems [33] but has since ceased production, and ProDisc (Centinel Spine, previously DePuy Synthes, USA) which when replacing IVD in cervical spine was shown to be as good as fusion at 24 months [34], with a lower rate of secondary surgeries than fusion at 7 year follow up [35]. While some studies have indicated TDR as at least as good as fusion [35, 36], clear benefits over rehabilitation were not seen in a randomized control trial [6] and there is evidence of the production of UHMWPE wear debris, leading to inflammation and subsequent pain [37, 38], as well as vertebral fracture resulting from the end-plate design [39] and progressive damage to other parts of the spine [40], which may be attributable to the design which does not imitate the natural joint.

Other designs use a more physiological core design, for example an elastomeric polyolefin rubber core between titanium end-plates (AcroFlex Lumbar Disc, DePuy Spine, USA; Physio-L, Nexgen Spine, USA)

had no failure or complications at 12 months [41] but clinical trials highlighted further concerns of wear particles, which contribute to osteolysis and make revision surgery more difficult [42].

In a more biomimetic approach, the Ranier compliant artificial disc (CAdisc) is made by reaction injection moulding of polyurethane to create a continuously varying modulus. The elastomeric design replicated the increase in stiffness under flexion seen in the natural disc [43], however, clinical trials of the disc required further surgery in multiple patients and led to the closure of the Ranier company [44].

It is possible to replace only the nucleus pulposus of an IVD using a hydrogel material, if nucleus degeneration is the cause of the problem, for example using a hydrogel core in a woven Polyethylene (PE) jacket [45] however, this does not achieve the aim of a replacement artificial disc. Prospective two-component solutions combining hydrogel nucleus and annulus of a different material also attempt to replicate the natural IVD [46], but do not form a continuous structure for TDR. A hypothesis of this thesis is that a suitable stiffness gradient can be achieved using sol-gel hybrids. Van der Broek *et al.* suggest via modelling that a multi-stiffness elastomer cannot replicate the non-linear behaviour of the IVD (their model gives an outer stiffness of 7 MPa and inner stiffness of 0.05 MPa) whereas a two component model could, so this non-linearity is an important aspect to consider [13].

1.2.2 Meniscus

The knee joint contains a medial and lateral meniscus, made up of fibrocartilage and anchored in place at their anterior and posterior horns to the tibia, Figure 1.3. The menisci of the knee act to transfer load across the joint, carrying approximately 50% of the total load through the knee [47, 48] by the development of hoop stresses, and to distribute the load evenly over an uneven joint surface, linked to small displacements at the horns [49]. They also contribute to the lubrication and to the stabilisation of the joint [50]. The mechanical function of the meniscus comes from the meniscus-meniscal ligament construct [51] as well as its own structure, consisting of collagen fibres which are mainly circumferentially orientated, providing tensile stiffness [52, 53] and an increased proteoglycan content in the anterior region, leading its higher stiffness [54].

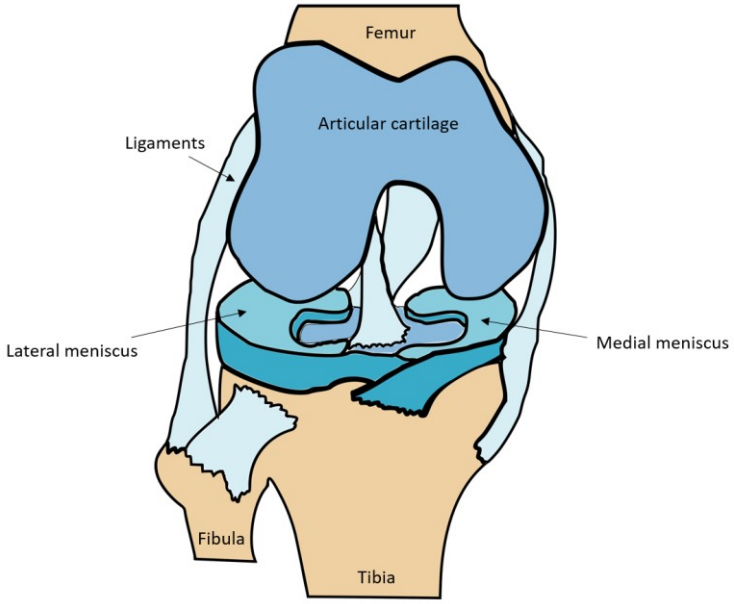

Figure 1.3: Schematic of knee joint without patella, showing the position of the lateral and medial meniscus (not all ligaments are shown).

This variation in composition and fibre alignment gives the meniscus an anisotropic structure, so its measured material properties depend on the position (posterior/central/anterior, depth) and orientation (radial/axial) of the tissue [55], as well as on the strain level and strain rate. The modulus is low at small strains and increases with increasing load. Chia and Hull found an order of magnitude difference in the maximum stiffness (anterior medial meniscus in axial direction) in compression measured at equilibrium and at a physiological strain rate (32 % s^{-1}), from 138 kPa to 1130 kPa at 12% strain [56]. A similar increase was seen when measuring at the same strain rate but increasing the strain: 41-139 kPa at 3 % strain (across all sample orientations) to 301-1130 kPa at 12 % strain, in both cases measured at a strain rate of 32 % s^{-1} [56]. The range of values is consistent with equilibrium values measured in medial porcine meniscus of 200-270 kPa at 10 % strain [57]. The modulus in

tension is at least an order of magnitude larger, with ranges in the circumferential direction of 58.0 – 150 MPa (medial and lateral meniscus range) [55], 43-141 MPa (medial) [58].

A summary of the compressive properties of cartilages tissues is given in Table 1.1.

Table 1.1: Mechanical property data for cartilage tissue. It should be noted that the values given are approximate ranges and actual values depend on the exact position of the tissue, as well as varying between individuals and conditions of the test. *Measured at 15 MPa applied compressive stress. †Bovine articular cartilage.

	Compressive Strength (MPa)	**Compressive Modulus (MPa)**	**Failure strain in compression**
Articular cartilage	18 [59] – 43† [60]	0.1 – 2 [61], 4*[60]	0.3† [60]
IVD	0.5 – 2.3 [28]	0.5 [29]	0.09 – 0.126 [62]
Meniscus	2.1 – 6.32	0.33 – 1.05	0.03 – 0.12 [56]

Current treatments

Tears to the meniscus as well as to the connected ligaments are commonly treated by arthroscopic repair using sutures and biodegradable screws with the aim of preserving the natural meniscus [63, 64]. Because the high circumferential tensile stiffness is crucial to the function of the meniscus, radial tears prevent the development of hoop strains in the meniscus and the ability to share the load through the knee joint [48]. Arthroscopic repair is a successful surgery: 80 % show no further issues at 18 months follow up [65], compared to earlier use of meniscectomy (total or partial removal of the meniscus), which led to increased likelihood of onset of osteoarthritis [66, 67]. Osteoarthritic changes are also seen after damage to the anterior cruciate ligament (ACL) [68, 69] which may be linked to the increased load on the meniscus, increasing the incidence of meniscal tears [50].

However, the success of repair of the meniscus relies on a limited tear (below 4 cm), patients must be aged below 40 years, and the tear must be close to vascular supply [63, 70]. Total meniscus substitutes made from polymers Teflon (PTFE) and Dacron (Polyethylene terephthalate, PET), but damage to the intact cartilage was observed and as well inflammation of the synovial membrane [71, 72]. Poly(vinyl alcohol) (PVA) hydrogel meniscus replacement, with sutures running through the device for fixation, showed improvement over meniscectomy but not over allograft with respect to [73]. Polycarbonate urethane (PCU) implants with knots at the horns for attachment were evaluated in goats over 12 months but showed evidence of cartilage degeneration [74].

Implants with both a too high or too low stiffness can cause damage to the surrounding tissue, directly or by causing increased loading of that tissue. The tribology of the material must prevent damage to the intact cartilage, which relates also to the fixation of the device as displacements can increase the friction. Thus far no successful total meniscal replacement has been developed.

1.3 Sol-gel organic-inorganic hybrids

Natural bone is a nanocomposite material of collagen triple helical fibrils, staggered, with orientated crystals of a calcium phosphate ceramic close in composition to hydroxyapatite. The ceramic nucleates on the fibrils during bone growth, producing excellent resistance to shear. There is good stress transmission between the collagen fibres and it is energy intensive for cracks to propagate horizontally. The significant difference over a conventional synthetically engineered composite is that the organic and inorganic components very finely integrated, producing synergy of their properties, and they appear to behave as a single phase, something which may be achieved synthetically by the synthesis of hybrid materials [75].

There is an important step in the path of hybrid materials to clinical use that is yet to be surmounted. Whilst a variety of hybrid compositions have been described for use in the field of biomaterials, little is reported of their mechanical properties. When it is mentioned, it is in general limited to uniaxial tensile or compressive testing (and not both) to failure, which does not give a full picture of the performance of the material in a biological application. In application, an implant will be subject to a three-dimensional, time varying stress state in the biological environment.

The sol-gel process

Sol-gel synthesis is a bottom-up synthesis route. Nanoparticles form and polymeric reactions lead to the formation of a gel, summarised in Equation 1.1, Equation 1.2 and Equation 1.3 [76, 77]. Tetraethyl orthosilicate, $Si(OC_2H_5)_4$ (TEOS), is the most common precursor for formation of a sol-gel silicate. It can undergo hydrolysis and condensation, in the presence of a catalyst, to form silica nanoparticles.

$$\textbf{\textit{Hydrolysis}}: \quad Si(OR)_4 + nH_2O \rightarrow (OH)_nSi(OR)_{4-n} + nROH \qquad \textbf{Equation 1.1}$$

$$\textbf{\textit{Condensation}}: \quad Si(OH)_4 + Si(OH)_4 \rightarrow (OH)_3Si - O - Si(OH)_3 + H_2O \qquad \textbf{Equation 1.2}$$

$$Si(OR)_4 + Si(OH)_4 \rightarrow (OH)_3Si - O - Si(OR)_3 + ROH \qquad \textbf{Equation 1.3}$$

Under acidic catalysis, a sol can be cast into a mould and gelation continues in the mould along with evaporation of the solvent. Because the sol-gel reactions are carried out at around room temperature, transition temperature considerations do not limit the range of compositions that can be produced. There is also the possibility of incorporating biological molecules into structures, which would be destroyed at high synthesis temperatures. The sol can be formed into bulk material by pouring into a mould and drying, or further processed (for example by foaming or additive manufacturing) to form three-dimensional scaffolds.

1.3.1 Hybrid synthesis

The sol-gel process is adapted to form hybrid materials by the addition of a polymer solution that must be soluble in the original sol, and around which the gel network forms. To form cross-links consisting of covalent bonds between the two networks, either the polymer must have the functionality to react or it must be bonded to a coupling agent, such as (3-glycidyloxypropyl)trimethoxysilane (GPTMS) used in this work, where one end of the coupling agent can bone to the polymer and the other to the silicate network. Figure 1.4 shows a schematic of a hybrid formed in this way, with covalent linkages between the silica nanoparticles and the polymer chains. Polymerisation, or functionalisation of a ready-made polymer, can be carried out before addition to the sol or *in situ* with the sol formation, so that the networks form around one another. The requirement for the chosen polymer to be soluble in the sol-gel for mixing to occur may limit the hybrid compositions that can be produced in some systems.

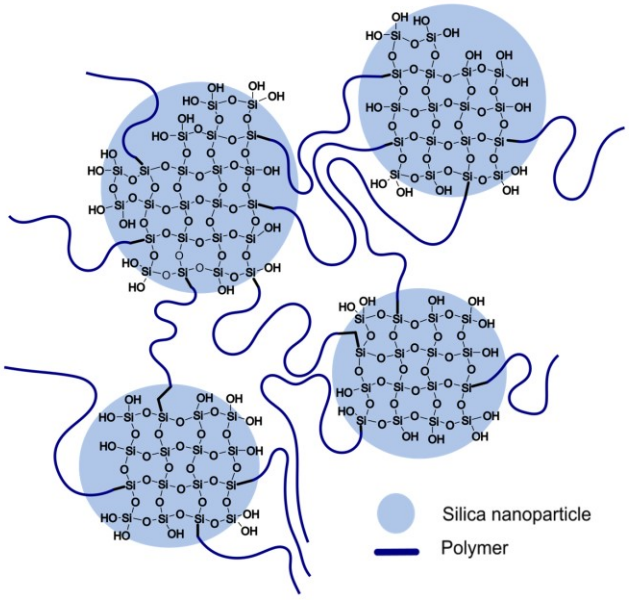

Figure 1.4: Hybrid schematic showing silica nanoparticles and covalent bonding to polymer component.

Using GPTMS along with TEOS, or another silicate precursor, means the degree of coupling and the silica content can be varied independently. Forming hybrids in this way is a method of overcoming the brittle property of bioactive ceramics, without the significant drawbacks presented by conventional composite materials. Most composites have interfaces between a reinforcing phase and the matrix, which have poor interfacial interactions, causing a source for stress concentration or crack propagation, as seen in PCL-Bioglass composites [78]. The scatter in properties inherent in brittle materials could also result in scatter in the composite material properties [79]. Other composites can be formed by 'self-reinforcing', which involves die drawing of polymers containing Bioglass spheres, so that the polymer fibres are orientated and strengthened (a process common in plastics synthesis).

For polylactide composite samples with the same draw ratio, increasing the bioactive glass content decreased mechanical properties (bending strength and modulus, torsion, shear and compressive strength) [80], perhaps because of interference of the glass particles with the alignment of the fibres.

Hydrogels, hydrated polymer gels, can be used to alter their mechanical properties in a way that mimics cartilage, e.g. by amount of water uptake and swelling, however they are generally regarded as having poor mechanical properties compared to polymers and hybrids [81]. Moutos *et al.* combined a hydrogel with a 3D woven polyglycolic acid structure to achieve mechanical properties close to those of cartilage: tensile strength of 75-85 MPa and elongation to failure of 22-27 % [82]. Incorporation of nanoparticles in hydrogels has been used to control mechanical properties [83], for example the grafting of silica nanoparticles in double network hydrogel poly(2-acrylamido-2-methylpropanesulfonic acid) / polyacrylamide (PAMPS/PAAm), using variation in the nanoparticle size and content to control the compressive strength at 90% strain (range of 1.8-16.5 MPa at 90% strain) and stiffness of 0.06-0.33 MPa [84]. Hybrids have the option of covalently linking the organic and inorganic networks by joint polymerisation of the two networks [85].

1.3.2 Classification of hybrids

Sol-gel hybrids are classified according to the bonding between the nanoscale interpenetrating networks of the two components and on the formation of the organic polymer. Class I and II hybrids are formed using a polymer produced ex-situ, whereas for Class III and IV hybrids the polymer is formed simultaneously with the sol-gel process. Class II and IV hybrids additionally have covalent bonding between the phases, as opposed to the weaker interactions (made up of Van der Waals forces, hydrogen bonds, electrostatic forces and mechanical entrapment) between the inorganic and organic phases of Class I and III hybrids [10].

Formation of covalent cross-linking for Class II and IV hybrids can be achieved using a coupling agent which functionalises the polymer source and has alkoxysilyl groups that can participate in the sol-gel reaction, co-condensing with the inorganic source. This control over covalent bonds can improve the mechanical behaviour as the material is behaving as a single phase above the nanoscale [86, 87], but also increases the complexity of processing.

1.3.3 Characterisation of hybrids

Forming hybrids achieves intimate mixing of the networks, so the domain sizes of the organic and inorganic components are of nanometre dimensions and they appear above the nanoscale as a single phase [10]. Solid state ^{29}Si nuclear magnetic resonance (NMR) can be used to determine the connectivity of silica tetrahedra, which gives values of the proportion of oxygen atoms in SiO_4 tetrahedra (the inorganic phase) that are bonded to 1, 2, 3 and 4 silicon atoms (i.e. bridging oxygens Si-O-Si), which can then be used to elucidate the type of crosslinking in a network [88] (described in Section 2.2.1). The level of connectivity in three dimensions and possibly the 'shape' of the connectivity (how and where the networks are connecting and interpenetrating) can affect the mechanical behaviour of the hybrid, with increased connectivity leading to an increase in stiffness [10].

TEM may also be used to image domains of silica and organic material; however, this relies on the regions being larger than a few nanometres. Maçon *et al.* used tapping mode Atomic Force Microscopy (AFM) and nanoindentation to map the surface mechanical properties of methacrylate-silica hybrids [89]. The Young's modulus was measured by nanoindentation was 1.41 ± 0.23 GPa and 2.53 ± 0.32 GPa for 29 and 50 wt.% silica respectively. The authors highlighted the importance of the density of silica bridging oxygen atoms and found the reduced modulus (obtained via nanoindentation) to be directly proportional to it.

1.3.4 Hybrid systems

For biomedical applications, the polymer component of the hybrid system must be biocompatible, as well as any of its degradation products in the case of degradable implants. Its chemistry must allow it to be soluble in the sol-gel reaction and to enable functionalisation for covalent coupling. Choices of polymer for hybrid system are discussed here with emphasis on the resultant mechanical properties. Degradable as well as non-degradable systems are considered although for comparison for use of SiO_2–PTHF as an implant material the latter are more relevant.

Hybrids made with natural polymers

Natural polymers are obvious candidates for the organic component of hybrid biomaterials since these are, or closely resemble, those employed in the body itself. Collagen is the principal constituent of bone and cartilage but is difficult to incorporate into the hybrid synthesis due to low solubility. Gelatin is a collagen derivative with a more open structure allowing for chemical attack and so is soluble in the sol-gel process (a requirement for hybridisation to work).

Mahony *et al.* used TEOS as a source of silica and GPTMS coupling agent to form porous freeze dried gelatin – silica hybrids [90]. The –COOH groups on the gelatin were hypothesised to open the epoxy ring of the GTPMS, so that the gelatin was functionalised with siloxane groups along the chain. When the functionalised gelatin was added to the sol, the siloxane groups hydrolysed, and the resulting Si-OH groups underwent condensation polymerisation, as in the conventional TEOS based sol-gel process. This was proven in subsequent NMR studies that showed –COOH to be a successful nucleophile to open the epoxy ring of GTPMS at certain pH values [91, 92]. Increasing the coupling increased the stiffness of the material, which is elastic (the authors suggest its suitability for applications with high cycle number at low load). The range of compressive strengths is 20-60 kPa (for are porous scaffolds with interconnect diameters of ~200 μm) [90]. For context, this strength is two orders of magnitude lower than those commonly experienced within an IVD.

Poologasundarampillai *et al.* investigated the effect of the degree of coupling, involving varying the amount of GPTMS coupling agent present in poly(γ-glutamic acid) (PGA)-silica hybrids. At first, increasing the coupling improved the measured mechanical properties (elastic modulus, strength and elongation to failure, all in compression) up to a plateau [93]. However, only three GPTMS contents were investigated, so there can be less confidence in the precise trend and more in the range of coupling agent contents that they conclude to be optimal.

Chitosan-silica hybrids can also be formed, again used GPTMS as a coupling agent [94], giving a greater compressive strength of 20-100 MPa for monolithic samples [95], however it was difficult to prove the bonding between the chitosan and the silica. Generally, natural polymers have the disadvantage that it is difficult to ensure their source is consistent. Gelatin is also animal derived, which limits its market. A hybrid formed of PGA chelated with calcium, produced a much great compressive strength of ~400 MPa with 26 % strain before failure and 1.9 GPa stiffness [96], however large monoliths could not be produced without cracking.

Hybrids containing synthetic polymers

Using synthetics polymers gives a greater degree of control of the polymer chain length, shape and coupling. Many are biodegradable over various timescales and already have approval for use within the body. PVA has been tested in the form of PVA-CaO-SiO_2 hybrids [97] but the PVA lacked functionalisation which precluded covalent cross-linking. Polycaprolactone (PCL) has received a lot of interest in the field of tissue engineering, due to its viscoelastic properties as well as its longer term degradation period over 3-4 years [98].

Rhee *et al.* used PCL-diol with 3-(triethoxysilyl)propyl isocyanate (ICPTS) coupling agent. They targeted the -OH groups of the PCL-diol chains with the isocyanate group of the ICPTS. A change in yield behaviour was observed as the PCL content increased (decreasing silica), with low levels of PCL (<40 wt.%) associated with typical brittle fracture. At high PCL content (80 wt.%) there was a period of straining with no increasing in stress, which is polymeric necking behaviour. The authors also note that it is not only the silica content that underlies the mechanical behaviour but also the processing conditions and the individual nature of the polymer [99].

In a subsequent investigation on PCL-organosiloxane hybrids, Rhee *et al.* conducted tensile tests and found a fracture strength of 18 MPa with 290% strain to failure. In this case the material did not contain silica but retained the ability to from apatite *in vitro*, due to the presence of silanol and calcium ions [100]. The authors postulated that the very high failure strain is linked to the strong siloxane linkages in the material. A similar PCL/TEOS derived hybrid was also developed earlier by Tian *et al.* [101], however in this case no attempt was made to characterise the mechanical properties of the hybrid.

Hendrikx *et al.* formed a hybrid by mixing silica sol with triethoxysilane-terminated crosslinking molecules, cured on a PCL template that was subsequently leached out, with a maximum in the compressive strength for intermediate organic contents (20 and 30 wt.%), described as 'tougher' scaffolds. Comparing hybrids made with linear linking molecules and molecules with 3 or 4 linking arms, the latter showed increased compressive strength (23 MPa compared to 18 MPa) [102]. This points to the importance of the network connectivity in influencing the mechanical behaviour of the material.

Methacrylate polymers can also be used for precise control of the polymerisation and thus polymer architecture, however the hybrid stiffness is around three orders of magnitude larger than those of IVD or meniscus. For example, SiO_2-poly(MMA-*co*-TMSPMA) and SiO_2-poly(TMSPMA) with stiffnesses of 0.7-1.0 and 3.1 ± 0.4 GPa respectively, and strengths of 27-54 MPa and 130 MPa in compression [103, 104]. Because of the high stiffness, their research application is focussed towards bone rather than cartilage replacement.

1.3.5 SiO_2-PTHF hybrids

A silica-poly(ε-caprolactone)-poly(tetrahydrofuran) hybrid (SiO_2-PCL-PTHF) has been developed with varying inorganic content for use as osteochondral scaffolds, using GPTMS as the coupling agent. The PCL-diol was first oxidised to produce COOH-PCL-COOH. The carboxylic acid groups at each end of the chain were targeted for reaction with the GPTMS.

It was discovered that the THF solvent used polymerised to PTHF (also known as poly(tetramethylene oxide), PTMO) *in situ* and incorporated into the hybrid along with the PCL, forming a Class IV hybrid [11]. Bulk SiO_2-PCL-PTHF hybrids had a maximum strength of 1.42 ± 0.47 MPa and stiffness of 132 ± 15 MPa in compression at 38.7 wt.% SiO_2 [12]. The same reaction can occur without the addition of PCL, forming a non-degradable SiO_2-PTHF hybrid system which will be the subject of this thesis.

Hybrids incorporating TEOS with PTHF have been developed previously, as thin films (forming Class I hybrids) [105] and in the form of PTHF-based polyurethane oligomers, with ICPTS forming covalent crosslinks with silica (Class II hybrids) [106]. This means there is a mixed polymeric chain with hard and soft (PTHF) segments [107] and therefore they were significantly different mechanically from the hybrids used in this work. The authors found an increasing tensile strength with increased silica content and with increased number of crosslinks, 10-39 MPa, with elongation at break between 48 and 260 % [106]: this indicates that PTHF gives highly elastomeric properties and strength.

The extensibility in tension of SiO_2-CaO-PTHF hybrids was found by Miyata *et al.* to be strongly dependent on the polymer content, as expected intuitively. This is also accompanied by a reduction in the tensile strength (from 7.5 to 5.5 MPa as the PTHF content increased from 40 to 50 wt.%) [108]. The strain at failure was not dependent on CaO content in the hybrids (calcium inclusion is important for bioactivity for bone regeneration) and compressive properties were not considered. Flexible Ta_2O_5-CaO-PTHF have been prepared with stiffness 122-296 MPa and 3-24 % strain to failure measured in 3-point bending [109].

This indicates that PTHF-silica based hybrids have the potential for mechanical properties that match the range cartilage in the IVD and meniscus, and the novel synthesis method produces Class IV hybrids and faster gelation [110], which also gives the potential for 3D extrusion printing. PTHF is non-degradable (measured up to 3 months in PBS) and biocompatible after 1 month subcutaneous implantation in rats [111, 112]. Thus, the SiO_2-PTHF Class IV hybrid system merits further investigation as a biomaterial.

1.4 Tuneable mechanical properties and stiffness gradients

To achieve the gradation in stiffness which would mimic a natural IVD (Section 1.2.1), precisely tuneable mechanical properties are required. This in turn requires control and understanding of the synthesis procedure for fabricating promising hybrid materials. It is desirable to be able to match the material properties to those of the host tissue in given application, which vary by orders of magnitude from bone to soft tissue. In the case of an IVD, property matching allows the natural mechanics of the spine to be maintained, and not increase damage at adjacent discs. It also helps to ensure the success of an implant which otherwise could displace and de-bond from the host tissue.

Tuneable properties in hybrid materials can be achieved by variation in the inorganic content of the [12] as well as control of the polymer architecture. Chung *et al*. found an improvement in toughness and ductility in SiO_2-poly(MMA-*co*-TMSPMA) hybrids using star shaped co-polymers over linear or branched architecture, with yield stress of bulk hybrids of 26-41 MPa and stiffness of 0.6-1.1 GPa in compression [113]. However, they did not produce a single material with a stiffness gradient.

As discussed in the case of the IVD and meniscus, many structures in the body show a graduation in mechanical properties, as well as transitions between tissues such as bone to cartilage and ligament to bone. In terms of tissue regeneration, interface tissue engineering is of interest to control the differentiation of different cell types [114], for example for osteochondral regeneration [115]. The physical architecture of pores in scaffold materials can also be used to control the mechanical properties, for example in hydroxyapatite scaffolds achieving a variation of 0.1 to 0.78 MPa [116], and this concept can be combined with compositional gradients to give a scaffold with zones of different properties [117].

For bulk hydrogel materials, various techniques have been developed to give a gradient in mechanical properties, including variation in the type of crosslinking [118], a gradient in the hydrogel precursors [119], UV light polymerisation [120], microfluidics [121] and 3D bioprinting [122]. Physical characteristics such as buoyancy have been employed in hydrogels and acrylate polymers to give a stiffness gradient [123]. Of particular interest because of their applicability to the hybrid synthesis are the generation of surface patterns in hydrogels by pre-polymerisation of one of the phases [124], developed further to use partially polymerised hydrogels which have sufficient viscosity to prevent their mixing [118], something which could be used with hybrid sols as the viscosity increases with time. Using the same method, single specimens with a difference in compressive stiffness of approximately 3 to 125 kPa between the ends [125]. The mechanical strength of the interface in tension was checked by pulling by hand, resulting in the specimen breaking consistently in the less stiff zone. The authors suggest the application to IVD replacement because of the promising variation

in stiffness, although the maximum measured compressive strength of the stiffer zone is around 2.5 MPa, which is close to that measured in the disc in normal activity [28].

Control of the orientation of electrospun nanofibers has been used to form scaffolds to imitate an individual lamella of the IVD annulus [126] and combined with a hydrogel nucleus to form a structure with areas of different stiffness [46], but not to form a continuous structure with variation in stiffness. This has been done as discussed in Section 1.2.1 using a variation in crosslinking density in poly urethane [127], however only relative mechanical properties were measured, along with the chemical variation to characterise the compositional gradient [128]. There is a need for new materials that can produced suitable mechanical properties and have a gradient of stiffness, without flaws or interfaces that can be sources of crack propagation or stress concentration. This is the aim of this thesis.

Monolithic samples of SiO_2-PCL-PTHF system had a large range of compressive strengths: 2-74 MPa with 33-4 % failure strain and 5-440 MPa stiffness with increasing silica content: 21 to 63 wt. % SiO_2 [110]. An IVD replacement implant material must be non-degradable, so if similar mechanical properties can be achieved with SiO_2-PTHF system (without the degradable PCL component), this could be a suitable biomaterial.

1.5 Scaffolds for device fixation

To make a scaffold, allowing for tissue integration, rather than a monolithic implant, it is necessary to use one of a number of techniques to form a porous material: e.g. using a template, which may be subsequently leached out or removed by heating; foaming using a surfactant; 3D printing. Porous surfaces of an IVD implant would allow fixation to the adjacent vertebrae endplates: successful 3D printing and chondrogenesis was achieved with SiO_2-PCL-PTHF scaffolds [12], so it was investigated whether the same fabrication method could be applied to SiO_2-PTHF hybrids. Porosity is required in order for ingrowth, blood supply and sites for cell growth, with a minimum size of 100 µm generally considered to be adequate [129], and an improvement over larger pores of around 700 µm [130, 131].

Bioglass scaffolds have been developed with a range of compressive strengths: 2.3-15 MPa produced by foaming [132-134], which can be enhanced by the production via 3D printing [135, 136]. However, in cartilage replacement applications where scaffolds will be subject to cyclic loading under high strains, glasses are too brittle. Conversely, hybrids formed with natural polymers have strengths in compression that are much lower than cartilage: SiO_2-chitosan scaffolds produced by freeze drying have a failure stress 62-143 kPa (compressive stiffness 0.7-1.4 MPa) [95] and the same order of magnitude is seen for SiO_2-gelatin hybrid foams at 20-60 kPa [90].

Robocasting of scaffolds gives better control over the structure than foaming, as the strut and channel size are programmed in, but it also puts some limits on the composition and synthesis procedure, since to print there is a certain viscosity required so that the material can be extruded but will not collapse under its own weight and will maintain the printed form. In this work robocasting or 3D printing refer to layer-by-layer extrusion printing, rather than other additive manufacturing techniques.

3D printing of hybrids has been done before using gelatin [131, 137], and the SiO_2-PCL-PTHF hybrid system [12], exploiting the gradual gelation of the sol-gel process to give a printable viscosity at a given time range during the gelation process. SiO_2-gelatin scaffolds had a compressive strength of 1 MPa and 7 MPa stiffness with 700 µm pore channel size, values which were reduced by a factor of ten after soaking [131], and stronger than foam scaffolds of the same material [90]. Bioglass-gelatin printed scaffolds had a compressive strength of 5 MPa with 550 µm channel size [137].

SiO_2-PCL-PTHF scaffolds had a lower failure strength of 1.2 ± 0.2 MPa with strain to failure of 36.0 ± 7.8% and 5.1-8.7 MPa stiffness, at a channel width of 200 µm and with 24.7 wt.% silica content [12]. Although the compressive strength is lower, in this case a Class IV hybrid was formed, which improves stability, with finer struts and channel size and no post-stabilisation of the scaffolds was required. Additionally, fusion between the printed struts was achieved, which was not evident in SEM images of Bioglass-gelatin scaffolds.

The printing of the SiO_2-PCL-PTHF is the starting point for the attempt fabrication of SiO_2-PTHF scaffolds in this work.

1.6 Thesis outline and objectives

Cartilaginous structures like the IVD and meniscus have complex forms with variation in stiffness which allow them to fulfil their biomechanical functions. Current replacement devices do not successfully replicate this function, whereas sol-gel hybrid materials have tuneable mechanical properties via the variation in inorganic/organic content, giving the potential to match the varying properties through the natural tissue structure. The aim of this thesis is to characterise a novel hybrid system of silica-poly(tetrahydrofuran) in order to develop the tunability of its mechanical properties and the formation of gradients in those properties, with a view to the replacement of cartilage structures in the body. Work towards this aim was broken down into the following objectives.

The first objective is the development of synthesis protocol for SiO_2-PTHF hybrids to synthesise hybrids with a range of organic/inorganic composition. To develop a system of tuneable mechanical properties requires understanding of (1) the hybrid structure and (2) the connection between the starting reagents and the final mechanical properties. This is set out in Chapter 3.

The second objective addressed in Chapter 4 is the formation of single hybrid specimens with gradients in stiffness, by joining partially gelled sols before gelation is completed. The multicomponent gels were optimised though investigating: (1) variation of the joining time of hybrids of different composition; (2) tensile and compressive testing; and finally (3) using optical techniques to map the strain distribution around the join interfaces.

The third and final objective, Chapter 5, was the development of an IVD implant device with 3D printed surfaces for fixation via (1) successful 3D extrusion printing of one hybrid composition; (2) moulding to a simplified human IVD shape and dimensions and (3) compression testing in comparison with human IVDs. Concurrent to this was the objective of moulding a hybrid meniscus implant which shared the same steps in mould development and testing.

Chapter 2

Characterisation Techniques

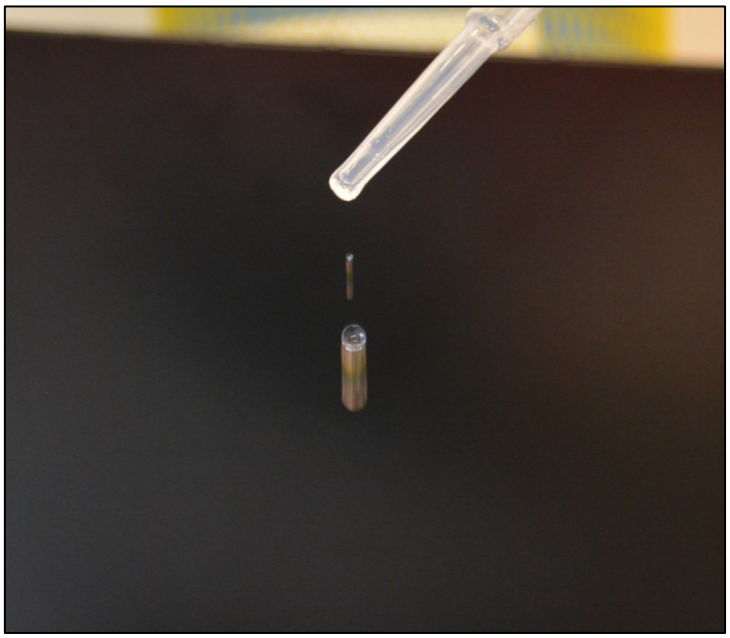

2.1 Introduction

An overview of the techniques used to characterise the hybrid material is given here, comprising the chemical characterisation by a combination of techniques, imaging and mechanical characterisation. Machines, setting and software are specified. The details of individual experimental parameters and set up are given in the methods section of the relevant chapter.

2.2 Characterisation of structure and composition

2.2.1 Nuclear Magnetic Resonance (NMR) spectroscopy

Nuclear Magnetic Resonance (NMR) spectroscopy uses the response of atoms in a changing magnetic field to determine their environment within a molecule. NMR relies on the nuclear magnetic moment of atoms with an odd number of protons/neutrons. When nuclei are held in a strong external magnetic field, a pulse of radio waves of different frequencies can cause the nuclei to flip their spin state between parallel and anti-parallel alignment with the external magnetic field. The difference in energy between these two spin states corresponds to a specific resonance frequency of the nuclei (Larmor frequency), the signal of which decays over time on return to the equilibrium spin state. The resonance frequency depends on the nucleus itself and the structure and bonding of the molecule: two nuclei bonded together shield each other because of the local magnetic field produced by their electrons.

Using a radio wave pulse containing a range of frequencies (covering the whole range of possible Larmor frequencies) produces a time domain signal of the combination of all the resonances, which when Fourier transformed produces the frequency domain NMR spectrum.

Solution state NMR

Solution state NMR gives narrow resonances due to the "tumbling" of molecules in the liquid state, which means the magnetic field at the nucleus is constantly changing and so most interactions are averaged out. NMR spectroscopy of hydrogen (^{1}H atoms) was used to confirm the formation of PTHF and the opening of the GPTMS epoxide ring, which together indicate the formation of a polymer network. H^1 NMR was carried out in $CDCl_3$ solvent at 400 MHz. Samples of GPTMS/THF solution were taken for NMR during the synthesis, just before the addition of the TEOS solution, to confirm the formation of PTHF.

In this work, solution state ^{1}H-NMR was performed with 400 MHz Bruker spectrometer and TopSpin software, over a range of chemical shifts of 0-12 ppm. Samples were prepared for ^{1}H NMR by dissolution in approximately 500 µL of deuterated chloroform ($CDCl_3$) in a borosilicate glass NMR tube.

MestReNova software was used for analysis of spectra. All references in this thesis to ^{1}H NMR can be assumed to refer to the solution state.

Solid state NMR

Solid state NMR spectra are broader than those in solution state, and in the case of ^{29}Si analysed here, required cross-polarisation to increase the observed signal because of the low abundance of the ^{29}Si isotope. All solid-state NMR measurements were carried out at Warwick University with Dr. Joshua Clark and Prof. John Hanna. ^{29}Si solid-state NMR was carried out in single pulse magic angle spinning (MAS) and cross polarisation (CPMAS) using 7.0 T Varian/Chemagnetics InfinityPlus spectrometer with a Larmor frequency of 69.62 MHz, using a Bruker 7 mm HX probe and MAS at 5 kHz. CPMAS gives information on the chemical shift, and MAS gives quantitative information on the relative abundance of the species termed $Q^n = Si(O\text{-}Si)_n(OH)_{4-n}$ and $T^n = C\text{-}Si(O\text{-}Si)_n(OH)_{3-n}$. The order *n* is thus the number of bridging oxygen bonds (Si-O-Si) that are connected to the central Si atom. The relative abundance of ^{29}Si species with different number of bridging oxygens connected can be used to calculate the degree of condensation (D_c) of the silica network, according to Equation 2.1 [138].

$$Degree\ of\ condensation, D_c = \left(\left[\frac{4Q^4 + 3Q^3 + 2Q^2}{4}\right] + \left[\frac{3T^3 + 2T^2 + T^1}{3}\right]\right) \times 100\% \qquad \textbf{Equation 2.1}$$

Solid state measurements were required because it was not possible to find a solvent for the inorganic-organic hybrid material, which were instead prepared by machining of a bulk sample. Solid-state NMR measurements were used to confirm the formation of a hybrid material.

2.2.2 FTIR

When infrared radiation passes through a sample, some will be transmitted and some will be absorbed by covalent bonds at their resonant frequencies, when the frequency of the radiation matches the frequency of the specific bond vibrations. This results in a spectrum of absorption (or its inverse, the transmission) that is characteristic of a given compound. To absorb infrared radiation, a change in the dipole moment of a covalent bond must occur, so a symmetrical diatomic molecule will not be IR active. All vibrations are made up of 6 normal modes of vibration: asymmetric and symmetric stretching, wagging, twisting, rocking, scissoring; the number and type of active modes depends on the individual molecule.

Fourier Transform Infrared Spectroscopy (FTIR) means that instead of using a frequency scan, multiple beams with range of wavelengths are used and is subsequently processed by Fourier transform to give the range of absorption at each individual wavelength.

FTIR can be used in Attenuated Total Reflectance (ATR) mode, which means that the IR beam produces an evanescent wave inside a crystal (by a process of total internal reflection), and the sample is directly in contact with this crystal. The evanescent wave extends into the sample at a depth of 0.5-2 μm [139]. This allows solid and liquid samples to be analysed in this form without further preparation.

A Thermo Scientific Nicolet iS10 FTIR equipped with Smart Golden Gate for Single-Reflection Diamond ATR Analysis with OMNIC software was used. 64 scans were done at a resolution of 4 LP/mm to produce spectra between 4000 and 400 cm^{-1}. Bulk samples and liquid were analysed in their original form as solid pieces and liquid respectively, whereas scaffolds and heat-treated samples were ground with a pestle and mortar. The technique is non-destructive, and the crystal is around 0.5 mm length so small volumes of sample are required.

FTIR gives information on the structure of hybrid materials, namely the polymer formation and the condensed silica network, and on the progressive change in composition with change in ratio of starting reagents, by normalising to the highest peak. It is used in combination with other techniques of NMR and DSC/TGA to characterise the hybrid structure.

2.2.3 Differential Scanning Calorimetry (DSC) and Thermogravimetric Analysis (TGA)

Thermogravimetric analysis (TGA) is the measurement of mass change as a function of temperature. The sample is heated at a constant rate in a crucible under controlled atmosphere, on a precise balance. Mass loss is measured when a volatile component is lost, by evaporation or burning out.

In Differential Scanning Calorimetry (DSC) the heat flow required to heat the sample at a constant rate is measured with respect to a reference. Reactions which may not result in a mass change can be detected by DSC, for example polymer crystallisation, as well as degradation.

Here simultaneous DSC/TGA was carried out on Netzsch Jupiter STA 449C with Proteus software. Hybrid samples were prepared for analysis after drying and storage at 40°C by fine cutting with a razor blade for bulk samples or grinding in a pestle and mortar for scaffold samples. 10-15 mg of hybrid was added to a platinum crucible, then DSC/TGA was conducted to 800°C at 10°C min^{-1}. Over this temperature range, the organic part of the hybrid is burnt out leaving the silica intact. The total mass lost is the organic component of the hybrid and the quoted silica weight percentage for a given hybrid sample is equal to the total percentage mass lost subtracted from 100%.

2.3 Imaging

2.3.1 Electron Microscopy

Scanning Electron Microscopy (SEM) and Transmission Electron Microscopy (TEM) use the interaction with the material of scattered and transmitted electrons respectively. SEM provides surface morphological information, in this work using the secondary electrons from the low-energy electrons excited at the sample surface by the primary electron beam. Secondary Electron Imaging (SEI) is sensitive to the topography of the surface, as these electrons arises from close to the surface of the sample. This was used herein to image the fracture surface of the hybrid material.

A JEOL 6010 LV SEM was used at 20 kV in SEI mode, with a working distance of 14-20 mm. Samples were prepared for SEM by mounting on aluminium stubs with carbon tape followed by coating with 10 nm of chromium (Q150T sputter coated, Quorum Technologies, UK) to prevent charging of the sample.

In TEM, the primary electron beam passes through the sample and the transmitted electrons are imaged, giving through-thickness information on the sample. The higher resolution of TEM was used to investigate the homogeneity of the hybrid at the nanoscale.

Samples were prepared for TEM by Precision Ion Polishing System (Gatan Inc., Pleaston, USA) for 10 hours at 2 keV, on a copper grid. Characterisation of the morphology and elemental composition was done via TEM and STEM-EDS with a TEM/STEM at 200 kV (JEM-2100F, JEOL, Japan) equipped with an EDS detector (X-Max detector STEM-EDS, Oxford Instruments, UK) by Dr Oriol Gavaldà Diaz.

2.3.2 X-ray micro-computer tomography (Micro-CT)

Micro-CT uses x-ray scans at progressive angles over 360° to build up a 3D picture of an object. The object is rotated on its central axis while the x-ray source and scanner are fixed. X-rays passing through the object are partially absorbed (some transmitted directly through the specimen) and differentially absorbed (different parts of the object absorb differently to give contrast). The scans taken at each angle are then reconstructed to form a 3D image of the object.

This is a non-destructive technique (although in some cases high doses of radiation may change the material) and gives microscale resolution. Because the sample does not need to be treated or sectioned for imaging, *in situ* testing like compression can be conducted. This can be combined with Digital Volume Correlation (Section 2.4.4) to map the 3D strain inside an object. This technique was employed to image multiphase hybrids under load, to correlate with the 2D strain measured at the surface.

In this thesis, a micro-CT scanner (Versa 510, Zeiss, Germany) was used at the Natural History Museum (London, UK) in collaboration with Brett Clark and Jeff Clark. Under all conditions the instrument was set up with a voltage of 70 kV and a current of 86 µA. An exposure time of 6 s was applied for each projection. The isotropic effective pixel size was 7.7 µm and the resolution of the detector was 2048 x 2048. No filter was applied to the source.

2.4 Mechanical characterisation

2.4.1 Uniaxial compression and tension

Force was applied to a sample along a single axis, in tension or compression, and the dimensions of the sample were used to measure the conventional stress and strain (also referred to as nominal or engineering values) by Equation 2.2 and Equation 2.3 respectively. In this thesis all mechanical tests were run in displacement control.

$$Conventional\ stress, \sigma_c = \frac{applied\ force\ (F)}{nominal\ crosssectional\ area\ (A)} \quad \textbf{Equation 2.2}$$

$$Conventional\ strain, \varepsilon_c = \frac{displacement\ (\Delta l)}{inital\ length\ (l_0)} \quad \textbf{Equation 2.3}$$

In order to take account of the increase in cross-sectional area with increased applied force in compression, and decrease in tension, the true strain and stress can be calculated according to Equation 2.4 and Equation 2.5 respectively [140]. Note that these equations use the sign convention of positive tensile stress and strain and negative compressive stress and strain. The true stress and strain are used herein, except when optical measurements for compressive samples indicated that the nominal strain should be used (Section 3.3.4), as the assumptions of the equations (constant volume and homogeneous stress state) are no longer valid when the samples barrel in compression.

$$True\ strain, \varepsilon^* = \ln(1 + \varepsilon_c) \quad \textbf{Equation 2.4}$$

$$True\ stress, \sigma^* = \sigma(1 + \varepsilon_c) \quad \textbf{Equation 2.5}$$

A Zwick/Roell testing machine with 10 kN load cell was used for compression testing to failure and cyclic compression on bulk cylindrical samples of approximate dimensions 15 mm height by 10 mm diameter (measured prior to testing). Samples were ground to flat before testing.

Tensile testing was conducted on a Bose Electroforce Series III testing machine with a 450 N load cell. Samples for tensile testing were cut with a razor blade to the dimensions shown in Figure 2.1, with thickness 0.5-2 mm (measured for each samples). 10 mm length on each end was covered in tape to protect from tearing in the grips and prevent slipping at the grips.

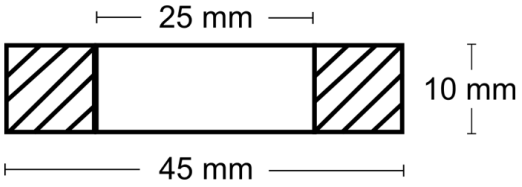

Figure 2.1: Schematic tensile test specimen. Hatched area is covered in tape and inside the grips.

2.4.2 Dynamic Mechanical Analysis

To characterise the viscoelastic properties of the hybrid materials, Dynamic Mechanical Analysis (DMA) was used in tension and compression over a range of frequencies and strains. Considering an applied sinusoidal displacement to the sample, the force required to produce this displacement is measured, which will have a phase lag when the sample has a viscoelastic response. That is, some energy is lost rather than the material behaving elastically (with no phase lag). This is illustrated schematically in Figure 2.2.

A complex modulus is defined from DMA analysis comprising the in-phase elastic component, termed the storage modulus (E'), and the 90° out of phase viscous component, termed the loss modulus (E''). These are defined according to Equation 2.6 and Equation 2.7, where σ_o and ε_o are the amplitude of the stress and strain sine waves respectively, and δ is the phase lag in the stress response.

$$Storage\ Modulus, E' = \frac{\sigma_0}{\varepsilon_0}\cos(\delta) \qquad \textbf{Equation 2.6}$$

$$Loss\ Modulus, E'' = \frac{\sigma_0}{\varepsilon_0}\sin(\delta) \qquad \textbf{Equation 2.7}$$

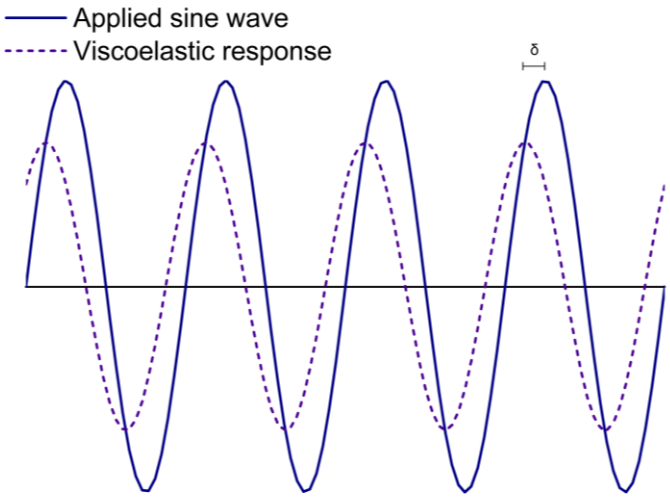

Figure 2.2: Schematic showing the applied stress/strain sine wave with the viscoelastic stress/strain response at phase lag = δ. For elastic materials, δ = 0, and the applied strain will be in phase with the resultant stress.

The ratio between the loss and storage moduli measures the damping of the material and is calculated by Equation 2.8.

$$Loss\ tangent, \tan(\delta) = \frac{E''}{E'} \qquad \textbf{Equation 2.8}$$

When the value of tan δ is small, the material is behaving elastically (over the strain range investigated), and in this case the storage modulus can be considered as a measure of the stiffness of the material.

In this work, DMA was conducted in uniaxial compression and tension in displacement control, using a Bose Electroforce Series III testing machine with 450 N load cell. Relevant strain ranges and frequencies are quoted when used. Compression samples were cylinders of approximate dimension 10 mm height x 5 mm diameter (measured prior to testing). Tensile DMA samples were the same as those used in uniaxial tensile tests to failure.

2.4.3 Digital Image Correlation (DIC)

Digital Image Correlation (DIC) is an optical technique to measure displacements and strain by tracking a speckle pattern on the surface of a sample. A facet (square box) is used on the surface within which the initial pattern at zero load is recognised by the software, which then correlates it with the loaded pattern to determine the relative movement of the facet. This is done between each photo as the load increases. Each facet contains a unique pattern which allows a good correlation between the unloaded and loaded state, producing one displacement vector per facet. For accurate measurements to be taken, the facet size as well as the pattern size and the overlap of the facets must be optimised. Reducing the size of facets increasing the spatial resolution of the technique, as the vector in a smaller area is considered. However, this also increases the error in the measurement, as there is an increased likelihood of mistaken correlation of the pattern.

DIC was used in this thesis as an optical measure of the strain around interfaces in hybrid samples, where mechanical characterisation was not straightforward. An ink pattern was drawn by hand on the surface of the hybrid to create a speckle pattern for correlation between images. A Canon 750D camera with EF-S 60 mm macro lens and 34 mm extension tubes was used, to further increase the magnification. The exposure time was 1/60 s, aperture f / 5.6 and ISO 800. The camera was set up on a tripod and protected by a screen from the testing rig. Photos were taken every 2 seconds during compression tests and testing was paused every 1 mm of displacement in order to briefly refocus the camera. This is because the barrelling of samples in compression leads them to gradually go out of focus which affects the tracking of the pattern. Photos were post-processed using ImageJ [141] to crop and stack images. Then, GOM Correlate 2018 software was used to produce maps of the principal strain [11] and the settings optimised as set out in Section 4.3.5.

2.4.4 Digital Volume Correlation (DVC)

Digital Volume Correlation (DVC) can be considered as a 3D extension of DIC. In this case, the facet is a box or subvolume, which also overlap in three dimensions. As with DIC, the position of the transformed subvolume is found by correlating the pattern within it (contrast in voxels, which are 3D pixels) with that of the initial untransformed subvolume. Then a displacement vector can be drawn between the initial and transformed volumes as shown in Figure 2.3, following [142].

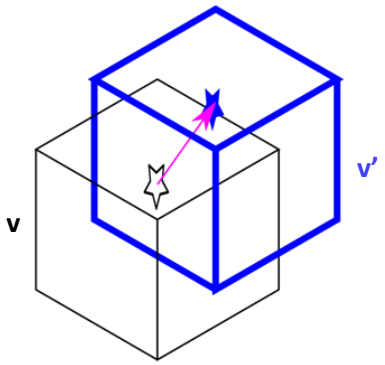

Figure 2.3: DVC schematic of vector (pink arrow) between 3D volumes, *v* the initial volume and *v'* the transformed state. The transformed volume is found by correlation of the pattern with that of the initial volume.

In this thesis, DVC was used with Micro-CT imaging to create a strain map in loaded two-phase hybrid samples. In order to create a pattern for tracking, microwave opaque zirconia particles were incorporated into the hybrids. The optimisation and use of DVC are set out in Chapter 5.

Chapter 3

Tuneable SiO_2-PTHF hybrids

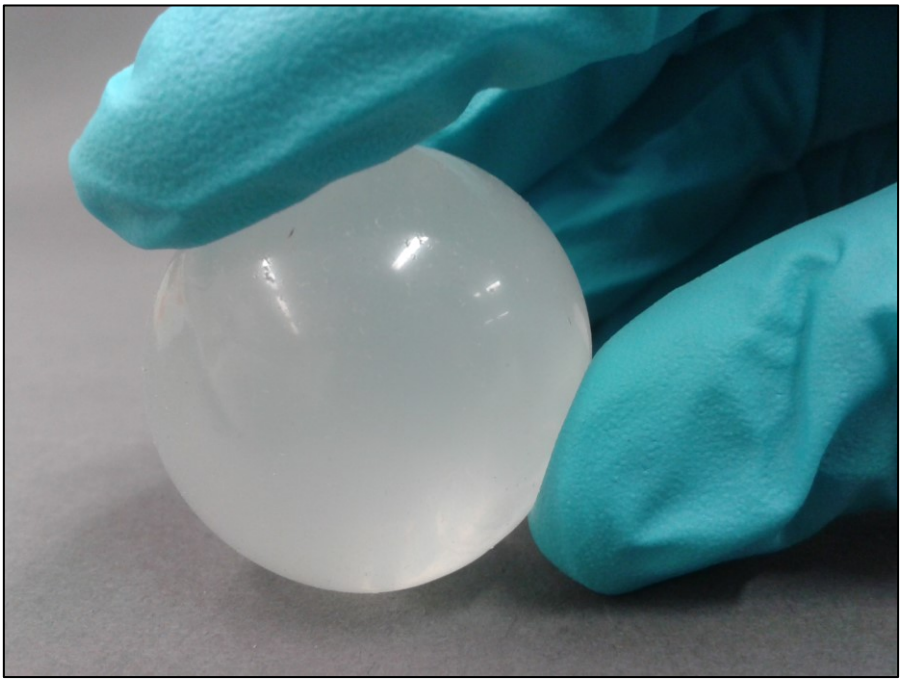

3.1 Introduction

Hybrid biomaterials offer the possibility of tuneable mechanical properties. They are made up of nanoscale and interpenetrating co-networks of organic and inorganic components [10], the relative amounts of the which can be altered to produce hybrid materials with a range of compressive and tensile strength and stiffness. Silica-poly(tetrahydrofuran), SiO_2-PTHF, is a novel Class IV hybrid system, where the organic component, PTHF, is formed *in situ* and bonded covalently to the nanoscale silica. Silica is formed via the sol-gel method and the organic polymer is added during the polymerisation, which continues in tandem with the co-condensation of the covalent cross linker with the silica precursor.

This hybrid system is based on previous work by Tallia *et al.* [11, 12], who developed the silica-poly(ε-caprolactone)-poly(tetrahydrofuran) hybrid, SiO_2-PCL-PTHF. In addition to producing a Class IV hybrid with unique mechanical properties, they found that the *in situ* cationic ring opening polymerisation reaction could occur without the inclusion of the biodegradable component, PCL.

Here the aim was to investigate the SiO_2-PTHF hybrid system as a non-degradable biomaterial with highly elastomeric and tuneable properties. Tuning is achieved via variation in the inorganic/organic composition of the hybrid allowing its mechanical behaviour to be matched the surrounding tissue in implant applications.

The objective of this chapter is to characterise the hybrid structure and synthesis along with its mechanical behaviour, understanding the relationship between the inorganic/organic composition and that behaviour. SiO_2-PTHF hybrids with a range of silica contents were obtained: from 3 wt.% SiO_2 to 45 wt.% SiO_2, limited by their ability to dry without shattering. The mechanical behaviour of the hybrid material was measured over this composition range. Hybrids were also tested in cyclic loading, over large cycle numbers, and after soaking in a simulated body environment to understand the potential for the use of these hybrids as cartilage replacement implant materials. As a first step to the assessment of the biocompatibility of this hybrid system, the cytotoxicity and cell attachment to hybrid surfaces were assessed. The results of this chapter form the basis for continuing the work to develop multiphase hybrid structures, 3D printing and eventual device development.

3.2 Methods

3.2.1 Synthesis

Materials

All materials were obtained from Sigma Aldrich (Dorset, UK) and used as obtained without further purification. The chemical structures of reagents used in hybrid synthesis are shown in Figure 3.1. All pots for synthesis were made from perfluroalkoxy (PFA, VWR, UK), and moulds from polytetrafluoroethylene (PTFE, Cowie Technology, Corby, UK).

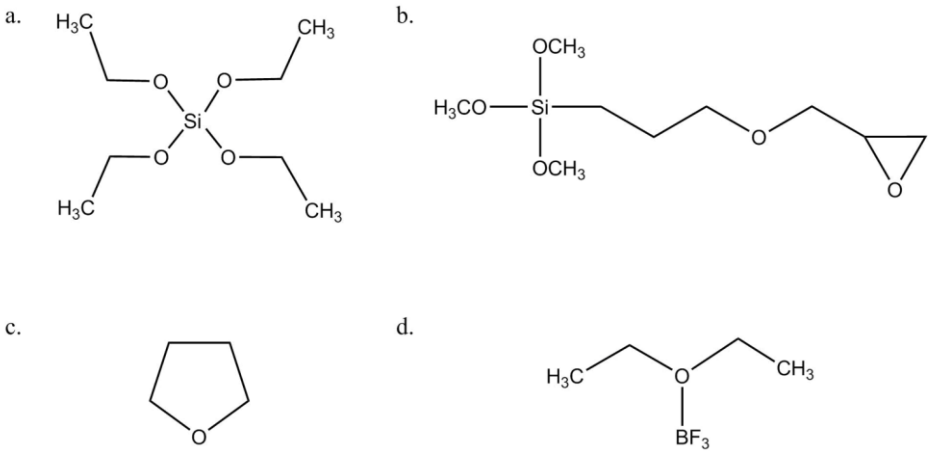

Figure 3.1: Chemical structures of reagents used in synthesis, **a.** Tetraethylorthosilicate (TEOS), **b.** (3-Glycidyloxypropyl)trimethoxysilane (GPTMS), **c.** Tetrahydrofuran (THF) and **d.** Boron trifluoride diethyl etherate ($BF3{\cdot}O(C_2H_5)_2$).

Synthesis protocol

SiO_2-PTHF hybrids were prepared by a two-pot synthesis, following the method outlined by Tallia *et al.* without the addition of poly(ε-caprolactone) [11, 12]. Molar ratios and typical synthesis quantities are shown in Table 3.1.

Table 3.1: Example synthesis quantities where *x* refers to the moles of TEOS and *a* refers to the moles of GPTMS, the ratio of which controls the inorganic/organic ratio (in this case *x*/*a*=2.5). The total hybrid sol volume is 92 mL before drying.

Reagent	Molar ratio	Typical quantity (mL)
GPTMS	*a*	2.21
$BF_3{\cdot}O(C_2H_5)_2$	0.25*a*	0.31
THF	100*a*	81.11
TEOS	*x* = 2.5*a*	5.58
H_2O	3*a* + 4*x*	2.34
HCl (1 M)	(1/3 volume of H_2O)	0.78

The inorganic precursor solution was prepared by hydrolysis of TEOS in deionised water with 1 M hydrochloric acid catalyst (1:3 vol. %). The amount of water was calculated to give a stoichiometric ratio of 4:1 with TEOS and 3:1 with GPTMS. The hydrolysis was carried out in a sealed beaker stirring at 400 rpm for 1.5 hours, during which time the solution went from phase separation to a homogeneous clear solution and water condensation could be observed on the underneath of the lid. Ageing this solution alone at 40°C would result in solid sol-gel silica glass.

Separately, THF was mixed with GPTMS at 400 rpm with a molar ratio THF:GPTMS of 100:1 in a PFA round bottom flask with plug to prevent significant THF evaporation. The cationic ring opening polymerisation (CROP) of THF monomer was initiated by the addition of boron trifluoride diethyl etherate catalyst with molar ratio $BF_3{\cdot}O(C_2H_5)_2$ 1:4 GPTMS, for which the proposed mechanism is discussed in Section 3.3.1. Evidence of the polymerisation was visible after 6-7 minutes: the viscosity and temperature of the solution increased, and bubbles were visible in the solution. The polymerisation was confirmed with ^1H NMR as discussed in Section 3.3.1. After the polymerisation was underway, 7 minutes after $BF_3{\cdot}O(C_2H_5)_2$ addition, the solution was poured into a beaker and stirred at 400 rpm whilst the hydrolysed TEOS solution was added dropwise. Droplets of TEOS solution are immiscible when first added so it is important that this is done slowly to ensure proper mixing of the solutions. The resultant hybrid sol was further mixed for a minimum of 10 minutes and then left to stand without stirring for 10 minutes to allow any bubbles to travel to the surface. A schematic of the reaction protocol is shown in Figure 3.2.

This solution was added to PTFE moulds by pouring (for discs) or via Pasteur pipettes (for cylinders). Moulds of diameter 150 mm were filled to approximately 2 mm depth to form hybrid discs. Moulds of 5 and 10 mm were filled to 10 and 15 mm height respectively to form cylindrical hybrid samples. Moulds were sealed using layers of aluminium foil (discs) or in poly(methyl pentene) (PMP) pots (cylinders) and were then placed in an oven at 40°C where they remained sealed for 3 days. This is an ageing time during which the polymerisation continued and the THF was prevented from evaporating: at 3 days the hybrid had gelled but retained its original volume. After this time, the pots were opened gradually over a period of 1 week to prevent sudden evaporation of THF, and then the samples were allowed to dry in open moulds for a further week, still at 40°C.

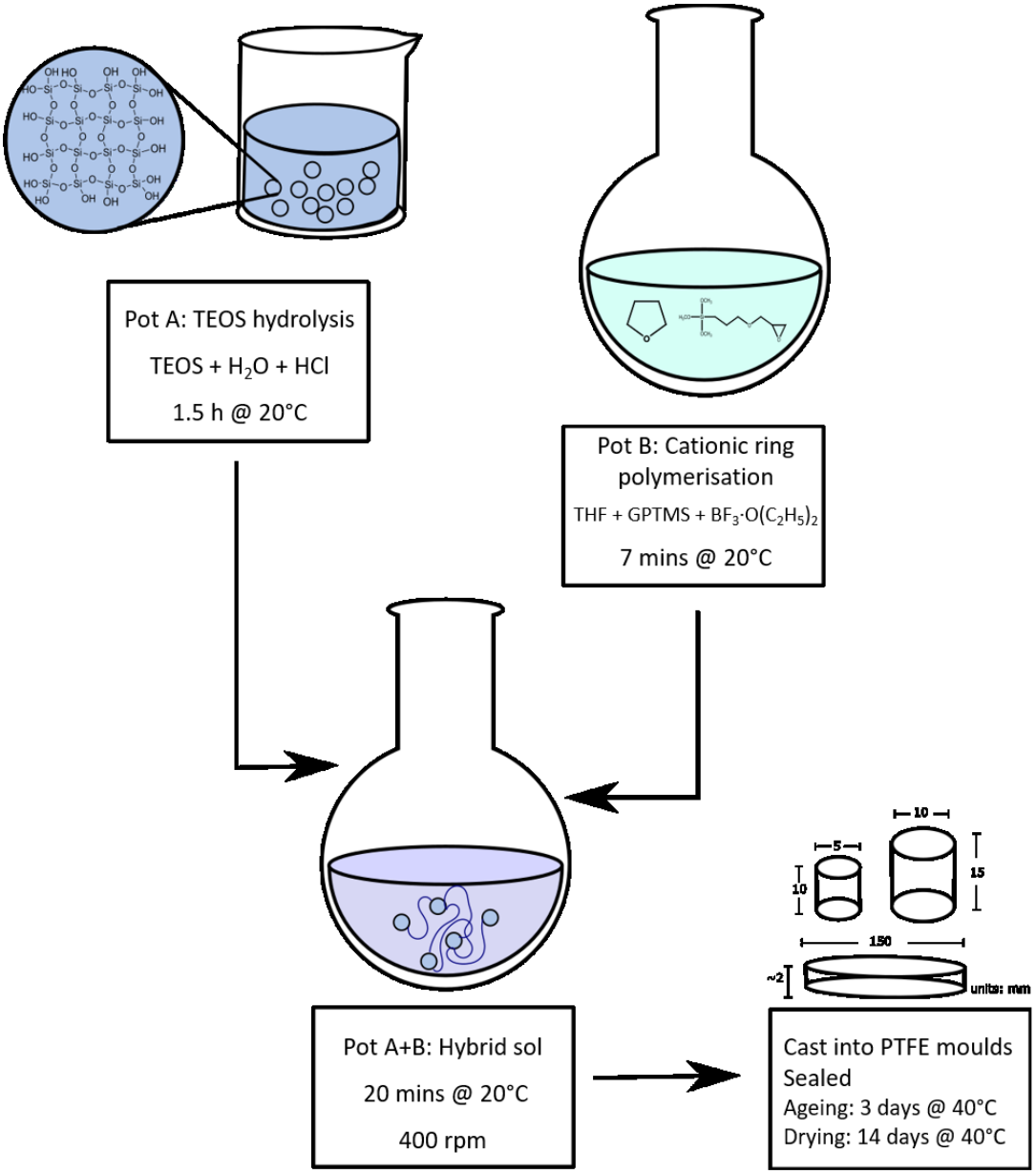

Figure 3.2: The hydrolysed TEOS (pot A) is added dropwise to the solution undergoing cationic ring polymerisation (pot B), forming a hybrid sol which gels gradually over time.

A range of hybrid compositions were prepared, controlled by the ratio of moles of TEOS (*x*) to the moles of GPTMS (*a*) and denoted using this TEOS/GPTMS ratio (*x*/*a*) as Si(*x*/*a*)-PTHF, from Si0-PTHF with no addition of TEOS to Si20-PTHF with a TEOS/GPTMS ratio of 20 (Table 3.2). The final silica contents that resulted ranged from 4-45 wt.% of which an intermediated range were characterised. Beyond Si20-PTHF the resulting hybrid of greater than 45 wt.% SiO_2 was extremely glassy and often shattered on drying, so this work discusses only hybrids with higher polymer content than this.

Table 3.2: List of hybrids synthesised as denoted by their TEOS/GPTMS ratio

TEOS/ GPTMS	Sample code
0	Si0-PTHF
1	Si1-PTHF
1.75	Si1.75-PTHF
2.5	Si2.5-PTHF
3.75	Si3.75-PTHF
5	Si5-PTHF
7.5	Si7.5-PTHF
10	Si10-PTHF
20	Si20-PTHF

The synthesis can have a high level of variability with identical starting reagents producing hybrids of differing composition and properties. The theoretical final silica content cannot be calculated because of lack of knowledge of the molar mass of the PTHF formed *in situ*. This is discussed further with solid state NMR in Section 3.3.3 and when 3D printing (Chapter 5).

Removal of bubbles

Bubbles remaining in the solution can become trapped once the hybrid is added to closed moulds. In the case of open moulds the bubbles can often escape or travel to the surface but this can still be a problem for making intact samples for mechanical testing. The viscosity of the solution at the point of addition to the moulds should be low enough that letting the solution rest without stirring before adding to mould is sufficient to allow the bubbles to travel to the surface and be removed. However, in the case of closed moulds it is necessary to hit the base of the mould to force out the bubbles, and to ultrasound (camSonixc1800T, Camlab, Cambridge, UK) for five minutes.

3.2.2 Mould development

In order to assess the effect of mould roughness and composition on the shrinkage and final surface roughness of the hybrid samples, three PTFE moulds in the shape of discs of 50 mm diameter were produced with different roughness and two hybrid compositions of Si2.5-PTHF and Si10-PTHF were tested. The roughness of all moulds is set out in the results in Section 3.3.2.

Shrinkage factor

The ratio of the dimensions of the mould to the dimensions of the resulting hybrid sample was used to evaluate a shrinkage factor, in each dimension. The relationship between the composition and

shrinkage factor was assessed alongside the roughness using Si2.5-PTHF and Si10-PTHF as described below.

Mould roughness

Final roughness of the hybrid sample depends on the roughness of the mould except the free surface, which has very low surface roughness, varying slightly according to the silica content. The material used to make moulds is restricted however, as the solution will bind with glass and THF is corrosive to metals and many plastics, so only PTFE and PFA were used. PTFE moulds were manufactured by Cowie Technology (Corby, UK) or by computer numerical control (CNC) drilling of block PTFE supplied by the same company.

To investigate the relationship between the roughness of the mould and that of the hybrid, two PTFE discs were polished using a metallographic grinder with 600 and 4000 grit sandpaper respectively, and a third disc was left with the machine lathe marks from the manufacturer. In each case, the roughness only refers to the bottom surface and the sides of each had the same roughness. The surface roughness was measured with a profilometer (Taylor Hobson). The same hybrid solution was added in equal volume to each of these moulds, and the final dimensions of the hybrid discs were measured.

In order to produce moulds with a lower surface roughness, PTFE moulds were produced by CNC, designed using Solid Works (resolution tolerance = 0.5 degrees and deviation of 0.007 mm) and manufactured with a path interval of 0.01 mm. A closed rectangular mould was produced with different surface roughness and dimensions to investigate the effect of roughness on the shrinkage in different dimensions within a closed mould.

To further decrease the roughness from this point, it was necessary to melt PFA between the top and bottom of a glass petri dish at 320°C for 7 hours in air to create a flat-bottomed PFA mould, diameter 100 mm, with a roughness below 100 nm. Subsequent work showed in tribological testing that SiO_2-PCL-PTHF hybrids produced on these PFA moulds did not damage cartilage, when the hybrids were tested against living bovine cartilage as a counter surface (unpublished work, Dr Maria Parkes).

3.2.3 Characterisation of the hybrid structure

To understand the nature of the hybrid network, several characterisation techniques were combined. Firstly, ^{1}H NMR was used during the synthesis to confirm the polymerisation of the THF. Samples were taken before and after the addition of $BF_3{\cdot}O(C_2H_5)_2$ (but before the addition of hydrolysed TEOS) and diluted in deuterated chloroform ($CDCl_3$) with settings described in Section 2.2.1.

To quantify the relative quantities of THF and PTHF present, 1,3,5-Trioxane was added to the reaction mixture at a calculated concentration of 0.6 mg mL^{-1}. Aliquots of 100 µL were taken at 5 minute intervals from time zero at which the $BF_3{\cdot}O(C_2H_5)_2$ was added until the gelation had progressed to make the solution too viscous. These were diluted in 600 µL of $CDCl_3$ for analysis by ^1H NMR. MestReNova software was used to calculate the area of peaks of THF and PTHF (labelled in Section 3.3.1) relative to the area of the Trioxane peak, used as a measure of the relative quantities of each [143].

After synthesis of the hybrids, FTIR was used to compare the relative absorption from bonds from the inorganic and organic parts of the hybrids over a wide composition range of samples. TGA was used to determine the polymer weight percentage, corresponding the to the percentage mass loss on heating to 800°C, since is not directly quantifiable from the initial synthesis quantities.

TEM was used to investigate the homogeneity of the hybrid at the nanoscale. A thin sample of Si2.5-PTHF hybrid (0.1 mm) was cast and dried as for bulk samples and prepared for imaging as set out in Section 2.3.1.

Solid state NMR

Solid state NMR was carried out by Dr Josh Clark and Professor John Hanna at University of Warwick. Samples were synthesised by MEng student Enric Juan Alcocer.

Samples of Si10-PTHF and Si15-PTHF, which had the same final hybrid silica content, despite the different initial ratio TEOS/GPTMS of 10 and 15 respectively, were analysed to see if any differences in the structure could be detected. The hybrids were prepared by machining with a lathe to required diameter. The relative contribution of Q^4 and Q^2, Q^3 where $Q^n = Si(O\text{-}Si)_n(OH)_{4-n}$ and T^2, T^3 where $T^n = C\text{-}Si(O\text{-}Si)_n(OH)_{3-n}$ species indicated the degree of condensation of the silica network (Equation 2.1) formed from the combined contributions of GPTMS (T^n) and TEOS (Q^n) as described in Section 2.2.1.

3.2.4 Mechanical characterisation

Uniaxial compression testing and cyclic compression testing were carried out on cylindrical samples of height x diameter ≃ 15 x 10 mm with a minimum aspect ratio of 1 following [110]. The exact dimensions of each sample were measured prior to testing. A Zwick machine was used fitted with 1 kN load cell in displacement control at a rate of 1 mm min^{-1}. The average of 5 valid repeats was calculated and plotted with error bars of the standard deviation.

Cyclic testing was conducted on the same machine with a strain rate range of 1-150 mm min^{-1} for samples of Si5-PTHF composition. 90 mm min^{-1} was chosen as an estimated physiological strain rate [56]. Cycle lengths were from 100 to 10000 cycles as specified.

Uniaxial tensile testing to failure was carried out according to ASTM D1708−13 [144] on samples of length x width x thickness ≃ 45 x 10 x 0.5-2 mm (measured for each sample) with 25 mm exposed length, using Bose Electroforce Series III machine fitted with 450 N load cell, in displacement control at a rate of 1 mm min^{-1}. The average of 5 valid repeats was calculated and plotted with error bars of the standard deviation. Samples failing at grips were excluded. Stress relaxation was carried out on samples of the same dimension to 50% $\varepsilon_{failure}$ at 3 mm min^{-1} and held for 1 hour. DMA was conducted in tension on samples of the same dimension, of composition Si1, 2.5, 5-PTHF at 4 points per decade 0.01-10 Hz (16 frequencies in total) over engineering strain range ε_c = 5-10%.

DMA was conducted in compression using Bose Electroforce Series III machine fitted with 450 N load cell on cylinders of height x diameter 10 x 5 mm, of composition Si2.5, Si5, Si7.5-PTHF at 4 points per decade 0.01-10 Hz (16 frequencies in total) over three engineering strain ranges: ε_c = 2-5, 5-10 and 10-15%.

SEM was used to image the fracture surfaces at a range of compositions.

3.2.5 Behaviour in wet environment

Characterisation was repeated after varying soaking times (2 hours to 1.5 years) in phosphate-buffered saline (PBS), at 37°C and 120 rpm stirring to provide a first approximation to the body environment including the presence of salts. FTIR and TGA were conducted to check for any change in the chemical properties or mass loss respectively. Cyclic testing was used to assess the progressive change in properties over time, at 90 mm min^{-1} to 100 cycles for Si5-PTHF composition. DMA in compression was used to compare the change in stiffness for lower (Si2.5-PTHF) and higher (Si7.5-PTHF) silica content samples. Compression testing to failure was conducted after 1 month soaking on Si1, 1.75, 2.5, 3.75, 10-PTHF. The same settings were used as for dry testing and samples were tested immediately upon removal from solution, with excess liquid removed from the surface.

3.2.6 Cell studies

All cell studies and analyses were conducted by Dr Silvia Ferreira, Faculty of Medicine, Imperial College London.

Sterilisation

Gamma irradiation was carried out by Christoph Salzelechner, Centre for Craniofacial and Regenerative Biology, King's College London. The first attempt at sterilisation was at 25 kGy (minimum dose), then at 50 and 100 kGy. DMA was used to assess any change in properties with gamma irradiation as it is more reliable for a limited sample number than tensile testing. DMA was conducted in tension at 4 points per decade 0.01-10 Hz (16 frequencies in total) over three engineering strain ranges: ε_c = 2-5, 5-10 and 10-15%. Three samples were tested per strain range and irradiation condition: 0 and 25 kGy for the first experiment and 25, 50 and 100 kGy for the second experiment. The average and standard deviation between three repeat samples is plotted. First assessment of the effectiveness of the sterilisation was carried out by storage in cell culture medium with media change every 2 days and observation of changes to the media. After this initial assessment, cell studies for attachment and cytotoxicity were conducted.

Cytotoxicity

Cytotoxicity was assessed following ISO 10993-5 (Tests for *in vitro* cytotoxicity) [145] in conjunction with ISO 10993-12 (Sample preparation and reference materials) [146] on the biological evaluation of medical devices. Extracts were prepared from strips of sample: 24 hybrids strips with 0.25 cm^2 exposed area each were placed in 2 mL fresh serum Dulbecco's modified Eagle medium (DMEM, Sigma, UK), to give a concentration of 3 cm^2 mL^{-1}, at 37°C for 72 hours in a falcon tube placed on a roller-shaker. Samples used were not gamma irradiated and instead washed three times in DI water prior to testing.

Extractable solutions were prepared in an identical manner for the positive and negative controls. High density polyethylene film was used as negative control (non-cytotoxic) and polyurethane film containing 0.1% zinc diethyldithiocarbamate (ZDEC) was used as positive control as it shows a reproducible cytotoxic response. Non-sterilized strips of 2 x 15 mm, 0.5 mm thickness were used as supplied by Hatano Research Institure, Food and Drug Safety Centre, Japan.

Extractable solutions were filtered at 0.2 µm in a non-pyrogenic, sterile, surfactant-free cellulose acetate filter (Cat. No. 431219, Corning, UK) to sterilise and prepared into a dilution series of 25, 50, 75 and 100% by further dilution in DMEM, then supplemented with 10% (v/v) Foetal Bovine Serum (FBS), 1% (v/v) Antibiotic Antimycotic (ABAM) and 1% (v/v) L-glutamine.

Mouse chondrogenic cell line ATDC5 were seeded on 96-well tissue culture plates with 1 x 10^4 cells per well and allowed to attach overnight. Cells were treated with 100 µL of extractable per well (n=7 wells per treatment condition) and incubated for 24 h, after which an MTT cytotoxicity assay was performed. This is a colorimetric assay that assess the metabolic activity of cells using absorbance, via

the conversion of 3-(4,5-dimethylthiazol-2-yl)-2,5-diphenyltetrazolium bromide (MTT) to formazan by enzymes produced by the cells. Media was removed from cells and replaced with MTT in serum-free DMEM at a concentration of 1 mg mL^{-1} (50 µL per well). After 2 h of incubation, the solution was removed and 100 µL of isopropanol was added to dissolve the formazan derivatives. After shaking for 15 minutes at room temperature, the absorbance of the solution was measured on a Spark Multimode Microplate Reader (Tecan, Switzerland) at a wavelength of 570 nm. The proportion of viable cells was calculated according to Equation 3.1, where A is the absorbance, blank refers to the cell media alone and control to the negative (non-cytotoxic) control.

$$Viable\ cells\ (\%) = \frac{A_{sample} - A_{blank}}{A_{control} - A_{blank}} \times 100 \qquad \textbf{Equation 3.1}$$

Materials pass ISO 10993-5 tests if the cell viability is above 70% following exposure to the extract media. The ISO standard allows for use of a variety of cell lines (to give a homogenous response as opposed to the heterogeneous behaviour of primary cells). Mouse chondrogenic cell line was chosen as a first test when considering the application of the material in attachment to cartilaginous end-plates that connect the vertebrae of the spine to the intervertebral discs.

Cell culture on hybrid discs

In a 2D cell attachment experiment, mouse chondrogenic cell line ATDC5 were seeded on hybrid samples in the shape of squares cut from discs to determine the attachment of cells and their behaviour on the hybrid surface. Cells were seeded at two different cell densities to determine the optimum cell density.

Hybrid squares of approximately 5 x 5 x 2.5 mm were stored in DI water for one month and subsequently sterilized in water at 100 kGy. Each sample was washed in fresh serum-free DMEM supplemented with 1% (v/v) ABAM for 30 minutes, then centrifuged at 2000 rpm for 2 minutes on 48-well cell suspension plates (Greiner Bio-One), to leave the samples flat at the bottom of the well and remove air bubbles. ATDC5 cells were seeded onto each hybrid sample in a concentrated cell suspension (60 µL per sample) at two different cell densities: 1 x 10^4 cells cm^{-2}, 2500 cells per sample (Low density, n = 5) and 5 x 10^4 cells cm^{-2} = 12500 cells per sample (High density, n = 5). Cells attached to the scaffolds within 2.5 hours when incubated in humidified atmosphere at 37°C, 5% CO_2 and 21% O_2. Then, 1 mL of fresh cell culture medium was added to each well to submerge the sample. Medium was exchanged every other day for 14 days.

Cell viability was evaluated using RealTime-Glo MT Cell Viability Assay (Promega, UK) following the manufacturer's instructions on day 1, 3, 7, 14. Luminescence was measured on a Spark Multimode Microplate Reader (Tecan, Switzerland).

Immunohistochemistry staining and confocal microscopy

After 10 days in culture, cell-seeded samples were fixed with 4% paraformaldehyde for 20 minutes at room temperature and then permeabilized with 0.1% (v/v) Triton-X 100 in PBS (PBT) for 10 min and blocked for 1 h with 10% (v/v) horse serum in 0.15% (w/v) glycine and 0.2% (w/v) bovine serum albumin (Sigma, UK) in PBT. Samples were then incubated overnight at 4°C with 1:400 in PBT primary antibody Rat IgG2a monoclonal anti-tubulin [YOL1/34] (Cat. Nº. ab6161, Abcam). After 3 washes in phosphate buffered saline, cell-seeded samples were incubated in the darkness for 1 h at room temperature with 1:300 Alexa Fluor® 568 goat anti-rat (Cat. Nº. ab175476, Abcam). Negative controls (omission of the primary antibody with the presence of secondary antibodies) were performed.

Other cell-seeded samples were stained for 1 h at room temperature in darkness with 1:100 Phalloidin-TRITC (Cat. Nº. P1951, Sigma UK). After washing with PBS, nuclei were counterstained with 10 µg/mL Hoechst 33342, trihydrochloride, trihydrate (ThermoFisher Scientific) for 15 min. After washing, stained samples were transferred to a sterile, hydrophobic and uncoated µ-Slide 8-Well (Cat. No. 80821, Ibidi) and imaged in a Leica SP8 inverted confocal laser scanning microscope. Detector gains were set to be constant between samples to facilitate comparison. Z-series with 0.5 µm Z-spacing were obtained using sequential acquisition and Kalman filter mode, with a 20× dry objective and numerical aperture of 0.75 and 2048 × 2048 pixel size. Images for tubulin and actin were max projections of 30 Z-slices of 0.5 µm obtained using Image J.

Statistical analyses

Metabolic activity is shown as bar graphs expressing average and standard deviation. Statistical analyses were carried out using a non-parametric Kruskal-Wallis test followed by Dunn's multiple comparison test for multiple comparisons. Statistical analyses were carried out using GraphPad Prism version 7 for Windows (GraphPad Software, USA).

3.3 Results and discussion

3.3.1 Synthesis

Polymerisation mechanism

The synthesis procedure set out in Section 3.2.1 is timed to give enough time for the TEOS to hydrolyse before a fast polymerisation occurs and then the separate reactions are combined. The beginning of the polymerisation, after addition of $BF_3{\cdot}O(C_2H_5)_2$ catalyst, causes a gradual gelation. The viscosity of the solution was observed to increase, accompanied by formation of bubbles and release of heat. Samples were removed for ^1H NMR before and 7 minutes after the addition of the catalyst. The peaks arising from the hydrogens on the GPTMS epoxide ring carbons (labelled 5 and 6 on Figure 3.3a and highlighted in the blue region on Figure 3.3b disappeared, indicating the opening of the epoxide ring. Meanwhile, peaks arising from PTHF appeared at a chemical shift just below the THF peaks (δ = 1.85, 3.76 ppm tabulated values [147]), which are still present.

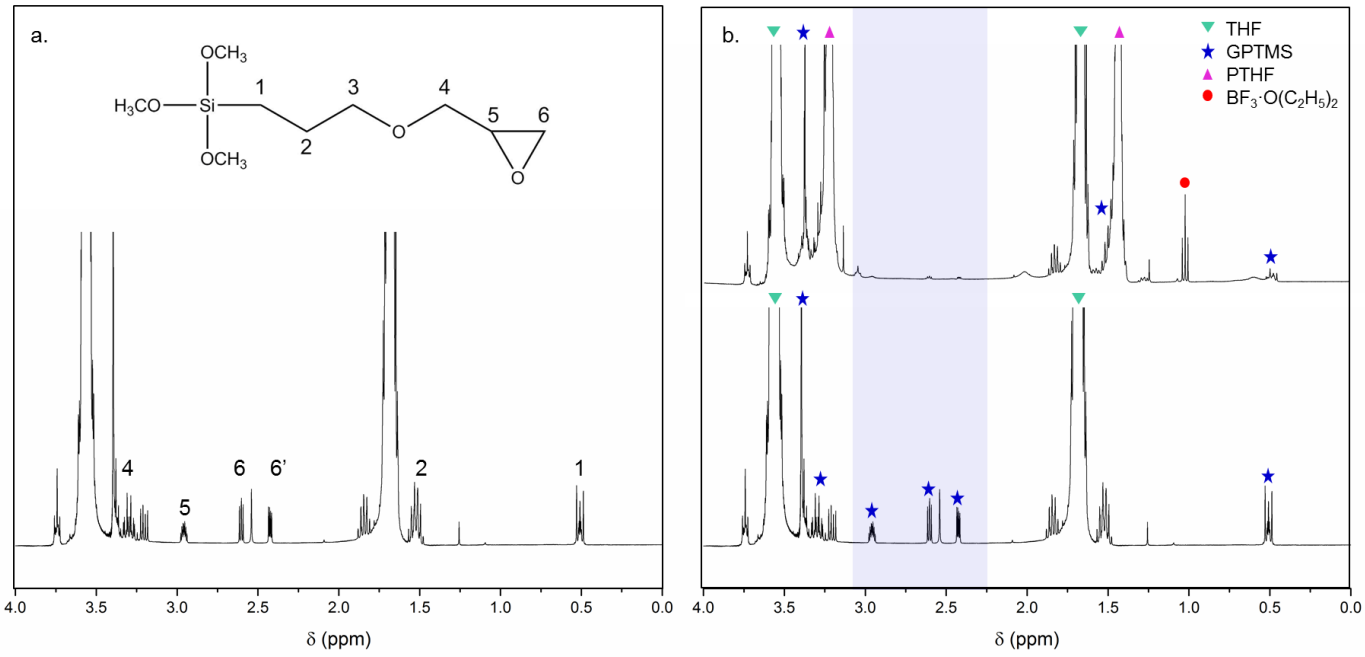

Figure 3.3: ^1H NMR of **a.** GPTMS-THF solution before the addition of $BF_3{\cdot}O(C_2H_5)_2$ catalyst, showing the positions of the hydrogen atoms on carbons 1-6 of GPTMS from which the correspondingly labelled peaks arise, and **b.** below, the same spectrum before the addition of $BF_3{\cdot}O(C_2H_5)_2$ and above, 7 minutes after the addition of $BF_3{\cdot}O(C_2H_5)_2$. The blue highlighted region relates to the hydrogens on the carbons of the epoxide ring, which is opened during the polymerisation and thus the peaks disappear. Peaks arising from the formation of PTHF (pink triangles) appear at a lower chemical shift than the THF peaks (green upside-down triangles). The peaks at δ = 2.17 and 1.25 ppm may arise from acetone and ethanol respectively, used to clean labware and at 2.6 ppm from presence of water.

The proposed mechanism for the ring opening polymerisation (CROP) is shown in Figure 3.4 and outlined in the patent application relating to this material [11]. Evidence for this synthesis mechanism comes firstly from the doctoral thesis of Dr. Francesca Tallia on the SiO_2-PCL-PTHF hybrid system [110], finding that the reaction cannot occur without the presence of THF or GPTMS and observing the opening of the epoxide ring of GPTMS and formation of PTHF in ^{1}H NMR. Here, this mechanism is confirmed for the SiO_2-PTHF system by the combination of evidence from ^{1}H NMR and ^{29}Si solid-state NMR and FTIR spectroscopy, discussed in Section 3.3.3.

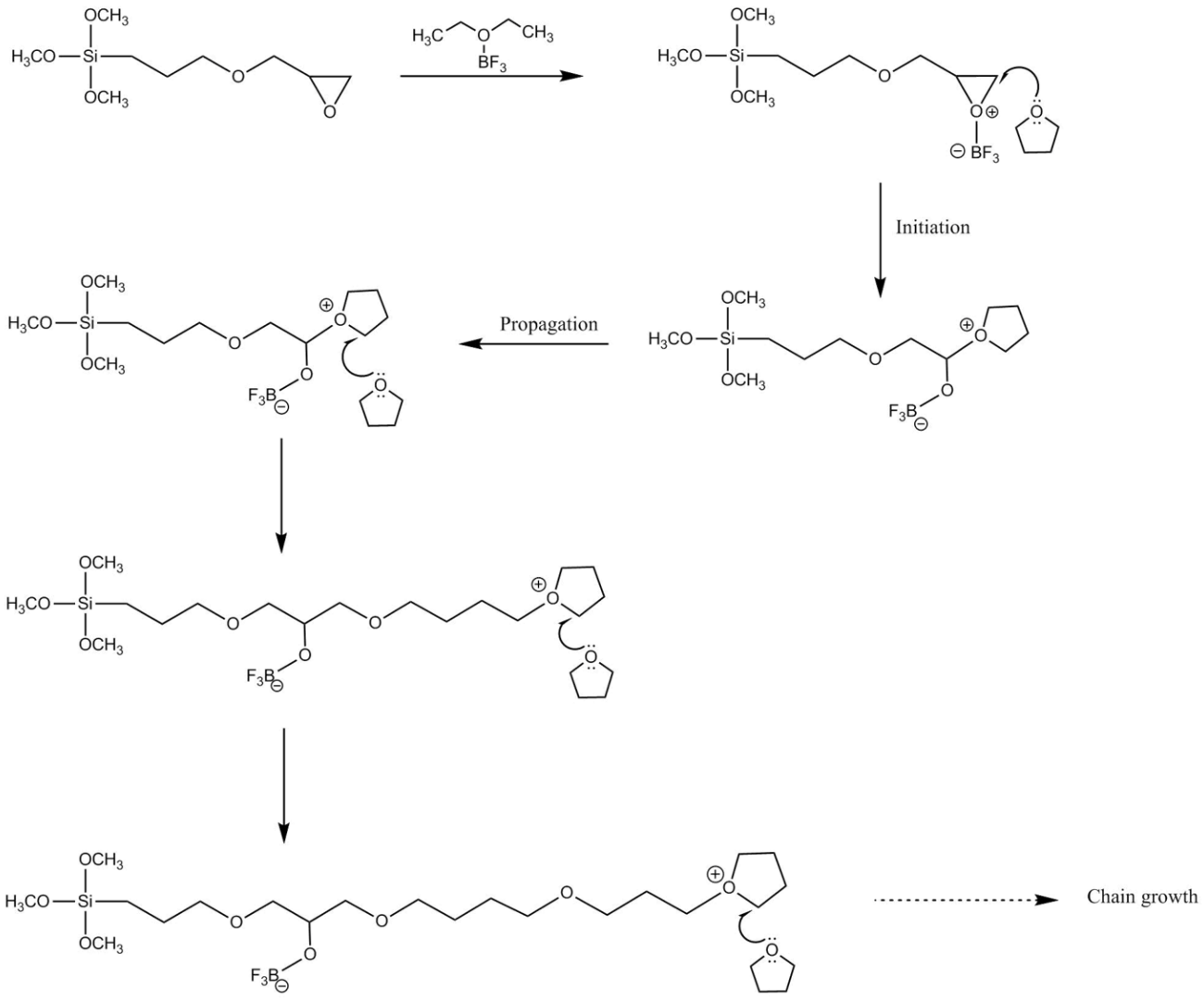

Figure 3.4: Proposed mechanism for the polymerisation of THF on to a growing chain with one molecule of GPTMS at the end. The epoxide ring is activated by the $BF_3 \cdot O(C_2H_5)_2$ Lewis acid in the first step, then the intermediate compound formed undergoes nucleophilic attack from the oxygen in the THF monomer. This is the initiation of ring opening polymerisation (CROP) which continues in chain elongation steps.

In the polymerisation mechanism, GPTMS acts as the initiator, catalysed by $BF_3{\cdot}O(C_2H_5)_2$. Without GPTMS, the reaction will not occur. The epoxide ring of GPTMS is activated by the Lewis acid $BF_3{\cdot}O(C_2H_5)_2$, producing an intermediary compound which is then subject to nucleophilic attack by the THF monomer.

The product of this is also susceptible to attack by another monomer of THF, so the Cationic Ring-Opening Polymerisation (CROP) is initiated. Propagation occurs whereby the chains elongate by the addition of further cyclic THF monomers. CROP is a living polymerisation without an inbuilt termination mechanism, and as such will continue until there is no further THF to react or there is another molecule present that causes termination. In the SiO_2-PCL-PTHF system, OH groups on PCL could act to terminate the reaction [110]. In this case, since the reaction is not carried out in anhydrous and airless conditions, a water molecule could act as a terminator.

Usually, a living polymerisation will produce polymers with similar chain lengths, *i.e.* a dispersity, Đ, close to 1 [148]. However, it has so far not been possible to measure this directly for example using gel permeation chromatography, GPC, as no chain terminator has been found to freeze the reaction (phenolate was not successful). It is not possible to dissolve the final hybrid in a suitable solvent for GPC because of the inorganic part of the hybrid which is covalently bonded to the polymer.

Therefore, understanding of the structure of the hybrid comes from consideration of a combination of techniques: ^{1}H NMR, FTIR and solid state NMR. A schematic representation of the SiO_2-PTHF structure, with covalently connected co-networks of silica nanoparticles and PTHF, is shown in Figure 3.5.

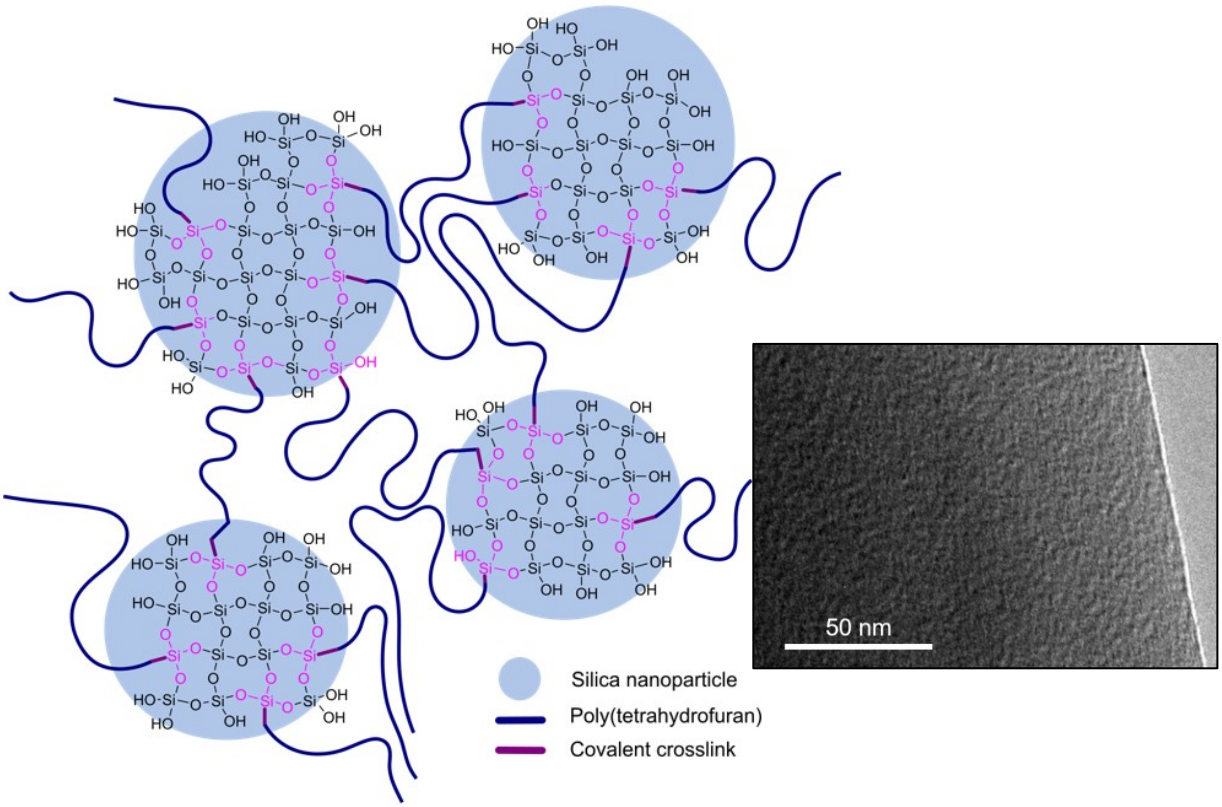

Figure 3.5: Schematic of the structure of SiO_2-PTHF hybrids. The Si-O bonds originating from GPTMS are shown in pink, joined to the covalent crosslinks between the silica nanoparticles (with dimensions of a few nanometres diameter) and the polymer chains. The lengths of the polymer chains and the connectivity between the inorganic and organic components are unknown and shown as an example. There may be non-covalent interactions between the polymer chains. The TEM image inset shows the homogeneity of the hybrid at the nanoscale for Si2.5-PTHF.

Control of synthesis parameters

THF is in excess in the reaction, at a molar ratio of 100:1 with GPTMS. This arises from the original use of THF as a solvent for PCL in SiO_2-PCL-PTHF hybrid system after which the unexpected polymerisation of THF was discovered [110]. Here, the 100:1 ratio was experimentally determined to allow gradual polymerisation.

Samples were placed in an oven at 40 °C after synthesis and sealed for the first 3 days, to prevent the evaporation of THF whilst the polymerisation was ongoing. After 3 days, the samples were opened gradually and the THF began to evaporate, causing the samples to shrink by around one third (this can also depend on the geometry of the mould used, Section 3.3.2). The boiling point of THF is 66°C but 40°C was enough to fully evaporate the excess THF, as evidenced by the lack of solvent peak in the TGA mass loss curve. THF is very volatile so evaporated over the drying period of two weeks, even below its boiling point.

As a result of this loss of THF, the final inorganic/organic ratio of the hybrid produced was not equal to that theoretically calculated from the molar ratio of the reagents. A typical TGA curve used to calculate the mass loss, corresponding to the organic content of the hybrid, is shown in Figure 3.6a. Figure 3.6b plots the initial molar ratio against the final silica content, determined by TGA, for the full range of compositions synthesised, where the data was available (averages were not taken as there were multiple syntheses for some compositions and few or one for others) having been collected for other purposes. There was a linear trend between the variables but there is also a large range of final compositions produced by identical starting molar ratios (total volume of the reaction varied).

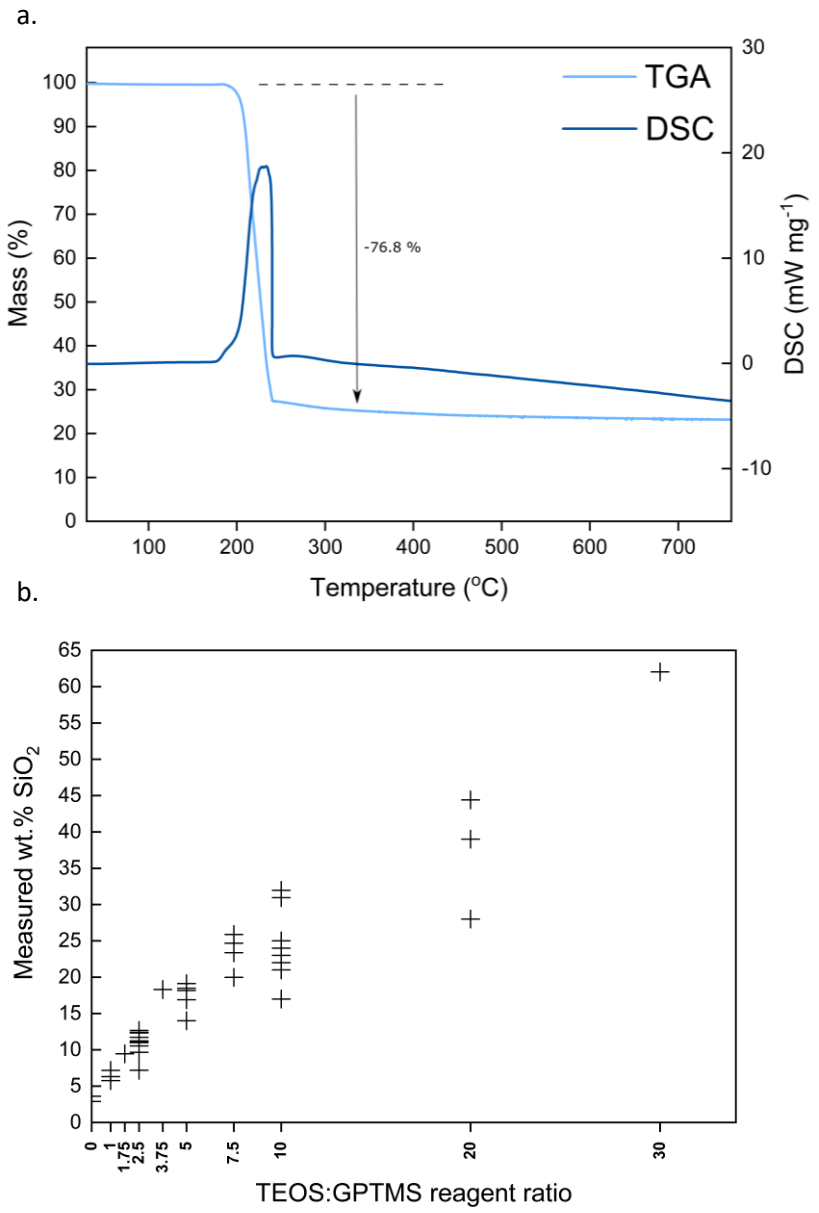

Figure 3.6: a. Typical TGA/DSC curve for Si10-PTHF, showing the calculation of the polymer content as the mass loss. The final silica content is 100 – 76.8 = 23.2 wt.% SiO_2. **b.** Relationship between the starting ratio of the reagents, namely between the silica source TEOS and the GPTMS which controls the proportion of PTHF formed, and the final measured silica content of the hybrid produced. Two syntheses with the same initial reagent quantities can produce hybrids with different final silica contents.

It was hypothesised that the observed variation in final inorganic/organic ratio produced from identical synthesis conditions could be the result of differing THF evaporation during the synthesis due to different temperatures. However, no correlation was found between different synthesis temperatures (17-25^{o}C corresponding to the variation in laboratory temperature) and the final inorganic/organic ratio. There could also be an effect of variation in the amount of THF evaporation during the 3 day ageing period, since the sealing of the hybrids was not airtight. Measuring the silica content at 2 mm intervals through a cylinder indicates that there is a small decrease in the inorganic/organic ratio from the bottom of the mould to the top of around 1 wt.% SiO_2, illustrated in Figure 3.7. Since the top surface is exposed, it is unexpected that the silica content decreased closer to the top of the mould, but this indicates that the sealing was good enough to prevent uneven THF evaporation.

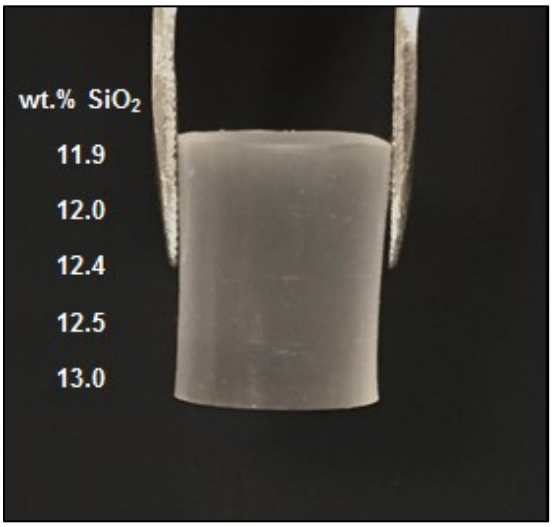

Figure 3.7: An example of Si2.5-PTHF cylindrical sample and SiO_2 content, which was determined by cutting 2 mm sections that were individually tested by TGA. The cylinder is pictured in same orientation as it was in the mould, so there is a small difference 1 wt.% SiO_2 from top to bottom.

Experimentally, it was found that a small change in the 'interval time' – the time period between addition of $BF_3{\cdot}O(C_2H_5)_2$ and the subsequent addition of the hydrolysed TEOS solution to the ongoing polymerisation – had a significant effect on the time taken for the solution to reach a given viscosity. In other words, the addition of the hydrolysed TEOS has the effect of partially quenching the reaction. This is because OH groups can terminate the reaction, for example OH groups in PCL [110]. This effect is more pronounced the lower the TEOS:GPTMS ratio, since a lower amount of hydrolysed TEOS will be added. If the TEOS was added after 5-6 minutes, the solution stayed at the same viscosity for many hours without gelling. Whereas, when the TEOS was added after an interval time of 10 minutes, the

polymer solution was already viscous with significant amounts of bubbles, and the addition of the TEOS did not stop the ongoing gelation. To make bulk hybrid samples, the solution should be bubble free so an intermediate interval time of 7 minutes was chosen, having been optimised for Si2.5-PTHF composition. This correlates with an estimation of the conversion from THF to PTHF in Figure 3.8, comparing the area of NMR peaks relative to 1,3,5-trioxane at fixed concentration.

It was hypothesised that changing the interval time may alter the structure or lengths of the polymer chains or silica condensation, and this was investigated with solid state NMR (Section 3.3.3) and was tailored for 3D printing (Chapter 5).

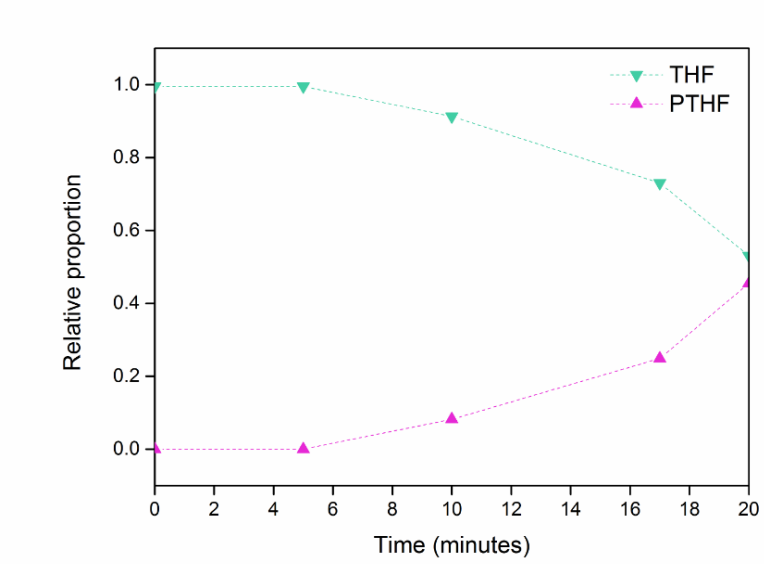

Figure 3.8: Relative proportion of THF/PTHF with time after the addition of the $BF_3 \cdot O(C_2H_5)_2$ catalyst, as calculated from ^1H NMR samples using trioxane peak as reference. After 22 minutes the solution became too gelled to analyse via liquid state NMR as it does not dissolve well.

3.3.2 Mould development

Roughness and shrinkage were assessed alongside each other for each mould, using Si2.5-PTHF hybrids in each case and additionally Si10-PTHF for the disc moulds described below. Moulds were developed based on the approximation of the shrinkage and then sample dimensions measured to calculate the shrinkage factor in each dimension. This was used in Chapter 5 for moulds with complex shapes, where the uneven evaporation or constraint at certain points meant that the shrinkage factor was not the same in each dimension.

Mould roughness

The correlation between the roughness of the mould and that of the hybrid sample produced for three PTFE discs (with three different surface roughness values) is shown in Figure 3.9. The roughness of the hybrid was always less than that of the surface it was cast on, possibly because the gel did not penetrate fully into the troughs of the surface. The Si10-PTHF had, in all cases, lower surface roughness than the Si2.5-PTHF which was consistent with the roughness of the free surface: when silica content increased, roughness decreased, which is expected as the material becomes glassier. The shrinkage factor was independent of the mould roughness for the range of roughness values tested here, although it should be noted that only the bottom surface roughness was varied, with the mould edge having a constant roughness. Varying this may alter the shrinkage if the hybrid gel sticks to the edges of the mould. The average shrinkage factor for Si10-PTHF was 0.77 compared to 0.73 for Si2.5-PTHF.

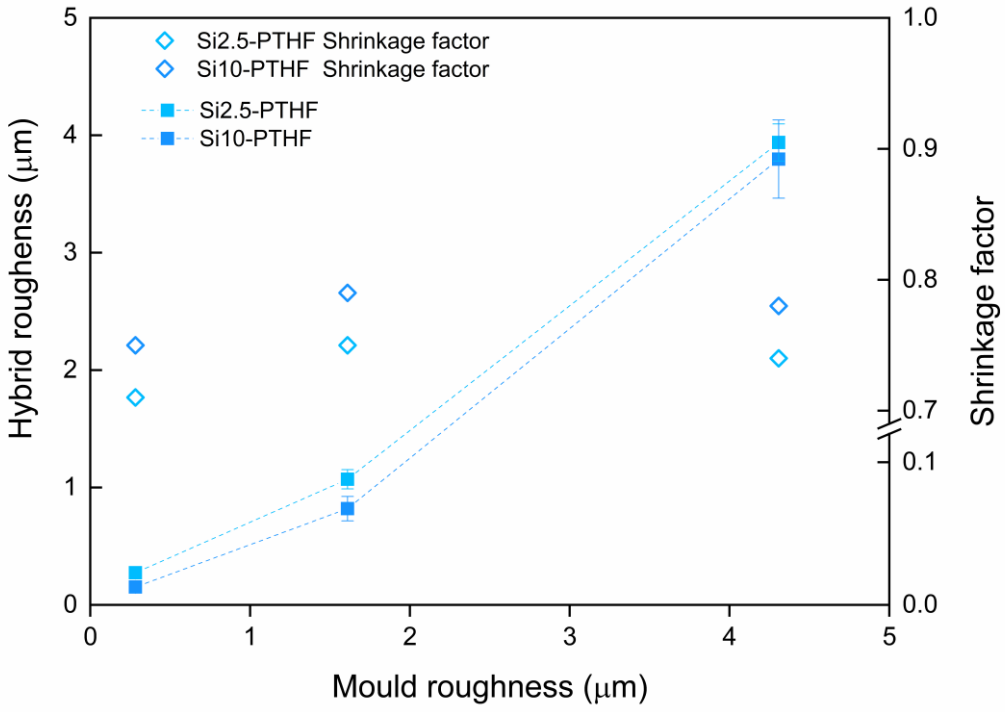

Figure 3.9: Hybrid roughness (arithmetic average, Ra) and shrinkage factor as a function of the roughness of the mould bottom surface for two hybrid compositions of Si2.5-PTHF and Si10-PTHF.

Rectangular mould

A Si2.5-PTHF hybrid was cast in a closed rectangular mould, drilled by CNC from a block of PTFE, with the mould and sample roughness tabulated (Table 3.3). As for the discs of different roughness, the shrinkage factor did not change with roughness.

Table 3.3: Average roughness and dimensions of Si2.5-PTHF hybrid sample in rectangular PTFE mould.

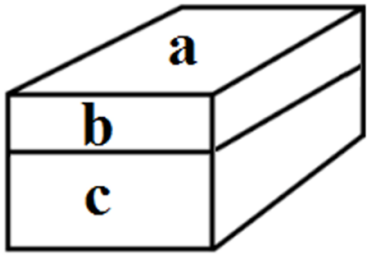

	Ra (nm), ± 20				
Surface	**Mould**	**Hybrid**	**Difference (%)**	**Dimension**	**Shrinkage factor**
a	400	250	-38	Length	0.62
b	700	480	-31	Width	0.63
c	330	320	-5	Height	0.59

PFA moulds were produced with an average roughness of 125 ± 27 nm but these were not used as it was only possible to produce flat disc moulds, rather than complex closed 3D moulds, using the method of melting PFA.

3.3.3 Characterisation of the hybrid

Inorganic/organic composition

Due to the role of THF as a 'solvent' and monomer in the reaction, the inorganic/organic ratio is not theoretically determined by the starting molar ratio of reactants. The description of THF as the solvent is more relevant to the original discovery of this reaction by Tallia *et al.* [11, 12], in which the THF was intended to be the solvent for the hybridisation of PCL with GPTMS, but in fact unexpectedly underwent the CROP described in Section 3.3.1. Since for sample series there was a linear relationship between the starting molar ratio TEOS:GPTMS and the final inorganic content, the TEOS to GPTMS molar ratio format is chosen for naming samples for clarity, except when discussing mechanical properties as a function of silica content (Section 3.3.4). The relationship between the two for the samples tested in tension and compression is set out in Table 3.4 for reference.

Table 3.4: Silica content and sample codes of hybrid samples used for mechanical testing.

TEOS/ GPTMS	Sample code	Measured wt. % SiO_2
0	Si0-PTHF	3.6
1	Si1-PTHF	5.8
1.75	Si1.75-PTHF	9.5
2.5	Si2.5-PTHF	12.7
3.75	Si3.75-PTHF	18.3
5	Si5-PTHF	19.1
7.5	Si7.5-PTHF	24.6
10	Si10-PTHF	32.0
20	Si20-PTHF	44.4

For each synthesis, the final organic content was determined as the total mass lost in the TGA cycle from room temperature to 800°C, at a heating rate of 10°C min^{-1} (Figure 3.10). For compositions with higher silica content (Si5,10,20-PTHF), the peak in burn out was sharper, as can be seen in both the mass loss curves (Figure 3.10a) and the DSC trace (Figure 3.10b). The burnout occurs over a temperature range and the peak indicates the temperature at which burn out is fastest. For a narrow distribution in polymer chain lengths, it would be expected to see a narrower peak as they burn out concurrently.

There is a non-zero inorganic content of the Si0-PTHF composition, which has no addition of hydrolysed TEOS, due to the contribution of the inorganic part of the GPTMS to the silica content.

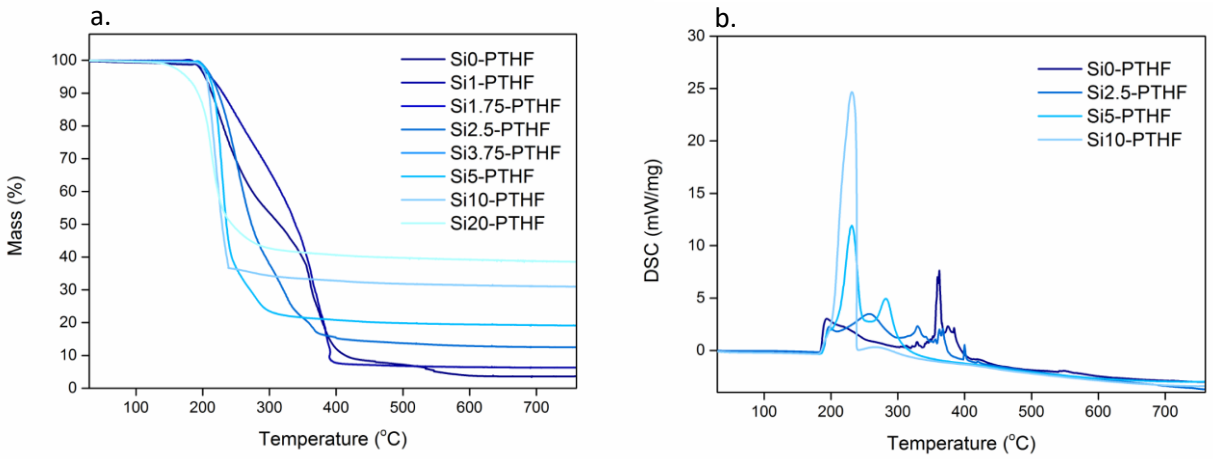

Figure 3.10: a. TGA analysis of eight Si-PTHF compositions, showing the mass % with temperature. The mass loss was sharper at lower polymer content. **b.** DSC for four different Si-PTHF compositions. At low polymer content the DSC peak was sharp as the burn out happens at one time, with high polymer contents the trace is messier as the polymer burns out more unevenly. Fewer compositions are shown for clarity.

Evidence for the ongoing nature of the polymerisation comes from the difference in the final inorganic/organic ratio with different drying conditions. For the disc and cylinder, no difference was seen because in both cases the samples are well sealed, either in layers of foil or in screw top PMP pots (Figure 3.11). Whereas, the rapid drying of the 200 µm diameter hybrid struts (printed scaffolds, Chapter 5) led to a higher final silica content, as more THF evaporates rather than the gelation continuing.

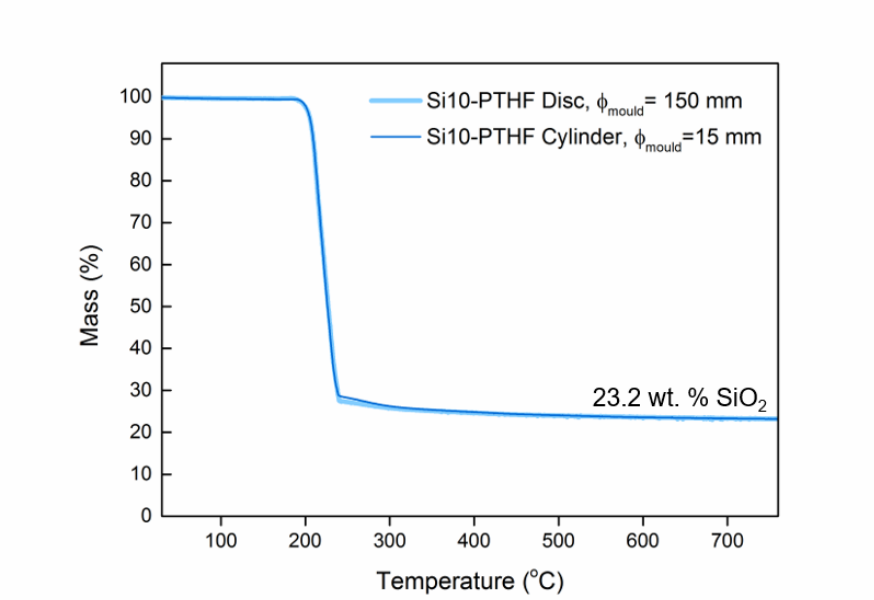

Figure 3.11: TGA of samples of the same composition with different drying conditions: disc and cylinder have the same silica content.

Hybrid structure

FTIR for hybrid discs made from eight different hybrid compositions (Si0-PTHF to Si20-PTHF) is shown in Figure 3.12. Spectra were normalised to the highest band, namely the Si-O-Si asymmetric stretch and overlapping Si-O-C, C-O-C stretches at 1100-1000 cm^{-1} [149, 150].

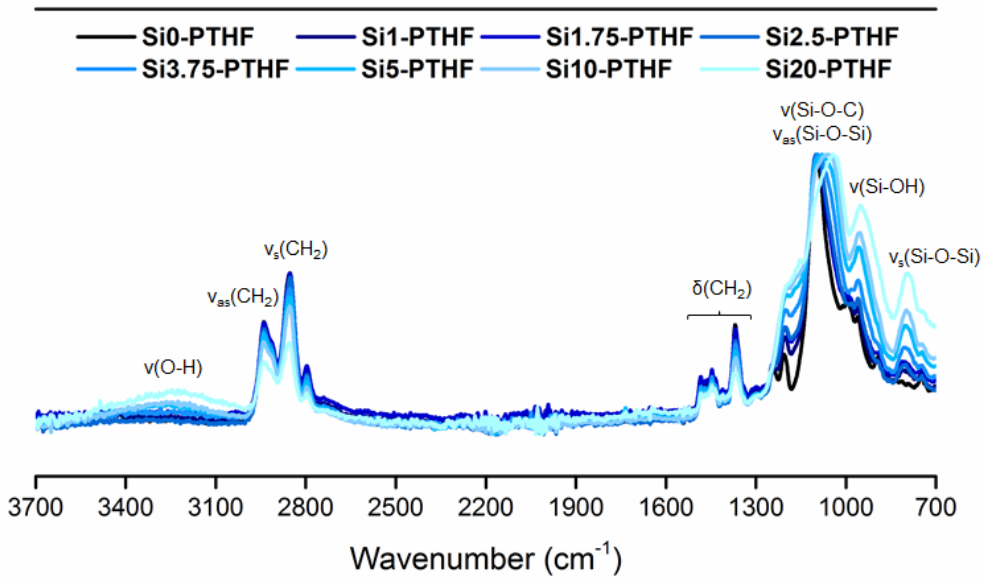

Figure 3.12: FTIR spectra of eight SiO_2-PTHF hybrid discs with varying silica content, normalised to the highest peak at around 1100 cm^{-1}. Spectra are overlaid to highlight the change with composition.

A relative increase in the absorption of the Si-O-Si symmetric vibration (around 800 cm^{-1}) and of the Si-OH stretch at around 950 cm^{-1} was seen as the TEOS:GPTMS ratio increased (Figure 3.13a, going from Si0 to Si20-PTHF). There was also a shift to lower wavenumber of the band with highest relative intensity, as the contribution of Si-O-C peaks increased relative to Si-O-Si. The increase in the absorption of the broad O-H stretch centred at 3200 cm^{-1} is attributable to silanol (Si-OH) groups [151]. Any adsorbed water would also contribute to this band but would also show H-O-H bending vibration at around 1640 cm^{-1}, and water mass loss below 100°C in the TGA, neither of which are observed.

Correspondingly, a decrease in the relative amount of the organic bands H-C-H at 2800-3000 cm^{-1} was seen over the same composition range, as the polymer content decreased (Figure 3.13b, going from Si0 to Si20-PTHF).

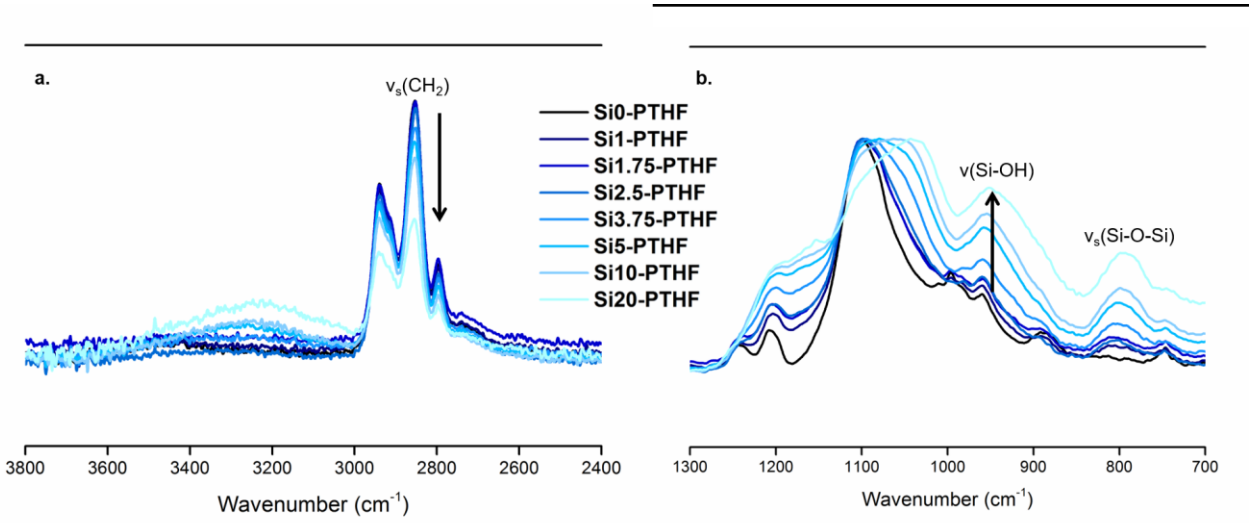

Figure 3.13: Expanded sections of FTIR of eight hybrid compositions all normalised to the Si-O-Si peaks at around 1100 cm^{-1}, to highlight the change in intensity in the direction of the arrows shown when the silica content of the hybrid is increased. In **a.** the $v(CH_2)$ bands decrease with increased wt. % SiO_2 and in **b.** there is a corresponding relative increase in the height of the v(Si-OH) and v_s(Si-O-Si). The absorptions for v(Si-O-C) and v_{as}(Si-O-Si) overlap so the trend here cannot be seen without deconvolution of the spectra.

Si0-PTHF contains only the silica from the GPTMS, with no additional TEOS and so can be compared directly with commercial PTHF (average M_n = 2000 g mol^{-1}, Sigma Aldrich UK) and GPTMS (Figure 3.14). The symmetric and asymmetric epoxide ring stretches in the GPTMS at 915-800 cm^{-1} were not present in spectrum for the Si0-PTHF hybrid. It can also be noted that there is no absorption related to the boron trifluoride in the catalyst at 1500 cm^{-1} [152]. However, it is not possible to see the v(C-O-C) formation or if the GPTMS is hydrolysed as the C-O-C, Si-O-C and Si-O-Si bands overlap.

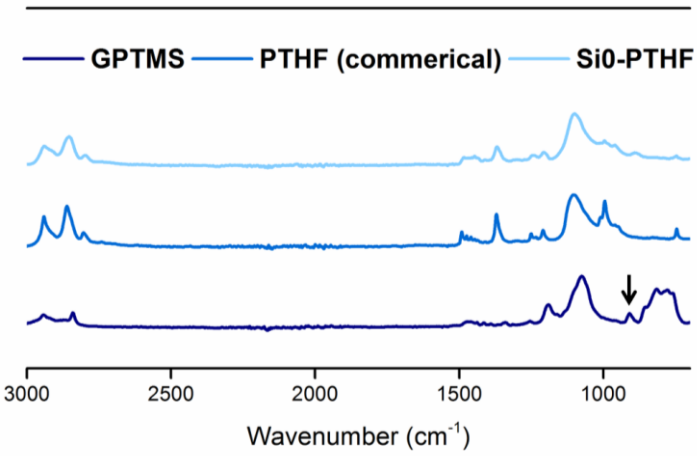

Figure 3.14: FTIR spectra of GPTMS, commercial PTHF and Si0-PTHF. Symmetric and asymmetric deformation of the epoxide ring is evidenced between 915-800 cm^{-1} (arrow) which is not visible in Si0-PTHF sample.

Solid state NMR

Two samples with different initial TEOS/GPTMS ratios (Si10-PTHF and Si15PTHF) but the same final hybrid silica content (32 wt.% SiO_2 and 31 wt.% SiO_2 respectively) were analysed by ^{29}Si solid state NMR. The aim of comparing these two compositions was to try to indirectly understand the structure of the hybrid. This was because it was noticed that seemingly identical syntheses produced samples with different properties; or conversely, that syntheses with different initial TEOS:GPTMS ratios resulted in samples with the same silica contents.

The chemical shifts of $Si(O\text{-}Si)_n(OH)_{4-n}$ (Q^n) and $C\text{-}Si(O\text{-}Si)_n(OH)_{3-n}$ (T^n) species are tabulated in Table 3.5, following [89] for both samples, and shown with peaks labelled in Figure 3.15. These peaks arise from the TEOS and GPTMS silica sources respectively. The only noticeable difference in the results between the two samples is in the relative amount of Q^2 species, possibly indicating that the TEOS is more condensed in the Si10-PTHF sample with the higher than expected silica content.

Table 3.5: Chemical shifts (δ) and percentage abundance (I) of $C\text{-}Si(O\text{-}Si)_n(OH)_{3-n}$ (T^n) and $Si(O\text{-}Si)_n(OH)_{4-n}$ (Q^n) silicon species determined from CPMAS data in conjunction with quantitative information from decoupled single pulse experiments (v_r = 5 kHz) for Si10-PTHF and Si15-PTHF.

Sample code	wt. % SiO_2	T^2		T^3		Q^2		Q^3		Q^4	
		δ [ppm]	*I* [%]	δ [ppm]	*I* [%]	δ [ppm]	*I* [%]	δ [ppm]	*I* [%]	δ [ppm]	*I* [%]
Si10-PTHF	**32**	-58.5	1.7	-66.1	6.5	-93.1	0.9	-102.4	30.1	-111.3	59.9
Si15-PTHF	**31**	-58.4	2.4	-65.6	2.5	-92.4	6	-102.2	29.5	-111.2	59.7

The degree of condensation, D_c, as calculated by Equation 2.1, was very close for the two samples: 90.6 % for Si10-PTHF and 88.9% for Si15-PTHF, which makes sense since they differ by only 1% in the measured SiO_2 content and the D_c is due to the silicate. This D_c is also consistent with other hybrid materials prepared via the sol-gel method using GPTMS as a coupling agent [95, 153]. There was a slight difference in the relative amounts of T^2 and T^3 species, with the Si10-PTHF, which had a higher than expected silica content, having more T^3 units. This could indicate that the crosslinks from the GPTMS were more condensed into the silica network for Si10-PTHF, which also led to the higher than expected silica content.

Previous work by Dr Francesca Tallia indicated that changing the silica content in the hybrid system SiO_2-PCL-PTHF did not alter the chemical shifts of Q^n and T^n species, therefore the *in situ* polymerisation does not affect the sol-gel condensation to siloxane bonds [110], which is assumed to hold true in this system without the addition of PCL.

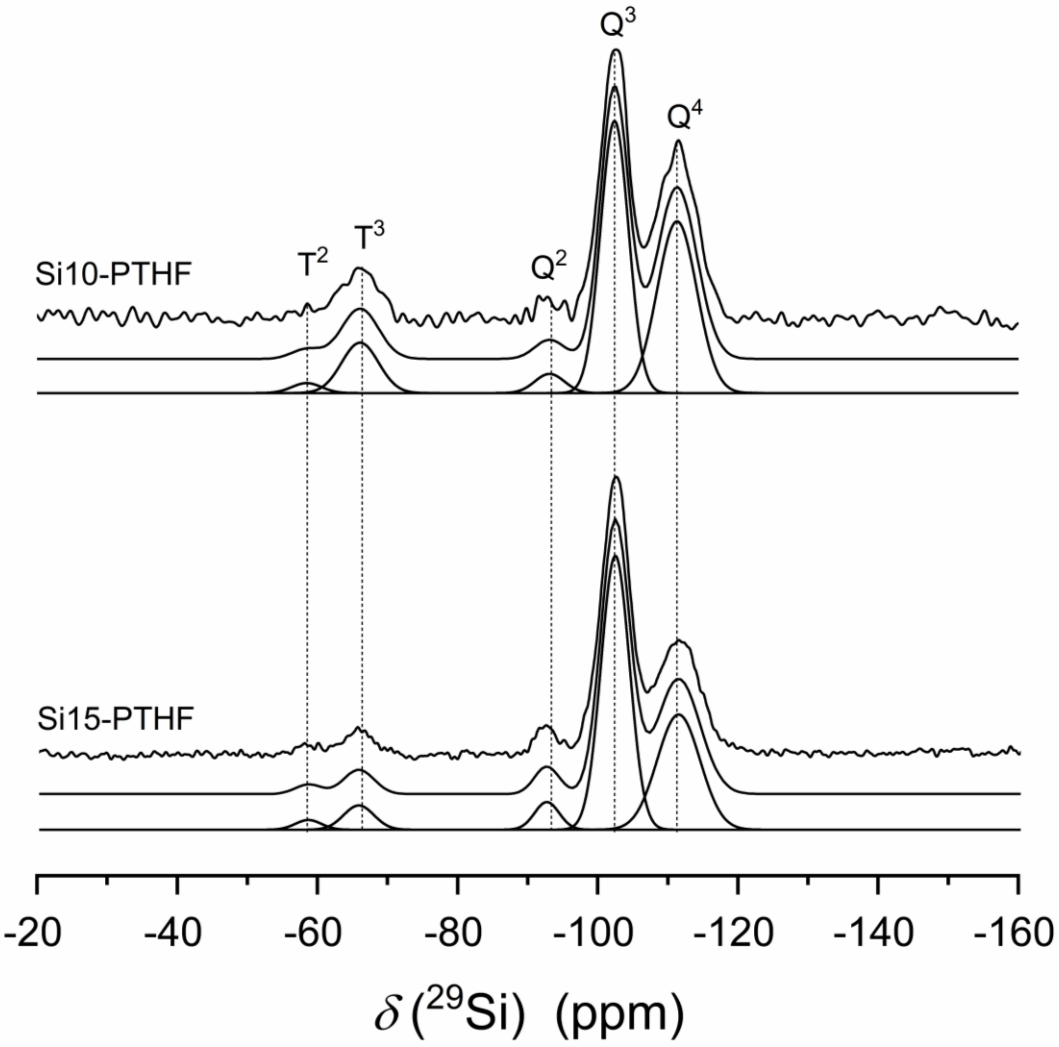

Figure 3.15: Solid state ^{29}Si MAS NMR for Si10-PTHF (32 wt.% SiO_2, above) and Si15-PTHF (31 wt.% SiO_2, below). $Q^n = Si(O\text{-}Si)_n(OH)_{4-n}$ (Q^n) and $T^n = C\text{-}Si(O\text{-}Si)_n(OH)_{3-n}$

3.3.4 Mechanical behaviour

Cylindrical hybrid samples of the compositions set out in Table 3.4 were tested in uniaxial compression without constraint and cyclically in compression. Rectangular samples of a subset of these compositions (with lower silica content) were tested in uniaxial tension and stress relaxation was measured for one composition. DMA was conducted in tension on the same samples and in compression on smaller cylindrical samples, for a subset of compositions.

Compression testing

The stress-strain curves were non-linear and j-shaped, showing an increase in the gradient of the tangent to the curve with increased strain. The hybrid samples can undergo large strains and recover when the applied force is removed. True stress and strain (σ*, ε*) are calculated to take into account the changes in cross-sectional area according to Equations 2.4 and 2.5. During the compression, the samples barrelled, therefore the cross-sectional area of the samples changed significantly. This invalidates the constant volume assumptions of these equations In order to determine the best method of stress and strain calculation, values were measured directly from photographs using ImageJ, labelled as σ and ε in Figure 3.16. A plot of true stress (σ^*) with engineering strain (ε_c) shows the best agreement with the direct measured stress and strain, so these were chosen for calculation of the mechanical properties of samples.

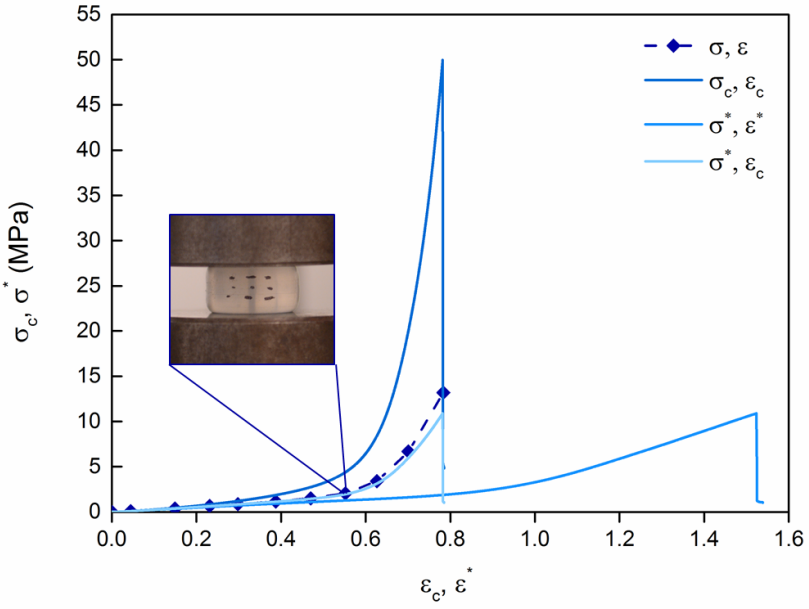

Figure 3.16: Comparing the engineering values of stress and strain (σ_c, ε_c) with the true values of stress and strain (σ^*, ε^*) and the values measured optically from a series of photos (σ, ε), suggests that the most accurate values to use are the true stress with the engineering strain (σ^*, ε_c). Sample composition: Si5-PTHF, inset shows the barrelling effect that occurred.

There was a large variation in the true stress at failure and stiffness with composition, from a highly elastomeric material, cylinders of which could be compressed between two fingers, to glassy materials that shattered at failure. It is this variation in the properties that gives the possibility of tuning the material to match desired property requirements.

Figure 3.17a shows the compressive strength increased as silica content increased, up to a limit after 32 wt.% SiO_2. The highest silica content samples had a large degree of variability, which could be due to the higher dependence on the presence of flaws in the material when it is glassier. Strain to failure reduced with increasing inorganic content, Figure 3.17b, with even samples of 44.4 wt.% SiO_2 undergoing 13 % strain before failure. Figure 3.17c shows the stiffness measured as the tangent to the curve at 10% strain (with lower portion shown again in Figure 3.17d) which varies from 2-240 MPa with increasing silica content.

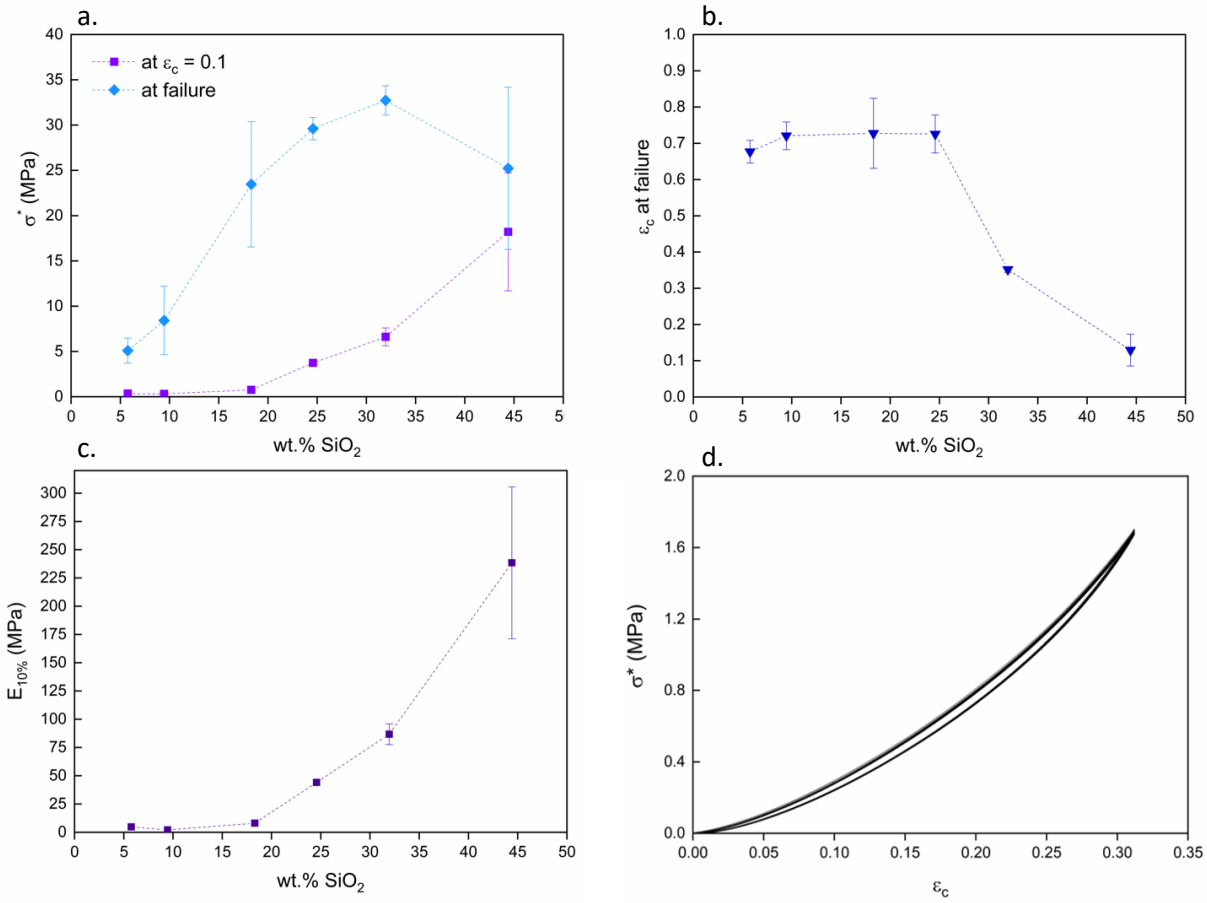

Figure 3.17: Mechanical properties in compression of hybrid cylinders as a function of silicate content **a.** The σ^* at failure and at an engineering strain, ε_c = 10%, **b.** ε_c at failure, **c.** modulus at ε_c = 10%, calculated as the tangent to the curve at this point, and **d.** example stress-strain curve during loading and unloading over 10 cycles, for 18 wt.% SiO_2.

Considering the practical use of the material, large deformations may result in displacement of the device from implantation site, therefore the stress at 10% strain (purple line on Figure 3.17a) could be used for comparison between samples that deform by more than 10% without showing a yield point, following [154]. This varies from 0.35 ± 0.01 MPa at 5.8 wt.% SiO_2 to 6.6 ± 1.0 MPa at 32.0 wt.% SiO_2. The pressure in the IVD was found to vary 0.5-2.3 MPa for varying degrees of activity, so a sample with below about 15 wt.% SiO_2 would experience significant deformation (>10%) under normal activity [28], which is not desirable.

Observing the fracture mode of the samples with high polymer content, the barrelling effect led to splitting at the outer surface parallel to the applied force. For high silica content samples which do not deform as much, the sample cracks. Fracture surfaces show characteristics of brittle fracture like mirror-hackle in Figure 3.18 [155].

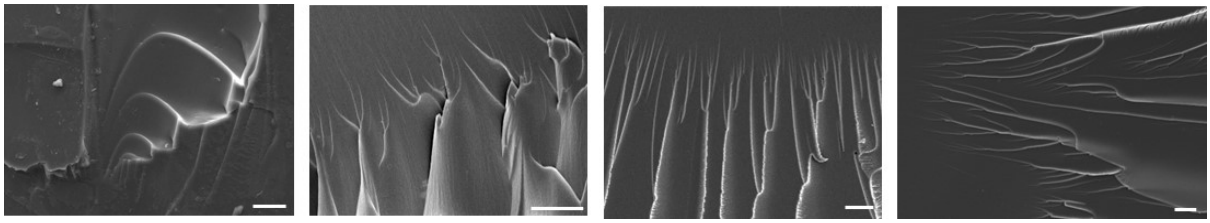

Figure 3.18: Typical fracture surfaces for Si1.75, 5, 10, 20 –PTHF (L-R). Scale bar = 50 µm.

The hybrids are not linear elastic, so it is not possible to calculate the elastic modulus, except as the tangent to the curve at a specific stress or strain, therefore DMA was used to measure the storage modulus, representing the energy stored elastically. Figure 3.19 shows the DMA in compression for three hybrid compositions, Si2.5, 5, 7.5-PTHF, and three strain ranges: ε_c = 2-5, 5-10, 10-15%. The storage modulus increased with increasing strain (consistent with the shape of the stress strain curve in Figure 3.16) and for the Si.5-PTHF composition, the increase with frequency was also evident. The loss modulus was an order of magnitude smaller in all cases and tan δ ≤ 0.12, so the hybrids can be considered to behave elastically at the chosen strains, with E' appropriate as a measure of the stiffness. Comparing E' values with $E_{10\%}$ (Figure 3.17c,d), for Si7.5-PTHF (24.6 wt.% SiO_2) $E_{10\%}$ was 44 ± 2 MPa, which was higher than E' at ε = 10-15% (34 ± 2 MPa at 10 Hz); for Si2.5-PTHF (11.0 wt.% SiO_2) $E_{10\%}$ was 2.2 ± 0.3 MPa, which is similar to E' at ε = 10-15%. This is higher than some measures of the stiffness of the IVD annulus (0.56 MPa) [29] and of the range of stiffness used for multi-stiffness elastomer IVD designs (0.05-7 MPa) [13], suggesting that the material is too stiff even at low silica contents. However, this is measured at 10% strain, and the material shows a non-linear stress-strain curve with lower initial gradient, reflective of the stress-strain behaviour of the natural disc [31].

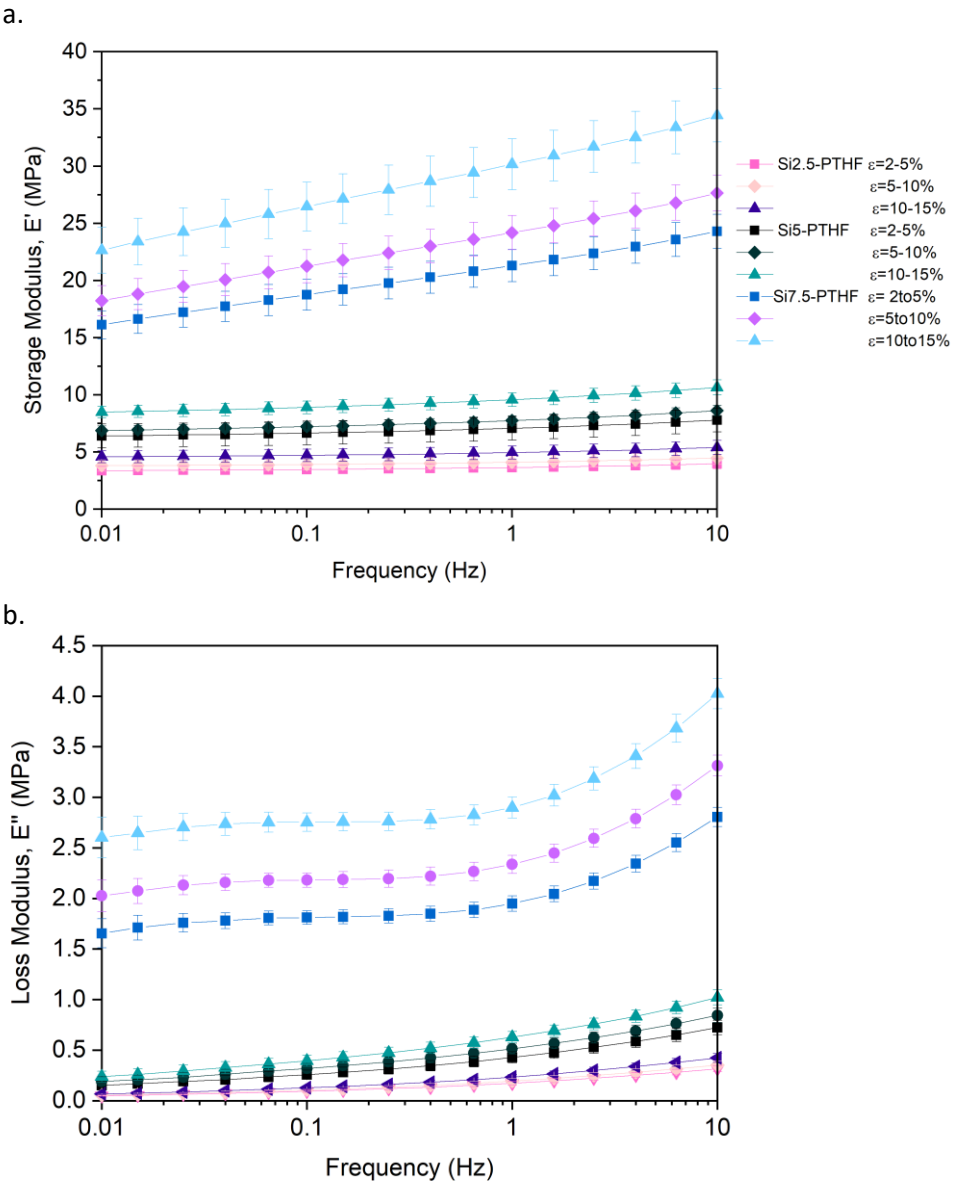

Figure 3.19: DMA in compression for three hybrid compositions: Si2.5, Si5, Si7.5-PTHF, **a.** Storage modulus and **b.** Loss modulus. The storage and loss moduli increase with increasing silica content and increased strain range, and for the stiffer sample Si7.5-PTHF there is also an increase in the storage modulus with frequency.

Cyclic compression

Cyclic testing was carried out as it was not possible to conduct a fatigue test (at a range of loads up to a maximum of 10 million cycles). To compensate for the low cycle number the displacement was chosen to give the maximum strain at 20% of the original height, and in this case 90 mm min^{-1} represented a strain rate approximately 20% s^{-1}, an estimated physiological strain rate calculated following the method in [56]. A range of strain rates were tested from 1-150 mm min^{-1} on hybrid composition Si5-PTHF, and the material did not show a different response at increased strain rates (Figure 3.20). The strain rate dependence is also investigated in Chapter 5 in comparison with human IVDs. Therefore, subsequent tests to a maximum of 10^4 cycles were conducted at 90 mm min^{-1}, and no change was observed in the mechanical response or damage to the samples over this cycle number. However for implant testing, coupled movement must also be considered rather than uniaxial compression [42].

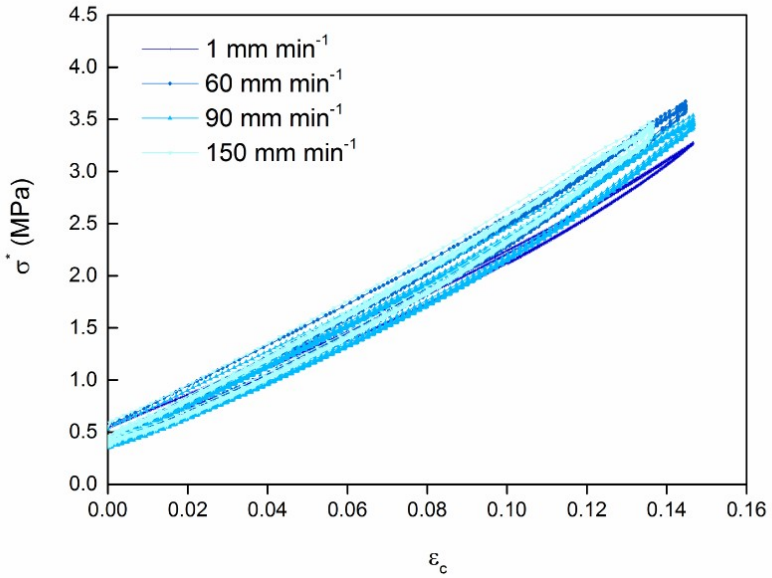

Figure 3.20: Cyclic compression on Si5-PTHF (22.3 wt.% SiO_2) at four different strain rates: 1, 60, 90, 150 mm min^{-1}. The first 40 cycles of 10^4 are shown.

Tensile testing

In tension, the true stress and strain (σ^*, ε^*) were used because in tension the true strain is less than the engineering strain, taking account of the reduction in cross sectional area as the material strains. The true stress, σ^*, at failure in tension, as calculated by Equation 2.5, increased with increasing silica content in the hybrid, from 1.1 ± 0.1 MPa at 6.3 wt. % SiO_2 to 13 ± 2 MPa at 19.1 wt. % SiO_2, Figure 3.21a.

Higher silica content compositions than this were more prone to cracking when cut and slipped in the grips due to the smoother surface finish. Over the same range of compositions, the true strain at failure did not show the trend that might be predicted (a decrease in strain to failure with increasing silica content), perhaps because of the limit in the tensile strength at very low silica contents. Similarly, the modulus $E_{10\%}$ defined as the tangent to the curve at $\varepsilon^* = 10\%$ shows the hybrid becoming less stiff at 10% strain between 6.3 and 9.5 wt.% SiO_2, then gradually stiffer to $E_{10\%}$ = 9 ± 2 MPa at 19.1 wt.%

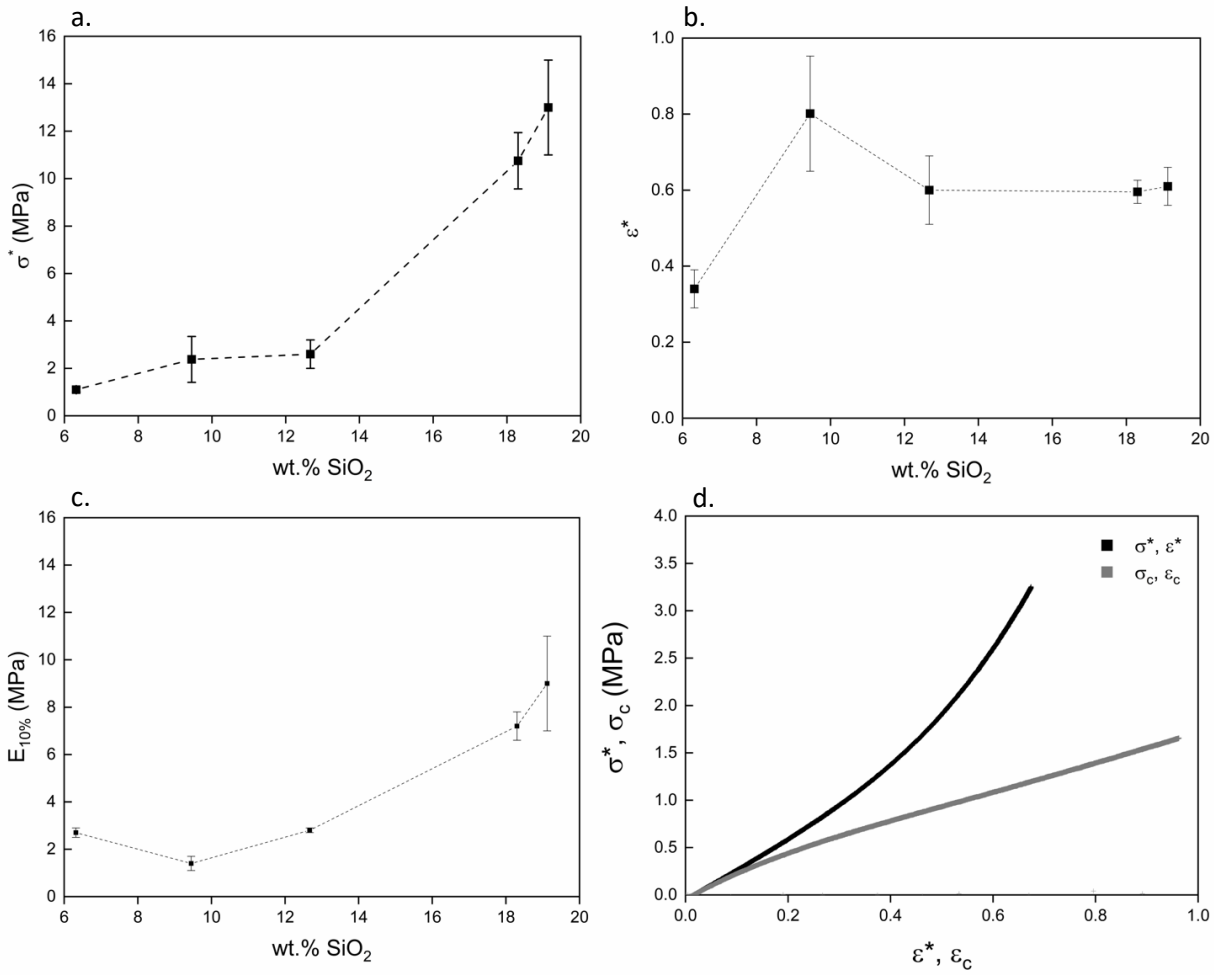

Figure 3.21: a. True stress at failure in tension, showing an increase with increasing silica content. **b.** True strain at failure in tension with silica content. **c.** Stiffness in tension as defined as the tangent to the curve at true strain = 10%. **d.** Example of 13 wt.% SiO_2 sample stress-strain curve with true stress and strain in comparison with engineering stress and strain, which does not account for the change in cross-sectional area.

SiO_2 (Figure 3.21c). Engineering stress and strain calculations match the true stress and strain at lower strains (up to 10%) and then give an underestimate of the stress and overestimate of the strain. True stress and strain values were chosen for calculation of the values at failure.

E' and E'' were measured by DMA in tension for three lower compositions, set out in Figure 3.22. As in compression, the loss modulus was small (tan $\delta \leq 0.08$), so the hybrid behaved elastically in this strain range. The values of storage modulus match the tangent to the curve at 10% strain: $E_{10\%}$ = 8.0 ± 0.4 MPa was consistent with E' = 8.1 ± 0.3 MPa (at ε = 5-10%, 1Hz) for 18.3 wt.% SiO_2; $E_{10\%}$ = 2.7 ± 0.2 MPa was consistent with E' = 2.6 ± 0.1 MPa (at ε = 5-10%, 10Hz) for 6.3 wt.% SiO_2.

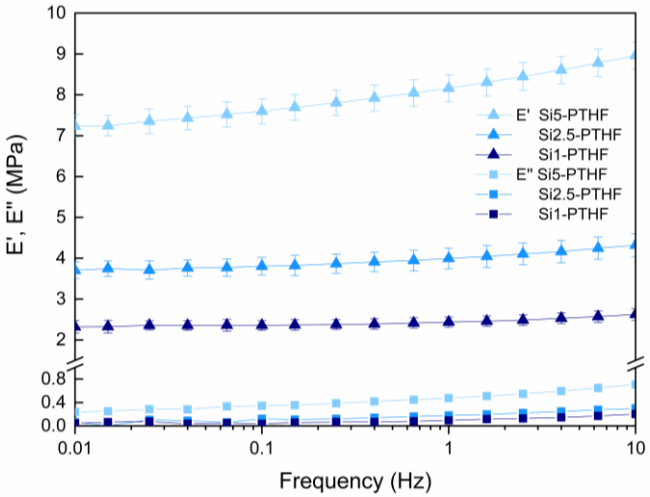

Sample code	wt.% SiO_2	$E_{10\%}$ (MPa)
Si5-PTHF	18.5	9 ± 2
Si2.5-PTHF	12.4	2.8 ± 0.1
Si1-PTHF	6.3	2.7 ± 0.2

Figure 3.22: Storage and loss moduli of three hybrid compositions: Si1, Si2.5, Si5-PTHF at ε =5-10% in tension. Table gives the relevant silica content for each sample tested here and $E_{10\%}$ measured from the stress-strain curve, which is consistent with the measured storage modulus for Si1-PTHF and Si5-PTHF.

Stress relaxation in tension

Stress relaxation measures the mechanical stability of the material. It was measured for one low silica content composition (6 wt. % SiO_2) and shows a fast initial relaxation (8.5 ± 0.9 % in the first minute), followed by a slower relaxation over the following hour, Figure 3.23. The total stress loss in this time was 14.6 ± 2.1 %, behaving like hybrids of higher silica content in the SiO_2-PCL-PTHF system (24.7 wt.% SiO_2 lost 15.3 ± 1.7 % stress after 1 hour) [12]. The samples are viscoelastic rather than viscoplastic as evidenced by the recovery of the strain in compressive loading and unloading curves (Figure 3.17d).

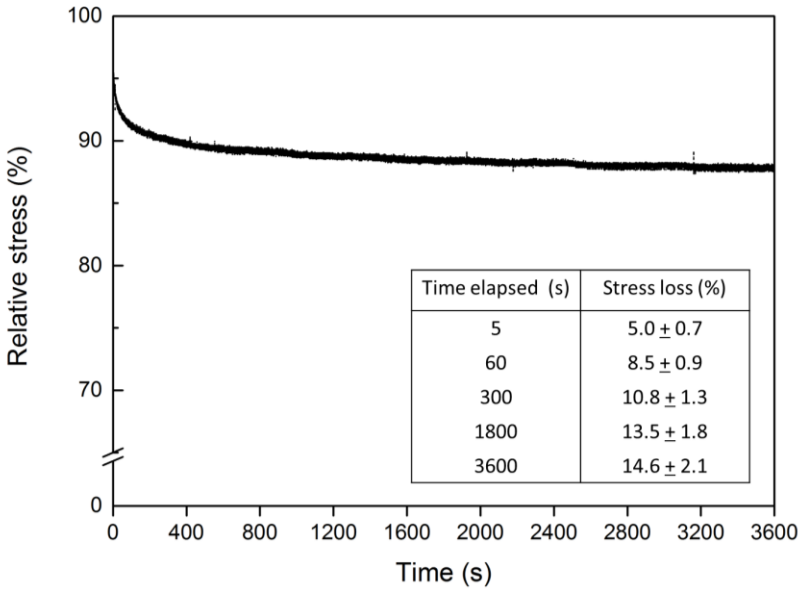

Figure 3.23: Stress relaxation in tension over one hour for Si2.5-PTHF. The initial strain is 50% of ε_c at failure. Inset shows the average and standard deviation percentage stress loss after 5 seconds, 5 minutes, 30 minutes and 1 hour from five repeats.

3.3.5 Behaviour in wet environment

Si5-PTHF samples with 22.3 wt.% SiO_2 were stored in PBS at 120 rpm and 37°C for 1.5 years to assess the change in the properties. No difference in the final inorganic content as measured by TGA is observed or any change in the DSC peak which indicates no degradation of the polymer (or potentially, concurrent degradation of polymer and silica), Figure 3.24a. The FTIR shows an increase in the O-H absorption centred around 3300 cm^{-1} due to water absorbed into the structure, however no difference in the relative heights of organic or inorganic bands were observed.

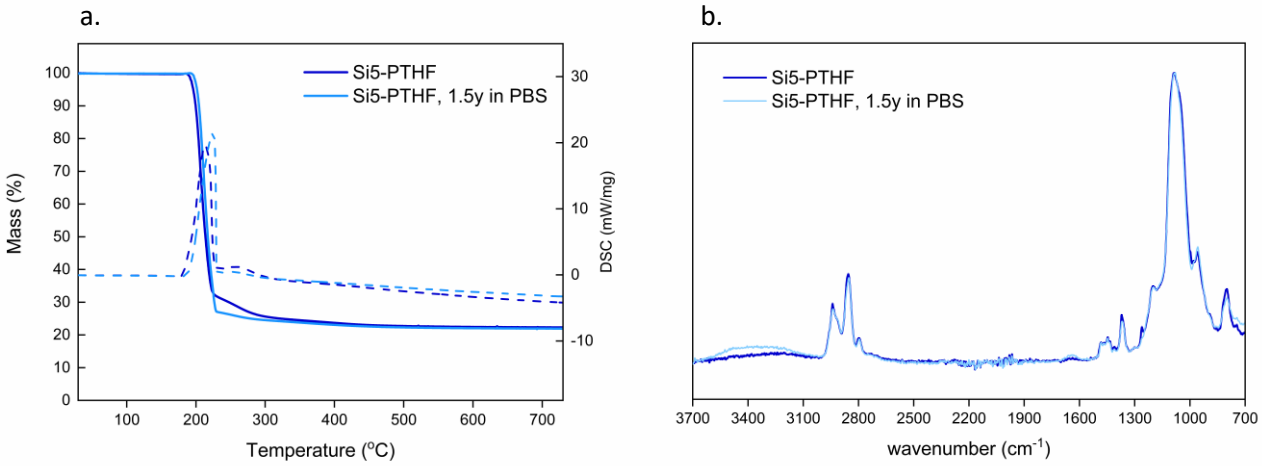

Figure 3.24: TGA and DSC analysis before and after soaking for 1.5 years. Samples are Si5-PTHF from the same synthesis. There is a slight change in the shape of the mass loss curve which could be due to the size distribution of the pieces analysed. It also cannot be ruled out that deposits from PBS could counter act any weight loss from the sample.

Samples were tested after soaking and removal from solution. Samples soaked for 1 month in PBS underwent 10000 cycles at physiological strain rate without damage or deterioration of mechanical behaviour. A change in the mechanical properties on soaking was observed immediately (2 hours in PBS), which increased over a period of between 2 weeks and 1 month, however after this the properties stabilised and after a further 1.5 years the cyclic compression curves overlap with those at 1 month soaking (Figure 3.25a). This change was observed using cyclic testing to 100 cycles as it allowed the same sample to be tested repeatedly at various time points. Figure 3.25b compares the stress at failure in dry conditions and after 1 month soaking, showing a decrease in the strength. This difference is small at lower silica contents but at 32.0 wt.% SiO_2 the failure stress is reduced from 32 to 5 MPa, probably because the larger amount of hydrophilic silica means a higher uptake of water and therefore greater internal stresses. However, samples should be tested under compression whilst still in solution to assess if this is a result of the drying that occurs on removal from solution.

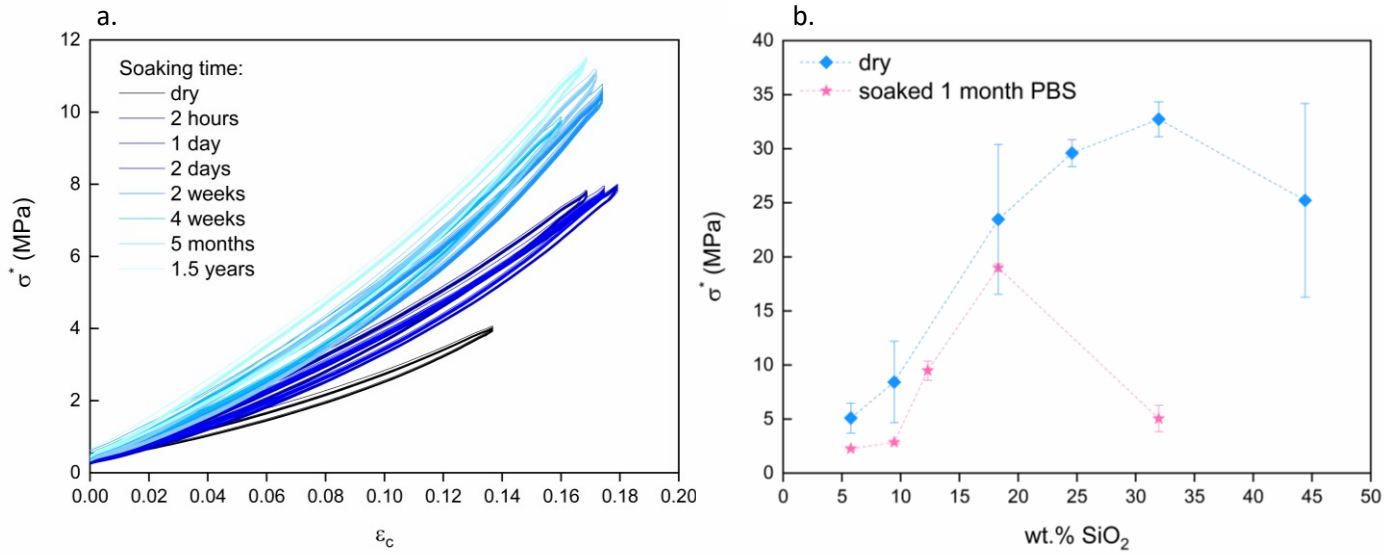

Figure 3.25: a. Cyclic compression for Si5-PTHF at different time points soaking for between 2 hours and 1.5 years in PBS at 37°C and 120 rpm to simulate the body environment (10 cycles shown of 100 tested). **b.** Failure stress in compression for dry samples compared to samples soaked for one month in PBS at 37°C and 120 rpm.

Soaking of samples shifted the stiffness to that of a higher wt.% SiO_2 dry sample, as seen in Figure 3.25a and confirmed with DMA in compression (Figure 3.26). Comparing Figure 3.26a DMA of Si2.5-PTHF dry and soaked, with Figure 3.26b of Si7.5-PTHF, highlights that the increase in stiffness is greater for samples with more silica content: the error bars overlap for Si2.5-PTHF dry and soaked samples, whereas the storage modulus of Si7.5-PTHF increase by 4-5 times on soaking.

This was consistent with what was found for the SiO_2-PCL-PTHF system [110] and Class II PTHF hybrids (Ta_2O_5-CaO-PTHF) which showed an increase in stiffness and strength on soaking (2 weeks in Simulated Body Fluid, SBF) [109]. The mechanism for this is not confirmed, but it may be that the attraction of water to the hydrophilic SiO_2 means that the hydrophobic polymer chains are aligned or more restricted in their movement than under dry conditions. The same stiffening effect was observed on soaking in DI water, so is not an effect of the ions present in PBS. However, no crystallisation was seen via XRD. There is no change in dimensions of the samples on soaking (they do not swell), although some change to the optical properties is seen, as they become less translucent and the absorbance of the OH bands in FTIR increased. No polymer was seen in solution after 1 month soaking in D_2O in ^1H NMR.

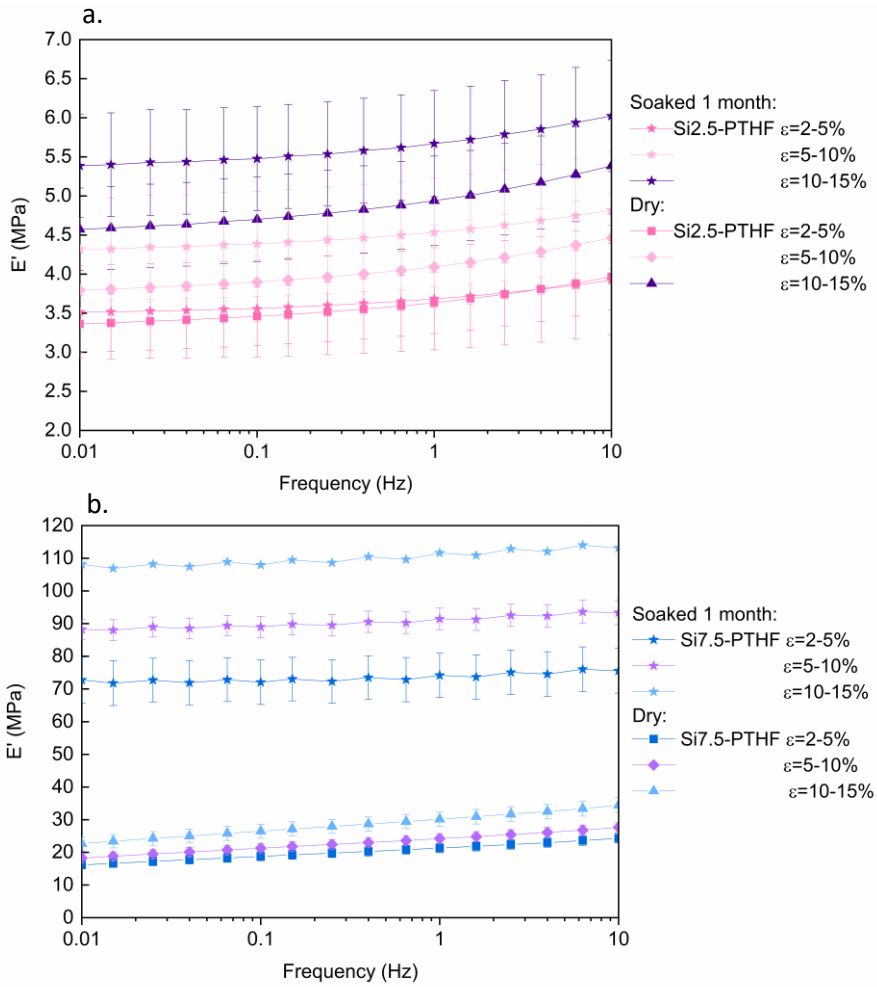

Figure 3.26: DMA in compression at strain ranges of 2-5, 5-10 and 10-15 % for dry samples and samples soaked for one month of composition **a.** Si2.5-PTHF and **b.** Si7.5-PTHF. At the lower silica content, the error bars overlap for each strain range, whereas for the higher silica content hybrid there is a significant increase in the storage modulus, highlighting the effect of the silica on the stiffening.

Behaviour relative to cartilage

SiO_2-PTHF hybrids show stiffening on soaking, with higher silica content samples becoming particularly brittle due to the hydrophilic nature of the silica. Because of this, attention for cartilage replacement application should focus on lower silica content hybrids, below 20 wt.% SiO_2.

Over the whole composition range, the hybrids showed compressive strengths to failure greater than those experienced by native IVD when dry [28]: the failure stress in compression was 5 ± 1 MPa at 5.8 wt.% SiO_2, the lowest silica content tested; and the ability to deform significantly in compression before failure (72 % at 18.3 wt.% SiO_2 was four times the compressive strain in the IVD [62]).

However, above around 20 wt.% SiO_2 the stiffness of the hybrids at 10% strain became much larger than the natural tissue, and a significant reduction in strength on soaking, therefore subsequent work on device development concentrates on Si2.5-PTHF and below.

Table 3.6 compares the properties of 9.5 wt.% SiO_2 (Si1.75-PTHF) to those of the IVD, highlighting the possible problem of too high stiffness whilst meeting the minimum compressive strength requirement.

Table 3.6: Mechanical property data for IVD cartilage tissue, compared with 9.5 wt.% SiO_2 hybrid composition.

		Compressive Strength (MPa)	Compressive Modulus (MPa)	Failure strain in compression
	IVD	0.5 – 2.3 [28]	0.5 [29]	0.09 – 0.126 [62]
9.5 wt. % SiO_2	**dry**	8 ± 4	2.1 ± 0.3	0.72 ± 0.04
	soaked 1 month	2.8 ± 0.1		0.51 ± 0.01

The cyclic testing conducted here is not to sufficient cycle numbers or range of stresses to assess the fatigue life of the samples, considering the intended lifespan of an implant material.

In general there is a difficultly in matching properties to natural tissues, because of the variation in samples and testing conditions. This is addressed in Section 5.3.5 by testing hybrid samples moulded to the same dimensions as natural IVDs and tested under the same conditions.

3.3.6 Sterilisation

To progress with the application of this hybrid system as a cartilage replacement material, it was necessary to consider the behaviour of cells on the surface of the hybrid and its potential for toxicity. Before doing this, a sterilisation technique was required as the hybrids are synthesised in a non-clean environment and thus will contain pathogens that could lead to a false positive result for cytotoxicity. Often, for cell culture studies, soaking in 70% ethanol or exposure to UV light is used for sterilisation, however these processes are not sufficiently robust for future clinical use. Autoclaving and chemical sterilisation methods like ethylene oxide, which has been used to sterilise PTHF [111], were rejected due to the lack of porosity in the hybrid samples and their potential for damage to the material. Gamma irradiation was considered as an alternative which has already been used to successfully sterilize hybrids, including PDMS-SiO_2 [156] and hydrogels [157] at a standard dose of 25 kGy, and has been shown to cause less damage to the polymer structure than ethylene oxide [158]. Gamma irradiation at 25, 50 and 100 kGy was evaluated to assess effectiveness and for any deterioration in the properties of the hybrids.

The first attempt at sterilisation was at 25 kGy and the aim was to assess any damage to the samples of Si5-PTHF (18.5 wt.% SiO_2). There was no visible damage to samples and no differences in surfaces observed in SEM. The DMA results over the frequency range 0.01-10 Hz show that the error bars overlap for the storage and loss modulus (Figure 3.27). However, subsequent storage in cell media, showed that the samples were not sterile as bacterial growth in cell media was observed after 1 day.

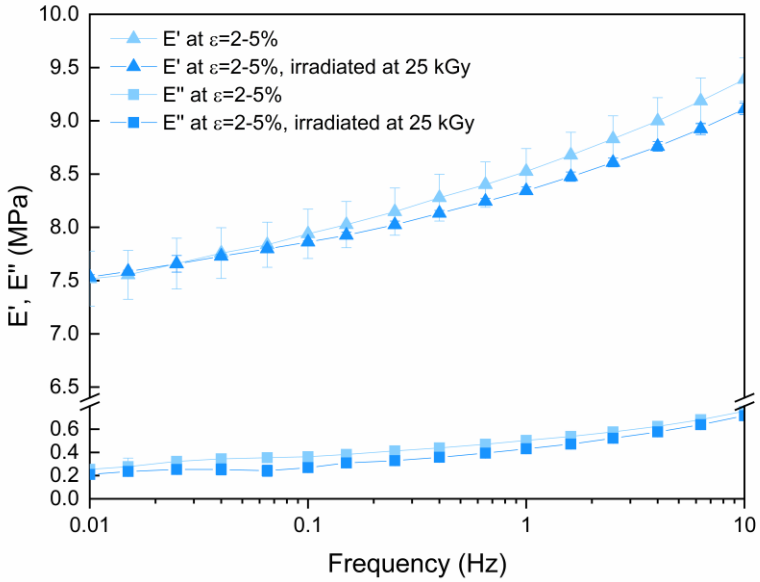

Figure 3.27: Storage and loss modulus in tension for the same sample (18.5 wt.% SiO_2) without irradiation and irradiated at 25 kGy, over a strain range of 2 to 5 %.

Thus the next step was to compare the effect of 25, 50, 100 kGy irradiation as shown in Figure 3.28. Samples were soaked in DI water for 1 month prior to sterilisation and the irradiation was carried out on samples still under DI water. This was because the cyclic testing suggested that one month was the time required for water to fully penetrate the structure (Section 3.3.5), therefore if there was any remaining catalyst (for example) this would be diluted and removed after this time, and no further release would occur.

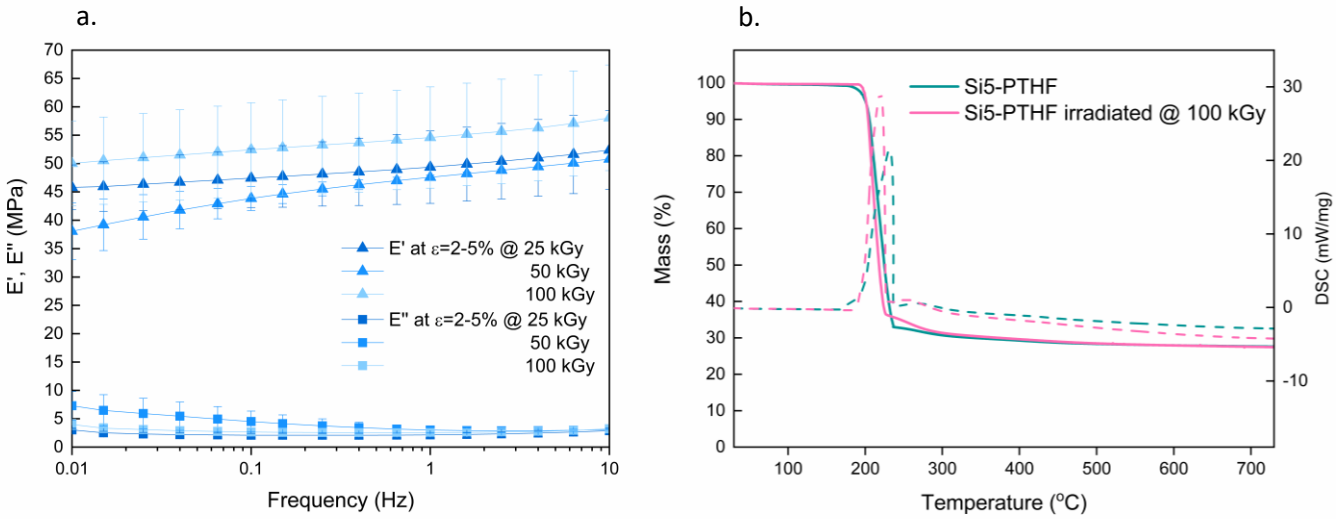

Figure 3.28: a. Storage and loss modulus in tension over 2 to 5 % strain, for samples of 27.6 wt.% SiO_2 irradiated at 25, 50 and 100 kGy. **b.** TGA and DSC traces of the same material before and after gamma irradiation at 100 kGy.

Note that this experiment is not directly comparable with the previous result as the hybrid compositions were different (here 27.6 wt.% SiO_2). No progressive damage to the samples was observed on increasing the irradiation from 25 to 100 kGy: error bars overlap for storage and loss moduli. SEM imaging showed no evidence of damaged sustained to surfaces during gamma irradiation. Only samples sterilized at 100 kGy in DI water showed no contamination (no bacterial growth) in culture over the period of 21 days that they were observed so this gamma irradiation dose was chosen for sterilisation for *in vitro* tests.

Gamma irradiation was confirmed as a potential solution to device sterilisation which does not have a detrimental effect on materials properties, for use in cell studies and any future animal studies.

3.3.7 Cell studies

Cell culture on hybrid discs

ATDC5 mouse chondrocyte cells were seeded onto the hybrid surface and onto tissue culture plates (TCP) as described in Section 3.2.6. The cell line was chosen as one commonly used to assess tissue engineering scaffolds [159-161]. The cells attached to the hybrid surface and no differences were observed in cell viability on day 1 when compared to the cells seeded on the TCP alone (Figure 3.29a, day 1). Over the 14 days of the experiment the cells remained metabolically active and viable, but they did not proliferate. They attached to the surface and spread. Therefore, the viability remained constant over time, Figure 3.29a.

Figure 3.29b shows the cells on the hybrid surface at day 10, with cytoskeleton staining (actin) and microtubular staining (tubulin). The latter is important in mechanotransduction and taken together the stainings provide an indication of the cell morphology. In both cases the cells are spread, however at the high cell density there are also aggregates of cells visible, indicating that there was no advantage in increasing the cell density from 1 x 10^4 cells cm^{-2} to 5 x 10^4 cells cm^{-2}.

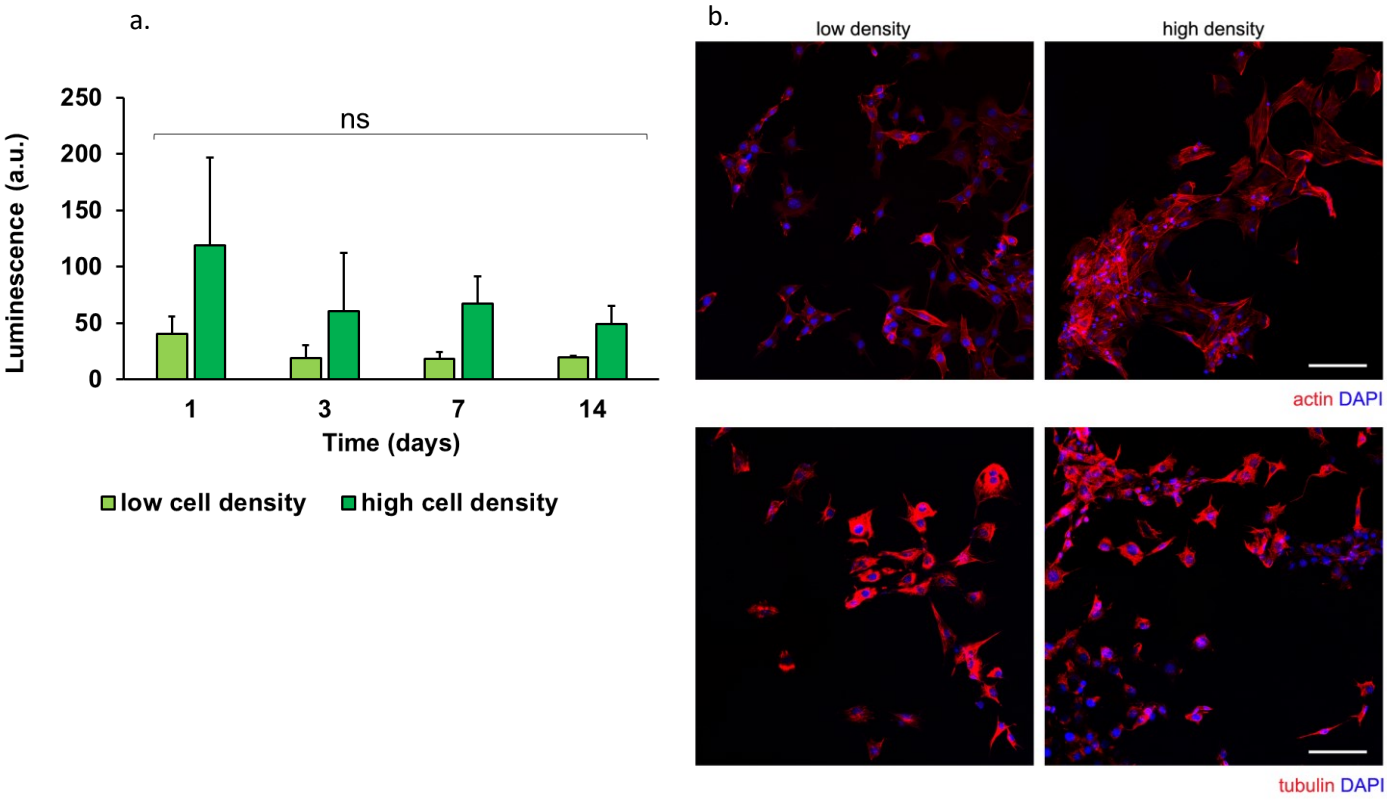

Figure 3.29: a. Cell viability over time, for high and low cell density conditions. **b.** Cytoskeleton staining (actin and tubulin) of mouse ATDC5 chondrocytes on the surface of hybrid samples at day 10. Cells attach, spread and remain viable over time although they do not proliferate. Scale bar is 100 µm.

The spreading of the cells on the surface and their constant viability over the 14-day period of the experiment indicates that the hybrid surface is not toxic. Cells attached quickly to the cell surface: when the cell media was added, four hours after the cell suspension was placed as a droplet on the hybrid surface, the cells remained attached to the hybrid surface and did not float off into the cell media or migrate onto the tissue culture plastic. There were no cells growing on the tissue culture plastic away from the hybrid samples. The reason for this may be the hydrophobic nature of the hybrid surface which leads to protein adsorption to the surface in a physiological environment. Cells require adhesive motifs to attach and recognise the surface and this allows their fixation to the hybrid surface. Negative controls (omission of the primary antibody with the presence of secondary antibodies) were performed and no staining was observed in these samples.

The next step was to test for cytotoxicity of extractables from the material, following ISO 10993-5. Figure 3.30 shows the cell viability in comparison with the positive control for cytotoxicity (polyurethane containing 0.1% zinc diethyldithiocarbamate) and negative control (polyethylene). Percentage cell viability was calculated according to Equation 3.1 and at all dilutions (25, 50, 75, 100%) the extract solution passes the test for non-cytotoxicity as set out in the ISO standard (greater than 70% viability). Therefore, the SiO_2-PTHF hybrids have the potential to be used as implant materials, subject to further *in vitro* and then *in vivo* testing.

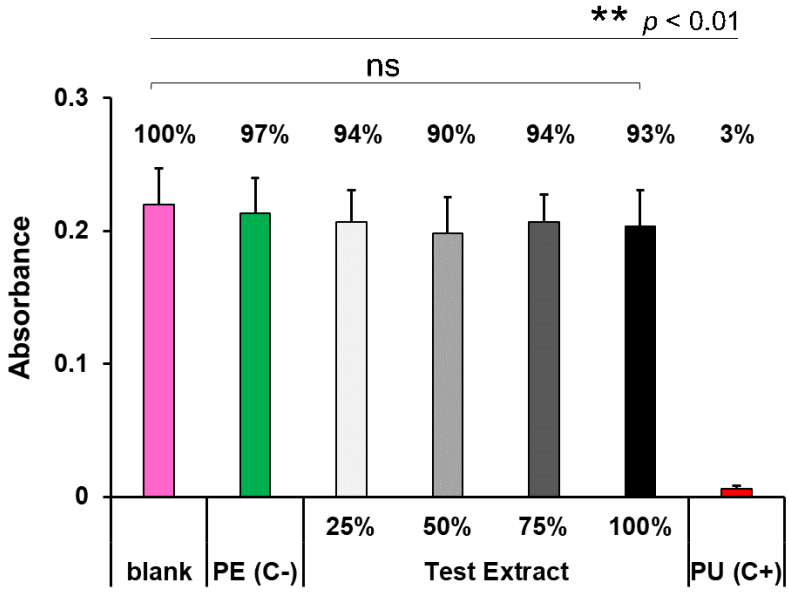

Figure 3.30: MMT results after 24 h with mouse chondrogenic cell line ATDC5 1 x 10^4 cells per well, n=6. There is a significant difference between the positive control and all other conditions, and none between the blank, positive and test extracts of all dilutions ($p<0.01$) which are all above the 70% viability threshold for non-cytotoxicity.

3.4 Conclusions

A novel hybrid system of SiO_2-PTHF, using GPTMS as a covalent coupling agent, was synthesised at inorganic contents ranging from 4 to 45 wt.% SiO_2 by a cationic ring opening polymerisation mechanism. The hybrids were transparent and free from cracks and bubbles as bulk samples. A combination of FTIR, TGA and NMR confirmed covalent bonding between the inorganic and organic networks. TEM showed a uniform structure at the nanoscale.

Over this composition range, the hybrid material showed a wide range of strength and stiffness, deforming significantly at lower silica contents and conversely behaving in a more brittle manner at higher silica contents. The strength in compression was greater than in tension at each composition.

Samples underwent 10^4 cycles at a physiological strain rate with no visible damage or change to the loading-unloading curve, in dry and wet conditions. Soaking in PBS to simulate the environment of the body causes a change in the mechanical properties, increasing the stiffness, leading to embrittlement at high silica contents. This change occurs in the first month of soaking and further change is not seen after 1.5 years in cylinders of 22 wt. % SiO_2.

Following gamma irradiation at 100 kGy, hybrid surfaces supported mouse chondrocyte cell attachment, with cells attaching within 4 hours and remaining viable and spread after 14 days. Extractables from the hybrids were not cytotoxic according to ISO 10993-5. This supports the possibility of using this hybrid system as a cartilage replacement material.

The progressive gelation of the hybrid, along with the tuneability of the mechanical properties by change in the composition, led to the exploration of the use of this hybrid system to form structures with a gradation in mechanical properties, which are present in natural cartilage. This will be the subject of the following chapter.

Chapter 4

Multiphase hybrid materials

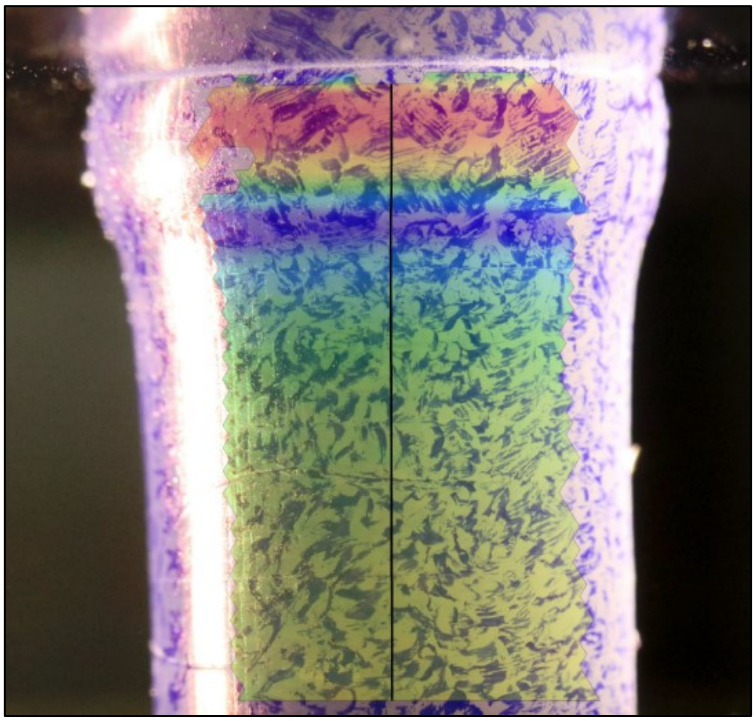

4.1 Introduction

The aim of this chapter was the formation of novel multiple phase hybrid samples. The formation of inorganic-organic hybrids in the way described in Chapter 3 has two properties that are combined here. First, SiO_2-PTHF hybrids have tuneable mechanical properties, based on altering the ratio of the inorganic to organic component, and controlled by the ratio of the starting reagents in the synthesis. Secondly, the hybrids form by a gradual gelation, during which polymerisation continues. This ageing process is 3 days, in a mould with minimal THF solvent evaporation, after which the mould is opened gradually to allow evaporation.

The hypothesis was that two gels, of different composition and stiffness, could be joined prior to completion of gelation to produce a single material with a stiffness gradient and no interface between the original gels. Considering time zero to be the point at which the hybrid sol is introduced to a mould, the aim was to add a second new hybrid (of the same or different silica content) at any point between 0-3 days. Joining of the two hybrids at an optimal time point should mean that no visible interface remains between them, and complete mixing should not occur because of the high viscosity of the solution. Thus it is possible to form a single sample with a gradation in properties through it, by creation of a gradient in the silica content. This constitutes an innovative method for formation of a stiffness gradient in an organic-inorganic hybrid material. Samples formed in this way are referred to as multi- or two-phase samples in this thesis, where phases denote regions originating from different hybrid sols.

The objectives were to test this hypothesis by joining gels at different points of gelation and characterise the new material by measuring the gradient of silica content and the strength of the interface in tension and compression. Digital Image Correlation was used to image the strain distribution around the interface in two-phase samples formed at different ageing times. To isolate the effect of the interface, two-phase samples were made from hybrids of identical composition at different ageing times.

Gradients of stiffness are present in natural structures in the body, including intervertebral discs, in which a variation in stiffness arises from the density and orientation of concentric rings of collagen fibres in the annulus, in addition to fluid flow through the cartilage, as described in Section 1.2.1. This structure allows the disc to be stiffer under increased flexural load and thus support the full motion of the spine. The work of this chapter is an attempt to imitate this with a sol-gel hybrid.

4.2 Methods

4.2.1 Synthesis

SiO_2-PTHF hybrids were synthesised by the method described in Section 3.2.1. In one pot, TEOS was hydrolysed in DI water catalysed by 1 M hydrochloric acid. Separately, the cationic ring opening polymerisation of THF monomer was activated by GPTMS and catalysed by $BF_3{\cdot}O(C_2H_5)_2$, leading to a gradual gelation during which the hydrolysed TEOS was added dropwise. The gelation of the hybrid sol continued, increasing in viscosity with time. The solution was stirred for minimum 10 minutes at 400 rpm after the addition of the hydrolysed TEOS to ensure mixing. After this hybrid sol was added to a mould, sealed (by putting the mould in screw top PMP pots or covering with layers of aluminium foil) and placed at 40°C for 3 days ageing. During the 3-day ageing period, the polymerisation continued and there was minimal evaporation of THF, so that at the 3-day ageing point, the hybrid held the form of the mould without shrinkage. Then, the seal was opened gradually over the period of one week and samples were left to dry in open moulds for a further week (still at 40°C) before testing.

The gradual gelation of the hybrid sol was exploited to form multiphase hybrids with a gradation in the composition through the structure. The previous synthesis method was interrupted during the gelation/ageing period. The aim was to join two sols before they completed gelation. Therefore, ageing times (t_{age}) of two hours and three days, plus an intermediate time point of one day, were used to create the first hybrids made by joining two partially gelled sols.

Joining of different compositions (TEOS/GPTMS ratio of the reagents) between the first and second sol were investigated: Si2.5-PTHF/Si7.5-PTHF, chosen based on mechanical properties measured in Section 3.3.4, for which typical synthesis quantities are shown in Table 4.1; Si5-PTHF/Si20-PTHF (stiffer combination of phases); Si1-PTHF/Si20-PTHF to maximise the difference in stiffness between each region; and three-phase hybrids of composition Si1-PTHF/Si5-PTHF/Si20-PTHF, to attempt a gradual composition change. Two-phase samples of identical composition Si2.5-PTHF/Si2.5-PTHF were compared with single phase Si2.5-PTHF (referred to as ‘zero hour’ joining time).

For cylindrical moulds, formation of two-phase samples involved half-filling the mould with the first solution and then filling the remaining height with the second solution, using the same process at all ageing times. For discs, half of the solution was removed with a PTFE spatula at two hours of gelation, then for t_{age} = 2 hour the second solution was added immediately. For t_{age} = 1 day and 3 days, the sample was returned to the oven at 40°C until the required time was reached, at which point the

second solution was added. To prevent distortion or movement of the first half of the disc, a PTFE weight was used to hold it in place.

Table 4.1: Typical synthesis quantities for first and second hybrid sols to form a two phase Si2.5-PTHF/Si7.5-PTHF hybrid, at joining times of t_{age} = 2 hour, 1 day, 3 day in the ageing of the first sol. *x* refers to the moles of TEOS and *a* to the moles of GPTMS, the ratio of which (*x/a*) controls the inorganic/organic ratio.

	Solution 1: Si7.5-PTHF		Solution 2: Si2.5-PTHF	
Reagent	**Molar ratio**	**Typical quantity (mL)**	**Molar ratio**	**Typical quantity (mL)**
GPTMS	*a*	2.16	*a*	2.43
$BF_3{\cdot}O(C_2H_5)_2$	0.25*a*	0.30	0.25*a*	0.34
THF	100*a*	79.49	100*a*	89.20
TEOS	*x* = 7.5*a*	16.41	*x* = 2.5*a*	6.14
H_2O	3*a* + 4*x*	5.82	3*a* + 4*x*	2.57
HCl (1M)	(1/3 volume of H_2O)	1.94	(1/3 volume of H_2O)	0.86

Characterisation of the interface

To confirm the variation in the silica content in the multiphase hybrids, cylindrical samples were sliced at approximately 2 mm height sections. Each section was then analysed by TGA. This method is limited in resolution by the ability to slice sections and was used to confirm the presence of different hybrid compositions rather than characterisation of the steepness in the compositional change at the 'interface' or 'join' (where the two sols meet) itself.

4.2.2 Mechanical behaviour

Compression testing

Vertical uniaxial compression testing was carried out on cylindrical samples of height x diameter ≃ 15 x 10 mm with the long axis of the cylinder parallel to applied force (as for single phase samples, Section 3.3.4), using a Zwick machine with 1 kN load cell, in displacement control at a rate of 1 mm min^{-1}. The 'join' in multiphase samples was located at the centre of the sample perpendicular to the applied force.

Horizontal compression testing was carried out on the same cylindrical samples, with the long axis of the cylinder perpendicular to the applied force. In this case the 'join' in multiphase samples was parallel to the applied force.

Three samples were tested in each orientation.

Tensile testing

Uniaxial tensile testing to failure was carried out according to [144] on samples of length x width x thickness ≃ 45 x 10 x 0.5-2 mm (measured for each sample) with 25 mm exposed length, using Bose Electroforce Series III machine fitted with 450 N load cell, in displacement control at a rate of 1 mm min^{-1}, with a minimum of five valid repeats (samples failing at grips were excluded). As for compression test samples, the 'join' in multiphase samples was located at the centre of the sample perpendicular to the applied force, shown schematically in Figure 4.1.

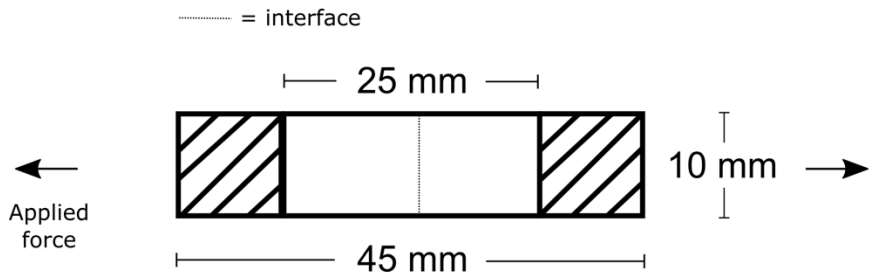

Figure 4.1: Tensile test sample schematic with the join interface shown as the dotted line. Each end is covered in tape to prevent tearing inside the grips (hatched region).

For comparison between two-phase hybrids with different compositions formed at different ageing times, the dimensions of the less stiff phase were used to plot stress-strain curves, as all of the deformation was assumed to be in that phase.

4.2.3 Digital Image Correlation

All Digital Image Correlation (DIC) work was carried out in collaboration with Jeff Clark. A speckle pattern for DIC was created using an ink pen on the surface of the hybrid sample. The sample was then photographed every 2 seconds during compression tests with an image resolution of 6000 x 4000 pixels, resulting in an approximate pixel size of 6 µm. A lamp was placed directly behind the sample to increase the contrast in the pattern as the sample itself is transparent. ImageJ [141] was used to process the images and GOM Correlate 2018 software [162] was used to produce strain maps with surface component facet size = 100 pixels, point distance = 40 pixels, optimised as discussed in Section 4.3.5. This ensures that the facet size (600 µm) is larger than the scale of the speckle size. The strain was measured across a line along the centre of the specimen to reduce the error from out of plane motion of the sample as it was compressed.

Two-phase hybrid samples with phases of identical and different composition were analysed by DIC in vertical compression, with the interface centrally located and perpendicular to the applied force, and in horizontal compression, so that the interface was parallel to the axis of the applied force. The identical composition hybrids were Si2.5-PTHF/Si2.5-PTHF and the different composition hybrids were Si2.5-PTHF/Si7.5-PTHF with the silica content measured by TGA. Samples were formed at ageing times of two hours, one day, three days and additionally '0 hour' samples were tested for the identical composition, which were single phase hybrids of Si2.5-PTHF.

Stationary test

The point distance was chosen to give 40% overlap of facets used for DIC and the facet size was optimised as the smallest facet size achievable without increase in strain error. The optimisation was done for one sample in the horizontal and one in the vertical orientation, with 8 stationary photos at the beginning of the test. The surface component facet size was set at 150, 125, 100, 75 and 50 pixels (with the point distance set at 40% of this), and the maximum in the absolute value of the major strain was measured at each of the eight stationary photos to give a value of the error in the strain.

4.2.4 Micro-CT

All Micro-CT scanning was carried out by Jeff Clark and Brett Clark (Micro-CT scanning specialist, Natural History Museum, UK). Jeff Clark conducted all image processing and DVC analysis of the data.

Synthesis incorporating ZrO_2

The hybrid itself did not have any intrinsic pattern that could be employed for tracking using DVC. To create a pattern, zirconia powder (Sigma, UK) was added to the hybrid sol before pouring into moulds. The zirconia powder was ground and sieved to 38 μm and stirred into the hybrid sol at 400 rpm for 10 minutes. 20 mg of ZrO_2 powder was added to 10 mL of hybrid sol (concentration of 2 mg mL^{-1}). Dual phase hybrids were made in this way with compositions Si2.5-PTHF and Si7.5-PTHF joined at two hours ageing.

This method was used for single phase samples of Si2.5-PTHF to check the concentration of zirconia powder that would give a trackable pattern (comparing 2 mg mL^{-1} and 10 mg mL^{-1}) and subsequently for two-phase hybrid samples to assess the 3-dimensional form of the interface and the strain state around that interface when under compression. The Si2.5-PTHF/Si7.5-PTHF, t_{age} = 2 hour two-phase hybrid was scanned uncompressed and at 10% and 20% nominal strain in compression.

Micro-CT: Zero strain study

Samples were loaded into a custom-made *in-situ* mechanical testing rig equipped with a load cell (LBS100, Interface) for micro-CT scanning (Versa 510, Zeiss, Germany). The Fast Fourier Transform

(FFT) pre-shift window size was set to 12 voxels larger than the subset size (76) and the peak search radius was set to 4. To quantify the error an initial series of scans (n=3) were taken with no strain induced between the scans, referred to as zero strain scans. To ensure good contact with the platens a preload of 10 N was applied prior to testing in displacement control. This is larger than the preload considered for the loaded study to prevent any wobbling of the sample during testing, which would invalidate the zero strain study.

Loaded study

To ensure that the movement of the particles was captured, the FFT pre-shift and peak search radius were increased for the loaded study. An initial unloaded scan was taken with a preload of 5 N applied. Following this, further scans were taken with two loading stages applied, at nominal strains of 10% and 20%, calculated from the distance between platens measured after the unloaded scan. The number of projections was increased to 1600 for the mechanical loading series to maximise the image quality across the sample.

Digital Volume Correlation (DVC)

Reconstruction of the projection images to produce 3D volumetric data sets was performed using Reconstructor Scout-and-Scan software (Zeiss, Germany). The reconstructed CT volumes were aligned and cropped using Fiji Is Just ImageJ software version 1.52g (NIH, USA).

Scan data for zero strain conditions was imported to the DVC software (DaVis 8.4.0, LaVision, Germany). Three scans were run of which the second and third were analysed. These scans are used to optimise the DVC software for three variables. Firstly, the choice of DVC method used from: a) direct correlation (DC); b) FFT; and c) combining both (FFT+DC). DC compares directly each voxel of the unloaded and loaded conditions to create the 3D map whereas FFT uses the product of Fourier transform of volumes to find the cross correlation [142]. The second variable is the overlap of the voxels, which are the subset volumes or boxes used for tracking. Overlapping reduces the error (greater number of vectors are measured in a given volume) without decreasing the size of the voxels which would otherwise increase the noise in the data. This was tested at 0, 50 and 75% as allowed by the software. The third variable is the subset size (size of the voxel). As for DIC, this should be minimised whilst still maintaining strain accuracy, *i.e.* use the minimum subset size that is small enough for good spatial resolution and large enough for the strain vector in each voxel to be accurate. Results of optimisation are discussed in Section 4.3.6, resulting in the use of FFT+DC at 64 subset size with the overlap set at 50%.

4.3 Results and discussion

4.3.1 Observations of the synthesis process

Polymerisation of THF continued during the ageing time while the hybrid samples were sealed for three days, after which gradual opening of the moulds allowed THF evaporation to occur and led to the shrinkage of the sample. A second hybrid solution (of the same or different composition) can be added to the first during this time, at ageing time t_{age} measured from the addition of the first hybrid to the mould. Adding two sols together immediately caused complete mixing. To maintain the separation of the two hybrids, the minimum joining time is around two hours of gelation (sealed at 40°C), after which the viscosity of the sol was sufficient such that addition of a second sol to the mould did not cause mixing. After three days gelation/ageing of the original sol the hybrid had gelled to the point that a solid sample had formed but shrinkage has not occurred. Beyond three days, the gel began to shrink.

The formation of two-phase cylinders was straightforward, pouring a second solution on top of the first, using a Pasteur pipette to control the volume of solution so the interface falls in the centre of the cylinder. Forming discs was more difficult than forming cylinders, in particular achieving the same height of solution whilst also not overlapping the solution at the interface. At the longest t_{age} of three days, the first hybrid tended to curl up at the edges, allowing the second solution to flow underneath. This was countered by weighing down the first part with a PTFE weight and by leaving the second hybrid sol until it reached a higher viscosity than that used for single phase samples before adding to the mould. At three days ageing the hybrid has gelled enough that the weight did not deform the disc.

After the three day ageing period, it was still possible to join a second hybrid solution, and it bonded to the first. This caused the samples to distort because of the shrinkage of the first hybrid while the second was still gelling. Therefore time points after three day ageing time were not considered.

4.3.2 Characterisation

Silica content

The cylinders formed were cut into slices with a razor blade, at approximately 2 mm intervals along their height. TGA of each individual section allows the measurement of the silica content in each slice. The composition variation over the height for a single phase sample is around 1 wt.% SiO_2, as discussed in Chapter 3 and shown again in Figure 4.2a. Comparing this to Figure 4.2b, which is a two phase hybrid of the same composition (Si2.5-PTHF) formed at t_{age} = 2 hour shows that the constant composition throughout the sample has been maintained despite the joining. Figure 4.2c again shows a cylinder formed at t_{age} = 2 hour but this time with two different hybrid compositions: Si2.5-PTHF/Si7.5-PTHF,

reflected in the difference of the silica content from 11.8 to 23.7 wt.% SiO_2 through the length of the cylinder. The difference in stiffness was apparent when handling the sample. Figure 4.2d shows a three-phase hybrid of composition Si1-PTHF/Si5-PTHF/Si20-PTHF and shows the change in composition occurs through a larger central portion of the cylinder and a total of 36 wt.% SiO_2 difference between top and bottom of the cylinder. All the cylinders show faint horizontal lines which results from the machining lines inside the mould and are not related to the formation of the interface.

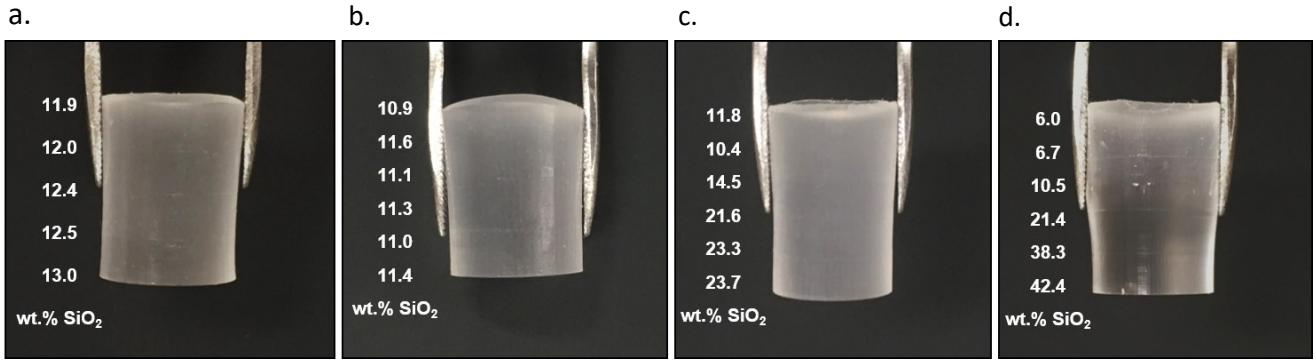

Figure 4.2: Silica content in multiphase hybrids measured by TGA. **a.** Single phase Si2.5-PTHF **b.** Two-phase hybrid with identical composition Si2.5-PTHF/Si2.5-PTHF, **c.** Two-phase hybrid with different composition Si2.5-PTHF/Si7.5-PTHF and **d.** Three-phase hybrid with different composition Si1-PTHF/Si5-PTHF/Si20-PTHF. Cylinder dimensions ≈ 10 x 15 mm.

This technique confirms the formation of multiphase hybrids, however it is limited in its resolution to approximately 2 mm, because of the minimum amount of material required for TGA. Since the interface covers a distance smaller than this, it does not provide information on the steepness of the compositional change at the interface itself.

To improve the precision, AFM was used to measure the stiffness of the surface, to attempt to understand how the silica content is changing over the interface, but since the surface roughness also changed with increased silica content, these effects interfered with each other. Therefore no characterisation of the precise compositional change at the interface was achieved, and instead optical methods were used in conjunction with mechanical testing to understand the interface.

4.3.3 Tensile testing

Two-phase hybrids of different composition

For tensile testing, rectangular samples with the interface horizontal across the centre were cut from discs. Figure 4.3 shows discs formed at t_{age} of two hours (Figure 4.3a), one day (Figure 4.3b) and three days (Figure 4.3c) from Si2.5-PTHF/Si7.5-PTHF. When joining at one day and three days, the interface was clearly visible, but at two hours the join did not show the same clear line across the disc.

Sometimes, when joining after one and three days, bubbles formed at the interface, possibly due to the evaporation of THF from the first hybrid into the second or trapping of air when the second solution was added. Since the exposed area of the disc samples is large (diameter = 150 mm) compared to the cylinders (diameter = 10 mm) and the opening of the samples must be done under a fumehood, there is significant evaporation of THF when the second solution is added. However, the formation of bubbles is regarded as part of the weakness that comes from the formation of the interface, so samples containing bubbles were not discounted.

Figure 4.3d shows a tensile test specimen cut from a two component Si2.5-PTHF/Si7.5-PTHF disc that was joined at 1 day. The setup of tensile tests was complicated for two phase samples as there was a difference in the surface finish and in the thickness of the two components. The ends of samples were covered in tape as for the single phase samples, however a higher proportion of samples failed in the grips.

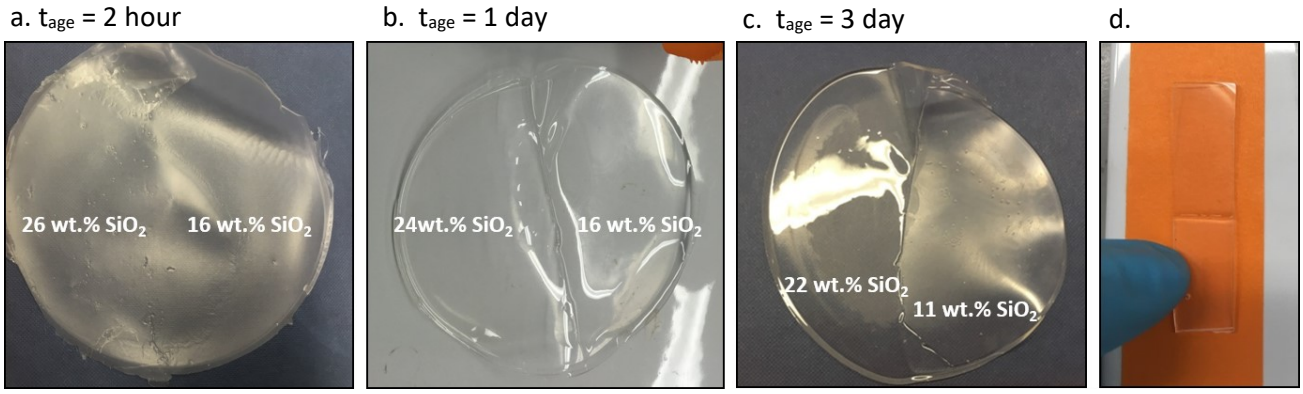

Figure 4.3: Discs formed from Si2.5-PTHF/Si7.5-PTHF at joining times of **a.** 2 hours, **b.** 1 day, **c.** 3 day. **d.** shows a sample for tensile testing cut from a disc joined at 1 day, with the interface horizontal across the centre of the specimen.

The results from tensile testing of Si2.5-PTHF/Si7.5-PTHF samples joined at t_{age} = 2 hour and 1 day are summarised in Table 4.2, with comparison to single phase samples of Si2.5-PTHF. All samples formed at t_{age} = 3 day failed in the grips, due to a large discrepancy in the thickness of the two phases. Results for samples formed at t_{age} = 2 hour and 1 day are the average and standard deviation of five samples,

none of which failed at the grips. Due to the difference in stiffness of the joined phases, the two phases deformed differently in tension. Therefore, calculation of stress and strain in tensile tests was done using the dimensions of the less stiff phase (Si2.5-PTHF), since observations of the tests indicated that only this phase was deformed (Figure 4.4c). However, this gave a higher true stress at failure than the single phase samples (Table 4.2), so it may indicate instead that the strain in both phases should be measured by another method, e.g. optically or calculated from the stiffness values. To isolate the effect of the interface and ameliorate this problem, two phase hybrid samples of identical compositions were formed at t_{age} = 2 hours, 1 day and 3 days, discussed in the next section.

Table 4.2: Tensile testing of samples of different compositions compared to the single phase ('0 hour' joining)

Sample	Joining time	σ^* at failure (MPa)	ε^* at failure
Si2.5-PTHF	0 hour	2.6 ± 0.6	0.60 ± 0.09
Si2.5-PTHF/Si7.5-PTHF	1 day	4.6 ± 2.6	0.52 ± 0.06
Si2.5-PTHF/Si7.5-PTHF	3 days	2.2 ± 1.7	0.55 ± 0.22

Figure 4.4a and b compare the appearance of Si2.5-PTHF/Si7.5-PTHF at t_{age} = 2 h and t_{age} = 1 day in a tensile test set up. The Si2.5-PTHF deformed significantly more than the Si7.5-PTHF (Figure 4.4c). The join interface was seen in the t_{age}= 2 h samples by the difference in surface finish but was not visible in the photo (Figure 4.4a). The true stress-strain curves of all samples including single phase samples for comparison are shown in Figure 4.4d. There was a large range of results for both t_{age} = 2 h and t_{age} = 1 day samples, with the samples becoming stronger and stiffer at the shorter joining time. At 2 hours the samples never failed directly at the interface whereas at 1 day they did fail sometimes (2/5 samples e.g. Figure 4.4e) at the interface.

Hydrogel samples have been developed with distinct zones, so that under tension elongation is seen only in the less stiff zone, followed by failure within that zone rather than at the join [118], as found in this work when joined at t_{age} = 2 hour, however this was not accompanied by a systematic study of the strength of the join for comparison.

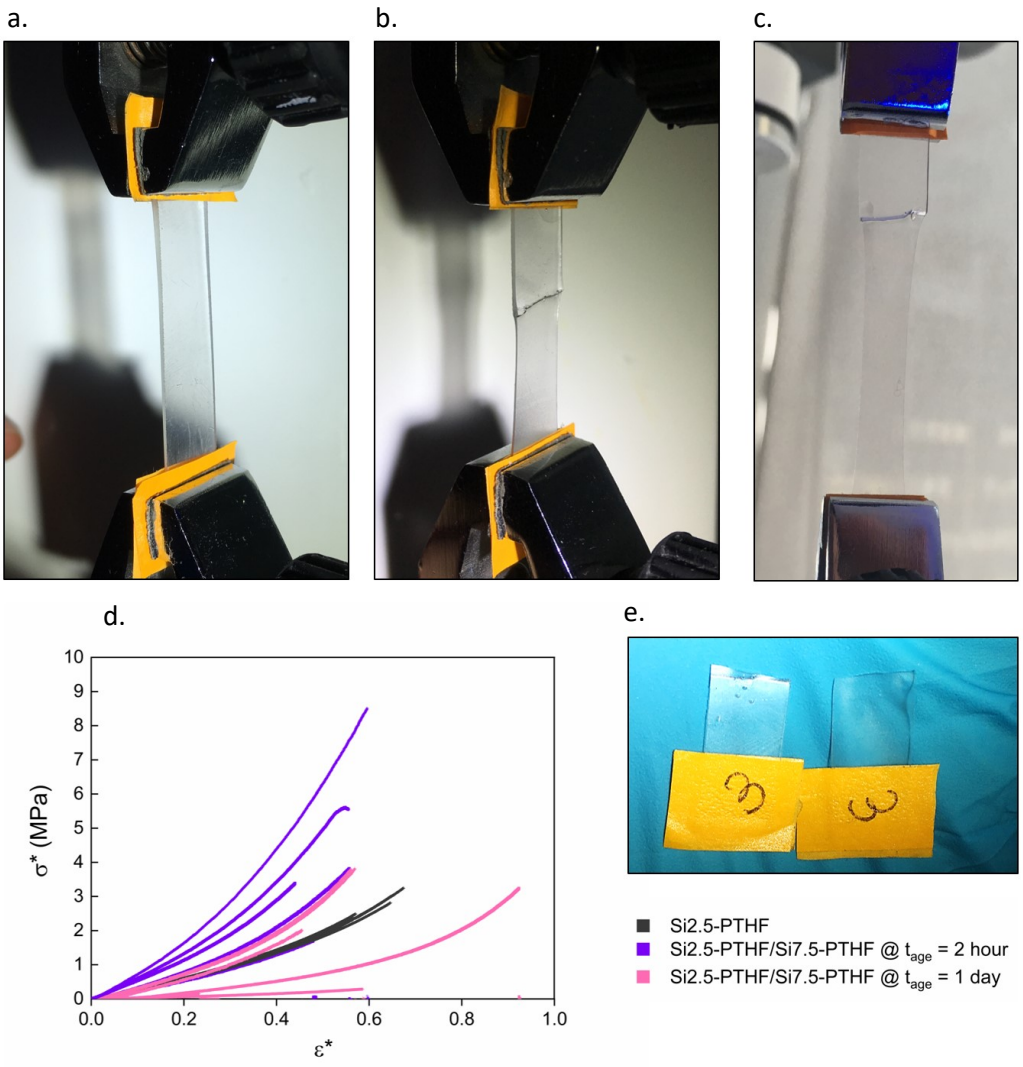

Figure 4.4: Tensile testing of Si2.5-PTHF/Si7.5-PTHF samples at **a.** t_{age} = 2 hour, **b.** t_{age} = 1 day, **c.** t_{age} = 1 day at a larger extension, highlighting that deformation occurs in the less stiff phase, **d.** σ^* v ε^* curves for single phase Si2.5-PTHF samples and Si2.5-PTHF/Si7.5-PTHF samples joined at t_{age} = 2 hour and 1 day. **e.** A sample joined at t_{age} = 1 day which failed along the interface.

Two-phase hybrids of identical composition

To avoid the complication of two different compositions with different mechanical properties, Si2.5-PTHF/Si2.5-PTHF samples were formed from the same hybrid compositions at the same series of joining times: two hours, one day and three days, and compared to the '0 hour' joining time, which was a single phase hybrid of Si2.5-PTHF. In this case, the stress-strain curves were produced as they were for single phase samples, with the aim to isolate the effect of the formation of the join.

Samples joined at t_{age} = 3 days failed more often at the interface: three out of five valid samples failed at the interface, compared to none for samples joined at t_{age} = 2 hour and one at t_{age} = 1 day. Figure 4.5 shows the mean and standard deviation of the five repeats, with blue shaded area showing that

of the single phase Si2.5-PTHF samples. The reason for the higher mean stress at failure for the samples at t_{age} = 2 hours, over the single phase, may be a slight discrepancy in the composition (samples were not made in the same synthesis batch).

This test suggested that the joining of two gels at two hours of ageing did not reduce the strength of a sample compared to a single phase specimen: the material was continuous at the interface.

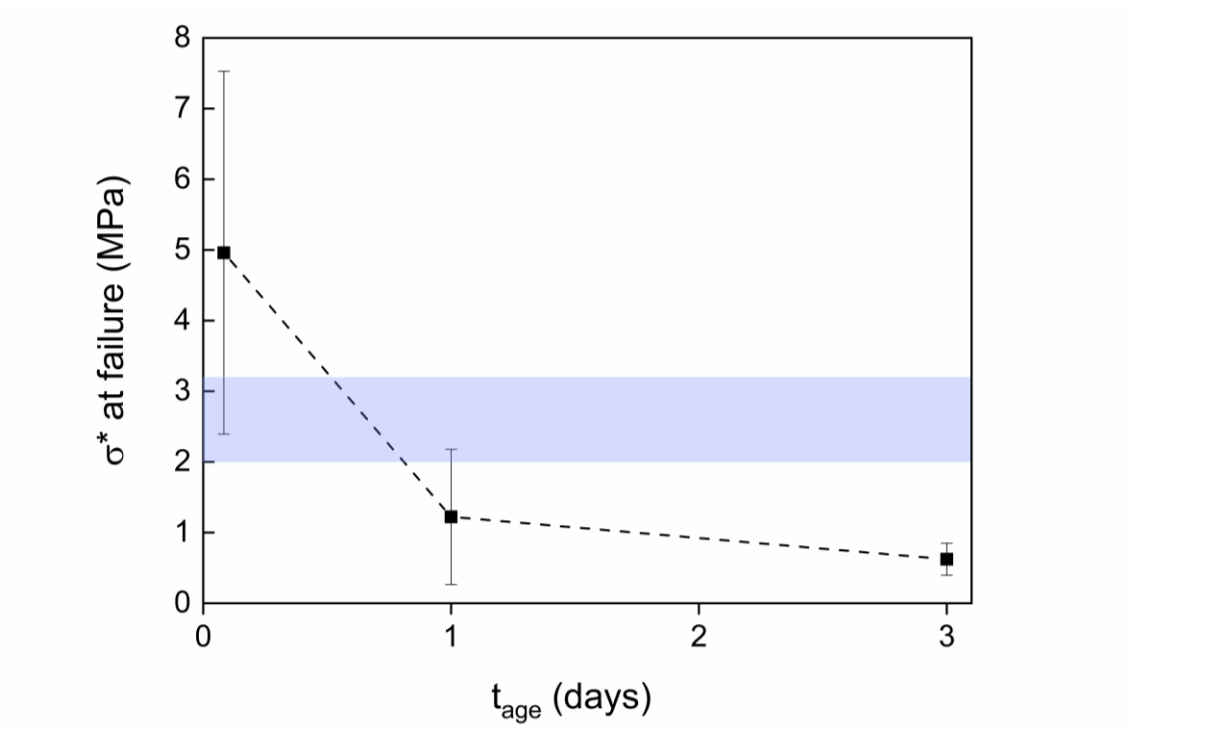

Figure 4.5: Tensile testing of identical composition samples (Si2.5-PTHF/Si2.5-PTHF) formed at different joining times, t_{age}. Using a t-test with unequal variance there was a significant difference between the failure stress of gels joined after 2 h of ageing compared to those joined after 1 day ($p \leq 0.01$).

4.3.4 Compression testing

Two-phase hybrids

Compression testing was conducted in vertical and horizontal orientation, referring respectively to the long axis of the cylinder parallel and perpendicular to the applied force. Stress-strain curves were only produced for the vertical compression tested samples, using the mean cross-sectional area of the sample. This is because the two phases were in series with each other and the stress is assumed to be the same in both phases (they have the same initial cross-sectional area). It was not possible to see exactly where the interface was for cylindrical samples, unlike for the discs, therefore it was not feasible to measure the height of each phase. The height of each phase was therefore assumed to be half the overall height (*i.e.* the interface was assumed to be in the centre of the sample, which was the intention after grinding the top surface of the sample to flat).

The first trial of compression testing of two-phase hybrids was done on a stiffer combination of phases, Si5-PTHF/Si20-PTHF formed at t_{age} = 2 hours. Figure 4.6a shows a photograph of a Si20-PTHF/Si5-PTHF two-phase hybrid cylinder with the silica content gradient shown, as measured from in 2 mm sections by TGA. Si20-PTHF region is denoted with a blue † and Si5-PTHF with a red * (Figure 4.6a and c).

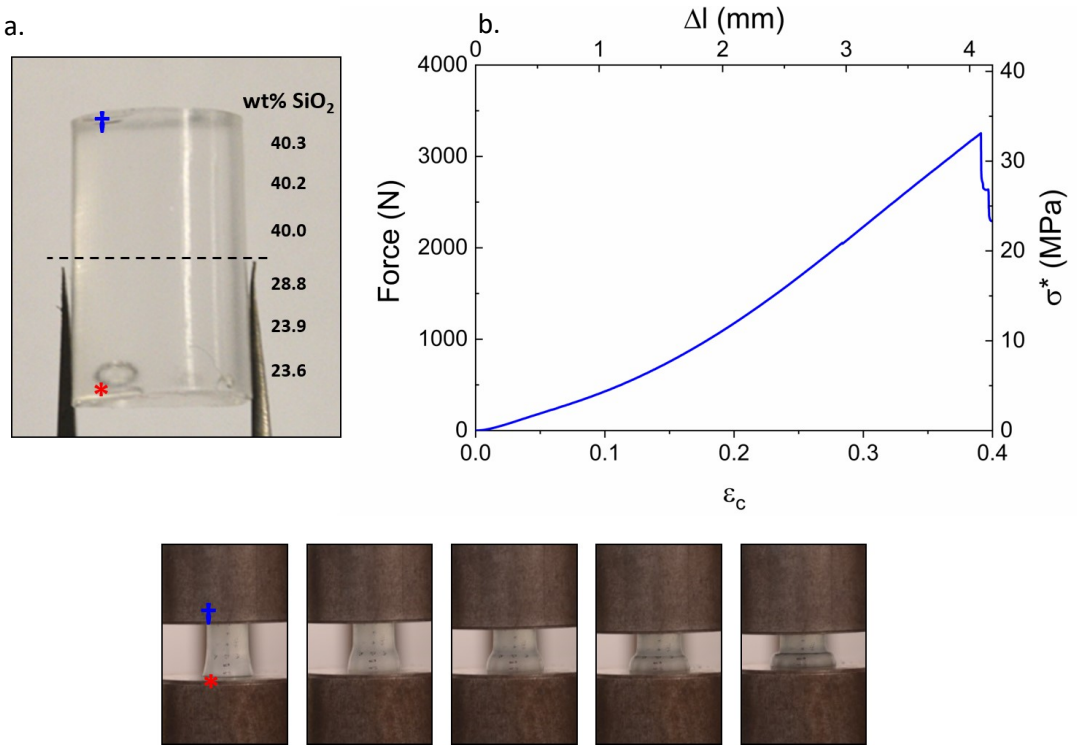

Figure 4.6: a. Si5-PTHF/Si20-PTHF two-phase hybrid with the silica content gradient shown as measured in 2 mm sections by TGA, and **b.** compression test of a sample of the same composition. **c.** shows photos of the sample at approximately 10% strain intervals up to just before failure. †(blue) labels the Si20-PTHF region and * (red) the Si5-PTHF.

Uniaxial compression of the sample is shown in Figure 4.6b, with photos at approximately 10% strain intervals in Figure 4.6c showing that the deformation and barrelling effect were greater in the less stiff (Si5-PTHF) part of the sample, where the final failure occurred. The final true stress at failure is in the range of values measured at the same silica content: here the average silica content is 25.4 wt.% SiO_2 and the true stress at failure was measured at 29.6 ± 1.2 MPa for 24.6 wt.% SiO_2.

Compression testing was conducted in this way for a series of joined hybrids: identical composition samples (Si2.5-PTHF/Si2.5-PTHF) and different composition samples (Si2.5-PTHF/Si7.5-PTHF), at t_{age} = 0 h, 2 h, 1 day, 3 days. There was a large variation in the results, so individual results were plotted rather than average values, Figure 4.7. Because of the variance in the results, no conclusions can be drawn from this test about how the strength of the interface changes with joining time at increasing t_{age}. For this reason, DIC was used to investigate whether or not the interface acts to concentrate the strain and therefore whether or not it will act as a point of failure in the material.

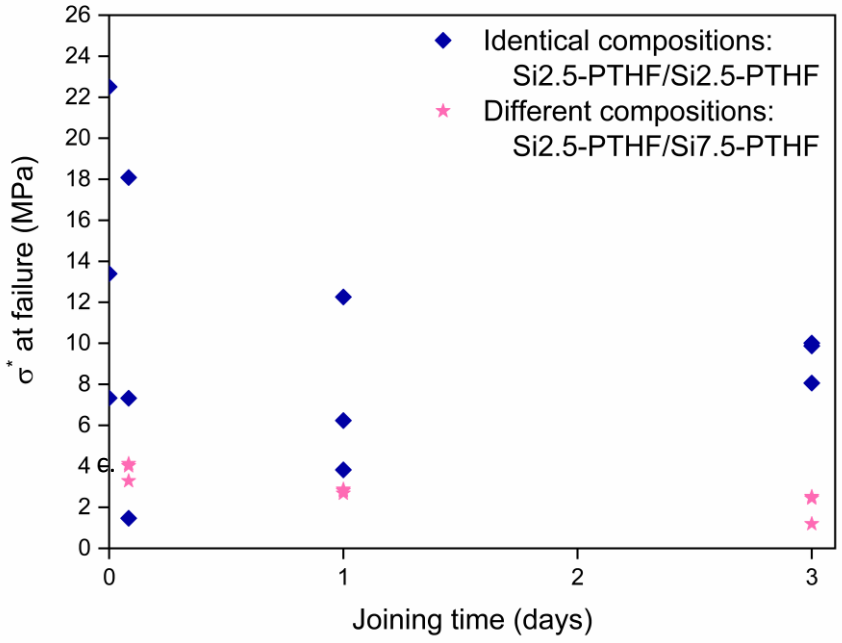

Figure 4.7: Vertical compression testing of two phase hybrids of: identical composition (diamonds) and different composition (stars), as a function of time lapsed before joining (t_{age}), calculated from the height of only the less stiff phase.

4.3.5 Digital Image Correlation

Digital Image Correlation (DIC) tracks the surface displacement of a pattern, and has been used extensively with both biomaterials and biological tissues [163]. Cylindrical samples were tested vertically and horizontally to investigate the strain around the joining interface. Figure 4.8 shows the speckle pattern of ink drawn on the surface.

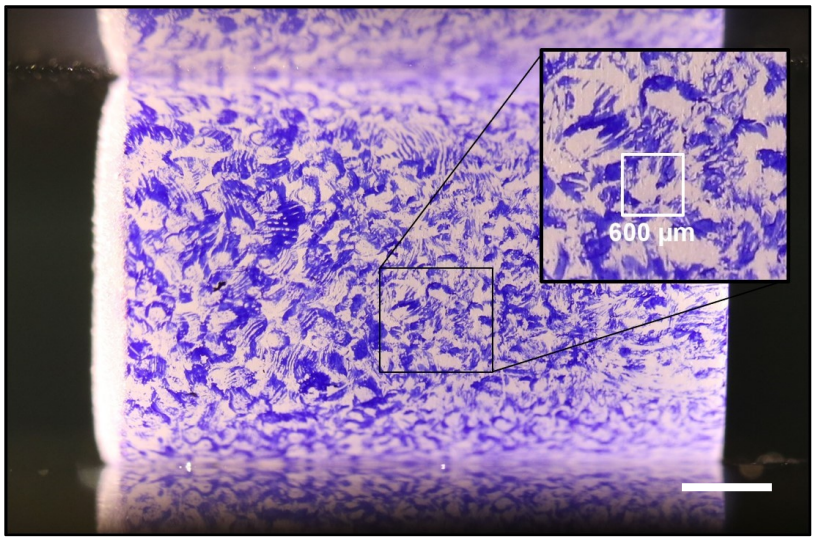

Figure 4.8: Horizontal compression sample Si2.5-PTHF/Si7.5-PTHF with speckle pattern for DIC tracking and illumination from behind. Scale bar = 2 mm. Inset shows the facet size used with DIC software, square size length = 600 µm (100 pixels).

The surface finish depends on the composition of the hybrid, which can affect the drawing of the pattern. Both the compositions used here had sufficiently low silica content that the pattern could be drawn well onto the surface with ink pen. The camera was focussed on the central horizontal line of the sample, as away from the centre the material moved out of plane.

Stationary test

Measuring the strain between stationary photos at the beginning of the test gave an estimation of the error in the strain calculated. This was also used to optimise the size of the facets used for tracking. Using a fixed overlap of facets of 40% and minimum pattern quality of 1.1, the facet size was varied at 50, 75, 100, 125, 150 pixels. Increasing the facet size will give a smaller the error, at the expense of the spatial resolution. Therefore, the aim is to minimise the facet size without a large increase in the error. The stationary test was done for three samples over eight stationary photos, and 100 pixels was selected as the optimum facet size, Figure 4.9. 100 pixels was approximately 600 µm, slightly larger than the size of the speckle (which varies 100-400 µm in its longest dimension). The facet size must be larger than the speckle size to ensure that each facet contains a unique pattern for tracking [164]. The randomness of the shapes of each speckle also improved the 'uniqueness' of the pattern in each facet

box, so smaller facets were used here than would be possible with a homogeneous speckle (*e.g.* uniform dots).

This gave an overall strain error of approximately 0.2 %, therefore a measured strain of 0.1 ± 0.002, much smaller than the differences in strains close to and away from the interface that were considered.

Variation between individual samples can arise due to illumination conditions and different pre-strain conditions, depending on the evenness of the surface in contact with the platen. Three samples were measured over 8 stationary photos to estimate the strain error.

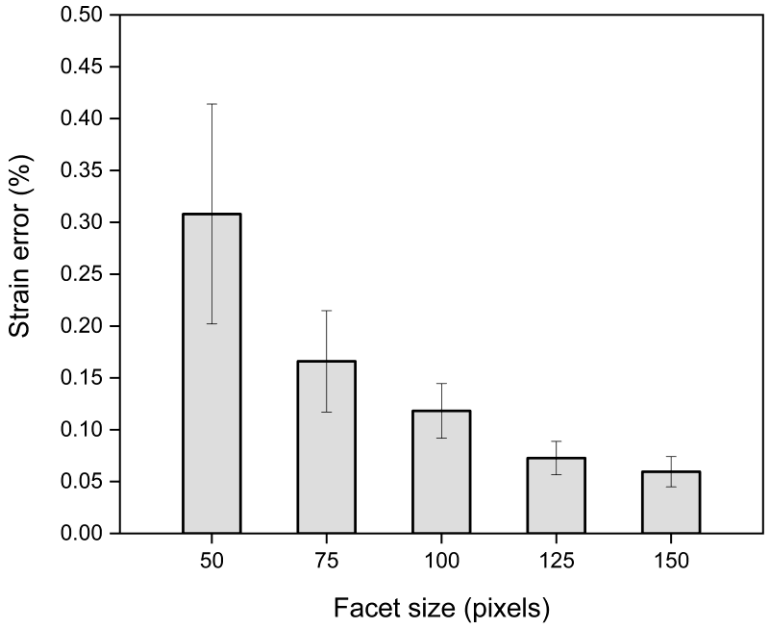

Figure 4.9: Stationary test to optimise facet size vertical compression testing, at 40% overlap of facets. A 100 pixel facet size was selected to minimise error whilst maintaining unique pattern inside each box.

Horizontal compression testing

Since the vertical compression testing of multiphase hybrids did not discriminate between samples formed at different t_{age}, it was considered to not be a useful test of the strength of the interface itself. Horizontal compression testing does not allow a straightforward calculation of failure stress, but when combined with DIC, it can show the concentration of strain around the join interface in this orientation. This may be more relevant to the application for IVD replacement, as the interface in this case would be parallel to the applied compressive force in the spine.

Horizontal compression testing was run on samples of identical composition (Si2.5-PTHF/Si2.5-PTHF) and of different composition (Si2.5-PTHF/Si7.5-PTHF) at t_{age} = 2 hours, 1 day and 3 day, and additionally for single phase samples of Si2.5-PTHF (termed 0 hour ageing). An example of Si2.5-PTHF/Si7.5-PTHF at t_{age} = 3 days is shown in Figure 4.10: the map of the strain (0 – 6 % tensile strain as the material expands horizontally) in the direction perpendicular to the applied force is shown along with the central black line along which strain is additionally measured.

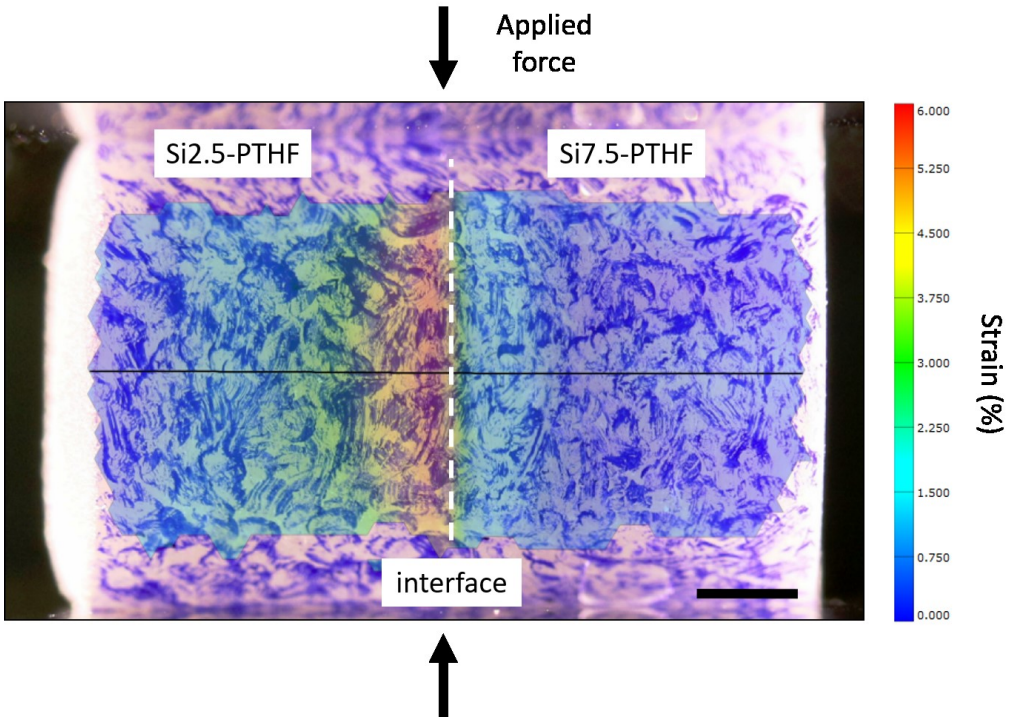

Figure 4.10: Example of horizontal compression of Si2.5-PTHF/Si7.5-PTHF joined at t_{age} = 3 days and 10% applied strain, showing the two regions, approximate position of the interface and the applied compressive force (top platen moves). The strain is measured along the central black line for subsequent plots. Scale bar = 2 mm.

For the subsequent Figure 4.11, cropped images of the cylinders in horizontal compression are shown, overlaid with the strain measured along the central line (this overlaid white graph is a graphical version of the same strain map, just along the central line of the cylinder, shown in black). DIC mapped the strain in the direction along the long axis of the cylinder, perpendicular to the applied force, mapped

across the surface. The strain in the direction parallel to the applied force was uniform along the central length of the cylinder. The central portion of the cylinder is shown along its whole length, at a 10% nominal strain in the vertical direction in each case. Three samples were tested in each condition of which one representative sample is shown here.

Comparing two-phase samples of constant composition with those with two different compositions separates the effect of the formation of an interface from the effect of the mismatched compositions. In Figure 4.11, no significant difference is seen in the identical composition samples as t_{age} increases, with a possible increase in the peak strain comparing between the single phase (0 hour) sample and the two-phase samples. No interface was apparent, in terms of the strain maps.

Conversely, with different compositions the strain concentration around the interface was visible and became sharper at longer t_{age}. This suggests that this strain concentration arose from the mismatch in properties due to differing compositions, rather than from the formation of the interface itself between the phases, even with t_{age} = 3 days.

The most important difference is in comparing the strain map picture at t_{age} = 2 h with t_{age} = 1 day, for the different composition samples: t_{age} = 2 h has a strain gradient that is symmetrical each side of the interface, with a lower peak strain at the interface. This suggests that the interface was more diffuse for the t_{age} = 2 h sample and thus indicated that mixing occurred over a longer distance than t_{age} = 1 day and t_{age} = 3 days samples, which had a sharper interface. This may be due to polymerisation occurring across the interface when the samples are joined at t_{age} = 2 h, as well as physical mixing of the two solutions close the interface. However, this should be confirmed with chemical composition measurement at the scale of the interface.

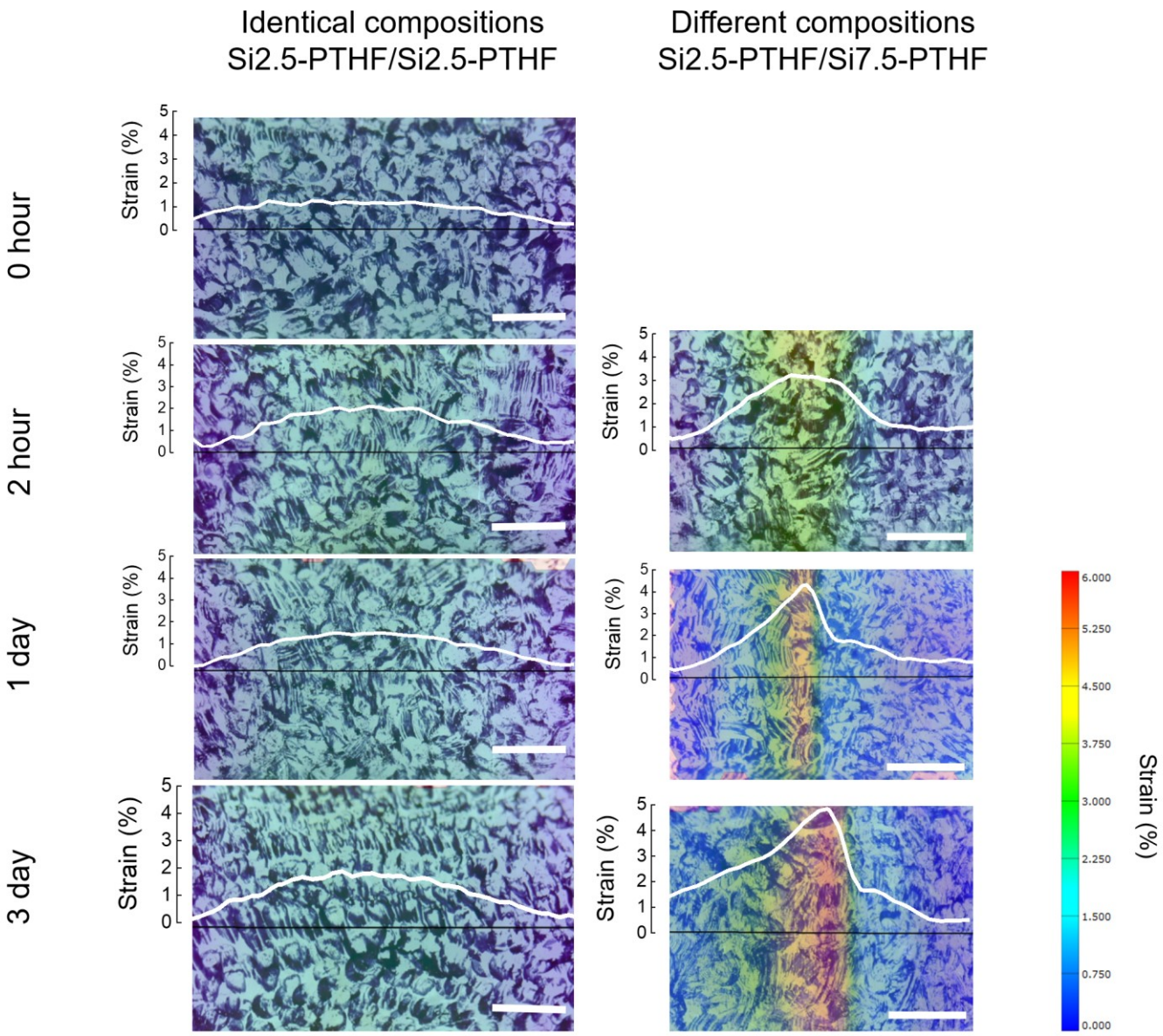

Figure 4.11: Horizontal compression testing showing the strain map in the direction perpendicular to the applied force as tracked by DIC, for identical composition samples (Si2.5-PTHF/Si2.5-PTHF) and different compositions (Si2.5-PTHF/Si7.5-PTHF) at t_{age} = 2 h, 1 d, 3 d and for single phase Si2.5-PTHF sample (0 h) at 10% strain. Overlaid graph (white) is the same strain measured specifically along the black line through the centre of the cylinder. Scale bar = 2 mm. Three samples were tested in each condition of which one representative strain map is shown, at the centre of the cylinder.

Vertical compression testing

In this case, differently to the horizontal compression, the strain parallel to the applied force (along the longer axis of the cylinder) was measured during compression of vertically orientated cylinders. Figure 4.12 shows an example of Si2.5-PTHF/Si7.5-PTHF joined at t_{age} = 1 day at 10% nominal strain, with the two phases, position of interface and direction of the applied force labelled. The DIC map shows the strain in the direction parallel to the applied force. The subsequent images are cropped from the cylinder to just show the interface and overlain with a graph of the same strain measured down the centre line of the cylinder (black vertical line on Figure 4.12).

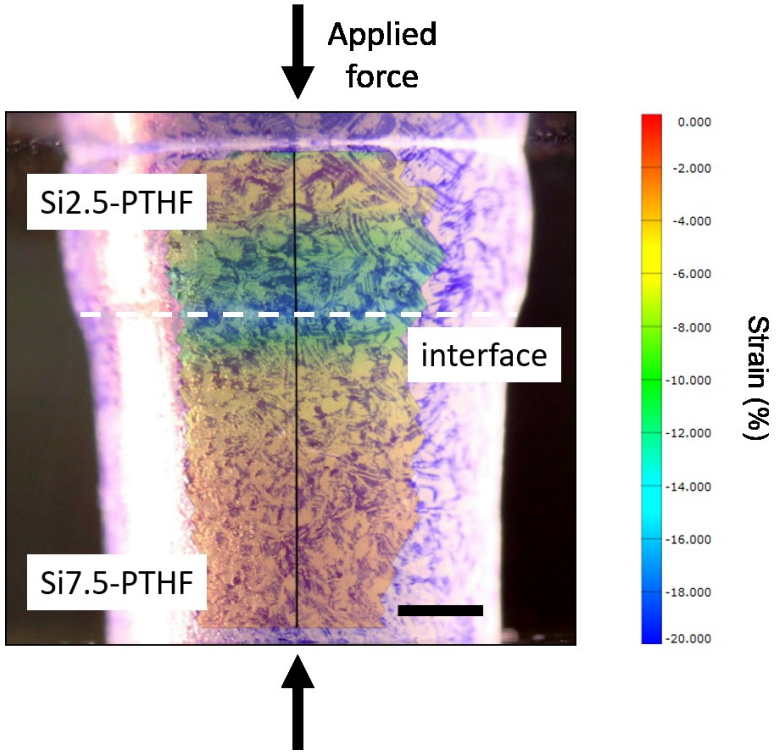

Figure 4.12: Vertical compression of Si2.5-PTHF/Si7.5-PTHF formed at t_{age} = 1 day, with the two regions labelled, the approximate position of the interface and the direction of the applied force. The black line is the central line in the cylinder along which the strain is graphed (for overlaying on pictures). Scale bar = 2 mm.

Figure 4.13 shows this for Si2.5-PTHF/Si2.5-PTHF and Si2.5-PTHF/Si7.5-PTHF cylinders at t_{age} = 2 h, 1 d, 3 d and for single phase Si2.5-PTHF samples ('0 hour'). Three tests were run for each condition, of which one representative sample is shown.

As for the horizontally compressed cylinders, a difference was seen for the different composition cylinders which is not seen for the cylinders of identical composition. Considering first the identical composition samples, the single phase sample (0 hour) showed zero strain at the top platen, increasing to around 10% compressive strain through the centre and lower portion of the cylinder. The variation

in strain is gradual. At t_{age} = 2 h and 1 day, the strain distribution is the same, and the sample formed at t_{age} = 3 day showed a more distinct maximum in the compressive strain close to the assumed position of the interface.

For the samples of different composition, strain concentration at the interface was seen in every case but most sharply at t_{age} = 2 h. It is also clear for this sample that the interface was not in the centre along the height of the cylinder, which could be caused by the difference in shrinkage of the two regions. Therefore it is possible that the inequality in the heights of the two phases means that the choice of 10% nominal strain for all of the samples may create error: *i.e.* the less stiff phase could actually be under greater strain for t_{age} = 2 h than 1 day or 3 day. This indicates the need for a mechanical analysis of the loading scenario, taking into account the proportions of each phase and their moduli (which varies with the applied strain).

As is observed by the barrelling in only the less stiff region, most of the deformation occurs in that region (Si2.5-PTHF). However, there is non-zero compressive strain measured in the stiff region (Si7.5-PTHF) which should be taken into account when calculating the failure stress and strain.

This test suggests that the composition transition is sharp at the interface, even at 2 hour joining time, unlike for the horizontal compression testing. This means that even at t_{age} = 2 h there is not long range mixing across the interface: the interface is still quite sharp. Better control of the viscosity would allow this to be less steep and potentially strengthen the interface.

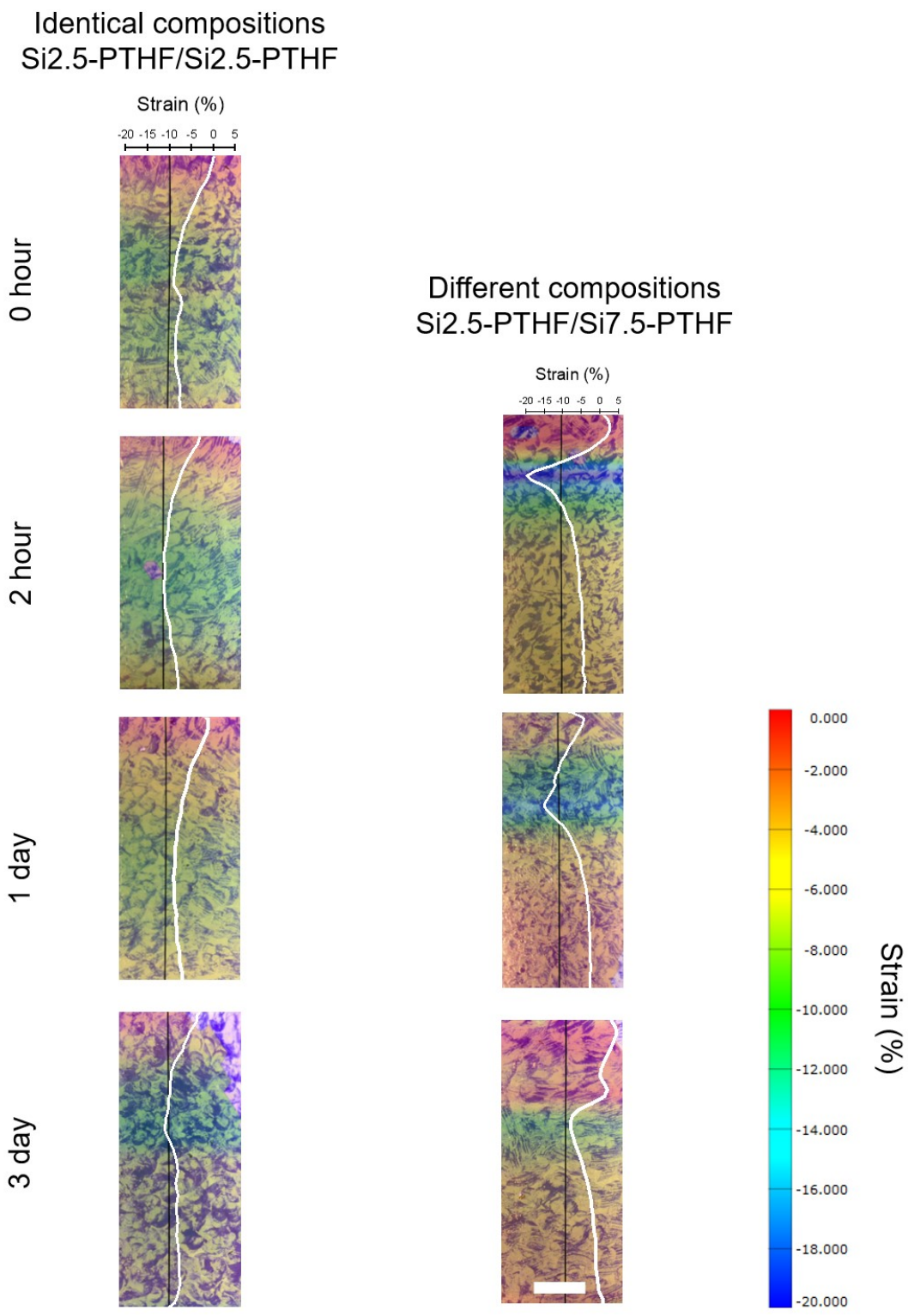

Figure 4.13: DIC of vertical compression samples for identical composition (Si2.5-PTHF/Si2.5-PTHF) and different composition (Si2.5-PTHF/Si7.5-PTHF) at t_{age} = 2 hour, 1 day, 3 days and additionally for single phase Si2.5-PTHF ('0 hour'). The overlaid white graph is a graphical version of the same strain map, along the central line of the cylinder (shown in black). Scale bar = 2 mm.

Testing of 3-phase sample with greater compositional difference

To maximise the compositional difference seen across the length of the cylinder, samples were created with Si20-PTHF as the first hybrid and Si1-PTHF as the second solution. In another sample, an intermediate thin layer of Si5-PTHF was added between the two. These samples are termed Si1-PTHF /Si20-PTHF and Si1-PTHF/Si5-PTHF/Si20-PTHF respectively. As was seen in Figure 4.2d, the inorganic content varied from 6 wt.% to 42 wt.% SiO_2. This corresponds to a difference in the stiffness, measured as the tangent to the stress-strain curve at 10% nominal strain, of 4 to 200 MPa between the top and bottom of the cylinder in compression (Section 3.3.4).

The compression test highlights the barrelling of the less stiff phase (Figure 4.14a-c), due to the greater disparity in stiffness. The sample failed in the less stiff phase, with a ring of material coming off (Figure 4.14c,e). The compression of samples with and without the intermediate phase were compared but there was no significant difference in the compression curve, Figure 4.14d. Looking at the transition between the phases in the SEM, there was a sharp difference in the fracture surface from the glassy phase to the flexible phase (Figure 4.14f).

Because of the smoother surface finish on the Si20-PTHF phase, it was not possible to draw a pattern for DIC tracking in the same way, and therefore DIC was only applied in the less stiff phase and around the interface. The strain maps in the horizontal long axis of the cylinder were compared for the two samples, for which the Si1-PTHF/Si5-PTHF/Si20-PTHF sample showed a less steep gradient of strain in the flexible phase (Figure 4.14g.). However, both showed a sharp increase in compressive (negative) strain at the interface (Figure 4.14g,h).

Overall, the addition of the intermediate phase of Si5-PTHF did not produce a sufficiently gradual transition in the composition through the cylinder to improve the properties over the Si1-PTHF/Si20-PTHF sample. This may be due to the lack of precise control over the viscosity of the hybrid sols, so optimisation of this along with the timings of additions of second and third sol are required to form a more gradual gradient in composition.

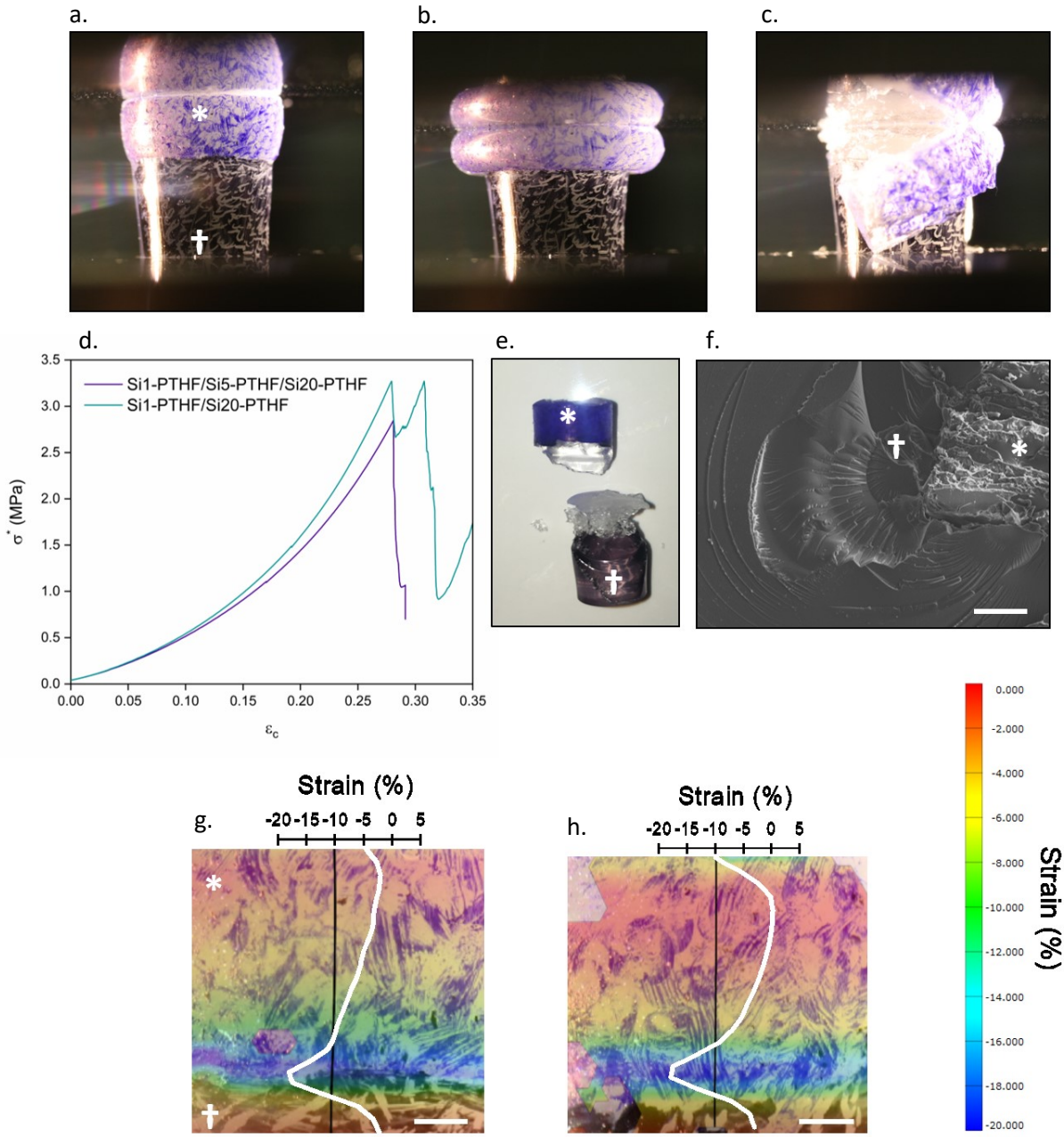

Figure 4.14: Compression of Si1-PTHF/Si5-PTHF/Si20-PTHF, with Si1-PTHF labelled with * and Si20-PTHF with †, at **a.** 1 mm displacement, **b.** just before and **c.** just after failure. **d.** σ^* v ε_c curves for Si1-PTHF/Si5-PTHF/Si20-PTHF and Si1-PTHF/Si20-PTHF. **e.** Si1-PTHF/Si5-PTHF/Si20-PTHF cylinder after failure and **f.** fracture surface of the same sample around the transition between phases, scale bar = 200 µm. Strain maps of the interface of **g.** Si1-PTHF/Si5-PTHF/Si20-PTHF and **h.** Si1-PTHF/Si20-PTHF for comparison. Scale bar = 1 mm.

As discussed in Section 1.4.1, the formation of graded stiffness structures is of interest as the gradation in properties and continuous interfaces are found in natural tissues, for example between bone and cartilage and within cartilage structures like the intervertebral disc. Approaches have been developed for the formation of gradients in bulk materials using differences in the materials properties, for example exploiting a difference in density to form a buoyancy-driven gradient in hydrogels and

acrylate polymers, and measuring the interface using differences in the RAMAN intensity arising from a given stretch and contact modulus across the surface [123]. Mechanical property gradients can also be produced by a difference in types of crosslinkers [118] or degree of polymerisation [165] in hydrogels or polymer crosslinking density in polyurethane [127].

Similar 50-fold differences in stiffness have been achieved in one hydrogel sample, but with much lower stiffness than achieved here, of the order of 100 kPa, and without systematic study of the strength of the interface [125].

4.3.6 Micro-CT imaging and Digital Volume Correlation

The aim here was to correlate the measured 2D surface strain with the 3D strain around the interface, and to develop a technique which could be applied to mechanical testing of whole devices made from inorganic-organic hybrids in the future. Zirconia particles were used as image contrast agents as they are used to give radio-opacity in bone cements [166].

ZrO_2 incorporation

To incorporate ZrO_2 particles into the hybrid material they must be added after the formation of the hybrid sol, as particles added before the polymerisation block the polymerisation reaction and prevent or slow down the gelation. As such, they were added when the viscosity of the sol was already increasing, so it was important to ensure that the particles were fully mixed into the sol. Two concentrations of ZrO_2 in hybrid sol were tested first, one at 2 mg mL^{-1} and the other at 10 mg mL^{-1}. Micro-CT images (2D image of a 3D projection) of these two concentrations are shown in Figure 4.15a and in Figure 4.15b respectively. The lower concentration gave sufficient patterning for DVC tracking so was chosen for the lower effect on the properties of the hybrid. It should be noted that the concentration is only an estimate as not all of the powder is well mixed into the hybrid sol, and gives an approximate volume percentage of particles of 0.1%.

A cylinder of Si2.5-PTHF/Si7.5-PTHF was produced with ZrO_2 particles through the whole cylinder. Micro-CT images of one cross-sectional area (area perpendicular to the long axis of the cylinder) are shown in Figure 4.15d and Figure 4.15e for the top (Si2.5-PTHF) and bottom (Si7.5-PTHF) halves of the cylinder respectively. In fact, a constant concentration of ZrO_2 through the cylinder was not achieved, as can be seen by the patches of lower and higher concentration of dots in Figure 4.15d. There was still enough patterning for DVC tracking.

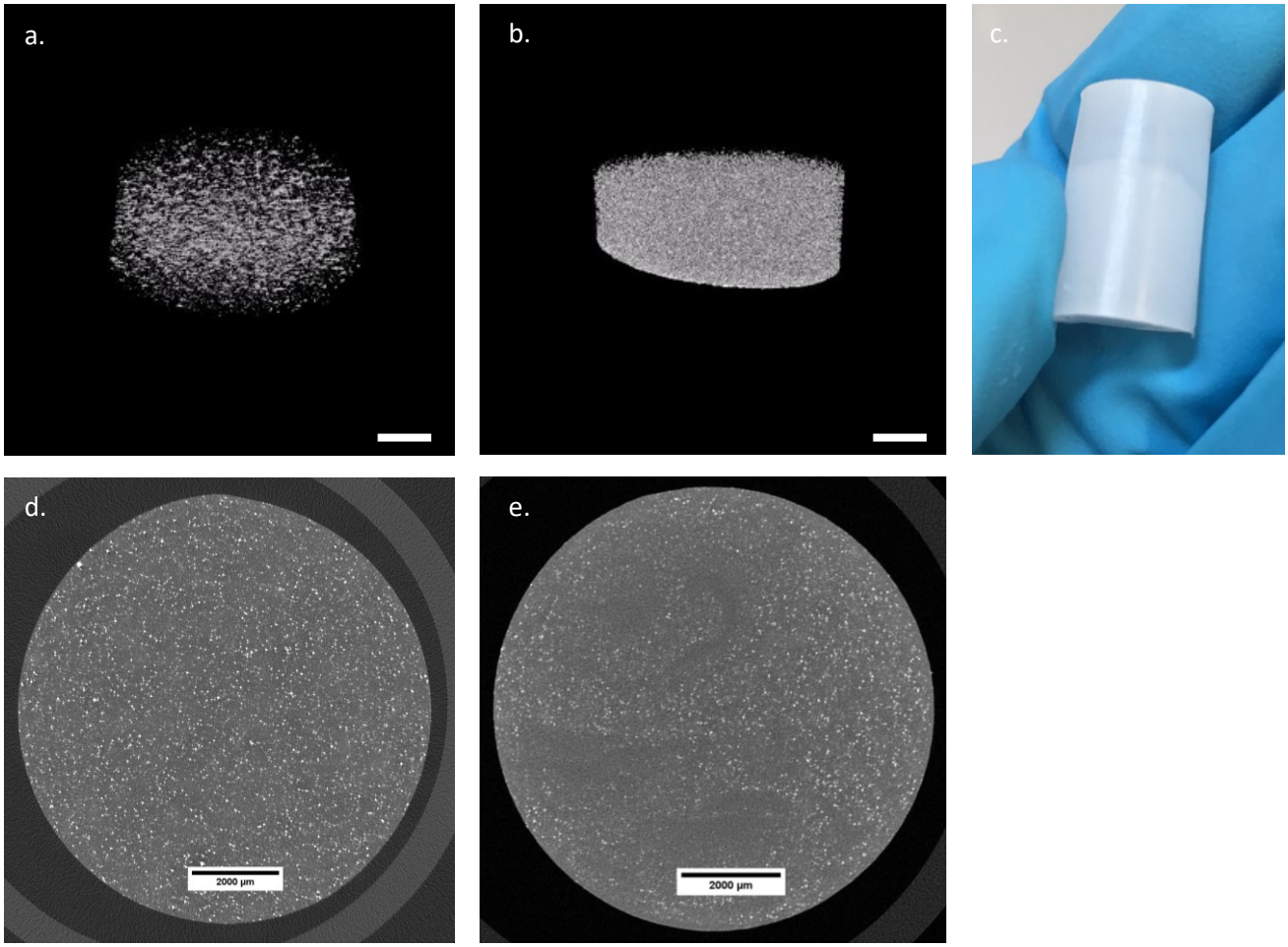

Figure 4.15: Micro-CT (3D combined image) of two concentrations of ZrO_2 in hybrid sol at **a.** 2 mg mL^{-1} and **b.** 10 mg mL^{-1}, scale bar = 2 mm. **c.** Photograph of a Si2.5-PTHF/Si7.5-PTHF cylinder with ZrO_2 incorporated. Micro-CT slices at zero strain in: **d.** top half (Si2.5-PTHF) of the cylinder and **e.** bottom half (Si7.5-PTHF) of the cylinder.

Optimisation of DVC

The pattern achieved with ZrO_2 particles is shown in the micro-CT image in Figure 4.16a, with an inset showing the box size used for tracking (cube side length is 492 µm = 64 pixels). The type of tracking (DC, FFT, FFT+DC) was optimised at two different subset (box/voxel) sizes of side length 64 and 112 pixels, from which FFT+DC gave the lowest error in the strain accuracy (Figure 4.16b). Strain accuracy refers to the average in the strain measured and its standard deviation, over the unloaded zero strain

scans. Then, considering only the FFT+DC tracking method, the overlap of voxels was trialled at 0, 50 and 75 %. Overlapping improved spatial resolution without decreasing the size of the voxels (which would otherwise increase the error), however 75% overlap increased the error in the strain and increased the number voxels by around 10 times, requiring much greater computation. Therefore the 50% overlap was chosen as the best compromise (Figure 4.16c.).

The subset size was optimised using 50% overlap and FFT+DC tracking at cube side lengths of 16, 32, 64, 112, 224 pixels. Decreasing the subset size improves the spatial resolution but the error in the strain measured increases. Therefore 64 pixels was chosen as the smallest subset size without significant increase in error (Figure 4.16d).

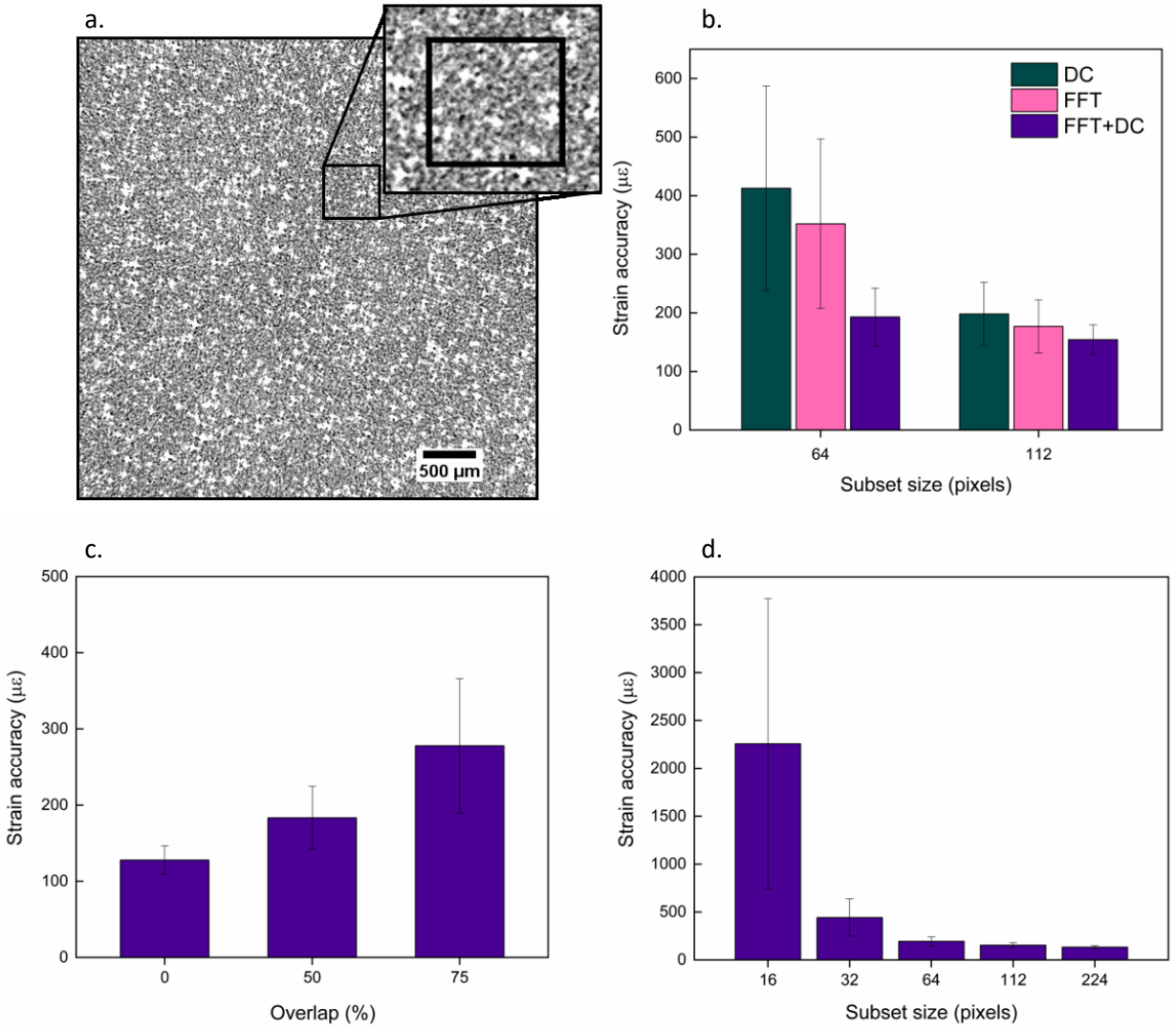

Figure 4.16: a. Micro-CT image of pattern produced in Si2.5-PTHF hybrid by addition of ZrO_2 particles, with inset showing the DVC subset size: cube of side length 492 µm = 64 pixels. **b.** DVC optimisation of the method used: FFT+DC was selected. **c.** Optimisation of the overlap of the voxels, from which 50% was selected. **d.** Optimisation of the subset size of which 64 gave the best compromise of accuracy and spatial resolution.

DVC of two-phase cylinder

Correlation between boxes can be lost when the sample is load, for example by distortion of the dots themselves (which should not occur here) but also by distortion of the pattern inside an individual box. In other words, high strains not only move the pattern but additionally causes the dots to not move uniformly relative to one another inside an individual box. This led to a loss of correlation when under load, particularly at high strains, leading to DVC measuring non-existent strains in the material. This was checked by increasing the box size (which decreases the error but loses spatial resolution) to ensure that the strain measured was consistent.

Figure 4.17a-c show the micro-CT image of the whole cylinder at 0, 10 and 20% nominal strain, of which a central portion was analysed by DVC to avoid edge effects (total cylinder width = 9 mm). The first thing to note is that the interface was not horizontal across the sample: rather it dropped at the edges, which may be a consequence of the surface of the first hybrid added to the mould having some affinity to the mould surface. Figure 4.17b and Figure 4.17c also show the progressive barrelling of the less stiff phase.

The DVC data shows a complicated strain map at both strains. Figure 4.17d and Figure 4.17e show the strain in the vertical direction parallel to the applied force at 10 and 20% nominal strain respectively. The bottom stiffer half shows between 0 and -0.05 strain, as expected as the stiffness was much greater than the top half which had lower silica content. Going up from the bottom half, across the join interface, the strain gets more compressive (negative) close to the interface, consistent with what was seen with DIC on vertical compression test (Figure 4.13). However, after this, the strain map is not straightforward to relate to the DIC experiment. Moving upwards away from the interface, there is a region of tension, then a region in compression before finally the contact with the platen (this shows up in red at the top of both strain maps). The maps are consistent between the 10% and 20% strain conditions with more negative compressive strain readings in those areas that show compressive strain.

The unexpected strain distribution could be a result of one or more of the following causes. Firstly, the platen used for loading the sample was not completely flat, due to the constraints of the design of the rig to fit inside the Micro-CT. This creates an uneven loading scenario at the top surface and may mean that one side of the cylinder was under greater load than the other side. Secondly, the samples showed significant extrusion perpendicular to the applied force. As a result, the strain in the less stiff phase was much more complicated than the expected: compressive strain only in the less stiff (Si2.5-PTHF) region, greatest close to the interface, and close to zero strain in the Si7.5-PTHF region.

Therefore, this requires further work to understand the strain distribution through the sample and indicates that the interface is not a straight line through the sample. Improved understanding of the synthesis procedure and viscosity of the sol are required.

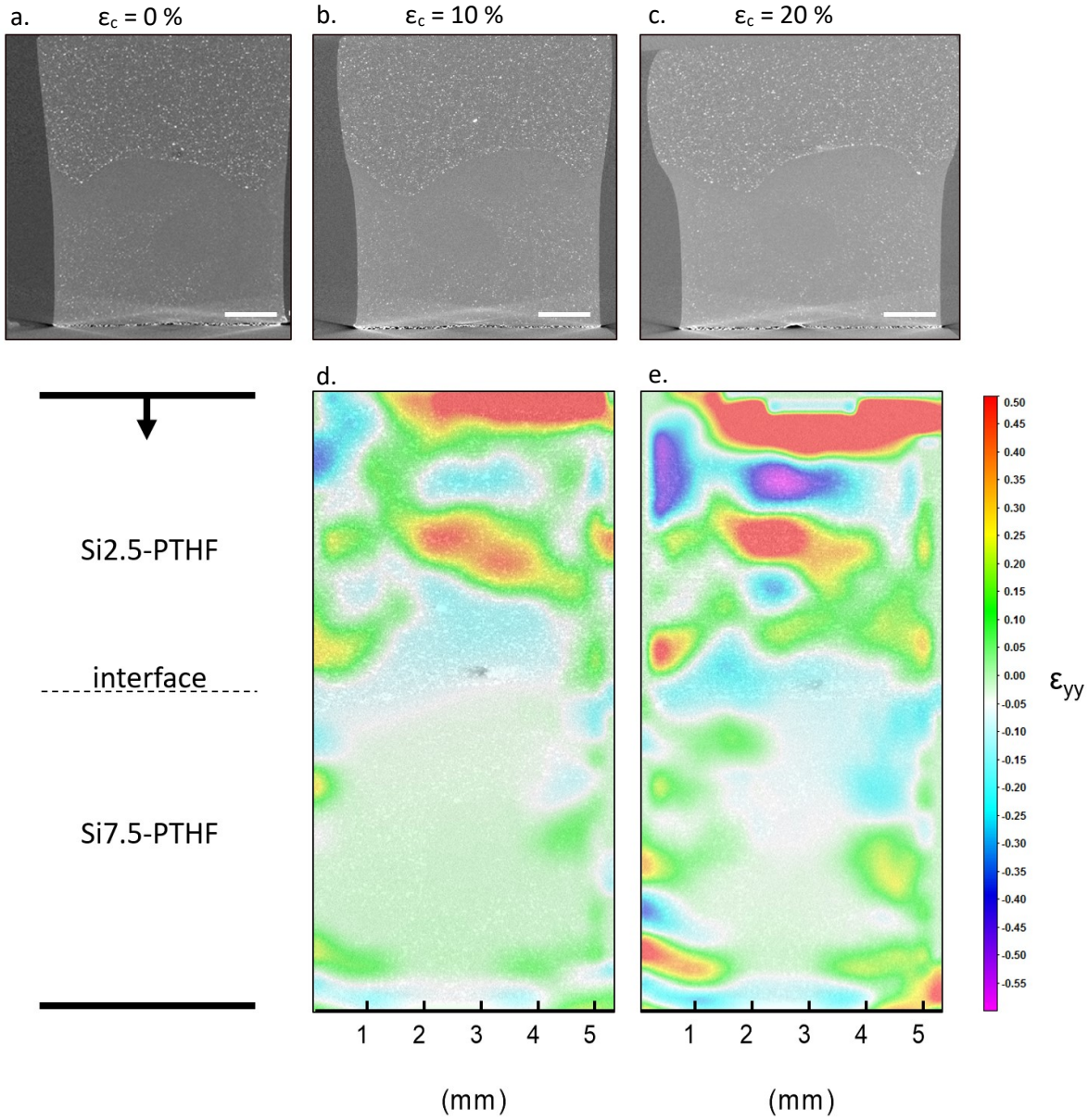

Figure 4.17: Micro-CT images of Si2.5-PTHF/Si7.5-PTHF with 2 mg mL^{-1} ZrO_2 particle incorporation at **a.** zero strain, **b.** 10 % and **c.** 20 % nominal strain (scale bar = 2 cm), along with the DVC maps of the strain in the horizontal direction (long axis of the cylinder) at **d.** 10 % and **e.** 20 % nominal strain in the centre of the cylinder (total width = 9.04 mm). The labels indicate the movement of the platen (arrow), the hybrid compositions and approximate position of the interface in **d.** and **e.**

This is an innovative approach to try to characterise multi-phase hybrids: ZrO_2 incorporation gives a successful technique for formation of a pattern for DVC tracking in Micro-CT that could be used in conjunction with the work in the next chapter on device development to understand the 3D strain in an IVD replacement device, comparing with the same experiment in human IVDs.

4.4 Conclusions

The tuneable properties of the hybrid system along with its gradual gelation period were employed together to produce multiphase hybrids with a variation in silica content, and therefore stiffness, through a single specimen. It was possible to join SiO_2-PTHF hybrids at any time up to 3 days ageing, after which the shrinkage of the hybrid led to internal stress of samples. Over the height of a 15 mm cylinder, the maximum difference in inorganic content produced was 6 to 42 wt.% SiO_2 which corresponds to a 50 times difference in the stiffness at 10% strain of 4 to around 200 MPa.

Two-phase samples were formed using identical composition hybrids which allowed the isolation of the effect of the formation of the interface. In tension, samples formed at 2 hours ageing time were at least as strong as the single phase material. A strong bond is formed at the interface even at the 3 day ageing time, demonstrated by the fact that samples joined at 3 days ageing time failed more often away from the interface than at it in tension. There is the potential to extend this method of joining hybrids to other sol-gel hybrid systems that show a gradual gelation period.

Digital Image Correlation was used to map the strain concentration around the interface. Using a horizontal compression test with the interface parallel to the applied stress indicated that the difference in composition rather than the formation of an interface itself led to strain concentration at the interface. There was lower strain concentration at the interface for samples joined at 2 hours ageing time than 1 or 3 days, consistent with the results from tensile testing.

A technique was developed to incorporate zirconia particles into the hybrid material that were used in Micro-CT imaging under load with Digital Volume Correlation to map the 3D strain through a two-phase sample. This method could be used in combination with the steps towards device development set out in the next chapter, in order to image the strain throughout a 3D device.

Chapter 5

Development of 3D SiO_2-PTHF structures

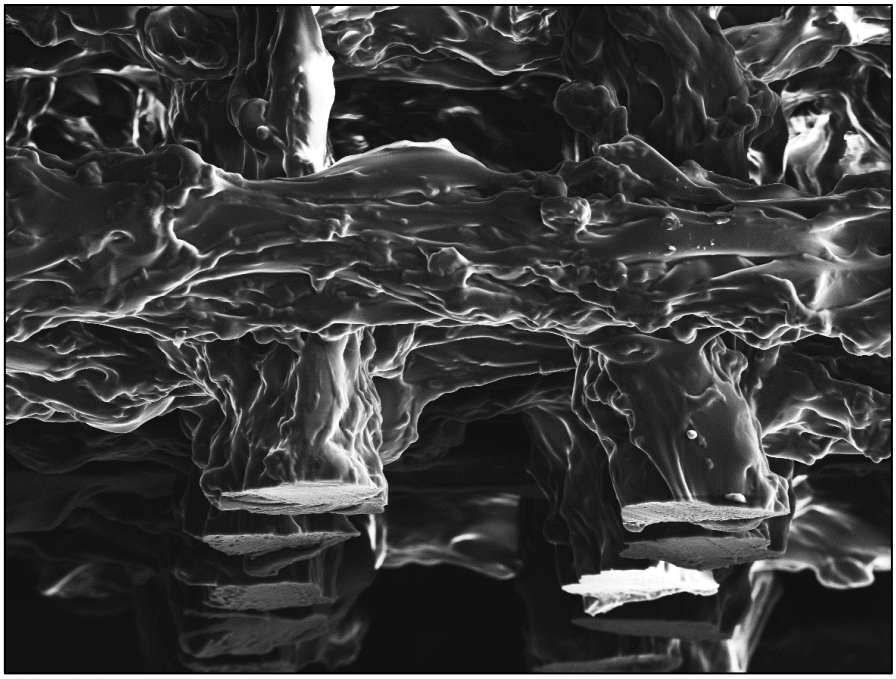

5.1 Introduction

SiO_2-PTHF hybrids form by a gradual gelation, during which polymerisation continues. This gelation period can be used as a window for additive manufacturing, during which the gel can be extruded through a syringe but will hold its own weight and form after extrusion. Importantly, as a subsequent layer is deposited on top of the previous layer, the layers can merge and continue to gel so that no interface between them is visible. After printing, the material can be dried to remove the remaining THF solvent.

The aim of this chapter is the optimisation of the additive manufacturing (3D printing) of the hybrid, with the intention to use it as a scaffold for cartilage or bone ingrowth. The scaffold could be joined to a bulk monolithic hybrid in the same way as multiphase hybrids were formed in Chapter 4. An example could be the addition of porous regions to the top and bottom of the IVD hybrid device to create surfaces that can bond with adjacent vertebrae or cartilaginous end-plates in the spine for IVD replacement. The material is not biodegradable, which may seem counter to the approach of tissue regeneration. However, there are many applications for devices that require fixation to host bone, for instance the integration of a prosthetic limb following amputation or blast injury. A hybrid could provide a lower stiffness device relative to porous titanium. A non-degradable scaffold may also be an intermediate step in the development and marketing of a degradable scaffold of similar composition for cartilage regeneration.

This chapter will also consider the possibility of forming a device by casting into a closed mould to form a bulk 3D structure. Two devices were investigated: 1. a meniscus; 2. an IVD. For the meniscus, the objectives were to: optimise the casting and mould production for a device that can mimic the stiffness gradient of a natural meniscus; investigate the surface roughness and shrinkage of the hybrid in a 3D mould; and preliminary compression testing of the resultant device. To simulate the compression on the meniscus from the femur, a bespoke platen was designed to match the top surface of the hybrid meniscus.

A hybrid intervertebral disc was formed by the same moulding technique and tested, in collaboration with the Biomechanics group, Department of Mechanical Engineering, Imperial College London, against human intervertebral discs in the same loading conditions. To imitate the structure of a natural intervertebral disc, the hybrids with different composition must be joined concentrically, to provide a radial variation in stiffness, combining the work of this and Chapter 4.

MEng student Toby Simpson conducted the injectability tests under supervision of myself and Dr Francesca Tallia. MSc student Manishankar Chellappan worked on the optimisation of the printing parameters under my direct supervision. Development of a meniscus sample was performed by MSc student Seyed Ataollah Naghavi under my direct supervision along with that of Jeff Clark. Testing in comparison with human IVD samples was done with Jeff Clark, Dr Nic Newell and Saman Tavana, in the Department of Mechanical Engineering, Imperial College London.

5.2 Methods

The overall aim to produce a printable hybrid ink, in the transition between a viscous sol and forming gel, was broken down into two stages. Firstly, injectability testing was used as a simulation of printing, to meet objectives to a) determine the maximum freezing time of syringes before printing, b) the "hold time" between removal of the syringe from the freezer and beginning to print, and c) the "printing window" which is the length of time between beginning to print and the ink becoming over gelled (*i.e.* the length of printing time). Secondly, trial and error optimisation of the synthesis and printing parameters were used to optimise the ink for 3D printing. Herein, the synthesis of ink for both parts is covered together, followed by separate discussion of the injectability testing and printing procedures.

5.2.1 Synthesis of hybrid ink

The first objective was to produce an ink which is printable, meaning it is possible to both extrude the ink and for it to maintain its form and hold the weight of subsequent printed layers. A significantly more gelled hybrid sol is required than that added to moulds in the production of bulk hybrids (Chapter 3). A hybrid ink was first produced for injectability testing, with no access to the printer, and subsequently optimised for 3D printing. Thus, the final synthesis procedure used to fabricate scaffolds differed from that initially used to make ink for injectability testing. The final synthesis procedure is set out here, with the differences highlighted in Figure 5.1. The printability of the hybrid inks depended on the "interval time," which is the time elapsed after the addition of the $BF_3{\cdot}O(C_2H_5)_2$ catalyst and until the hydrolysed TEOS is added, and the subsequent mixing time, which is the time elapsed after addition of the hydrolysed TEOS until the ink is added to printing syringes.

Hybrid ink for 3D printing was synthesised by the same procedure as bulk hybrids (Section 3.2.1) using the molar ratios and typical quantities set out in Table 5.1, but with different interval and mixing times. THF/GPTMS ratio was reduced with respect to that used for bulk hybrid fabrication, from 100 to 80, to reduce the evaporation of THF. TEOS/GPTMS ratio was varied in the printing optimisation and will be discussed in Section 5.3.2.

Table 5.1: Molar ratios and typical synthesis quantities used to synthesis hybrid inks, where *x* is the moles of TEOS and *a* is the moles of GPTMS.

Reagent	Molar ratio	Typical quantity (mL)
GPTMS	a	1.33
$BF_3{\cdot}O(C_2H_5)_2$	0.25*a*	0.185
THF	80*a*	38.9
TEOS	$x = 5a$	6.70
H_2O	$3a + 4x$	2.48
1M HCl	(1/3 volume of H_2O)	0.83

For the first part of this chapter on injectability testing (Section 5.2.2), the ink was left to stir in an open pot to further evaporate THF, continuing the gelation process until the ink was sufficiently viscous for printing. This viscosity was termed the 'threading point:' a hybrid gel had sufficient viscosity such that when a pipette of gel is pulled from the pot, a continuous filament formed between the end of the pipette and the sol, as shown in Figure 5.1a.

Conversely, for 3D printing, the ink was left to stir in an open pot for a longer time period of 1-2 hours and did not reach this threading point before addition of the ink to the syringe, because of the change in the synthesis procedure (Figure 5.1b). This procedure was a result of trial and error in printing and will be discussed in Section 5.3.2.

Hybrid sol-gel "ink" was placed into a capped 3 mL Luer-lock syringe (VWR, UK), sealed with parafilm and foil, and stored at -80°C, so as to reduce the speed of the gelation process as well as the evaporation of THF. However, since the freezing point of THF is -108°C we hypothesised that the gelation and evaporation continued at -80°C at a much slower rate. The effect of freezing time was investigated using injectability tests.

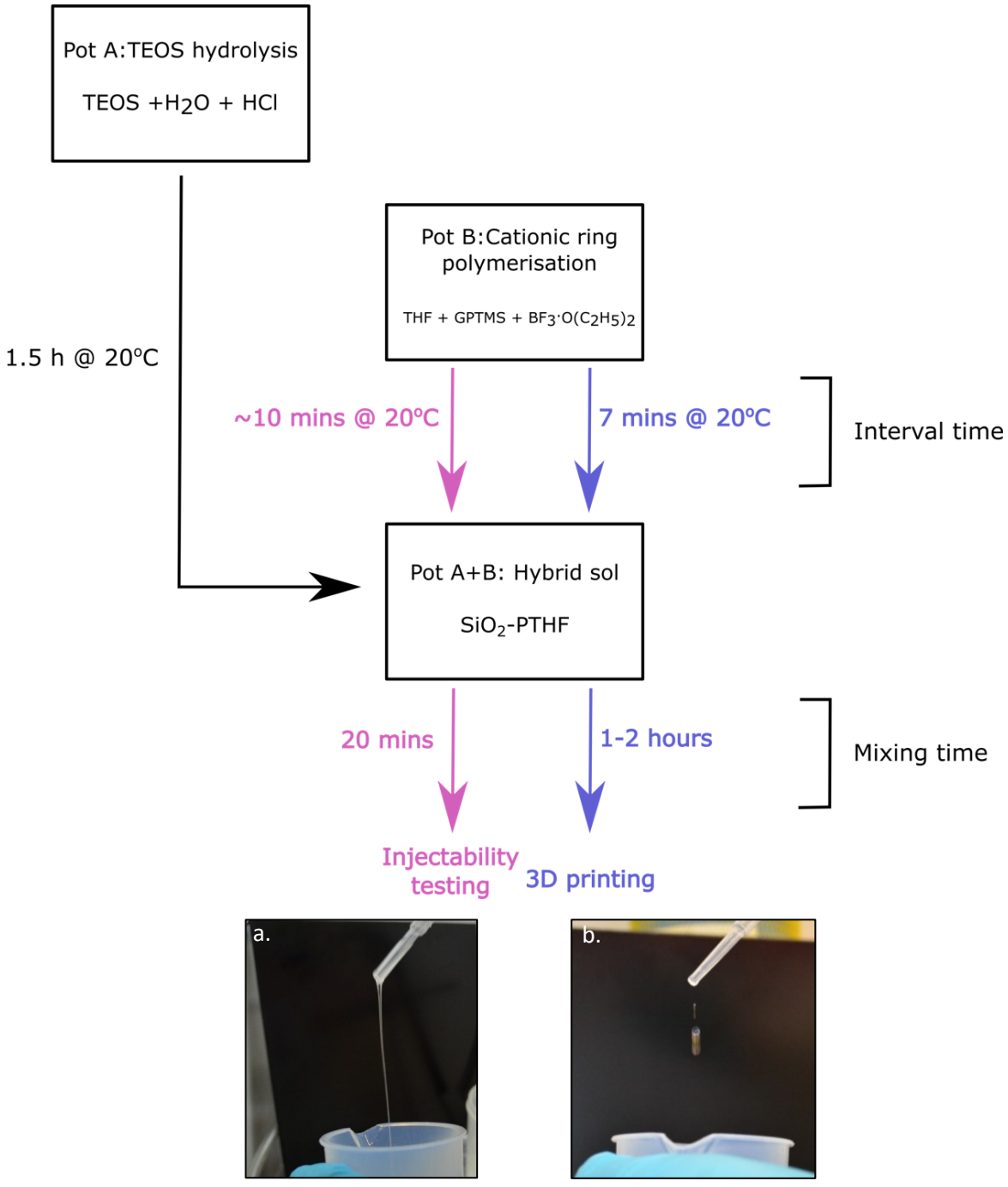

Figure 5.1: Synthesis protocol highlighting the differences in interval and mixing times when making the ink for injectability testing and 3D printing, along with photographs of **a.** Hybrid solution at the threading point, forming a continuous filament to the pot, the point at which the ink was added to syringes for injectability testing, and **b.** droplets of the less gelled condition of the hybrid solution at which ink was added to syringes for 3D printing.

5.2.2 Injectability testing

The objective of this work was to define a set period in the gelation of the hybrid at which the ink was printable, comprising of the hold time between removal from the freezer and beginning printing, and the subsequent printing time ("printing window"), relating this to the force required to extrude the ink. This was then used to investigate the limit in the freezing time for syringes.

Printing window

The viscosity of the ink increased with time as the polymerisation progressed and THF evaporation occurred. In order to successfully print, it must be possible to extrude the ink from the syringe, and the ink must also be sufficiently viscous to maintain the printed structure and support the weight of additional layers. This range of printable viscosities corresponds to a range of time in the gelation of the ink (printing window). In reality, this can also be affected by other variations in the synthesis procedure, but in this section it will refer to the time since defrosting for syringes that have been frozen with the ink at "threading point" in gelation stage, defined in Section 5.2.1.

Injectability test set up

Injectability testing was done by MEng student Toby Simpson and under supervision by myself and Dr Francesca Tallia. The objective was to define a printing window and determine the maximum freezing time at -80^{o}C. It was not possible to directly measure the viscosity of the ink in a rheometer due to its corrosive properties and the fact that the gelation rate will be increased by exposing a large surface area to the air (compared to a closed syringe), due to the increased evaporation of THF on the gelation rate. Thus, the injectability test was used as an indirect measurement, in the set up shown in Figure 5.2, in which the syringe was aligned vertically in the holder and compressed at a fixed displacement rate whilst measuring the force required. The displacement rate of 0.72 mm min^{-1} was calculated according to Equation 5.2, as that used during robocasting following the initial printing parameters as used by Dr Tallia [110] and the test was run until the force reached a plateau. This set up follows Franco *et al.* as a model for the extrusion of inks during robocasting [167]. A Zwick testing machine was used with 10 kN load cell, in displacement control.

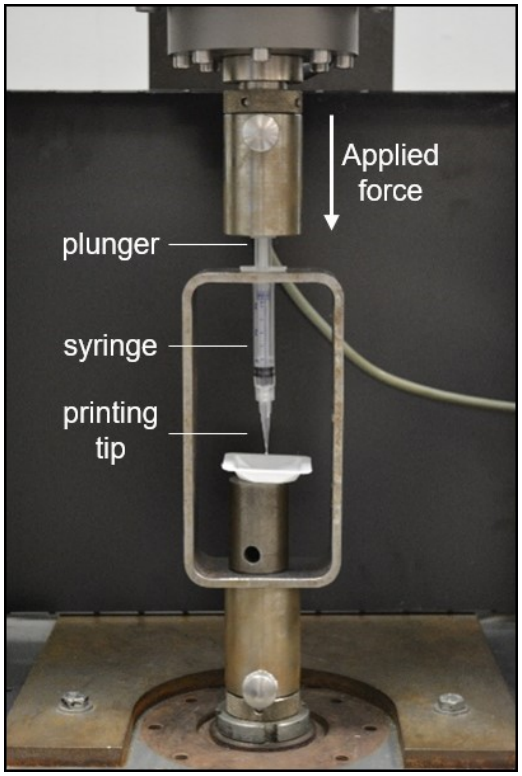

Figure 5.2: Injectability test set up. The force required to move the crosshead at 0.72 mm min^{-1}, extruding the syringe, was measured until the force reaches a plateau.

The extrusion ratio is an area ratio between the syringe (diameter = ϕ_s) and the tip (diameter = ϕ_t), Equation 5.1. For the robocaster set up, the required pressure is applied based on the inputted ϕ_t and printing speed, which are the only variables that can be inputted to the software (from which the software then calculates the required printing pressure). Therefore, if increased extrusion pressure is required because of the nature of the ink, the only way to adjust this is by inputting a false larger ϕ_t to the software. In this case, to give sufficient extrusion pressure it was necessary to give the inputted value of the tip diameter as 0.33 mm, larger than the true value of 0.20 mm. ϕ_t was subsequently optimised for printing in Section 5.3.2.

$$Extrusion\ ratio, ER = \frac{\emptyset_t^2}{\emptyset_s^2} \qquad \text{Equation 5.1}$$

Inputting ϕ_s = 9.54 mm and ϕ_t = 0.33 mm into Equation 5.1 gives an extrusion ratio of 1.20 x 10^{-3}. For injectability testing, a displacement rate must be calculated for moving the syringe plunger. The equivalent displacement rate for the initial printing conditions was calculated by Equation 5.2, where the printing speed, $v_{printing}$ = 10 mm s^{-1}, as 1.20 x 10^{-2} mm s^{-1} = 0.72 mm min^{-1}. The initial printing speed

and tip diameter used were based on those chosen from the work of Tallia *et al.* on 3D printing of the SiO_2-PCL-PTHF system [12] and were then varied as described in Section 5.3.2.

$$Displacement\ rate, DR = ER\ \times\ v_{printing} \qquad \text{Equation 5.2}$$

To determine the volume printed in a given time, the deposition rate can be calculated via Equation 5.3 as 52 $mm^3\ min^{-1}$ = 0.052 ml min^{-1} (for ϕ_t = 0.33 mm and $v_{printing}$ = 10 mm s^{-1}). The total volume of the syringe is 3 mL so would take one hour to print, assuming continuous printing. This is important when considering the effect of holding time (time between removal of the syringe from the freezer and commencement of printing).

$$Deposition\ rate, VR = DR \times \pi \times \left(\frac{\phi_s}{2}\right)^2 = \frac{1}{4}\phi_t^2 \pi v_{printing} \qquad \text{Equation 5.3}$$

The extruded ink was collected and examined by eye and SEM to assess the filament quality. There was no account taken of the compliance of the plastic syringe itself but this was constant between all tests.

Effect of hold time

Injectability tests were done on the same ink, frozen for 3 days at -80°C before testing, at zero hour and three hours after removal from the freezer (0 to 3 hour 'hold time') to investigate the rate of increase in the injectability force with time, as the ink gels. This linked the injectability force at zero hours with the time taken for the ink to become printable.

To investigate the printing window continuously over a period of 40 minutes, a stepwise test was used in which the strain was increased by 1.44 mm over 2 minutes (displacement rate = 0.72 mm min^{-1}) followed by a hold of 4 minutes before the next step, as shown in Figure 5.3. This test was run over 40 minutes, which gives a total extruded volume of 2.08 mL (extrusion rate = 0.052 mL min^{-1}), below the 3 mL capacity of the syringe. SEM imaging of the filament produced at different times over the test linked the strut morphology with the printability.

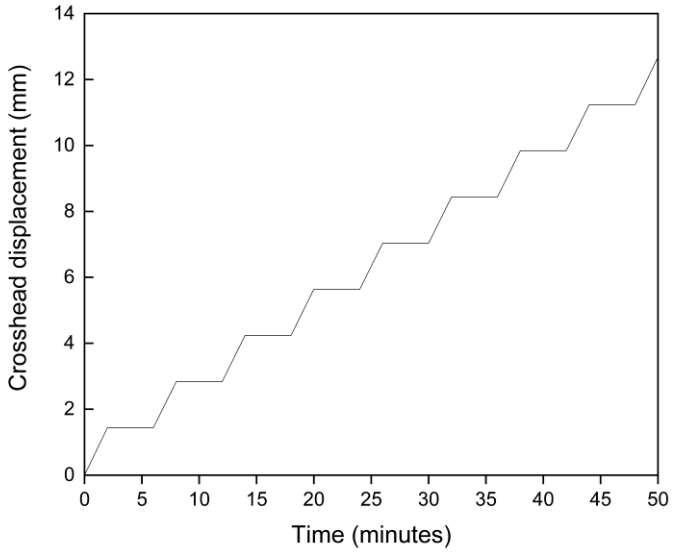

Figure 5.3: Stepwise injectability testing. Each 6 minute cycle consisted of 2 minutes of compression at 0.72 mm min^{-1} followed by 4 minute hold. The force applied to achieve this displacement of the syringe plunger was measured.

Effect of freezing time

Freezing the inks is a practical solution to allow batches of syringes to be produced from a single synthesis and printed at different times. A batch of syringes was frozen from a single synthesis and the injection force measured after they were frozen for one day (19-20 hours), 15 days (353-354 hours) and 29 days (690-692 hours). The force was measured as soon as the ink had defrosted to investigate the effect of prolonged freezing at -80°C and to determine the standard procedure for storing of inks. This also investigated whether the gelation process (polymerisation and evaporation of THF) was ongoing at -80°C.

Effect of interval time

Subsequently to the injectability testing, it was found that inks produced in this way using a longer (9 minutes or more) interval time and freezing at the threading point did not produce ink with good printability. The practical printing window was very small with the ink quickly become over gelled. Therefore, the synthesis method was altered to use a shorted interval time of 7 minutes and longer mixing time of at least 1 hour before ink was added to syringes. The differences in the synthesis procedures were highlighted in Figure 5.1.

5.2.3 Scaffold fabrication

3D printing

Hybrid inks were synthesised as set out in Section 5.2.1 from the Si5-PTHF composition, using a 7 minute interval time and minimum 1 hour stirring of the hybrid sol before adding to syringes. The syringes were stored at -80°C for a maximum of 3 days before printing. After removal from -80°C freezer, syringes were left for between 1 and 6 hours until they reached the required viscosity for printing.

Robocad software (3D Inks LLC, USA) was used for scaffold design, producing CAD files that were robotically deposited using a Robocaster (3D inks LLC, USA). The aligned pore 3D lattice structure was kept constant, based on previous work [12] indicating that this promotes tissue ingrowth and vascularisation. The lattice was printed with a continuous filament with subsequent layers at 0° and 90°. The initial intention was to produce channel sizes of 200 µm, as discussed in Section 1.5, however the optimisation of the printing procedure was done to create a 40-layer scaffold in the first instance, which required increase of the channel size.

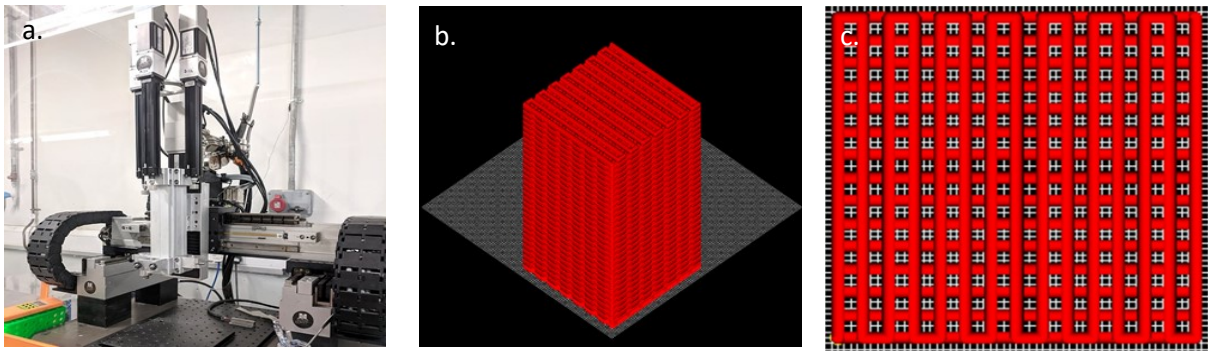

Figure 5.4: a. Robocaster, **b.** iso view of 40-layer scaffold, and **c.** top view of the scaffold pattern showing the aligned lattice structure.

Printing parameters

Optimisation of the printing parameters was conducted with MSc student Manishankar Chellappan. Variable parameters were flow rate, printing speed, z-spacing (height distance between subsequent layers), road width (width distance between centre of adjacent struts on the x-y plane lateral a of the lattice). The ranges used for different groups of syntheses in the optimisation process are set out in Table 5.2. Table 5.3 gives the staggered z-spacing used in Group C. These were controlled by direct input into the Robocad software except the flow rate which is indirectly controlled via changing the inputted value for the printing tip size. Tips of diameter 0.20 mm (Nordson EFD, UK) were used and the scaffold was printed onto the paper side of a secured sheet of parafilm.

Table 5.2: Printing parameters used in different synthesis groups during optimisation process. * refers to staggered z-spacing

Group	Flow rate (mL min^{-1})	z-spacing (mm)	Speed (mm s^{-1})	Road width (mm)
A	0.031	0.21	10	0.6
B	0.031	0.21-0.24	6-10	0.6-1
C	0.031	0.24, 0.24-0.32*	7-9	0.75

Scaffold ageing and drying followed the same procedure as for bulk samples (Section 3.3.3): sealed at 40°C for 3 days, followed by gradual opening over 1 week to prevent sudden evaporation of the solvent and damage to the scaffold. Scaffolds were then dried for a further week in open pots and stored at 40°C prior to mechanical testing.

Table 5.3: System of staggered z spacing to counteract spreading of the solution and tip crashing

z-spacing (mm)	Layer number
0.24	0-7
0.26	8-15
0.28	16-23
0.30	24-31
0.32	32-40
	Total 40 layers

5.2.4 Scaffold characterisation

Inorganic/organic ratio

The final silica content was determined by TGA as for the bulk hybrid samples (Section 3.2.1).

Compressive testing to failure

Uniaxial compression testing of scaffolds was carried out on Bose Electroforce Series III machine with load cell of 450 N, in displacement control at 0.5 mm min^{-1}. Scaffolds were cut into cubes of approximately 5 x 5 x 5 mm and measured prior to testing. True stress and strain (σ^*, ε^*) were calculated according to Equations 2.4 and 2.5 and five scaffolds were tested.

The stiffness of the scaffolds was calculated at 10% true strain as the tangent to the curve at this point, and failure was determined as the first cracking, from which maximum compressive strength is calculated. The mean and standard deviation from five tests was calculated.

Dynamic Mechanical Analysis

DMA was conducted as described in Section 2.4.2, at 3 frequencies (0.1, 1 and 10 Hz) and over 3 different compressive strain ranges (ε = 1 to 5%, 5 to 9 % and 9 to 13 %). One scaffold was tested as a preliminary investigation.

Imaging

Samples were coated with 30 nm chromium and imaged in JEOL JS-6010LA scanning electron microscope. Scaffolds were sectioned by cutting with a razor blade in the horizontal and vertical direction for SEM imaging of the internal surfaces as well as the top surface as printed. ImageJ [141] was used to determine the average channel size in the horizontal cross section.

5.2.5 Moulding a meniscus

Design and testing of a hybrid meniscus was conducted by MSc student Seyed Ataollah Naghavi under direct supervision by myself and Jeff Clark. The objective was to investigate whether it was possible to form a 3D moulded structure as the first step towards a cartilage replacement implant. It was hypothesised that introducing a complex mould profile may affect the shrinkage or lead to uneven shrinkage of the hybrid gel, therefore the first mould produced was straight mould with cross-section shape based on the natural meniscus. Two pins were added to allow addition of hybrid solution and escape of air.

The next iteration of design was a curved hemispherical meniscus with 3D profile (shaped on top and bottom halves of the mould). The shrinkage was measured in 6 directions and the surface roughness was measured on each of the 4 surfaces.

Moulds were designed using Solid Works (resolution tolerance = 0.5 degrees and deviation of 0.007 mm) and manufactured by CNC drilling with a path interval of 0.01 mm into PTFE blocks supplied by Cowie Technology UK. Roughness measurement were carried out by White Light Interferometry (WLIF) (Vecco instruments, NY, USA) with Vision for Profilers software.

Mechanical testing

For mechanical testing, a steel platen was designed with the inverse curvature of the hybrid meniscus sample, taken from a 3D scan of the sample. The aim was to simulate the compression from the end of the femur, with the contact area equal to the top surface area of the meniscus. The platen was machined from stainless steel by Mr Russell J Stracey (Imperial College London). Cyclic compression was conducted to 10 cycles at a rate of 10 mm min^{-1} and 10 N preload. Then the same sample was tested in compression to failure at a rate of 1 mm min^{-1}.

The two end surfaces of the hybrid meniscus were patterned using ink pen and photographs were taken every second of the testing for use in Digital Image Correlation, DIC (as for Section 4.3.5). The camera was positioned opposite to the two end surfaces as shown in Figure 5.5.

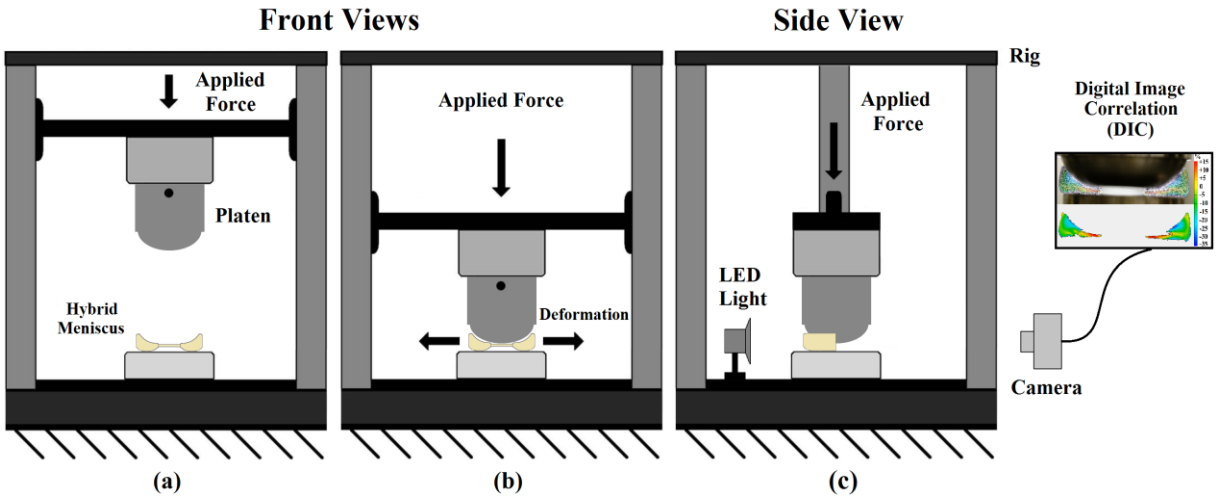

Figure 5.5: Schematic of the compression rig for testing the artificial meniscus: (a) before applying the load, (b) after applying the load, (c) side view. Schematic drawn by Seyed Ataollah Naghavi.

5.2.6 Hybrid IVD device

One of the challenges in comparing mechanical properties of biomaterials with the natural tissue or structures they would like to simulate is testing both in the same conditions. To attempt to do this, a collaboration was begun with Jeff Clark, Saman Tavana and Dr. Nic Newell in Biomechanics, Imperial College London, following their work on mechanical testing and imaging of human IVDs [168, 169].

A mould was designed to the average dimensions of the human intervertebral discs that they tested, in an idealised ellipse shape and increased by a factor of 1.5 to account for shrinkage (as calculated in Section 3.3.2, shown in Figure 5.6. The mould was produced by CNC milling with the same settings as for the meniscus mould (Section 5.2.5). The height of the sample was variable by the depth filled in the mould, targeted to produce a final sample height of 10.4 mm.

Mechanical testing

To compare directly with the mechanical properties of human IVD, hybrid samples were tested with the same dimensions in identical test set up to that used by Newell *et al.* [31]. Samples were tested at strain rates of 0.01, 0.1 and 1 s^{-1} to 10% of their initial height on Instron 5565 testing machine (Instron Ltd., High Wycombe, UK) and strain measured using LVDTs (D6/05000ARA, RDP Electronics Ltd., Wolverhampton, UK) fitted with an in-line 10V amplifier (E747, RDP Electronics Ltd., Wolverhampton, UK). Samples were ground with sandpaper to flatten the top surface before testing.

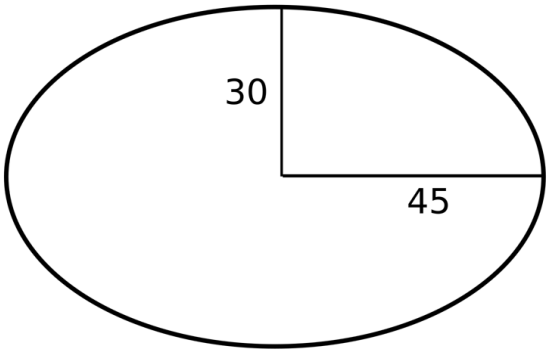

Figure 5.6: Dimensions of IVD mould, scaled to 1.5 times the desired dimensions to account for shrinkage. Units = mm

5.3 Results and discussion

5.3.1 Injectability tests

Definition of printing window

The printing window refers to a period in the gelation of the ink during which it can be successfully printed. Before this time the ink is not sufficiently gelled and will not hold its form after extrusion (under gelled), and after this time the ink will be too gelled for extrusion leading to an uneven, lumpy filament and deformation of the syringe (over gelled). Without a defined printing window, it is necessary to test the printability of each syringe at regular time intervals, wasting ink and potentially altering the progress of the hybrid gelation as large forces are passed through the syringe which can shear the gel (it was noticed that inks that were repeatedly tested at the printer never reached good printability).

However, the definition of a printing window is complicated by the nature of the living polymerisation and lack of precise control of the reaction. A small change in the synthesis procedure, e.g. a shorter interval time, can lead to a large change in the gelation time and printing window. This is discussed further in relation to actual 3D printing in Section 5.3.2. The first conclusion from this work was that this window cannot be specified without further control of the polymerisation. Following this realisation, the next stage was to work backwards from achieving a printable ink to determine the ideal synthesis parameters.

A crosshead displacement of 0.72 mm min^{-1} was calculated from the initial printing parameters in Section 5.2.2. If the ink extruded from the syringe at 0.72 mm min^{-1} produced an even filament that retains its shape, the ink was considered “printable”. Over a range of syntheses, the force required to achieve 0.72 mm min^{-1} was 10-60 N when the ink was deemed printable. This is consistent with the force required for injection of other inks for 3D printing [135].

Effect of hold time

Hold time was defined as the time period between the removal of the syringe from the freezer to the time of printing. Hybrid ink was added to the syringes at a series of five minutes intervals after the threading point was reached (A = 5, B = 10, C = 15, D = 20 minutes after). The ink defrosted quickly after removal from the freezer and was fully liquid after around 5 minutes. When held at room temperature, the gelation continued at an appreciable rate, meaning that the injectability force required to give a displacement rate of 0.72 mm min^{-1} increased as hold time increased. In fact, after 3 hours hold time, the force did not reach a plateau as the solution was over gelled. The force kept increasing and finally resulted in deformation of the syringe itself.

Figure 5.7 shows the injectability force at 0 hour hold and 3 hour hold for syringes filled at five minute intervals after the threading point. No difference was seen in the behaviour of inks added to syringes at 5-20 minutes after threading (A-D) at 0 hours or 3 hours (curves overlap), therefore the moment of putting ink into syringes is not an important factor in their printability, in the range of 0 – 20 minutes post threading point. The force required increased by around three times from 0 hour to 3 hours hold, however never reaches a plateau at 3 hour hold time.

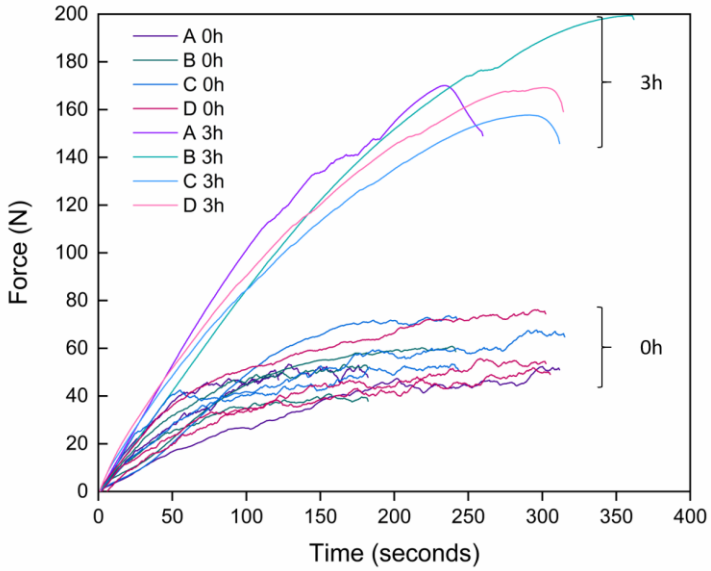

Figure 5.7: Injectability force required to achieve a crosshead displacement rate of 0.72 mm min^{-1} at 0 hour hold time (immediately on defrosting) and after three hours at room temperature for syringes from one synthesis that had been frozen for 3 days. The labels A, B, C, D refer to the order that hybrid sol was added to the syringes before freezing, at five minute intervals (A = 5, B = 10, C = 15, D = 20 minutes after threading point), however there is no clear correlation between this and the injectability force.

The silica content of the ink extruded in the experiment in shown in Table 5.4, indicating a possible small increase in the inorganic component of the hybrid produced after the 3 hour hold time. This is consistent with the continued evaporation of THF during the hold period. However, the error in the TGA from repeat measurements was around ± 0.5 wt.% so further investigation would be needed to confirm this.

Table 5.4: Silica content of extruded ink at 0 hour and 3 hour hold times.

Syringe	wt.% SiO_2	
	0 h	**3 h**
A	21.2	21.7
B	21.4	21.5
C	21.0	21.7

Stepwise injectability testing

Running an injectability test over a longer time allows investigation of the gradual increase in the gelation, and thus the force required for extrusion, over time. To do this, a stepwise test was used with 2 minutes of displacement followed by a hold time of 4 minutes. The gap between steps was limited by the evaporation of THF at the tip of the syringe which can lead to blockages and a therefore a higher force reading. Measuring from the previous trough, the increase in force for each step increased from 6 N for the first cycle to 57 N for the eighth cycle at 42 minutes (Figure 5.8a). Observations of the filament (Figure 5.8b) produced showed that the ink was printable from the second cycle onwards, consistent with the 10-60 N printable range. The SEM of the filament (Figure 5.8c-e at around 10, 30 and 50 minutes respectively) shows an increase in the surface roughness of the filament over time. This could be due to the ink being more gelled as it is extruded and the higher forces at the tip, so the surface is distorted and holds the shape after extrusion. This test shows that the syringe remains printable for its entire volume (3 mL).

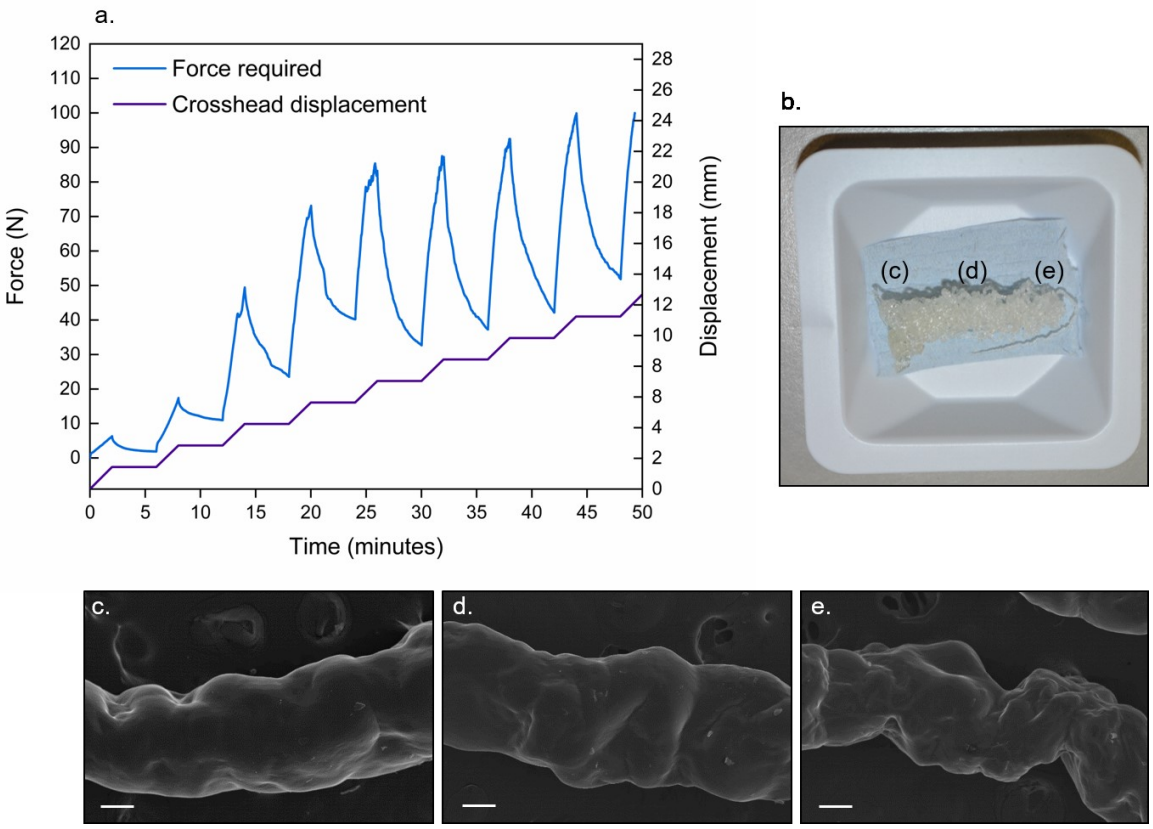

Figure 5.8: Stepwise injectability testing over 50 minutes. **a.** the measured force required for the displacement steps, **b.** the filament produced over the total time of the test and **c.**, **d.** and **e.** show SEM images of the filament at the points labelled, at around 10, 30 and 50 minutes respectively. Scale bar = 100 µm. The initial ink extruded did not retain the shape of the filament and therefore was not imaged.

Effect of freezing time

It is advantageous to be able to store syringes between synthesis and printing, so that multiple syringes can be filled in batches and printed at different time. The syringes were stored at -80°C, above the freezing point of THF (-108°C), so it was hypothesised that the gelation of the ink would continue but at a reduced rate. The effect of the time spent frozen at -80°C on the plateau force required to achieve 0.72 mm min^{-1} crosshead displacement (corresponding to the extrusion rate as calculated by Equation 5.1) is shown in Figure 5.9. After 15 days, the injection force increased by a factor of around five, increasing to seven after 29 days. This confirmed the continued gelation of the hybrid ink at -80°C and indicated that it was not possible to store the syringes for longer than approximately one week before printing. The printing window corresponds approximately to an injection force of 10-60 N (shown as a purple shaded region).

However, printing forces plotted in Figure 5.9 are those at 0 hour holding time. In order to print multiple scaffolds for a single syringe the printing force must stay within this range for the required time period. As an indication, the time to print a 40-layer scaffold is 15 minutes, so a one-hour printing window enables printing of four scaffolds. This means that the force required for extrusion needs to be below around 20 N at 0 hour, so that after 1 hour it is still below 60 N: the ink remains printable for the following hour. This reduces the ideal freezing time to a few days, assuming a linear interpolation.

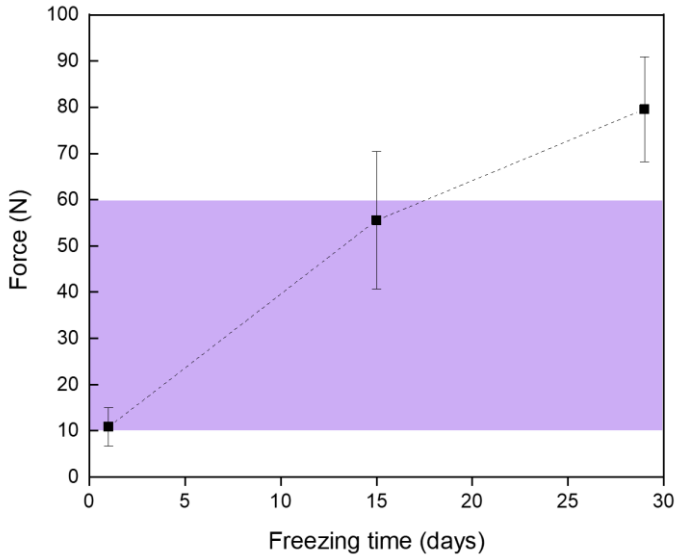

Figure 5.9: The injectability force required to give a crosshead displacement of 0.72 mm min^{-1} as a function of the freezing time of the syringe at -80°C. The purple box shows the estimated printable range of forces.

Mean and standard deviation of nine syringes were taken for each data point. All syringes came from the same synthesis for consistency and no variation was seen between syringes frozen at 0, 5 or 10 minutes after the threading point. The synthesis procedure for the hybrid inks differed between the injectability testing and the 3D printing. However, the results that: (1) a syringe is printable for 40 minutes continuously and (2) the syringes should be stored for a maximum of 3 days before printing, are still applicable.

5.3.2 Scaffold fabrication

When 3D printing, more information is available with which to optimise the printability. Injectability testing relies on the appearance of the extruded filament, whereas for 3D printing, the spreading of the ink after printing, the structural integrity of a multi-layer scaffold and the adhesion between subsequent layers must additionally be considered. In this section the optimisation was done by trial and error of layer-by-layer printing, which resulted in a change to the procedure for the synthesis of the hybrid ink and to the parameters for printing set up in the Robocaster.

Observations of synthesis

The initial composition of Si5-PTHF, following the initial synthesis method of reaching a threading point then adding the ink to a syringe, could not print more than a few layers before collapse. Si7.5-PTHF ink was fabricated to try and increase the structural integrity of the scaffold, however in this case the filaments were uneven and stretched to breaking apart in some places as shown in Figure 5.10a. The increased silica content meant the filaments had insufficiently elasticity for printing. Even though the Si5-PTHF has a lower silica content, there was still a problem with its printability (Figure 5.10b) as the ink was extruded in an uneven manner. This meant that although a the first few layers were printed well, there were lumps at certain points into which the tip subsequently crashed. Therefore, optimisation of the synthesis process was required to make this composition printable, rather than altering the composition.

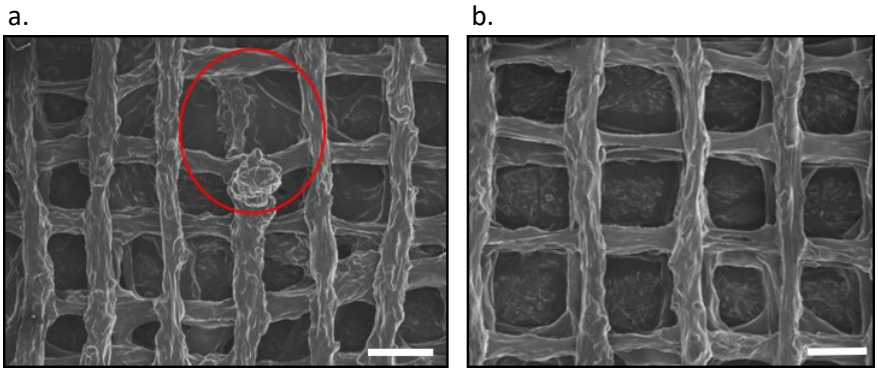

Figure 5.10: SEM of **a.** Si7.5-PTHF printed structure, showing over-stretched and uneven filaments which break up as highlighted, and **b.** Si5-PTHF with a more even structure (still with stretched filaments).

The interval time refers to the time elapsed between the addition of $BF_3{\cdot}O(C_2H_5)_2$ to catalyse the polymerisation, and the subsequent addition of hydrolysed TEOS. When the interval time was shortened during the synthesis, i.e. the hydrolysed TEOS was added earlier to the polymerisation, this resulted in longer mixing times, without ever reaching the point of threading (as was used in making ink for injectability testing) even after several hours under stirring. It was noticed that those inks with shortened interval times and longer mixing times resulted in improved printability, with an even extrusion of the ink. The relationship between interval times and mixing times is shown in Figure 5.11a, where all the syntheses had the same starting composition of Si5-PTHF.

If adding the hydrolysed TEOS earlier terminates chains in the polymerisation of THF, the consequence should be that less THF participates in the reaction and therefore a higher silica content should result from the use of a shorter interval time. Measuring the final inorganic content showed wt.% SiO_2 was increased as expected when interval time decrease from 9 to 7 minutes, starting from identical synthesis reagents, Figure 5.11b. This may be because a shorter interval time leads to a longer mixing time, implying a longer period of polymerisation and evaporation of THF, leading to better printability due to less shrinkage of the struts after extrusion. Therefore, it was decided to use a short 7 minute interval time for producing the ink.

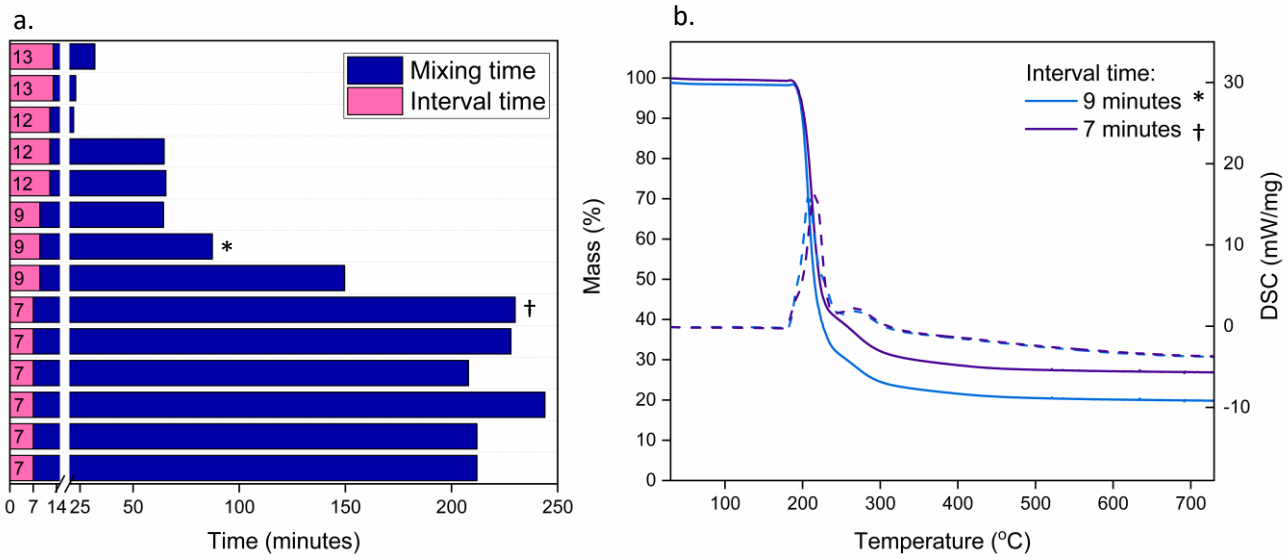

Figure 5.11: a. Variation in the interval time (listed along y axis) between addition of $BF_3{\cdot}O(C_2H_5)_2$ catalyst and the hydrolysed TEOS, with the subsequent mixing time taken before the hybrid sol is added to syringes. The end of the mixing time corresponds to the threading point except when the interval time was 7 minutes and in that case the sol never reached the threading point. **b.** TGA and DSC curve for two of the syntheses with interval times of 7 minutes (blue, †) and 9 minutes (purple, *). Reducing the interval time increases the final inorganic content of the printed scaffold from 21.4 to 26.8 wt.% SiO_2. All the syntheses are from the same starting reagents, Si5-PTHF.

Optimisation of printing parameters

This work began as an extension of the printing of the SiO_2-PCL-PTHF system by Tallia *et al.* [12, 110] but the absence of the PCL component changed the gelation properties of the hybrid system: the sol had to be at a later stage in gelation to be printable. Although the initial printing parameters that were trialled were successful printing conditions for SiO_2-PCL-PTHF, printing for the SiO_2-PTHF system had to be optimised from scratch.

There is a constant trade-off between different parameters in printing: increasing the printing pressure requires increasing the printing speed to deposit the same volume; printing an ink with a high viscosity requires increased flow rate to produce the same printing pressure to produce the same volume of filament. Since it is not possible to directly alter the pressure applied by the Robocaster using the software, it is necessary to change the inputted tip diameter (which is how the machine calculates the pressure required) to indirectly alter the applied pressure. Inputting a large tip diameter results in an increased flow rate and a higher pressure to have a continuous filament.

To counteract the stretching and breakage of filaments seen in Figure 5.10b, a higher printing pressure was needed to achieve a continuous filament. The flow rate was therefore increased by inputting a large tip size into the printer (tip diameter, ϕ_t = 0.41 mm, producing a flow rate of 0.063 mL min^{-1}). The printing speed was also decreased finally to 8 mm s^{-1}, which further increased the volume of material deposited. The spacing between struts in one horizontal layer, called the road width, was increased to account for the larger volume of ink deposited. The iterations of the variation in printing parameters are shown in Table 5.5.

When higher pressure is required to extrude the continuous filament, as in this case of increasing the flow rate to 0.063 mL min^{-1}, the ink continues to extrude even after stopping the printing. This higher pressure seems to cause expansion or spreading of the filament after extrusion, which results in the printing tip beginning to crash with previous layers after printing the first few layers. This is because the z-spacing is calculated based on the size of the tip (0.21 mm) but the expansion means this is not the correct distance as the layers increase in number, for example layer 9, after 8 layers of printing have all been slightly thicker than 0.21 mm. To counter this effect, a system of staggered z-spacing was developed by increasing by 0.02 mm every eight layers. This ensured that the tip remained at around the same distance from the previous layer all the way through the printing.

Table 5.5: Printing parameters varied in the optimisation process. * indicates a staggered z-spacing of 0.02 mm every 8 layers. Group C with flow rate of 0.063 mL min^{-1}, staggered z-spacing and a speed of 8 mm s^{-1} resulted in successful printing of a 40-layer scaffold.

Group	Flow rate (mL min^{-1})	z-spacing (mm)	Printing speed (mm s^{-1})	Road width (mm)	Comments
A	0.031	0.21	10	0.6	Filament breakage
B	0.031	0.21-0.24	6-10	0.6-1	Tip crashing
C	0.031- 0.063	0.24, 0.24-0.32*	7-9	0.75	Successful printing

5.3.3 Scaffold characterisation

Using the staggered z-spacing method, 40-layer scaffolds were successful printed as shown in Figure 5.12a, with a final silica content of 27.7 wt.% SiO_2. SEM imaging shows the top surface (Figure 5.12b) and internal slices in the vertical (Figure 5.12c) and horizontal (Figure 5.12d) directions. The latter shows line of sight interconnected channels through the structure and bonding between the struts of different layers at the crossing points. This real fusion between struts from different layers, in the same way that multiphase hybrids were formed in Chapter 4, means that the scaffold has a continuous structure which may improve its mechanical properties [12].

ImageJ was used on a larger image of the horizontal slices to measure the average pore channel size as 300 ± 50 µm. This was slightly larger than the channel size of around 200 µm formed with SiO_2-PCL-PTHF scaffold by Tallia *et al.* [12], but is smaller than those in similar hybrid systems for example 550 µm in gelatin-bioactive glass [137], 620 ± 40 µm in bioactive glass scaffolds [170]. Further work on the direct printing of this hybrid system could aim to reduce the channel size to the target level.

The pores in the vertical slice (Figure 5.12c), which are those running laterally through the scaffold as printed, are less regular than in the horizontal slice, partially due to collapse of the scaffold during printing but also due to damage and smearing caused by the sectioning itself (cutting with a razor blade) in order to image them. This is a problem seen in other hybrid inks [131, 171] that requires further optimisation of the ink and printing conditions to address. The total printing time for the scaffold is 17 minutes, during which time the ink continues to gel, so parts of the scaffold that are printed later will experience a lower contraction that the initial layers. It is also important in future to consider the effect of the staggered z-spacing, which may create a pore size variation from the bottom to top of the scaffold.

There was significant shrinkage of the scaffolds on drying and the filament morphology shows higher roughness due to the evaporation of solvent in the outer layers whilst printing was ongoing and shrinkage of the scaffold after printing. The roughness is higher than that seen in injectability testing (Section 5.3.1), possibly due to the higher extrusion pressure used. Cell attachment and differentiation including that of chondrocytes has been seen to improve with greater nanoscale roughness [172, 173] however, cell studies on 3D printed SiO_2-PTHF scaffolds would be needed to confirm this.

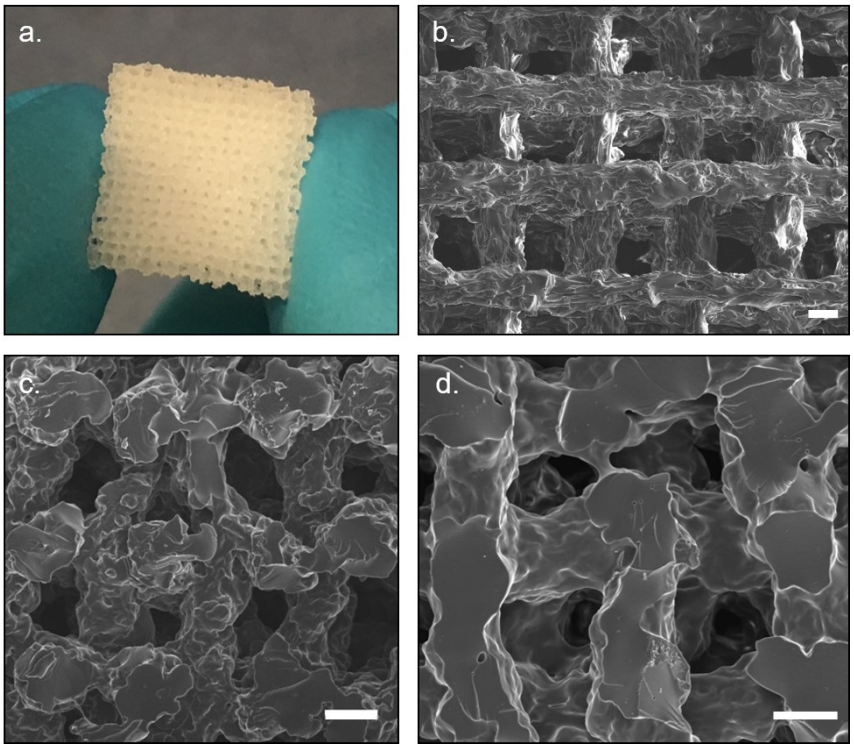

Figure 5.12: a. 3D printed scaffold and SEM images of its **b.** top, **c.** vertical internal and **d.** horizontal internal surfaces. Scale bar = 200 µm. Hybrid composition Si5-PTHF with final inorganic content of 27.7 wt.% SiO_2.

Compression testing

Si5-PTHF scaffolds with final inorganic content of 27.7 wt.% SiO_2 were cut with a razor blade prior to testing to give an even cubic shape. At the start of the test there was in some cases a small breakage of struts in contact with platens, which was not considered as a failure event. The difficulty in getting a flat top and bottom scaffold surface also increased the variability of the results.

Four compression tests are shown in Figure 5.13a, with the failure points marked, and a photograph of the set-up is shown in Figure 5.13b. True stress and strain values are reported as the scaffold deformation was much less than that of the monoliths tested in Chapter 3. This gives a preliminary estimation of the compressive strength of the scaffolds as 1.3 ± 0.5 MPa, which was similar to SiO_2-PCL-PTHF 3D printed scaffold with 24.7 wt.% SiO_2 and pore size ≈ 200 µm developed by Tallia *et al.* [12] and to that of PCL and polylactide-co-glycolide scaffolds with 0.6-10 MPa (51.5-80.9 % porosity) and 0.53 ± 0.07 MPa (pore size 116 µm) respectively [174, 175]. As expected, the strength was an order of magnitude lower than that of bioactive glass scaffolds [170]. It is also significantly below the compressive strength of articular cartilage at 14-59 MPa [60].

The tangent to the compression curve (σ^* v ε^*) at ε^*= 5% can be used as an estimation of the stiffness of the scaffolds, as for the bulk hybrid samples. This gives a value of $E_{5\%}$ = 10 ± 3 MPa which is consistent with the range of the storage modulus as measured by DMA at (engineering) strain ranges of 2-5% and 5-9% (Figure 5.13c) but higher than measured values of articular cartilage, for example bovine articular cartilage equilibrium stiffness at 0.677 ± 0.223 MPa [176]. Tan $\delta \leq 0.06$ indicating that the scaffold behaved elastically in this strain range. As for bulk samples, E' increased with increasing frequency and strain range, however only one sample was tested in this case.

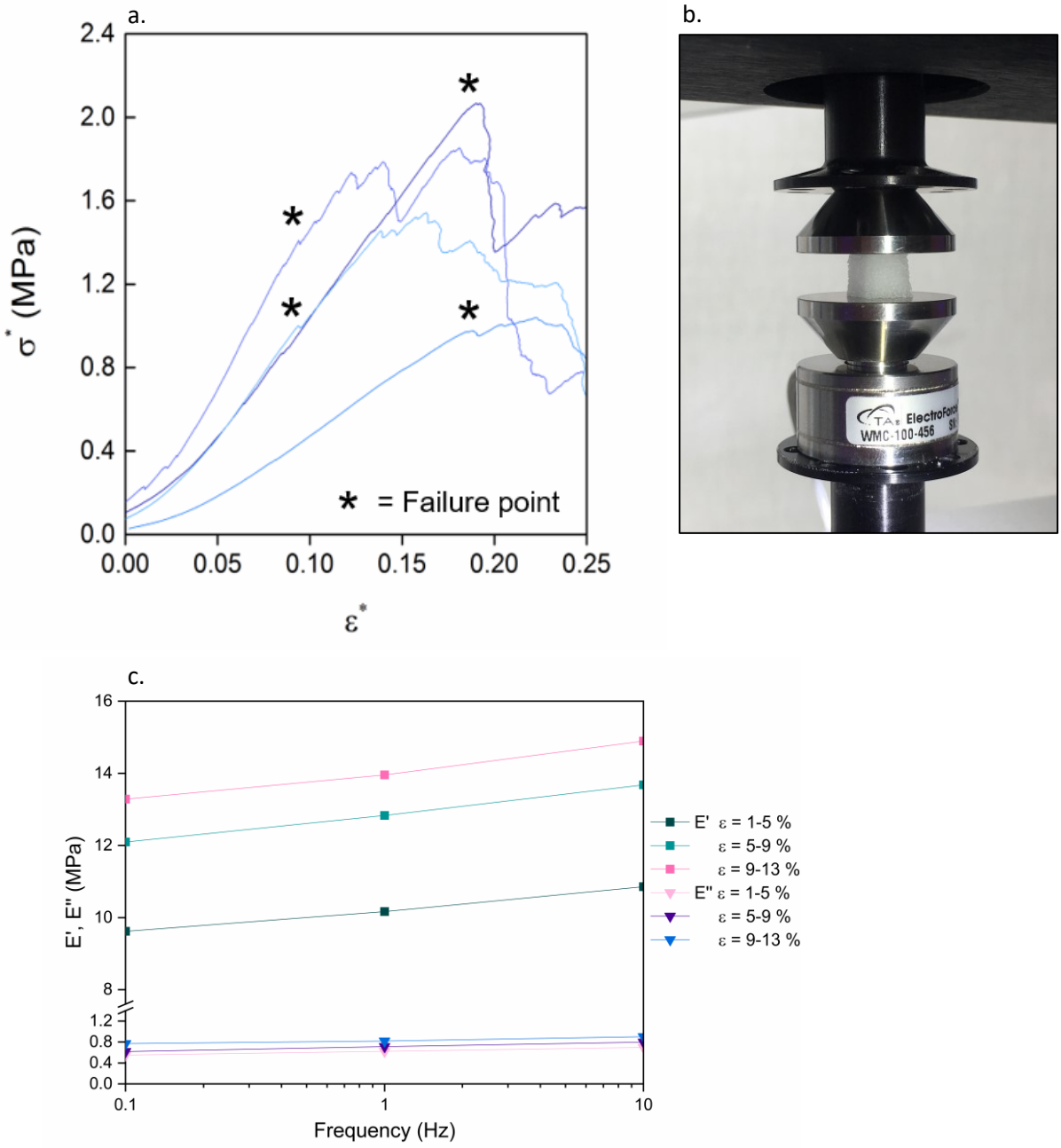

Figure 5.13: a. True stress and true strain in compression to failure for 4 scaffolds of the same composition, Si5-PTHF (27.7 wt.% SiO_2), **b.** the compression test set up, and **c.** storage moduli (E') and loss moduli (E'') measured by DMA of one scaffold over three strain ranges ε = 1-5, 5-9, 9-13% and at three frequencies, 0.1, 1 and 10 Hz.

5.3.4 Moulding a meniscus

This part of the work follows on from the investigation of shrinkage factor and surface roughness (Section 3.3.2). The first step was to confirm that the hybrid would conform to a 3D shape on drying, using a straight mould with a cross-section shape based on the natural meniscus. Then, a 3D hemispherical mould was produced with improved surface roughness to form a simple meniscus shape.

The straight mould (Figure 5.14) was very rough and resulted in the curved surface of the sample (C) having a roughness of close to 7 µm (Table 5.6). Si2.5-PTHF hybrid sample produced in this mould shrank on drying and kept the shape, showing that it was possible to form a 3D structure in this way. The shrinkage factor was calculated in three directions (Table 5.6) and the average value of 0.6 was used to calculate the size of the next mould and the roughness was improved by increasing the precision of the CNC to the settings set out in Section 5.2.5.

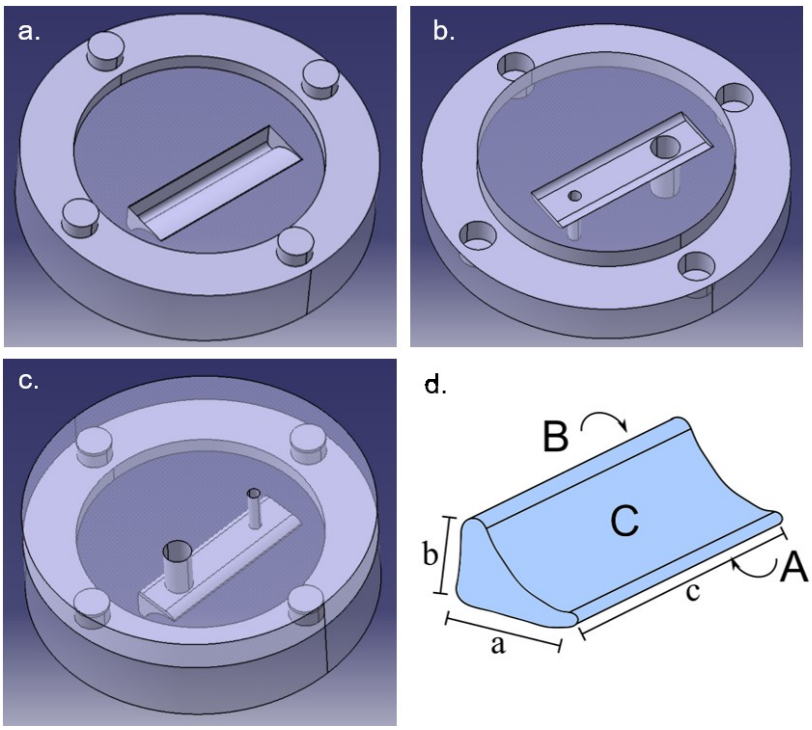

Figure 5.14: Straight mould design for **a.** bottom half of mould, **b.** top half, **c.** whole mould and **d.** resultant sample labelled with dimensions (lower case) and areas (upper case) for which the shrinkage factors and roughness were calculated respectively.

Table 5.6: Roughness and shrinkage factor for hybrid sample made in straight profile mould. Labels correspond to those shown in Figure 5.14a.

Surface	Ra (nm)	Dimension	Shrinkage factor
A	2400 ± 200	a	0.59
B	3180 ± 80	b	0.64
C	6700 ± 300	c	0.59

3D profile mould

CNC drilling is line of sight and requires a horizontal common surface through the centre of the mould cavity about which to form the halves of the mould. Therefore, a simplified meniscus shape was produced, based on average human meniscus dimensions, increased in size by a 60%, the shrinkage factor calculated above (Figure 5.15a). This shape has curved top and bottom surfaces and forms a hemisphere with parallel end faces; Si2.5-PTHF hybrid samples were produced in this mould free from bubbles and retaining the shape of the mould (Figure 5.15b,c). The roughness was lower than that found for polyurethane implants for meniscus replacement [177]. The roughness measurements and shrinkage factors for the hybrid meniscus produced are shown in Figure 5.15d.

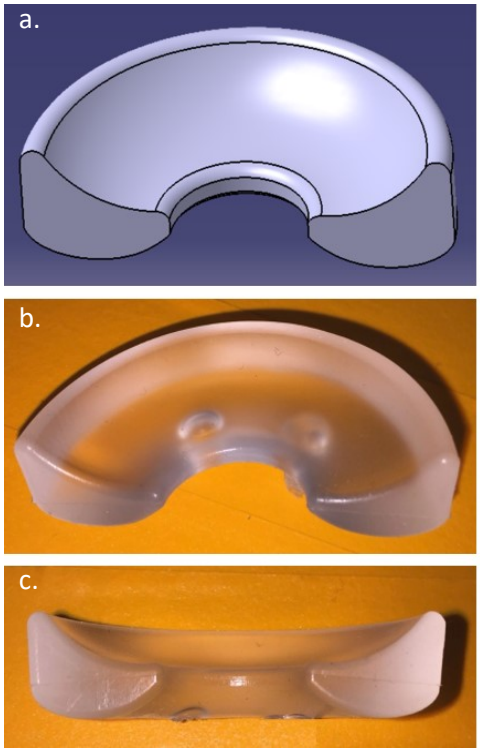

d.

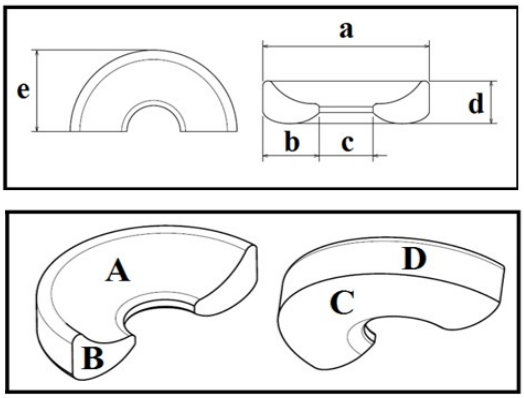

Surface	Ra (nm) ± 40	Dimension	Shrinkage factor
A	510	a	0.69
B	460	b	0.67
C	590	c	0.73
D	330	d	0.63
		e	0.67

Figure 5.15: a. 3D profile mould design and **b., c.** resultant Si2.5-PTHF hybrid meniscus. The average roughness of the hybrid sample was 470 ± 40 nm and shrinkage factor 0.68, calculated in the surfaces and directions shown in **d.**

Mechanical testing

Hybrid meniscus samples were tested in cyclic compression and then compression to failure on the same sample, using a platen designed to match the top curved surface of the sample. The force-displacement was plotted rather than the stress-strain curve due to the complex shape. An estimate of the stress may be obtained using the area of the top curved surface, and the strain was measured directly using DIC. The DIC image (Figure 5.16b) shows the principal strain, which is in compression for most of the sample and in tension for the inner most points. Here the material was extruded out under the central flat portion of the platen, which can be seen as a tensile strain in Figure 5.16b.

In the same way as for cyclic testing of cylindrical samples, there was a reduction in the loading curve, most markedly between the first cycle and subsequent cycles, due to the small effect of viscoelastic behaviour of the material. There could also be an effect of small motion of the sample during cycling, as it was not fixed in place.

The flaw in this experiment is that it is very sensitive to the positioning of the sample within the platen and there is no fixation method to make sure that this is the same each time, other than lining it up by eye. The platen concentrates the stress on the inner part of the meniscus, which may give an unrealistic picture at high strains.

The force-displacement in compression to failure is shown in Figure 5.16c. The stress was not calculated for this experiment due to the complex shape. Using the total top surface area of 573 mm^2 gives a stress at failure of 4.4 MPa and an initial modulus (tangent to the curve) of 28 MPa. However, this stiffness is an order of magnitude larger than the measured value for meniscal tissue [56], but similar to that of polycarbonate urethane trialled for synthesis whole meniscus implants which showed degeneration of adjacent intact cartilage at 12 months implantation in goats [74].

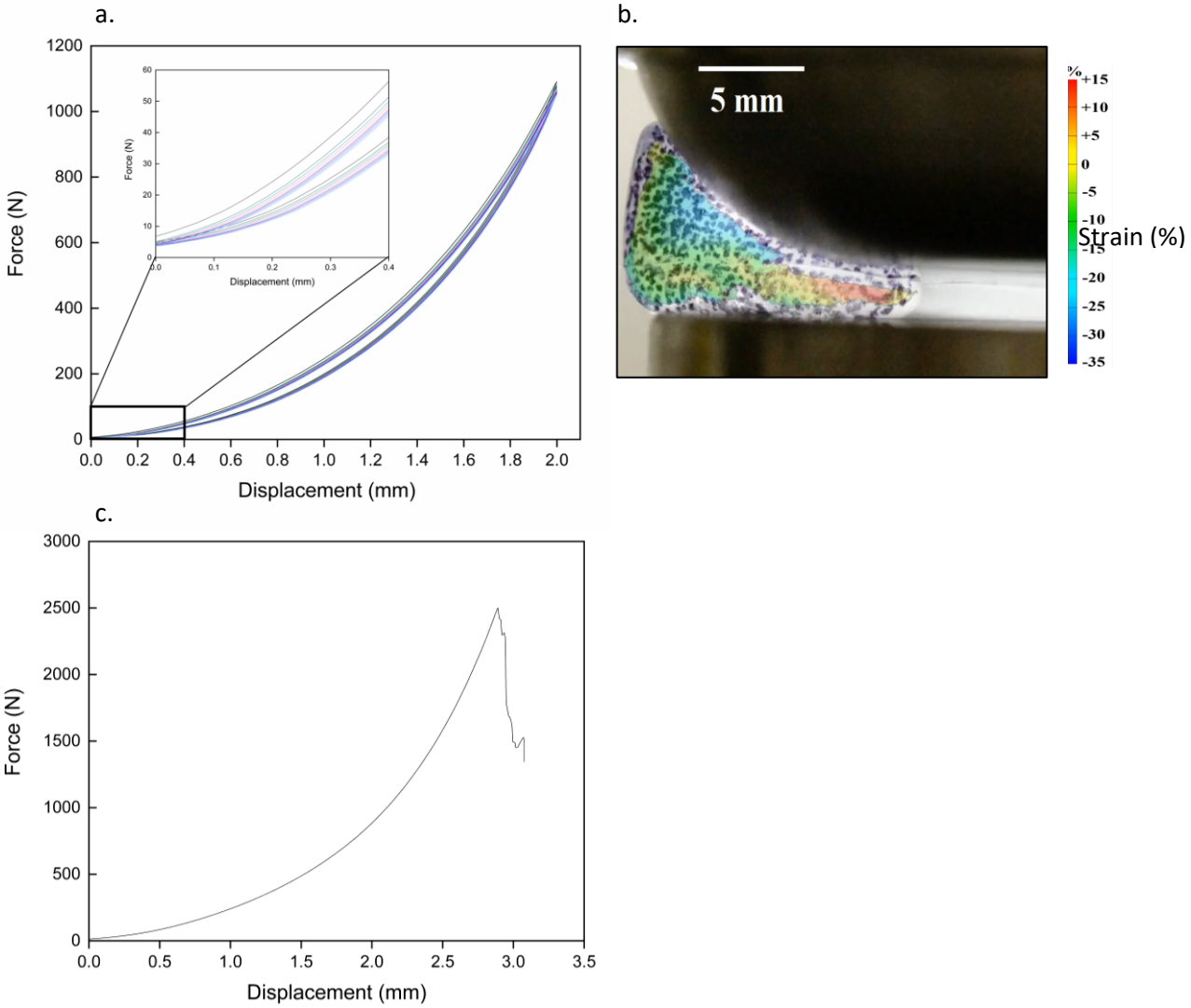

Figure 5.16: a. Force-displacement curve for 10 cycles of one hybrid meniscus sample and **b.**, major strain map on end surface at displacement = 2 mm, Force = 1100 N, shows the extrusion of the thin central edge under the platen. **c.** Force-displacement curve in compression to failure.

5.3.5 IVD replacement device

Total disc replacement devices have been developed that replace the disc with a three-component system [178, 179] but long term results do not show an improvement relative to the standard treatment of spinal fusion [180]. Elastomeric implant devices have been developed that instead attempt to recreate the natural biomechanics of the spine [43], which show a stiffening with increased applied load [181] and a gradation in properties resulting from the injection moulding manufacturing technique [127].

The aim with this work is to form a hybrid intervertebral disc, that can mimic the properties of the natural disc by using the possibility of tuning the hybrid composition to match the stiffness of the natural disc through the structure.

Hybrid IVDs were formed in an ellipse shaped by casting the sol into moulds designed to produce the hybrid IVDs to the average dimensions of human IVDs tested by Newell *et al.* (after shrinkage) [31]. Samples were formed free from bubbles, shown in Figure 5.17a. Hybrid IVDs were formed in composition of Si7.5, 3.75, 2.5, 1.75, 1-PTHF. Final heights and dimensions were measured prior to testing. The samples were dried for minimum one month due to the larger bulk volume.

Comparison with the natural human IVD

Hybrid IVDs were tested in the same test set up at three strain rates, 0.01, 0.1 and 1 s^{-1} to 10% of their initial height over three cycles, of which the final cycle is plotted in Figure 5.17, along with the curves from the human IVD samples by Newell *et al.* [31] (data available at [182]). Five repeats of Si2.5-PTHF were tested along with one sample each of Si7.5-PTHF, Si3.75-PTHF, Si1.75-PTHF and Si1-PTHF. The human IVD data lies between that of the composition with the most silica content, Si7.5-PTHF and the Si2.5-PTHF samples. Thus, an intermediate composition or Si2.5-PTHF after soaking could give good agreement with human data.

The hybrid samples also replicate the non-linear shape of the IVD force-displacement curve, which was highlighted as crucial to a successful disc replacement material [13]. This suggests that this hybrid system warrants further investigation as an IVD replacement device.

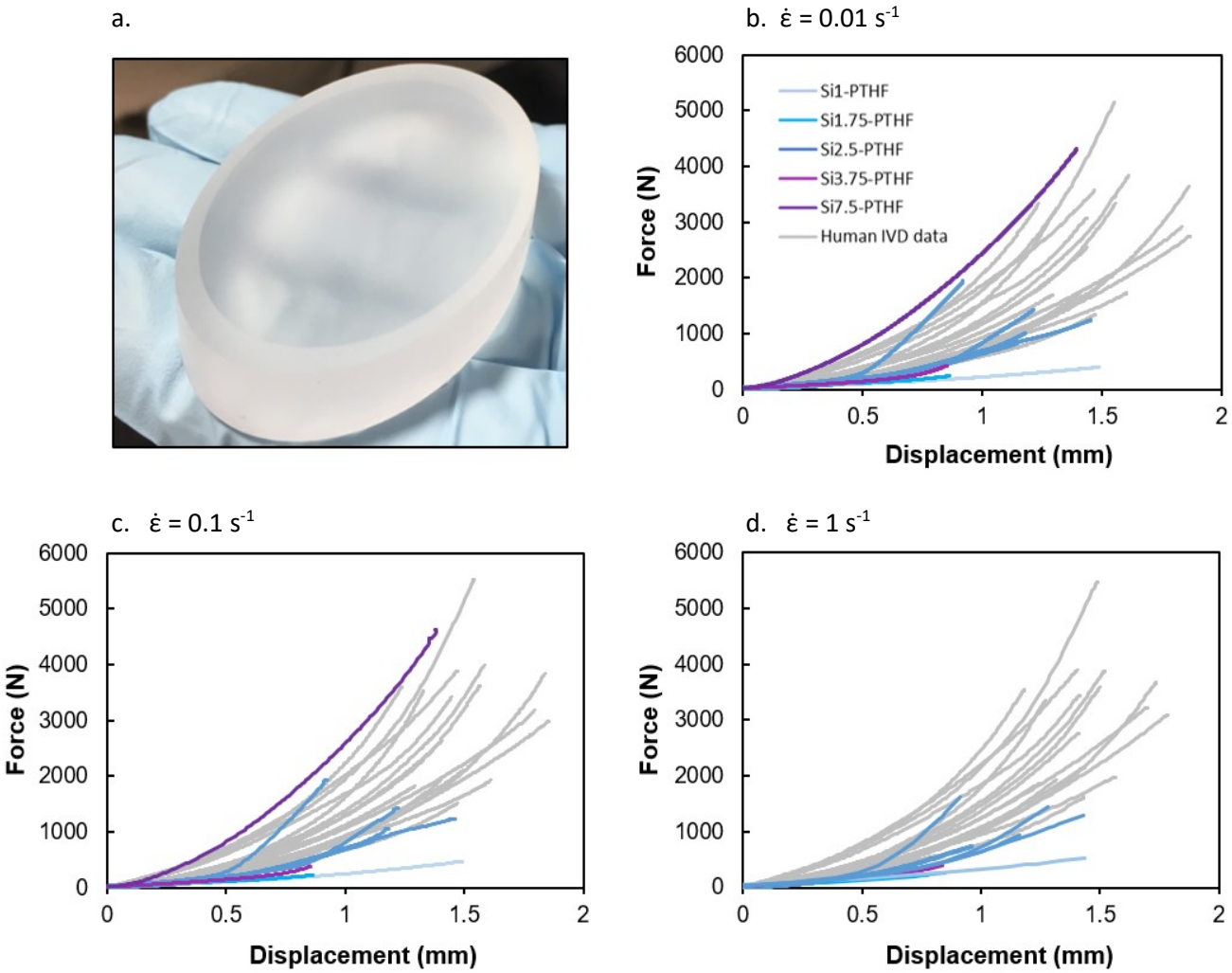

Figure 5.17: a. Moulded hybrid IVD Si2.5-PTHF. The top surface is ground to flat before testing. Hybrid IVD testing in comparison with human IVD data (shown in grey) at **b.** 0.01 s^{-1}, **c.** 0.1 s^{-1}, **d.** 1 s^{-1}. Si7.5-PTHF was not tested at 1 s^{-1} due to the limit of load cell.

5.4 Conclusions

The SiO_2-PTHF hybrid system can be used to produce complex 3D structures, namely printed scaffolds, model meniscus and IVDs. This is a first step to device development for cartilage replacement implants. These techniques have the potential to be used together, along with the work on multiphase hybrids in Chapter 4, to produce a total intervertebral disc replacement device which bonds to adjacent endplate tissue via ingrowth into scaffolds.

3D porous scaffolds were fabricated from SiO_2-PTHF hybrid ink by direct robocasting with Si5-PTHF composition and no post-printing treatment was required to stabilise the scaffolds. Injectability testing of the hybrid ink showed a printing window of 40 minutes and the possibility of storing the inks at -80°C for a period of days before testing, allowing a practical printing procedure for batches of scaffolds. Printing parameters were optimised for successful printing of a 40-layer scaffold with a final inorganic content of 27.7 wt.% SiO_2 and a channel size of 300 ± 50 μm. The struts showed fusion between the layers, in the same way that multiphase hybrids joined in Chapter 4. This contributes to the measured compressive strength of 1.3 ± 0.5 MPa.

It was possible to mould the hybrid gel into a defined 3D shape, in this case to form a simplified model meniscus and model intervertebral disc. In the case of the former this include moulding the top and bottom surfaces to a desired shape, taking account of the shrinkage factor of approximately 60%. This could be extended to form multiphase shapes with a gradation in stiffness through the structure.

Hybrid IVD samples in dry conditions were tested in identical conditions to human intervertebral discs for direct comparison and those of Si2.5-PTHF composition produced force-displacement curves that lay within the range of the human samples, giving a promising indication for the development of this material as an IVD replacement device.

Chapter 6

Conclusions and future work

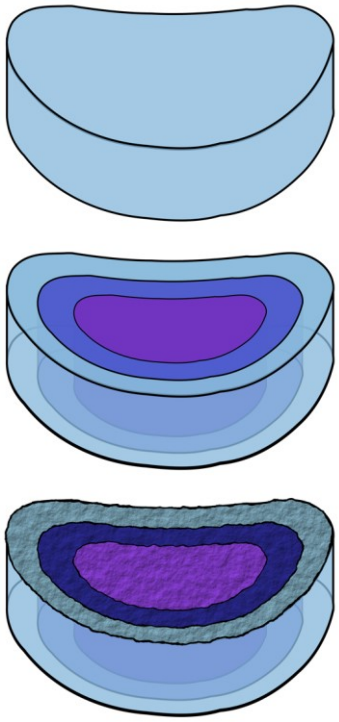

6.1 Conclusions

The overall aim of this thesis was the synthesis of SiO_2-PTHF hybrid system with gradients of mechanical properties, including characterisation of those properties, for the development of a device that could replicate the human IVD. Important steps towards this final aim have been made.

The synthesis protocol for a novel hybrid system SiO_2-PTHF was developed to fabricate monolithic hybrid samples with a range of compositions from 3.6-44.4 wt.% SiO_2. The cationic ring opening polymerisation mechanism for this reaction resulted in successful covalent coupling between the inorganic and organic components, and a hybrid structure with intimately mixed networks of these components. However, it was not possible to characterise the length of polymer chains or its dispersity after synthesis, which is crucial to gain a better understanding of the final hybrid structure and to have a finer control over the mechanical properties.

The hybrids were tested in tension and compression over a range of compositions, allowing their properties to be tuned by altering the inorganic content of the material. In compression a failure stress of 5-33 MPa was found for compositions tested, from a range of 5.8-44.4 wt.% SiO_2 with a maximum at 32 wt.% SiO_2. Over the same composition range, the stiffness measured at 10% strain varied between 4 and 240 MPa: hybrids between 4 and 10 wt.% SiO_2 have stiffness of the range of the IVD and compressive strengths greater than that experienced by the IVD [28]. In tension, the failure stress was 1-13 MPa and the stiffness at 10% strain 1-9 MPa over a range of compositions (6.3-19.1 wt.% SiO_2). Comparison to the force-displacement curves of the human IVD under the same strain rate conditions showed good agreement, however further work is needed to see if the hybrid material can match the non-linear behaviour of the natural disc.

SiO_2-PTHF surfaces and extractables were shown to be non-cytotoxic and support cell attachment and viability in *in vitro* cell studies using a mouse chondrocyte cell line. The mechanical properties of the hybrid were shown to be stable over a period of 1.5 years, in a simulated bodily environment, after an initial small increase in stiffness and reduction in strength over the first month of soaking. Samples above 19 wt.% SiO_2 were severely weakened on soaking because the higher silica content, which is hydrophilic, lead to greater internal stress development and subsequent fracture.

A novel method for the production of a gradient in stiffness in a single sol-gel hybrid specimen was developed, which took advantage of the gradual gelation of the hybrids to join a second hybrid sol of different composition to the first at various times within its 3 day ageing period. This method of joining hybrids was included into the patent covering the synthesis process and obtained hybrid materials (Tallia, F., Jones, J. R., Cipolla, L., Russo, L., and Young, G. R., *Hybrid materials and process for*

production thereof - Invention specifications GB 1605446.2. 2019). The maximum variation in compressive stiffness through a single sample produced was 4 to 240 MPa (measured at 10% strain) resulting from a compositional difference of 6 to 42 wt.% SiO_2.

The 'interface,' not visible by eye, between two hybrid sols joined at 2 hours ageing time of the first was at least as strong in tension and compression as a single phase sample, demonstrated by the formation and testing of hybrids with an interface but where the first and second solution had the same hybrid composition. Optical methods were used to map the strain around the interface, further supporting the strength of the interface formed at 2 hours ageing time and indicating that the sharp and significant compositional difference led to strain concentration rather than residual stresses at the interface from the fabrication. However, no chemical method was achieved to characterise the compositional change across the interface at the scale of the interface. Therefore, it was not possible to measure how steep the change in composition was or precisely alter this by controlling the viscosity of the hybrid sols.

A technique was developed for Micro-CT imaging of patterned hybrids which coupled with DVC allowed the strain to be mapped in 3 dimensions for two phase samples under load. This method could be useful for comparing devices with natural materials (for example, IVD strain distributions as measured by magnetic resonance image combined with DVC).

Porous SiO_2-PTHF scaffolds were successfully produced by 3D printing with a final inorganic content of 27.7 wt.% and an average channel size of 300 ± 50 µm. The fusion between subsequent layers (in the same way that multiphase hybrids were formed) contributed to the measured compressive strength of 1.3 ± 0.5 MPa. Porous scaffolds have the potential to be joined to the bulk material (at a 2 hour ageing time, as for multiphase hybrids) to provide a fixation to bone. This requires further work beginning with cell studies on hybrid scaffolds.

For the first time, a sol-gel hybrid material was fabricated into a complex 3D shape: SiO_2-PTHF hybrids were successfully fabricated in the forms of simplified meniscus and IVD. Comparing IVD moulded samples in compression tests with human IVDs showed that the stress-strain curves could be matched with tuning of the composition. However so far graded stiffness hybrid IVDs have not been fabricated.

6.2 Future work

There is still a lack of complete control of the polymerisation reaction and combination into the hybrid sol, and work on this is ongoing using solid state NMR to understand the structures of SiO_2-PCL-PTHF and SiO_2-PTHF by comparison at a series of burn-out temperatures, and using solid state NMR to investigate whether and how the boron present in the catalyst might be incorporated.

In order for SiO_2-PTHF hybrids to be considered as permanent implant materials, longer term studies of the changes in properties in a bodily environment are required. This should be accompanied by an understanding of what causes the increase in stiffness on initial soaking. Thus far the wet testing has been done by removal from solution and immediate testing, but testing while soaked is important particularly for porous scaffolds in which the flow of fluid through the material can affect the behaviour and to assess whether the drying process causes the embrittlement. The next stage will be animal studies on developed devices, beginning with biosafety studies in mice.

For the formation of a hybrid meniscus, the tribology of the bearing surface must be considered: without a low friction surface damage will be caused to the intact cartilage of the joint and the sample can be displaced, causing failure. Previous work on the SiO_2-PCL-PTHF hybrid system has shown that hybrid surfaces prepared with a surface roughness of 100 nm did not cause damage to a cartilage counter surface in tribological testing. This surface roughness was 3-5 times smaller than that achieved on the hybrid meniscus produced in PTFE mould, therefore, further work is needed to optimise the moulding, and then to test the tribological properties of this hybrid system. The work on the meniscus is being continued by PhD student Yu Chien Lin, with the objectives of decreasing the surface roughness, designing a method of fixation to the tibial plateau, and mechanical testing of the whole device to simulate the *in vivo* stress state.

IVD device development

In Chapter 4, the 'interface' between two hybrid materials has been a straight line, horizontally in the case of cylinders or across the middle of a disc. A new process, built on the methods used for the discs, has been developed for concentric rings: a thin piece of Teflon in a ring to contain the first hybrid during the time before the second is added. This works well but limits the thickness and produces rough edges where some of the solution sticks to or is pulled away by the PTFE sheet. Since the solution can be frozen, this allows a core of frozen material to be pushed from a mould without sticking to the sides of the mould. This is the first step in trying to combine the work from Chapter 4 on multiphase hybrids and the work in Chapter 5 on a hybrid intervertebral disc, to imitate the human IVD as described in Section 1.2.1.

So far in this work it has not been possible to precisely control the viscosity of the hybrid sol, as was seen for the 3D printing in Chapter 5. This limits the optimisation of the interface joining time and control over the steepness of the compositional interface formed when hybrid sols of different compositions are joined. Therefore, a better understanding and control over the synthesis would allow this control of viscosity, and the creation of more gradual compositional transitions. RAMAN or Small angle X-ray scattering could be used to measure the steepness of the compositional change across the interface, as has been done with PTHF [106] and poly urethane with a gradation in stiffness [128].

Work by Dr Francesca Tallia has shown that it is possible for scaffolds to be joined to the bulk materials for the SiO_2-PCL-PTHF hybrid system; trial and optimisation of the joining time for this in the SiO_2-PTHF system would allow the joining of 3D printed scaffold to the surface of an IVD device as a potential device fixation method. This has the potential to provide good fixation with the vertebrae endplates, if the scaffolds support tissue ingrowth, as the scaffold would form a continuous structure with the rest of the device. This also requires further work on optimisation of the 3D printing onto a gelling and not flat hybrid surface.

Continuation of this work has received funding as an EPSRC Post-doctoral Prize Fellowship. The objectives for this are: (1) the fabrication of prototype multi-phase IVD device**;** (2) whole device mechanical testing to tune the properties to match those of the natural disc; (3) bone bonding at top and bottom surfaces. The proposed work builds on two proofs of concept achieved during the PhD: formation of a hybrid device with graded properties, without interface, and 3D printed scaffolds from the same hybrid material. The whole multi-phase device that will be fabricated will be a novel concept that requires mechanical testing and investigation of the bone ingrowth into scaffold. The materials characterisation and the interface testing developed in the PhD will be translated to the new whole device. Mechanical properties of the device in wet and dry conditions will be compared directly to those of the natural intervertebral disc, as part of an on-going collaboration with members of the Biomechanics group (Prof Jonathan Jeffers, Dr Nic Newell, Jeff Clark and Saman Tavana) at Imperial College London. This will include continuation of ongoing Digital Image Correlation (DIC) strain measurements to look at the strain around interfaces and fatigue testing to high cycle numbers. Micro-CT with DVC will be used following the technique developed in this thesis for mapping of the 3D strain within the device, comparative with human IVDs. To address the objective of the fixation of the device in the spine, cell viability testing of human bone marrow derived stem cells**,** the cells present within the vertebrae responsible for bone integration, will be undertaken in collaboration with Dr Silvia Ferreira and Professor Sara Rankin (NHLI, Imperial College London).

References

1. *Monitoring health for the SDGs: Annex B Tables of health statistics by country, WHO region and globally*. 2016, World Health Organisation.
2. !!! INVALID CITATION !!! [2].
3. !!! INVALID CITATION !!! [3].
4. *12th Annual Report*. 2015, National Joint Registry for England, Wales, Northern Island and the Isle of Man.
5. Fairbank, J., Frost, H., Wilson-MacDonald, J., YU, L.-M., Barker, K., and Collins, R., *Randomised controlled trial to compare surgical stabilisation of the lumbar spine with an intensive rehabilitation programme for patients with chronic low back pain: the MRC spine stabilisation trial.* BMJ, 2005. **330**: p. 1233-1240.
6. Furunes, H., Storheim, K., Brox, J. I., Johnsen, L. G., Skouen, J. S., Franssen, E., Solberg, T. K., Sandvik, L., and Hellum, C., *Total disc replacement versus multidisciplinary rehabilitation in patients with chronic low back pain and degenerative discs: 8-year follow-up of a randomized controlled multicenter trial.* Spine J, 2017. **17**(10): p. 1480-1488.
7. Leung, V. Y., Chan, D., and Cheung, K. M., *Regeneration of intervertebral disc by mesenchymal stem cells: potentials, limitations, and future direction.* Eur Spine J, 2006. **15**: p. S406-413.
8. Serhan, H., *Advancements in the treatment of degenerative disc disease.* Hamdan Medical Journal, 2018. **11**(4).
9. Riviere, C., Lazennec, J. Y., Van Der Straeten, C., Auvinet, E., Cobb, J., and Muirhead-Allwood, S., *The influence of spine-hip relations on total hip replacement: A systematic review.* Orthop Traumatol Surg Res, 2017. **103**(4): p. 559-568.
10. Novak, B. M., *Hybrid nanocomposite materials - between inorganic glasses and organic polymers.* Advanced Materials, 1993. **5**(6).
11. Tallia, F., Jones, J. R., Cipolla, L., Russo, L., and Young, G. R., *Hybrid materials and process for production thereof - Invention specifications GB 1605446.2*. 2019.
12. Tallia, F., Russo, L., Li, S., Orrin, A. L. H., Shi, X., Chen, S., Steele, J. A. M., Meille, S., Chevalier, J., Lee, P. D., Stevens, M. M., Cipolla, L., and Jones, J. R., *Bouncing and 3D printable hybrids with self-healing properties.* Materials Horizons, 2018. **5**(5): p. 849-860.
13. van den Broek, P. R., Huyghe, J. M., Wilson, W., and Ito, K., *Design of next generation total disk replacements.* Journal of Biomechanics, 2012. **45**(1): p. 134-140.
14. Urban, J. P. G., *The chrondrocyte: a cell under pressure.* British Journal of Rheumatology, 1994. **33**: p. 901-908.
15. Wong, M. and Carter, D. R., *Articular cartilage functional histomorphology and mechanobiology: a research perspective.* Bone, 2003. **33**(1): p. 1-13.
16. Mow, V. C., Holmes, M. H., and Michael Lai, W., *Fluid transport and mechanical properties of articular cartilage: A review.* Journal of Biomechanics, 1984. **17**(5): p. 377-394.
17. Carter, D. and Hayes, W., *Bone compressive strength: the influence of density and strain rate.* Science, 1976. **194**(4270): p. 1174-1176.
18. Ge, Z., Li, C., Heng, B. C., Cao, G., and Yang, Z., *Functional biomaterials for cartilage regeneration.* Journal of Biomedical Materials Research Part A, 2012. **100**(9): p. 2526-2536.
19. Takahashi, I., Nuckolls, G. H., Takahashi, K., Tanaka, O., Semba, I., Dashner, R., Shum, L., and Slavkin, H. C., *Compressive force promotes Sox9, type II collagen and aggrecan and inhibits IL-1β expression resulting in chondrogenesis in mouse embryonic limb bud mesenchymal cells.* Journal of Cell Science, 1998. **111**: p. 2067-2076.
20. Breuls, R. G. M., Jiya, T. U., and Smit, T. H., *Scaffold stiffness influences cell behaviour: opportunites for skeletal tissue engineering.* The Open Orthopaedics Journal, 2008. **2**: p. 103-109.

21. Jung, Y., Kim, S. H., Kim, S. H., Kim, Y. H., Xie, J., Matsuda, T., and Min, B. G., *Cartilaginous tissue formation using a mechano-active scaffold and dynamic compressive stimulation.* Journal of Biomaterials Science, Polymer Edition, 2008. **19**(1): p. 61-74.
22. Hench, L. L. and Jones, J. R., *Bioactive glasses: Frontiers and challenges.* Frontiers in Bioengeering and Biotechnology, 2015. **3**: p. 194.
23. Bogduk, N., *Clinical anatomy of the lumbar spine and sacrum Fourth ed.* 2005, London, UK: Elsevier Health Sciences.
24. Yoganandan, N., Dickman, C. A., and Benzel, E. C., *Practical anatomy and fundamental biomechanics*, in *Spine Surgery*. 2012, Elsevier. p. 267-289.
25. Zander, T., Krishnakanth, P., Bergmann, G., and Rohlmann, A., *Diurnal variations in intervertebral disc height affect spine flexibility, intradiscal pressure and contact compressive forces in the facet joints.* Computer Methods in Biomechanics and Biomedical Engineering, 2010. **13**(5): p. 551-557.
26. Johannessen, W., Vresilovic, E. J., Wright, A. C., and Elliott, D. M., *Intervertebral disc mechanics are restored following cycic loading and unloaded recovery.* Annals of Biomedical Engineering, 2004. **32**(1): p. 70-76.
27. Zhou, S. H., McCarthy, I. D., McGregor, A. H., Coombs, R. R. H., and Hughes, S. P. F., *Geometrical dimensions of the lower lumbar vertebrae - analysis of data from digitised CT images.* European Spine Journal, 2000. **9**: p. 242-248.
28. Wilke, H.-J., Neef, P., Caimi, M., Hoogland, T., and Claes, L. E., *New in vivo measurements of pressures in the intervertebral disc in daily life.* Spine, 1999. **24**(8): p. 755-762.
29. Iatridis, J. C., Setton, L. A., Foster, R. J., Rawlins, B. A., Weidenbaum, M., and Mow, V. C., *Degeneration affects the anisotropic and nonlinear behaviors of human anulus fibrosus in compression.* Journal of Biomechanics, 1998. **31**: p. 535-544.
30. Park, S., Hung, C. T., and Ateshian, G. A., *Mechanical response of bovine articular cartilage under dynamic unconfined compression loading at physiological stress levels.* Osteoarthritis and Cartilage, 2004. **12**(1): p. 65-73.
31. Newell, N., Carpanen, D., Grigoriadis, G., Little, J. P., and Masouros, S. D., *Material properties of human lumbar intervertebral discs across strain rates.* Spine Journal, 2019. **10.1016/j.spinee.2019.07.012**.
32. Bono, C. M. and Lee, C. K., *Critical Analysis of Trends in Fusion for Degenerative Disc Disease Over the Past 20 Years.* Spine, 2004. **29**: p. 455-463.
33. McAfee, P. C., Fedder, I. L., Saiedy, S., Shucosky, E. M., and Cunningham, B. W., *SB Charité disc replacement.* Journal of Spinal Disorders & Techniques, 2003. **16**(4): p. 424-433.
34. Murrey, D., Janssen, M., Delamarter, R., Goldstein, J., Zigler, J., Tay, B., and Darden, B., *Results of the prospective, randomized, controlled multicenter Food and Drug Administration investigational device exemption study of the ProDisc-C total disc replacement versus anterior discectomy and fusion for the treatment of 1-level symptomatic cervical disc disease.* Spine J, 2009. **9**(4): p. 275-286.
35. Janssen, M. E., Zigler, J. E., Spivak, J. M., Delamarter, R. B., Darden, B. V., 2nd, and Kopjar, B., *ProDisc-C Total Disc Replacement Versus Anterior Cervical Discectomy and Fusion for Single-Level Symptomatic Cervical Disc Disease: Seven-Year Follow-up of the Prospective Randomized U.S. Food and Drug Administration Investigational Device Exemption Study.* J Bone Joint Surg Am, 2015. **97**(21): p. 1738-1747.
36. Ding, F., Jia, Z., Zhao, Z., Xie, L., Gao, X., Ma, D., and Liu, M., *Total disc replacement versus fusion for lumbar degenerative disc disease: a systematic review of overlapping meta-analyses.* Eur Spine J, 2017. **26**(3): p. 806-815.
37. Veruva, S. Y., Lanman, T. H., Isaza, J. E., Freeman, T. A., Kurtz, S. M., and Steinbeck, M. J., *Periprosthetic UHMWPE Wear Debris Induces Inflammation, Vascularization, and Innervation After Total Disc Replacement in the Lumbar Spine.* Clin Orthop Relat Res, 2017. **475**(5): p. 1369-1381.

38. Van Ooij, A., Kurtz, S. M., Stessels, F., Noten, H., and van Rhijn, L., *Polyethylene wear debris and long-term clinical failure of the Charite disc prosthesis.* Spine, 2007. **32**(2): p. 226-229.
39. Shim, C. S., Lee, S. J., Maeng, D. H., and Lee, S.-H., *Vertical Split Fracture of the Vertebral Body Following Total Disc Replacement Using ProDisc Report of Two Cases.* J Spinal Disord Tech, 2005. **18**: p. 465-469.
40. Phillips, F., Diaz, R., and Pimenta, L., *The fate of the facet joints after lumbar total disc replacement: a clinical and MRI study.* The Spine Journal, 2005. **5**(4).
41. Pimenta, L., Springmuller, R., Lee, C. K., Oliveira, L., Roth, S. E., and Ogilvie, W. F., *Clinical performance of an elastomeric lumbar disc replacement: Minimum 12 months follow-up.* SAS J, 2010. **4**(1): p. 16-25.
42. Fraser, R. D., Ross, E. R., Lowery, G. L., Freeman, B. J., and Dolan, M., *AcroFlex design and results.* Spine J, 2004. **4**(6 Suppl): p. 245S-251S.
43. Mahomed, A., Moghadas, P. M., Shepherd, D. E., Hukins, D. W., Roome, A., and Johnson, S., *Effect of axial load on the flexural properties of an elastomeric total disc replacement.* Spine (Phila Pa 1976), 2012. **37**(15): p. E908-912.
44. Osborne, H., *UK firm sold spinal implants that disintegrated* in *The Guardian*. 2018.
45. Ray, C. D., *The PDN prosthetic disc-nucleus device.* European Spine Journal, 2002. **11**(Suppl 2): p. S137-142.
46. Nesti, L. J., Li, W. J., Shanti, R. M., Jiang, Y. J., Jackson, W., Freedman, B. A., Kuklo, T. R., Giuliani, J. R., and Tuan, R. S., *Intervertebral disc tissue engineering using a novel hyaluronic acid-nanofibrous scaffold (HANFS) amalgam.* Tissue Eng Part A, 2008. **14**(9): p. 1527-1537.
47. Ahmed, A. M. and Burke, D. L., *In-Vitro Measurement of Static Pressure Distribution in Synovial Joints—Part I: Tibial Surface of the Knee.* Transactions of the ASME, 1983. **105**: p. 216-225.
48. Spencer Jones, R., Keene, G. C. R., Learmouth, D. J. A., Bickerstaff, D., Nawana, N. S., Costi, J. J., and Pearcy, M. J., *Direct measurement of hoop strains in the intact and torn human medial meniscus.* Clinical Biomechanics, 1996. **11**(5): p. 295-300.
49. Vedi, V., Williams, A., Tennant, S. J., Spouse, E., Hunt, D. M., and Gedroyc, W. M. W., *Meniscal movement: An in-vivo study using dynamic MRI.* British Editorial Society of Bone and Joint Surgery, 1999. **81**(1): p. 37-41.
50. Allen, C. R., Wong, E. K., Livesay, G. A., Sakana, M., Fu, F. H., and Woo, S. L.-Y., *Importance of the Medial Meniscus in the Anterior Cruciate Ligament-deficient Knee.* Journal of Orthopaedic Research, 2000. **18**(1): p. 109-115.
51. Masouros, S. D., McDermott, I. D., Amis, A. A., and Bull, A. M., *Biomechanics of the meniscus-meniscal ligament construct of the knee.* Knee Surg Sports Traumatol Arthrosc, 2008. **16**(12): p. 1121-1132.
52. Petersen, W. and Tillmann, B., *Collagenous fibril texture of the human knee joint menisci.* Anat Embryol, 1998. **197**: p. 317-324.
53. Fithian, D. C., Kelly, M. A., and Mow, V. C., *Material properties and structure-function relationships in the menisci.* Clinical orthopaedics and related research, 1990(252): p. 19-31.
54. Nakano, T., Thompson, J. R., and Aherne, F. X., *Distribution of Glycosaminoglycans and the Nonreducible Collagen Crosslink, Pyridinoline in Porcine Menisci.* Canadian Journal of Veterinary Research, 1986. **50**: p. 532-536.
55. Tissakhi, M. and Ahmed, A. M., *Tensile stress-strain characterisatics of the human meniscal materials.* Journal of Biomechanics, 1995. **28**(4): p. 411-422.
56. Chia, H. N. and Hull, M. L., *Compressive moduli of the human medial meniscus in the axial and radial directions at equilibrium and at a physiological strain rate.* Journal of Orthopaedic Research, 2008. **26**(7): p. 951-956.
57. Sweigart, M. A. and Athanasiou, K. A., *Biomechanical characteristics of the normal medial and lateral porcine knee menisci.* Proc Inst Mech Eng H, 2005. **219**(1): p. 53-62.

58. Lechner, K., Hull, M. L., and Howell, S. M., *Is the circumferential tensile modulus within a human medial meniscus affected by the test sample location and cross-sectional area?* Journal of Orthopaedic Research, 2000. **18**: p. 945-951.
59. Hodge, W. A., Carlson, K. L., Fijan, R. S., Burgess, S. B., Riley, P. O., Harris, W. H., and Mann, R. W., *Contact pressures from an instrumented hip endoprosthesis.* The Journal of Bone and Joint surgery, 1989. **71-A**: p. 1378-1386.
60. Kerin, A. J., Wisnom, M. R., and Adams, M. A., *The compressive strength of articular cartilage.* Proceedings of the Institution of Mechanical Engineers, 1998. **212**(H): p. 273-280.
61. Mow, V. C. and Guo, X. E., *Mechano-electrochemical properties of articular cartilage: their inhomogeneities and anisotropies.* Annual Review of Biomedical Engineering, 2002. **4**: p. 175-209.
62. Costi, J. J., Stokes, I. A., Gardner-Morse, M., Laible, J. P., Scoffone, H. M., and Iatridis, J. C., *Direct measurement of intervertebral disc maximum shear strain in six degrees of freedom: motions that place disc tissue at risk of injury.* J Biomech, 2007. **40**(11): p. 2457-2466.
63. Laible, C., Stein, D. A., and Kiridly, D. N., *Meniscal repair.* Journal of the American Academy of Orthopaedic Surgeons, 2013. **21**(4): p. 204-213.
64. Kim, S., Bosque, J., Meehan, J. P., Jamali, A., and Marder, R., *Increase in outpatient knee arthroscopy in the United States: a comparison of National Surveys of Ambulatory Surgery, 1996 and 2006.* J Bone Joint Surg Am, 2011. **93**(11): p. 994-1000.
65. Rubman, M. H., Noyes, F. R., and Barber-Westin, S. D., *Arthroscopic Repair of Meniscal Tears that Extend into the Avascular Zone.* The American Journal of Sports Medicine, 1998. **26**(1): p. 87-95.
66. Fairbank, T. J., *Knee joint changes after meniscectomy.* The Journal of Bone and Joint surgery, 1948. **30-B**(4): p. 664-670.
67. Roos, H., Lauren, M., Adalberth, T., Roos, E. M., Jonsson, K., and Lohmander, L. S., *Knee osteoarthritis after meniscectomy.* Arthritis and Rheumatism, 1998. **41**(4): p. 687-693.
68. von Porat, A., Roos, E. M., and Roos, H., *High prevalence of osteoarthritis 14 years after an anterior cruciate ligament tear in male soccer players: a study of radiographic and patient relevant outcomes.* Ann Rheum Dis, 2004. **63**(3): p. 269-273.
69. Lohmander, L. S., Ostenberg, A., Englund, M., and Roos, H., *High prevalence of knee osteoarthritis, pain, and functional limitations in female soccer players twelve years after anterior cruciate ligament injury.* Arthritis Rheum, 2004. **50**(10): p. 3145-3152.
70. Scott, G. A., Jolly, B. L., and Henning, C. E., *Combined posterior incision and arthroscopic intra-articular repair of the meniscus.* The Journal of Bone and Joint surgery, 1986. **68-A**(6): p. 847-861.
71. Messner, K., Lohmander, L. S., and Gillquist, J., *Cartilage mechanics and morphology, synovitis and proteoglycan fragments in rabbit joint fluid after prosthetic meniscal substitution.* Biomaterials, 1992. **14**(3): p. 163-168.
72. Messner, K., *Meniscal substitution with a Teflon-periosteal composite graft: a rabbit experiment.* Biomaterials, 1994. **15**(3): p. 223-230.
73. Kelly, B. T., Robertson, W., Potter, H. G., Deng, X. H., Turner, A. S., Lyman, S., Warren, R. F., and Rodeo, S. A., *Hydrogel meniscal replacement in the sheep knee: preliminary evaluation of chondroprotective effects.* Am J Sports Med, 2007. **35**(1): p. 43-52.
74. Vrancken, A. C. T., Hannink, G., Madej, W., Verdonschot, N., van Tienen, T. G., and Buma, P., *In Vivo Performance of a Novel, Anatomically Shaped, Total Meniscal Prosthesis Made of Polycarbonate Urethane: A 12-Month Evaluation in Goats.* Am J Sports Med, 2017. **45**(12): p. 2824-2834.
75. Schmidt, H., *New type of non-crystalline solids between inorganic and organic materials.* Journal of Non-Crystalline Solids, 1985. **73**: p. 681-691.
76. Hench, L. L. and West, J. K., *The sol-gel process.* Chemical Reviews, 1990. **90**: p. 33-72.

77. Livage, J. and Sanchez, C., *Sol-gel chemistry.* Journal of Non-Crystalline Solids, 1992. **145**: p. 11-19.
78. Fabbri, P., Cannillo, V., Sola, A., Dorigato, A., and Chiellini, F., *Highly porous polycaprolactone-45S5 Bioglass® scaffolds for bone tissue engineering.* Composites Science and Technology, 2010. **70**(13): p. 1869-1878.
79. Fiedler, T., Videira, A. C., Bartolo, P., Strauch, M., Murch, G. E., and Ferreira, J. M., *On the mechanical properties of PLC-bioactive glass scaffolds fabricated via BioExtrusion.* Materials Science and Engineering C, 2015. **57**: p. 288-293.
80. Niemela, T., Niiranen, H., Kellomaki, M., and Tormala, P., *Self-reinforced composites of bioabsorbable polymer and bioactive glass with different bioactive glass contents. Part I: Initial mechanical properties and bioactivity.* Acta Biomaterialia, 2005. **1**(2): p. 235-242.
81. Oyen, M. L., *Mechanical characterisation of hydrogel materials.* International Materials Reviews, 2013. **59**(1): p. 44-59.
82. Moutos, F. T., Freed, L. E., and Guilak, F., *A biomimetic three-dimensional woven composite scaffold for functional tissue engineering of cartilage.* Nature Materials, 2007. **6**(2): p. 162-167.
83. da Silva, M. A. and Dreiss, C. A., *Soft nanocomposites: nanoparticles to tune gel properties.* Polymer International, 2016. **65**(3): p. 268-279.
84. Wang, Q., Hou, R., Cheng, Y., and Fu, J., *Super-tough double-network hydrogels reinforced by covalently compositing with silica-nanoparticles.* Soft Matter, 2012. **8**(22).
85. Iurzhenko, M., Mamunya, Y., Boiteux, G., Lebedev, E., Davydenko, V., Seytre, G., and Matkovska, L., *Creep/stress relaxation of novel hybrid organic-inorganic polymer systems synthesized by joint polymerization of organic and inorganic oligomers.* Macromolecular Symposia, 2014. **341**(1): p. 51-56.
86. Jones, J. R., *Review of bioactive glass: from Hench to hybrids.* Acta Biomater, 2013. **9**(1): p. 4457-4486.
87. Valliant, E. M. and Jones, J. R., *Softening bioactive glass for bone regeneration: sol–gel hybrid materials.* Soft Matter, 2011. **7**(11): p. 5083.
88. Chaudhri, S. G., Rajai, B. H., and Singh, P. S., *Nanoscale homogeneity of silica–poly(vinyl alcohol) membranes by controlled cross-linking via sol–gel reaction in acidified and hydrated ethanol.* RSC Advances, 2015. **5**(81): p. 65862-65869.
89. Macon, A. L., Page, S. J., Chung, J. J., Amdursky, N., Stevens, M. M., Weaver, J. V., Hanna, J. V., and Jones, J. R., *A structural and physical study of sol-gel methacrylate-silica hybrids: intermolecular spacing dictates the mechanical properties.* Physical Chemistry Chemical Physics, 2015. **17**(43): p. 29124-29133.
90. Mahony, O., Tsigkou, O., Ionescu, C., Minelli, C., Ling, L., Hanly, R., Smith, M. E., Stevens, M. M., and Jones, J. R., *Silica-gelatin hybrids with tailorable degradation and mechanical properties for tissue regeneration.* Advanced Functional Materials, 2010. **20**(22): p. 3835-3845.
91. Gabrielli, L., Russo, L., Poveda, A., Jones, J. R., Nicotra, F., Jimenez-Barbero, J., and Cipolla, L., *Epoxide opening versus silica condensation during sol-gel hybrid biomaterial synthesis.* Chemistry, 2013. **19**(24): p. 7856-7864.
92. Gabrielli, L., Connell, L., Russo, L., Jiménez-Barbero, J., Nicotra, F., Cipolla, L., and Jones, J. R., *Exploring GPTMS reactivity against simple nucleophiles: chemistry beyond hybrid materials fabrication.* RSC Adv., 2014. **4**(4): p. 1841-1848.
93. Poologasundarampillai, G., Yu, B., Tsigkou, O., Valliant, E., Yue, S., Lee, P. D., Hamilton, R. W., Stevens, M. M., Kasuga, T., and Jones, J. R., *Bioactive silica–poly(γ-glutamic acid) hybrids for bone regeneration: effect of covalent coupling on dissolution and mechanical properties and fabrication of porous scaffolds.* Soft Matter, 2012. **8**(17): p. 4822.

94. Trujillo, S., Pérez-Román, E., Kyritsis, A., Gómez Ribelles, J. L., and Pandis, C., *Organic-inorganic bonding in chitosan-silica hybrid networks: Physical properties.* Journal of Polymer Science Part B: Polymer Physics, 2015. **53**(19): p. 1391-1400.
95. Connell, L. S., Romer, F., Suárez, M., Valliant, E. M., Zhang, Z., Lee, P. D., Smith, M. E., Hanna, J. V., and Jones, J. R., *Chemical characterisation and fabrication of chitosan–silica hybrid scaffolds with 3-glycidoxypropyl trimethoxysilane.* J. Mater. Chem. B, 2014. **2**(6): p. 668-680.
96. Valliant, E. M., Romer, F., Wang, D., McPhail, D. S., Smith, M. E., Hanna, J. V., and Jones, J. R., *Bioactivity in silica/poly(gamma-glutamic acid) sol-gel hybrids through calcium chelation.* Acta Biomater, 2013. **9**(8): p. 7662-7671.
97. Martín, A. I., Salinas, A. J., and Vallet-Regí, M., *Bioactive and degradable organic–inorganic hybrids.* Journal of the European Ceramic Society, 2005. **25**(16): p. 3533-3538.
98. Woodruff, M. A. and Hutmacher, D. W., *The return of a forgotten polymer : Polycaprolactone in the 21st century.* Progress in Polymer Science, 2010. **25**(10): p. 1217–1256.
99. Rhee, S.-H., *Bone-like apatite-forming ability and mechanical properties of poly(ε-caprolactone)/silica hybrid as a function of poly(ε-caprolactone) content.* Biomaterials, 2004. **25**(7-8): p. 1167-1175.
100. Rhee, S.-H., Lee, Y.-H., and Lim, B.-S., *Evaluation of a novel poly(e-caprolactone)-organosiloxane hybrid material for the potential application as a bioactive and degradable bone substitute.* Biomacromolecules, 2004. **5**: p. 1575-1579.
101. Tian, D., Dubois, P., and Jerome, R., *A new poly(e-caprolactone) containing hybrid ceramer prepared by the sol-gel process.* Polymer, 1996. **37**(17): p. 3983-3987.
102. Hendrikx, S., Kascholke, C., Flath, T., Schumann, D., Gressenbuch, M., Schulze, F. P., Hacker, M. C., and Schulz-Siegmund, M., *Indirect rapid prototyping of sol-gel hybrid glass scaffolds for bone regeneration - Effects of organic crosslinker valence, content and molecular weight on mechanical properties.* Acta Biomaterialia, 2016. **35**: p. 318-329.
103. Chung, J. J., Fujita, Y., Li, S., Stevens, M. M., Kasuga, T., Georgiou, T. K., and Jones, J. R., *Biodegradable inorganic-organic hybrids of methacrylate star polymers for bone regeneration.* Acta Biomater, 2017. **54**: p. 411-418.
104. Maçon, A. L. B., Li, S., Chung, J. J., Nommeots-Nomm, A., Solanki, A. K., Stevens, M. M., and Jones, J. R., *Ductile silica/methacrylate hybrids for bone regeneration.* Journal of Materials Chemistry B, 2016. **4**(36): p. 6032-6042.
105. Fidalgo, A. and Ilharco, L., *Hybrid silica gel-polytetrahydrofuran thin films.* Journal of Sol-Gel Science and Technology, 1998. **13**: p. 433-437.
106. Huang, H.-H., Wilkes, G. L., and Carlson, J. G., *Structure-property behaviour of hybrid materials incorporating tetraoxysilane with mulifunctional poly(tetramethylene oxide).* Polymer, 1989. **30**: p. 2001-2012.
107. Jewrajka, S. K., Kang, J., Erdodi, G., Kennedy, J. P., Yilgor, E., and Yilgor, I., *Polyisobutylene-based polyurethanes. II. Polyureas containing mixed PIB/PTMO soft segments.* Journal of Polymer Science Part A: Polymer Chemistry, 2009. **47**(11): p. 2787-2797.
108. Miyata, N., Fuke, K.-i., Chen, Q., Kawashita, M., Kokubo, T., and Nakamura, T., *Apatite-forming ability and mechanical properties of PTMO-modified CaO–SiO2 hybrids prepared by sol–gel processing: effect of CaO and PTMO contents.* Biomaterials, 2002. **23**(3033-3040).
109. Kamitakahara, M., Kawashita, M., Miyata, N., Kokubo, T., and Nakamura, T., *Preparation of bioactive flexible poly(tetramethylene oxide) (PTMO)-CaO-Ta2O5 hybrids.* J Mater Sci Mater Med, 2007. **18**(6): p. 1117-1124.
110. Tallia, F., *3-D printed flexible hybrids for tissue regeneration*, in *Materials*. 2016, Imperial College London.
111. Pol, B. J. M., Van Wachem, P. B., Van Luyn, M. J. A., Van der Does, L., and Bantjes, A., *In vivo testing of crosslinked polyethers. I. Tissue reactions and biodegradation.* Journal of Biomedical Materials Research, 1996. **32**: p. 307-320.

112. Pol, B. J. M., van Wachem, P. B., van der Does, L., and Bantjes, A., *In vivo testing of crosslinked polyethers. II. Weight loss, IR analysis, and swelling behavior after implantation.* Journal of biomedical Materials Research, 1996. **32**: p. 321-331.
113. Chung, J. J., Li, S., Stevens, M. M., Georgiou, T. K., and Jones, J. R., *Tailoring Mechanical Properties of Sol–Gel Hybrids for Bone Regeneration through Polymer Structure.* Chemistry of Materials, 2016. **28**(17): p. 6127-6135.
114. Phillips, J. E., Burns, K. L., Le Doux, J. M., Guldberg, R. E., and Garcia, A. J., *Engineering graded tissue interfaces.* PNAS, 2008. **105**(34): p. 12170-12175.
115. Di Luca, A., Longoni, A., Criscenti, G., Lorenzo-Moldero, I., Klein-Gunnewiek, M., Vancso, J., van Blitterswijk, C., Mota, C., and Moroni, L., *Surface energy and stiffness discrete gradients in additive manufactured scaffolds for osteochondral regeneration.* Biofabrication, 2016. **8**(1): p. 015014.
116. Cox, S. C., Thornby, J. A., Gibbons, G. J., Williams, M. A., and Mallick, K. K., *3D printing of porous hydroxyapatite scaffolds intended for use in bone tissue engineering applications.* Mater Sci Eng C Mater Biol Appl, 2015. **47**: p. 237-247.
117. Petit, C., Tulliani, J. M., Tadier, S., Meille, S., Chevalier, J., and Palmero, P., *Novel calcium phosphate/PCL graded samples: Design and development in view of biomedical applications.* Mater Sci Eng C Mater Biol Appl, 2019. **97**: p. 336-346.
118. Banik, S. J., Fernandes, N. J., Thomas, P. C., and Raghavan, S. R., *A New Approach for Creating Polymer Hydrogels with Regions of Distinct Chemical, Mechanical, and Optical Properties.* Macromolecules, 2012. **45**(14): p. 5712-5717.
119. Chatterjee, K., Lin-Gibson, S., Wallace, W. E., Parekh, S. H., Lee, Y. J., Cicerone, M. T., Young, M. F., and Simon, C. G., Jr., *The effect of 3D hydrogel scaffold modulus on osteoblast differentiation and mineralization revealed by combinatorial screening.* Biomaterials, 2010. **31**(19): p. 5051-5062.
120. Marklein, R. A. and Burdick, J. A., *Spatially controlled hydrogel mechanics to modulate stem cell interactions.* Soft Matter, 2010. **6**(1): p. 136-143.
121. Burdick, J. A., Khademhosseini, A., and Langer, R., *Fabrication of gradient hydrogels using a microfluidics/ photopolymerization process.* The ACS Journal of Surfaces and Colloids, 2004. **20**(13): p. 5153-5156.
122. Kang, H. W., Lee, S. J., Ko, I. K., Kengla, C., Yoo, J. J., and Atala, A., *A 3D bioprinting system to produce human-scale tissue constructs with structural integrity.* Nat Biotechnol, 2016. **34**(3): p. 312-319.
123. Li, C., Ouyang, L., Pence, I. J., Moore, A. C., Lin, Y., Winter, C. W., Armstrong, J. P. K., and Stevens, M. M., *Buoyancy-Driven Gradients for Biomaterial Fabrication and Tissue Engineering.* Adv Mater, 2019. **31**(17): p. e1900291.
124. Hu, Z., Chen, Y., Wang, C., Zheng, Y., and Li, Y., *Polymer gels with engineered environmentally responsive surfacepatterns.* Nature, 1998. **393**: p. 149-152.
125. Gharazi, S., Zarket, B. C., DeMella, K. C., and Raghavan, S. R., *Nature-Inspired Hydrogels with Soft and Stiff Zones that Exhibit a 100-Fold Difference in Elastic Modulus.* ACS Appl Mater Interfaces, 2018. **10**(40): p. 34664-34673.
126. Nerurkar, N. L., Elliott, D. M., and Mauck, R. L., *Mechanics of oriented electrospun nanofibrous scaffolds for annulus fibrosus tissue engineering.* J Orthop Res, 2007. **25**(8): p. 1018-1028.
127. Gwynne, J. H., Oyen, M. L., and Cameron, R. E., *Preparation of polymeric samples containing a graduated modulus region and development of nanoindentation linescan techniques.* Polymer Testing, 2010. **29**(4): p. 494-502.
128. Gwynne, J. H. and Cameron, R. E., *Using small angle X-ray scattering to investigate the variation in composition across a graduated region within an intervertebral disc prosthesis.* J Mater Sci Mater Med, 2010. **21**(2): p. 787-795.

129. Hulbert, S. F., Young, F. A., Mathews, R. S., Klawitter, J. J., Talbert, C. D., and Stelling, F. H., *Potential of ceramic materials as permanently implantable skeletal prostheses.* Journal of Biomedical Materials Research, 1970. **4**: p. 433-456.
130. Sobral, J. M., Caridade, S. G., Sousa, R. A., Mano, J. F., and Reis, R. L., *Three-dimensional plotted scaffolds with controlled pore size gradients: Effect of scaffold geometry on mechanical performance and cell seeding efficiency.* Acta Biomater, 2011. **7**(3): p. 1009-1018.
131. Nelson, M., *3D Silica-gelatin hybrid scaffolds for tissue regeneration*, in *Materials*. 2016, Imperial College London.
132. Jones, J. R., Ehrenfried, L. M., and Hench, L. L., *Optimising bioactive glass scaffolds for bone tissue engineering.* Biomaterials, 2006. **27**(7): p. 964-973.
133. Nommeots-Nomm, A., Labbaf, S., Devlin, A., Todd, N., Geng, H., Solanki, A. K., Tang, H. M., Perdika, P., Pinna, A., Ejeian, F., Tsigkou, O., Lee, P. D., Esfahani, M. H. N., Mitchell, C. A., and Jones, J. R., *Highly degradable porous melt-derived bioactive glass foam scaffolds for bone regeneration.* Acta Biomater, 2017. **57**: p. 449-461.
134. Fu, Q., Rahaman, M. N., Bal, B. S., Brown, R. F., and Day, D. E., *Mechanical and in vitro performance of 13-93 bioactive glass scaffolds prepared by a polymer foam replication technique.* Acta Biomaterialia, 2008. **4**(6): p. 1854-1864.
135. Nommeots-Nomm, A., *3D printing versus foaming of melt-derived bioactive glasses for bone regeneration*, in *Materials*. 2015, Imperial College London
136. Fu, Q., Saiz, E., and Tomsia, A. P., *Bioinspired strong and highly porous glass scaffolds.* Advanced Functional Materials, 2011. **21**(6): p. 1058-1063.
137. Gao, C., Rahaman, M. N., Gao, Q., Teramoto, A., and Abe, K., *Robotic deposition and in vitro characterization of 3D gelatin-bioactive glass hybrid scaffolds for biomedical applications.* Journal of biomedical materials research. Part A, 2013. **101**(7): p. 2027-2037.
138. Poologasundarampillai, G., Ionescu, C., Tsigkou, O., Murugesan, M., Hill, R. G., Stevens, M. M., Hanna, J. V., Smith, M. E., and Jones, J. R., *Synthesis of bioactive class II poly(γ-glutamic acid)/silica hybrids for bone regeneration.* Journal of Materials Chemistry, 2010. **20**(40): p. 8952.
139. Hind, A. R., Bhargava, S. K., and McKinnon, A., *At the solid/liquid interface: FTIR/ATR - the tool of choice.* Advances in Colloid and Interface Science, 2001. **93**: p. 91-114.
140. Callister, W. D. and Rethwisch, D. G., *Materials science and engineering: an introduction*. 2007, New York: Wiley.
141. Schneider, C. A., Rasband, W. S., and Eliceiri, K. W., *NIH Image to ImageJ 25 years of image analysis.* Nature methods, 2012. **9**(7): p. 671-675.
142. GmbH, L., *DaVis 8.4 Product-Manual Digital Volume Correlation*. 2017: Germany.
143. Malz, F. and Jancke, H., *Validation of quantitative NMR.* Journal of Pharmaceutrical and Biomedical Analysis, 2005. **38**: p. 813-823.
144. ASTM, *D1708-13: Standard test method for tensile properties of plastics by use of microtensile specimens*. 2013.
145. *Biological evalutation of medical devices*, in *Part 5: Tests for in vitro cytoxicity*. 2009, British Standards.
146. *Biological evaluation of medical devices*, in *Part 12: Sample preparation and reference materials*. 2012, British Standards.
147. Fulmer, G. R., Miller, A. J. M., Sherden, N. H., Gottlieb, H. E., Nudelman, A., Stoltz, B. M., Bercaw, J. E., and Goldberg, K. I., *NMR Chemical Shifts of Trace Impurities: Common Laboratory Solvents, Organics, and Gases in Deuterated Solvents Relevant to the Organometallic Chemist.* Organometallics, 2010. **29**(9): p. 2176-2179.
148. Nuyken, O. and Pask, S., *Ring-Opening Polymerization—An Introductory Review.* Polymers, 2013. **5**(2): p. 361-403.
149. Tian, D., Blacher, S., Dubois, P., and Jérôme, R., *Biodegradable and biocompatible inorganic-organic hybrid materials.* Polymer, 1997. **39**(4): p. 855-864.

150. Lee, H. J., Oh, K. S., and Choi, C. K., *The mechanical properties of the SiOC(-H) composite thin films with a low dielectric constant.* Surface and Coatings Technology, 2003. **171**(1-3): p. 296-301.
151. Tsuchiya, I., *Infrared spectroscopic study of hydroxyl groups on silica surfaces.* Journal of Physical Chemistry, 1982. **86**: p. 4107-4112.
152. *NIST Standard Reference Database 69: NIST Chemistry WebBook*. https://doi.org/10.18434/T4D303.
153. Poologasundarampillai, G., Yu, B., Tsigkou, O., Wang, D., Romer, F., Bhakhri, V., Giuliani, F., Stevens, M. M., McPhail, D. S., Smith, M. E., Hanna, J. V., and Jones, J. R., *Poly(gamma-glutamic acid)/silica hybrids with calcium incorporated in the silica network by use of a calcium alkoxide precursor.* Chemistry, 2014. **20**(26): p. 8149-8160.
154. ASTM, *D1621-16: Standard test method for compressive properties of rigid cellular plastics*. 2016.
155. Mecholsky, J. J., Rice, R. W., and Freiman, S. W., *Prediction of fracture energy and flaw size in glasses from measurements of mirror size.* Journal of the American Ceramics Society, 1974. **57**(10): p. 440-443.
156. Almeida, J. C., Lancastre, J., Vaz Fernandes, M. H., Margaca, F. M., Ferreira, L., and Miranda Salvado, I. M., *Evaluating structural and microstructural changes of PDMS-SiO2 hybrid materials after sterilization by gamma irradiation.* Mater Sci Eng C Mater Biol Appl, 2015. **48**: p. 354-358.
157. Ferreira, S. A., Motwani, M. S., Faull, P. A., Seymour, A. J., Yu, T. T. L., Enayati, M., Taheem, D. K., Salzlechner, C., Haghighi, T., Kania, E. M., Oommen, O. P., Ahmed, T., Loaiza, S., Parzych, K., Dazzi, F., Varghese, O. P., Festy, F., Grigoriadis, A. E., Auner, H. W., Snijders, A. P., Bozec, L., and Gentleman, E., *Bi-directional cell-pericellular matrix interactions direct stem cell fate.* Nat Commun, 2018. **9**(1): p. 4049.
158. Mazor, E. and Zilberman, M., *Effect of gamma-irradiation sterilization on the physical and mechanical properties of a hybrid wound dressing.* Polymers for Advanced Technologies, 2017. **28**(1): p. 41-52.
159. Kwon, H. J., Yasuda, K., Ohmiya, Y., Honma, K., Chen, Y. M., and Gong, J. P., *In vitro differentiation of chondrogenic ATDC5 cells is enhanced by culturing on synthetic hydrogels with various charge densities.* Acta Biomater, 2010. **6**(2): p. 494-501.
160. Deliormanlı, A. M. and Türk, M., *Investigation the in vitro biological performance of graphene/bioactive glass scaffolds using MC3T3-E1 and ATDC5 cells.* Materials Technology, 2018. **33**(14): p. 854-864.
161. Miranda, E. S., Silva, T. H., Reis, R. L., and Mano, J. F., *Nanostructured natural-based polyelectrolyte multilayers to agglomerate chitosan particles into scaffolds for tissue engineering.* Tissue Eng Part A, 2011. **17**(21-22): p. 2663-2674.
162. *GOM Correlate Rev. 111035, Build 2018-07-11*. 2018.
163. Arola, D., *Fatigue testing of biomaterials and their interfaces.* Dent Mater, 2017. **33**(4): p. 367-381.
164. Sutton, M. A., Orteu, J. J., and Schreier, H. W., *Image correlation for shape, motion and deformation meaasurements*. 2009, New York: Springer Science.
165. Wong, J. Y., Velasco, A., Rajagopalan, P., and Pham, Q., *Directed movement of vascular smooth muscle cells on gradient-compliant hydrogels.* Langmuir, 2003. **19**: p. 1908-1913.
166. Gillani, R., Ercan, B., Qiao, A., and Webster, T. J., *Nanofunctionalized zirconia and barium sulfate particles as bone cement additives.* International Journal of Nanomedicine, 2010. **5**: p. 1-11.
167. Franco, J., Hunger, P., Launey, M. E., Tomsia, A. P., and Saiz, E., *Direct write assembly of calcium phosphate scaffolds using a water-based hydrogel.* Acta Biomaterialia, 2010. **6**(1): p. 218-228.

168. Newell, N., Little, J. P., Christou, A., Adams, M. A., Adam, C. J., and Masouros, S. D., *Biomechanics of the human intervertebral disc: A review of testing techniques and results.* J Mech Behav Biomed Mater, 2017. **69**: p. 420-434.
169. Newell, N., Grant, C. A., Keenan, B. E., Izatt, M. T., Pearcy, M. J., and Adam, C. J., *Quantifying Progressive Anterior Overgrowth in the Thoracic Vertebrae of Adolescent Idiopathic Scoliosis Patients: A Sequential Magnetic Resonance Imaging Study.* Spine, 2016. **41**(7): p. E382-387.
170. Wu, C., Luo, Y., Cuniberti, G., Xiao, Y., and Gelinsky, M., *Three-dimensional printing of hierarchical and tough mesoporous bioactive glass scaffolds with a controllable pore architecture, excellent mechanical strength and mineralization ability.* Acta Biomater, 2011. **7**(6): p. 2644-2650.
171. Ting, H.-K., *Role of phosphate and calcium in sol-gel bioactive glasses and silica/poly(caprolactone) hybrids*, in *Materials*. 2016, Imperial College London.
172. Park, G. E., Pattison, M. A., Park, K., and Webster, T. J., *Accelerated chondrocyte functions on NaOH-treated PLGA scaffolds.* Biomaterials, 2005. **26**(16): p. 3075-3082.
173. Chang, H.-I. and Wang, Y., *Cell Responses to Surface and Architecture of Tissue Engineering Scaffolds*, in *Regenerative Medicine and Tissue Engineering - Cells and Biomaterials*, D. Eberli, Editor. 2011, IntechOpen.
174. Eshraghi, S. and Das, S., *Mechanical and microstructural properties of polycaprolactone scaffolds with one-dimensional, two-dimensional, and three-dimensional orthogonally oriented porous architectures produced by selective laser sintering.* Acta Biomater, 2010. **6**(7): p. 2467-2476.
175. Lu, H. H., El-Amin, S. F., Scott, K. D., and Laurencin, C. T., *Three-dimensional, bioactive, biodegradable, polymer–bioactive glass composite scaffolds with improved mechanical properties support collagen synthesis and mineralization of human osteoblast-like cells in vitro.* Journal of Biomedical Materials, 2003. **64A**(3): p. 465-474.
176. Jurvelin, J. S., Buschmann, M. D., and Hunziker, E. B., *Optical and mechanical determination of poisson's ratio of adult bovine humeral articular cartilage.* Journal of Biomechanics, 1997. **30**(3): p. 235-241.
177. Luo, Y., McCann, L., Ingham, E., Jin, Z. M., Ge, S., and Fisher, J., *Polyurethane as a potential knee hemiarthroplasty biomaterial: an in-vitro simulation of its tribological performance.* Proc Inst Mech Eng H, 2010. **224**(3): p. 415-425.
178. Delamarter, R. B., Fribourg, D. M., Kanim, L. E. A., and Bae, H., *ProDisc artificial total lumbar disc replacement: Introduction and early results from the United States clinical trial.* Spine, 2003. **28**: p. S167-S175.
179. Link, H. D., *History, design and biomechanics of the LINK SB Charite artificial disc.* European Spine Journal, 2002. **11**: p. S98-S105.
180. Putzier, M., Funk, J. F., Schneider, S. V., Gross, C., Tohtz, S. W., Khodadadyan-Klostermann, C., Perka, C., and Kandziora, F., *Charite total disc replacement--clinical and radiographical results after an average follow-up of 17 years.* Eur Spine J, 2006. **15**(2): p. 183-195.
181. Stokes, I. A. F. and Gardner-Morse, M., *Spinal stiffness increases with axial load: another stabilizing consequence of muscle action.* Journal of Electromyography and Kinesiology, 2003. **13**(4): p. 397-402.
182. Newell, N. *Material Properties of Human Lumbar Intervertebral Discs Across Strain Rates - Experimental Data*. 2019 DOI: http://dx.doi.org/10.17632/29hd3mdfyc.1#file-8f3ff09a-7c63-4590-bb9d-d0f0938db893.